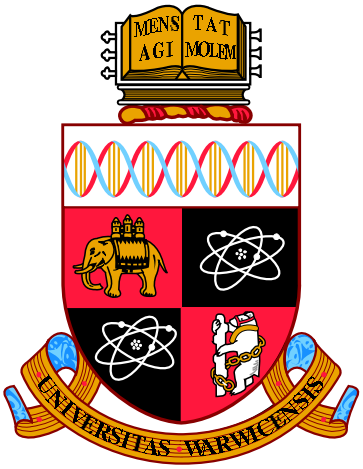

Multiple Scattering and Particle Identification in the Muon Ionisation Cooling Experiment

by

Celeste Pidcott

Thesis

Submitted to the University of Warwick

for the degree of

Doctor of Philosophy

Department of Physics

July 2017

THE UNIVERSITY OF WARWICK

Contents

List of Tables **iv**

List of Figures **viii**

Acknowledgments **xxiv**

Declarations **xxvi**

Abstract **xxvii**

Chapter 1 Introduction **1**

1.1 Neutrino Physics 2
1.1.1 Discovery 2
1.1.2 Neutrino Flavour Oscillations 2
1.2 Current state of the field 6
1.2.1 Measuring the absolute neutrino mass 6
1.2.2 Oscillation Experiments 8
1.2.3 Status of measurements 8
1.2.4 Future Facilities 10
1.3 Neutrino Factory 10
1.3.1 Proton Driver 12
1.3.2 Target 13
1.3.3 Decay Channel, Buncher and Phase Rotation 13
1.3.4 Cooling 13
1.3.5 Acceleration 13
1.3.6 Storage Rings 13
1.4 Accelerator Physics 14
1.4.1 Emittance 14
1.4.2 Traditional Cooling Methods 16

1.5 Ionisation Cooling 17

Chapter 2 The Muon Ionisation Cooling Experiment 20

2.1 Introduction 20
2.2 Beamline 21
2.2.1 ISIS 21
2.2.2 Target 22
2.2.3 Beamline 23
2.3 Cooling Channel 26
2.3.1 Absorber Focus Coil (AFC) 27
2.3.2 RF Cavities 28
2.4 Overview of Detectors 29
2.4.1 Scintillating Fibre Trackers 29
2.4.2 PID Detectors 31
2.5 Software 39
2.6 Controls and Data Acquisition 41
2.6.1 Controls and Monitoring 41
2.6.2 DAQ 42

Chapter 3 Global Particle Identification 43

3.1 Introduction 43
3.1.1 Global Reconstruction in MAUS 43
3.1.2 Datastructure Nomenclature 46
3.1.3 Detectors 46
3.2 Global PID 48
3.2.1 Framework 48
3.2.2 Log-Likelihoods 50
3.3 Commissioning PID 51
3.3.1 Variables 51
3.4 PID at Step IV 63
3.4.1 Variables 63
3.5 Determining the performance of the Global PID 75
3.5.1 Efficiency and Purity 75
3.5.2 Consistency between variables 76
3.5.3 Performance of Commissioning PID 77
3.5.4 Performance of Step IV PID 86
3.6 Results of Commissioning PID 96
3.6.1 For MC data set 96

3.6.2 For real data . . . 97
3.7 Results of Step IV PID for MC dataset . . . 98
3.8 Conclusions . . . 100

Chapter 4 Measurement of Multiple Scattering in LiH 101
4.1 Introduction . . . 101
4.1.1 Multiple Coulomb Scattering . . . 101
4.1.2 MuScat . . . 103
4.1.3 Multiple Coulomb Scattering in MICE . . . 104
4.2 Description of field on measurement . . . 106
4.2.1 Application of Field-On Method to Field-Off Data . . . 107
4.2.2 Comparison of Raw Scattering Distributions for Monte Carlo and Reconstructed Monte Carlo . . . 107
4.2.3 Measurement Procedure . . . 110
4.2.4 Unfolding Methods . . . 115
4.2.5 Systematics . . . 118
4.2.6 Predictions of θ_0 and θ_{3D} from PDG Equations . . . 121
4.3 Field-Off Measurement . . . 122
4.3.1 Particle selection . . . 122
4.3.2 Systematics . . . 122
4.3.3 Analysis . . . 122
4.4 Field-On Measurement . . . 131
4.4.1 Systematics . . . 131
4.4.2 Analysis . . . 134
4.5 Conclusions . . . 138

Chapter 5 Conclusions 139

Appendix A Global PID Consistency Plots 141
A.1 Commissioning Variable Consistency Plots (Monte Carlo) . . . 141
A.2 Commissioning Variable Consistency Plots (Data) . . . 159
A.3 Step IV Downstream Variable Consistency Plots . . . 177

Appendix B Multiple Coulomb Scattering Error Tables 184

List of Tables

1.1 Fermion masses and electric charges 2
1.2 Current best-fit values and 3σ allowed ranges of the netrino oscillation parameters. The values (values in brackets) correspond to the normal (inverted) mass hierarchy. $\Delta m^2 = m_3^2 - (m_2^2 + m_1^2)/2$, and is greater than zero for the normal mass hierarchy, less than zero for the inverted hierarchy [21]. 9

3.1 Commissioning PID variables. 54
3.2 Step IV PID variables. 66
3.3 Optimal settings for min/max values of commissioning PID variables based on efficiency/purity studies for a 3mm 200 MeV/c muon beam. One dimensional variables have only maximum and minimum X values, while two dimensional variables have both X and Y values. . . . 83
3.4 Consistency between ComPIDVars on MC. 84
3.5 Consistency between ComPIDVars on data. 86
3.6 Optimal settings for min/max values of Step IV PID variables based on efficiency/purity studies for a 6 mm 200 MeV/c pion beam. One dimensional variables have only maximum and minimum X values, while two dimensional variables have both X and Y values. No settings are given for PIDVarI as at the momentum studied the sample only contained 20 tracks that produced hits in CkovA and the trackers. 91
3.7 Consistency between upstream PIDVars for MC. 94
3.8 Consistency between downstream PIDVars for MC. 94
3.9 Results of PID for a MC 200 MeV/c, 3 mm muon beam. 96
3.10 Results of PID for all 200 MeV/c muon LiH runs. 97
3.11 Results of PID for a 200 MeV/c, 6 mm pion beam. 99

4.1 Scattering contributions from materials in the MICE channel. The combined thickness of four absorber windows increases from 0.72 to 36 mm as the distance from the beam centre increases, hence the range given for scattering due to the absorber. 105
4.2 Projected and space angles for Monte Carlo and reconstructed Monte Carlo distributions for field-on and field-off measurements, with estimates for the corrections required. 109
4.3 Predicted values of θ_0^{RMS} and θ_{3D}^{RMS} for helical (200 MeV/c) and straight (175 MeV/c) tracks for an empty and a LiH absorber. . . . 122
4.4 Summary of systematic errors for both an empty and LiH absorber, for straight MC tracks. 123
4.5 Summary of systematic errors for both an empty and LiH absorber for data. 124
4.6 Summary of scattering distributions for an empty channel in the absence of fields for reconstructed MC and unfolded distributions, and for Monte Carlo truth. Systematic and statistical errors combined for reconstructed and unfolded results, statistical only for Monte Carlo. 125
4.7 Summary of scattering distributions for a LiH absorber in the absence of fields for reconstructed and unfolded distributions, and for Monte Carlo truth. Systematic and statistical errors combined for reconstructed and unfolded results, statistical only for Monte Carlo. 127
4.8 Summary of scattering distributions for an empty absorber in the absence of fields for data and unfolded distributions. Systematic and statistical errors combined for reconstructed and unfolded results, statistical only for Monte Carlo. 129
4.9 Summary of scattering distributions for a LiH absorber in the absence of fields for data and unfolded distributions. Systematic and statistical errors combined for reconstructed and unfolded results, statistical only for Monte Carlo. 131
4.10 Summary of systematic errors for both an empty and LiH absorber, for helical MC tracks. 133
4.11 Summary of scattering distributions for an empty channel in the presence of fields. Systematic and statistical errors combined for reconstructed and unfolded results, statistical only for Monte Carlo. . . . 134
4.12 Summary of scattering distributions for a LiH absorber in the presence of fields. Systematic and statistical errors combined for reconstructed and unfolded results, statistical only for Monte Carlo. . . . 136

B.1 $\theta_{X,Y}$ bin contents for an empty absorber for straight MC and data. Statistical errors only. 185
B.2 Systematic errors on $\theta_{X,Y}$ bin contents for an empty absorber for data. 186
B.3 Systematic errors on $\theta_{X,Y}$ bin contents for an empty absorber for straight MC tracks. 187
B.4 $\theta_{X,Y}$ bin contents for an empty absorber for straight MC and data. Statistical and systematic errors combined. 188
B.5 θ_{3D} bin contents for an empty absorber for straight MC and data. Statistical errors only. 189
B.6 Systematic errors on θ_{3D} bin contents for an empty absorber for straight MC tracks. 190
B.7 θ_{3D} bin contents for empty absorber for straight MC and data. Systematic and statistical errors combined. 191
B.8 $\theta_{X,Y}$ bin contents for LiH for straight MC and data. Statistical errors only. 192
B.9 Systematic errors on $\theta_{X,Y}$ bin contents for LiH for straight MC tracks. 193
B.10 $\theta_{X,Y}$ bin contents for LiH for straight MC and data. Systematic and statistical errors combined. 194
B.11 θ_{3D} bin contents for LiH for straight MC and data. Statistical errors only. 195
B.12 Systematic errors on θ_{3D} measurement for straight MC tracks through LiH. 196
B.13 Systematic errors on θ_{3D} bin contents for LiH for data. Errors for denstiy taken from MC. 197
B.14 θ_{3D} bin contents for LiH for straight MC and data. Systematic and statistical errors combined. 198
B.15 $\theta_{X,Y}$ bin contents for an empty absorber for helical MC tracks. Statistical errors only. 199
B.16 Systematic errors on $\theta_{X,Y}$ bin contents for an empty absorber for helical MC tracks. 200
B.17 $\theta_{X,Y}$ bin contents for an empty absorber for helical MC tracks. Statistical and systematic errors combined. 201
B.18 θ_{3D} bin contents for an empty absorber for helical MC. Statistical errors only. 202
B.19 Systematic errors on θ_{3D} bin contents for an empty absorber for helical MC tracks. 203

B.20 θ_{3D} bin contents for an empty absorber for helical MC. Systematic and statistical errors combined. 204
B.21 $\theta_{X,Y}$ bin contents for LiH for helical MC tracks. Statistical errors only. 205
B.22 Systematic errors on $\theta_{X,Y}$ bin contents for LiH for helical MC tracks. 206
B.23 $\theta_{X,Y}$ bin contents for LiH for helical MC tracks. Statistical and systematic errors combined. 207
B.24 θ_{3D} bin contents for LiH for helical MC. Statistical errors only. . . . 208
B.25 Systematic errors on θ_{3D} bin contents for LiH for helical MC tracks. 209
B.26 θ_{3D} bin contents for LiH for helical MC. Systematic and statistical errors combined. 210

List of Figures

1.1 The relative decay amplitude for tritium, as a function of the electron energy, is shown in the left hand plot. The right hand plot shows the difference between the the electron and anti-neutrino energy, which can be measured in the high energy region in the tail of the electron energy distribution, where the neutrino is non-relativistic [11]. 7

1.2 Neutrino mass eigenstates for the Normal (left) and Inverted (right) hierarchies [22]. 9

1.3 Physics reach of different potential facilities for the discovery of δ_{CP} (top left), the mass hierarchy (top right), and $\sin^2 2\theta_{13}$ (bottom). BB refers to β beams, SPL and LBNE are proposed Super Beam experiments, MIND LE is a low energy Neutrino Factory, IDS-NF is the International Design Study for the Neutrino Factory[24]. 11

1.4 Neutrino Factory baseline schematic from the International Scoping Study for a Neutrino Factory. [24]. 12

1.5 Plot of emittance, ε, in trace space, showing the relation to the Twiss parameters, α, β and γ. [30]. 15

1.6 Changes to the transverse and longitudinal momentum due to energy loss (1) and multiple scattering (2) in the ionising material, and reacceleration (3) in the RF cavity. 18

1.7 Simulated change in emittance $\Delta\varepsilon$ for several materials as a function of the nominal transverse emittance ε of the simulated beam, taken from [34]. 19

2.1 MICE Step IV layout. The muon beam enters from the left. 21

2.2 Demonstration of Ionisation Cooling layout. The muon beam enters from the left. 21

2.3 The position of the MICE target and beamline with respect to the ISIS synchrotron. 22

2.4 MICE target mechanism. 23
2.5 Step I configration of the MICE beamline and PID detectors. In the Step IV configuration, and for the Demonstration of Ionisation Cooling, the cooling channel will be between TOF1 and TOF2, with the other downstream detectors (KL and EMR) immediately downstream of TOF2. The distance between D2 and the EMR is approximately 21.5 metres. 24
2.6 Pneumatically operated proton absorber. 25
2.7 MICE diffuser installed within the upstream spectrometer solenoid. . 25
2.8 Rendering of the Step IV cooling channel. 26
2.9 The absorbers to be studied in Step IV 27
2.10 Focus Coil. 28
2.11 One of the MICE scintillating fibre trackers. 29
2.12 The arrangement of the doublet layers is shown in figure (a). The inner circle is the active area of the tracker; the outer is the solenoid bore. The doublet layer structure of the fibres is shown in (b) [36]. . 30
2.13 Spectrometer solenoids installed in the MICE hall. The focus coil module is between them. 31
2.14 Residuals of track fit in the trackers for a 6 mm, 200 MeV/c beam, taken from [36]. 32
2.15 Time of flight between TOF0 and TOF1 for a muon beam (left) and pion beam (right) [38]. In the muon beam, a small electron peak can be seen at 26 ns, while the pion contamination of the beam is contained within the muon peak. For the pion beam, the electron, muon, and pion peaks are clearly separated, at 26, 29, and 31 ns respectively. 33
2.16 TOF2 in front of the KL. 33
2.17 Cherenkov detectors in MICE 34
2.18 The number of photoelectrons produced in the Cherenkovs with respect to the time of flight. A clear separation between the different particle species can be seen [25]. 35
2.19 The efficiencies of CkovB (solid line) and CkovA (dashed line), as a function of the particle time of flight (in ns) [39]. 35
2.20 Layout of the KL extruded lead and fibres [38]. 36
2.21 An exploded view of a single KL module (which contains 3 cells), with the light guides (A), metal shielding (B), PMTs (C) and voltage dividers (D) [25]. 37

2.22 KL response for different muon and pion momenta, and for 80 MeV/c electrons, taken from [25]. 37
2.23 Exploded view of KL assembly. The seven strips in the centre contain the active cells. The red bars cover the light guides, the dark blue is the magnetic shielding for the PMTs, the green is the iron bars that house the PMT voltage dividers, and the mechanical support for the KL is in yellow [25]. 38
2.24 EMR detector. 39
2.25 Event display of a muon decaying into a positron in the EMR [40]. . 40
2.26 Event display of an electron shower in the EMR [40]. 40

3.1 Structure of a global event in MAUS. 45
3.2 An example PDF, produced using ReduceCppGlobalPID, of ComPIDVarA. Shown are muons (red, peak at 32 ns), pions (green, peak at 35 ns) and electrons (blue, peak at 28 ns), for a simulated 200 MeV/c muon beam. As these distributions only include particles that make it through the entire channel, the electron distribution appears as a sharp monochromatic peak, as electrons that scatter out of the channel are omitted. While the pions contaminating the beam would initially have a higher momentum than the muons, the particles here have passed through both the diffuser and absorber in the channel, where the pions lose energy more quickly than the muons, resulting in the smeared distribution that peaks at a longer time of flight than if there were no material present. 55
3.3 Example PDFs, produced using ReduceCppGlobalPID, of ComPIDVarB for muons (a), pions (b) and electrons (c), for a simulated 200 MeV/c muon beam. Compared to ComPIDVarC, as shown in Figure 3.4, it provides far better separation between particle types 56
3.4 An example PDF, produced using ReduceCppGlobalPID, of ComPIDVarC. Shown are muons (red), pions (green) and electrons (blue), for a simulated 200 MeV/c muon beam. 57
3.5 An example PDF, produced using ReduceCppGlobalPID, of ComPIDVarD. Shown are muons (red), pions (green) and electrons (blue), for a simulated 200 MeV/c muon beam. 57
3.6 Example PDFs, produced using ReduceCppGlobalPID, of ComPIDVarE for muons (a), pions (b) and electrons (c), for a simulated 200 MeV/c muon beam. 58

3.7 An example PDF, produced using ReduceCppGlobalPID, of ComPIDVarF. Shown are muons (red), pions (green) and electrons (blue), for a simulated 200 MeV/c muon beam. 59
3.8 Example PDFs, produced using ReduceCppGlobalPID, of ComPIDVarG for muons (a), pions (b) and electrons (c), for a simulated 200 MeV/c muon beam. 60
3.9 Example PDFs, produced using ReduceCppGlobalPID, of ComPIDVarH for muons (a) and electrons (b), for a simulated 200 MeV/c muon beam. Pions at this beam momentum setting do not produce a signal in Cherenkov A. The muon distribution here peaks at a lower time of flight than that shown for ComPIDVarA; this is due to only the higher momentum muons producing a signal in the detector. . . 61
3.10 Example PDFs, produced using ReduceCppGlobalPID, of ComPIDVarI for muons (a), pions (b) and electrons (c), for a simulated 200 MeV/c muon beam. 62
3.11 An example PDF, produced using ReduceCppGlobalPID, of PIDVarA. Shown are muons (red, larger peak at 28 ns, smaller peak at 30 ns), pions (green, peak at 30 ns) and electrons (blue, peak at 25.5 ns), for a simulated 200 MeV/c pion beam. The secondary muon peak contained within the pion peak is due to pions that decay in flight. 65
3.12 Example PDFs, produced using ReduceCppGlobalPID, of PIDVarB for muons (a), pions (b) and electrons (c), for a simulated 200 MeV/c pion beam. 67
3.13 Example PDFs, produced using ReduceCppGlobalPID, of PIDVarC for muons (a), pions (b) and electrons (c), for a simulated 200 MeV/c pion beam. 68
3.14 An example PDF, produced using ReduceCppGlobalPID, of PIDVarD. Shown are muons (red), pions (green) and electrons (blue), for a simulated 200 MeV/c pion beam. 69
3.15 An example PDF, produced using ReduceCppGlobalPID, of PIDVarE. Shown are muons (red, peaks at 200 mm and 400 mm), pions (green, peaks at 100 mm and 200 mm) and electrons (blue, peak at 150 mm), for a simulated 200 MeV/c pion beam. 69
3.16 Example PDFs, produced using ReduceCppGlobalPID, of PIDVarF for muons (a), pions (b) and electrons (c), for a simulated 200 MeV/c pion beam. 70

3.17 An example PDF, produced using ReduceCppGlobalPID, of PIDVarG. Shown are muons (red), pions (green) and electrons (blue), for a simulated 200 MeV/c pion beam. 71
3.18 Example PDFs, produced using ReduceCppGlobalPID, of PIDVarH for muons (a), pions (b) and electrons (c), for a simulated 200 MeV/c pion beam. 72
3.19 Example PDFs, produced using ReduceCppGlobalPID, of PIDVarI for electrons, for a simulated 200 MeV/c pion beam. For the momentum of this simulated beam muons and pions did not produce a signal in the detector. 73
3.20 Example PDFs, produced using ReduceCppGlobalPID, of PIDVarJ for muons (a) and electrons (b), for a simulated 200 MeV/c pion beam. For the momentum of this simulated beam pions did not produce a signal in the detector. 74
3.21 Efficiency/purity plot for ComPIDVarA. The black squares show the overall particle identification efficiency, the red circles show the muon identification efficiency. With this variable an identification purity of 99.3% can be achieved, with muon and overall efficiencies of 62.2% and 61.9% respectively. 78
3.22 Efficiency/purity plot for ComPIDVarB. The optimal purity for this variable was found to be 99.3%, which corresponds to a muon efficiency of 50.4% and an overall identification efficiency of 50.1% . . . 79
3.23 Efficiency/purity plot for ComPIDVarC. The optimal purity for this variable was found to be 99.2%, which corresponds to a muon finding efficiency of 47.3% and an overall identification efficiency of 47.0% . 79
3.24 Efficiency/purity plot for ComPIDVarD. As can be seen, the EMR range alone cannot return either a reasonable purity or efficiency, making this variable clearly unsuitable for use in PID. 80
3.25 Efficiency/purity plot for ComPIDVarE. The optimal purity for this variable was found to be 99.2%, which corresponds to a muon finding efficiency of 64.5% and an overall identification efficiency of 64.2% . 80
3.26 Efficiency/purity plot for ComPIDVarF. The optimal purity for this variable was found to be 93.9%, which corresponds to a muon finding efficiency of 0.189% and an overall identification efficiency of 0.188%, so while it is not an efficient variable, its inclusion in PID may be useful for a small number of tracks. 81

3.27 Efficiency/purity plot for ComPIDVarG. The optimal purity for this variable was found to be 99.2%, which corresponds to a muon finding efficiency of 40.4% and an overall identification efficiency of 40.2% . 81
3.28 Efficiency/purity plot for ComPIDVarH. The optimal purity for this variable was found to be 91.5%, which corresponds to a muon finding efficiency of 71.5% and an overall identification efficiency of 62.0%. It should be noted that at this simulated beam momentum, there were only 208 tracks that produced signals in Cherenkov A and the time of flight detectors, hence the large error bars. 82
3.29 Efficiency/purity plot for ComPIDVarI. The optimal purity for this variable was found to be 97.5%, which corresponds to a muon finding efficiency of 25.5% and an overall identification efficiency of 25.2%. . 82
3.30 Comparison of P(μ) returned by ComPIDVarA and ComPIDVarB on MC dataset. For all particles identified by both variables, there was a muon identification consistency of 99.5%. 84
3.31 Comparison of P(μ) returned by ComPIDVarA and ComPIDVarB for LiH dataset. For all particles identified by both variables, there was a muon identification consistency of 99.0%. 85
3.32 Efficiency/purity plot for PIDVarA. With this variable an identification purity of 94.2% has been achieved, with muon and overall efficiencies of 49.9% and 47.1% respectively. 87
3.33 Efficiency/purity plot for PIDVarB. The optimal purity for this variable was found to be 94.1%, which corresponds to a muon efficiency of 49.7% and an overall identification efficiency of 46.7%. 87
3.34 Efficiency/purity plot for PIDVarC. The optimal purity for this variable was found to be 70.9%, which corresponds to a muon finding efficiency of 21.7% and an overall identification efficiency of 13.7%. . 88
3.35 Efficiency/purity plot for PIDVarD. The optimal purity for this variable was found to be 80.4%, which corresponds to a muon finding efficiency of 9.09% and an overall identification efficiency of 5.58%. . 88
3.36 Efficiency/purity plot for PIDVarE. The optimal purity for this variable was found to be 82.7%, which corresponds to a muon finding efficiency of 40.4% and an overall identification efficiency of 24.0%. . 89
3.37 Efficiency/purity plot for PIDVarF. The optimal purity for this variable was found to be 83.5%, which corresponds to a muon finding efficiency of 37.9% and an overall identification efficiency of 28.8%. . 89

3.38 Efficiency/purity plot for PIDVarG. The optimal purity for this variable was found to be 43.0%, which corresponds to a muon finding efficiency of 0.261% and an overall identification efficiency of 0.155%. 90
3.39 Efficiency/purity plot for PIDVarH. The optimal purity for this variable was found to be 92.0%, which corresponds to a muon finding efficiency of 8.39% and an overall identification efficiency of 4.97%. . 90
3.40 Efficiency/purity plot for PIDVarJ. The optimal purity for this variable was found to be 94.4%, which corresponds to a muon finding efficiency of 37.2% and an overall identification efficiency of 35.3%. . 91
3.41 Comparison of P(μ) returned by PIDVarA and PIDVarB on MC dataset. For all particles identified by both variables, there was a muon identification consistency of 98.9%. 92
3.42 Comparison of P(μ) returned by PIDVarA and PIDVarJ on MC dataset. For all particles identified by both variables, there was a muon identification consistency of 99.3%. 93
3.43 Comparison of P(μ) returned by PIDVarB and PIDVarJ on MC dataset. For all particles identified by both variables, there was a muon identification consistency of 99.8%. 93
3.44 Comparison of P(μ) returned by upstream PID and downstream PID on MC dataset. Though not easily seen due to the density of points around (0,0) and (100,100), there was a muon identification consistency of 89.9%. 95
3.45 The log-likelihoods returned by the PID for MC muons (red), pions (green) and positrons (blue) that were identifed as muons. 97
3.46 Percentage of tracks identified for all LiH data runs. 98
3.47 The log-likelihoods returned by the upstream PID for MC muons (red), pions (green) and positrons (blue) that were identifed as muons. 99
3.48 The log-likelihoods returned by the downstream PID for MC muons (red), pions (green) and positrons (blue) that were identifed as muons.100

4.1 Contributions of multiple single scatters in material to θ_{plane}. Image taken from [45]. 102
4.2 GEANT4 rendering of MuScat apparatus [51]. 104
4.3 MuScat results for the projected scattering angle distribution in data and simulation for 109 mm of LH_2, taken from [51]. 105

4.4 The thickness of a single absorber window as a function of radius (blue), and the corresponding RMS scattering angle (red). Thickness/radius values taken from [61]. 106
4.5 Scattering measurement method for a particle in the presence of magnetic fields, taken from [53]. 107
4.6 The beam distribution at the upstream absorber face for the field on (a) and field off (b) beams. 110
4.7 Monte Carlo (blue dashed line) and reconstructed Monte Carlo (red line) scattering distributions for an empty channel in the absence of magnetic fields. 111
4.8 Monte Carlo (blue dashed line) and reconstructed Monte Carlo (red line) scattering distributions for a LiH absorber in the absence of magnetic fields. 112
4.9 Monte Carlo (blue dashed line) and reconstructed Monte Carlo (red line) scattering distributions for an empty channel in the presence of magnetic fields. 113
4.10 Monte Carlo (blue dashed line) and reconstructed Monte Carlo (red line) scattering distributions for a LiH absorber in the presence of magnetic fields. 114
4.11 Residuals of the reconstructed transverse momentum components and their residuals after propagation through the fields, for an empty absorber. 115
4.12 Response objects for the projected and space scattering angles (shown are the response objects for field-off empty absorber configuration). . 116
4.13 Time of flight distributions for the 200 MeV/c muon beams, for data (solid lines) and MC (dashed lines). 120
4.14 Time of flight vs the upstream tracker momentum, for the Monte Carlo muon beams. 120
4.15 Reconstructed MC (red triangles), unfolded (blue quares) and Monte Carlo (empty circles) distributions of the 3D space and projected scattering angles, for an empty channel in the absence of fields. Only statistical errors shown. 126
4.16 Reconstructed MC (red triangles), unfolded (blue squares) and MC (empty circles) distributions of the 3D space and projected scattering angles, for the LiH absorber in the absence of fields. Only statistical errors shown. 128

4.17 Raw data (red triangles), unfolded (blue squares) and MC (empty circles) distributions of the 3D space and projected scattering angles, for an empty channel in the absence of fields. Only statistical errors shown. 130
4.18 Raw data (red triangles), unfolded (blue squares) and MC (empty circles) distributions of the 3D space and projected scattering angles, for a LiH absorber in the absence of fields. Only statistical errors shown. 132
4.19 Reconstructed MC (red triangles), unfolded (blue squares) and MC (empty circles) distributions of the 3D space and projected scattering angles, for a LiH absorber in the presence of fields. Only statistical errors shown. 135
4.20 Reconstructed MC (red triangles), unfolded (blue squares) and MC (empty circles) distributions of the 3D space and projected scattering angles, for the LiH absorber in the presence of fields. Only statistical errors shown. 137

A.1 Comparison of P(μ) returned by ComPIDVarA and ComPIDVarC on MC dataset. For all particles identified by both variables, there was a muon identification consistency of 99.1%. 141
A.2 Comparison of P(μ) returned by ComPIDVarA and ComPIDVarD on MC dataset. For all particles identified by both variables, there was a muon identification consistency of 26.9%. 142
A.3 Comparison of P(μ) returned by ComPIDVarA and ComPIDVarE on MC dataset. For all particles identified by both variables, there was a muon identification consistency of 99.6%. 142
A.4 Comparison of P(μ) returned by ComPIDVarA and ComPIDVarF on MC dataset. For all particles identified by both variables, there was a muon identification consistency of 100%. 143
A.5 Comparison of P(μ) returned by ComPIDVarA and ComPIDVarG on MC dataset. For all particles identified by both variables, there was a muon identification consistency of 99.2%. 143
A.6 Comparison of P(μ) returned by ComPIDVarA and ComPIDVarH on MC dataset. For all particles identified by both variables, there was a muon identification consistency of 100%. 144

A.7 Comparison of P(μ) returned by ComPIDVarA and ComPIDVarI on MC dataset. For all particles identified by both variables, there was a muon identification consistency of 99.3% 144
A.8 Comparison of P(μ) returned by ComPIDVarB and ComPIDVarC on MC dataset. For all particles identified by both variables, there was a muon identification consistency of 99.2%. 145
A.9 Comparison of P(μ) returned by ComPIDVarB and ComPIDVarD on MC dataset. For all particles identified by both variables, there was a muon identification consistency of 27.1%. 145
A.10 Comparison of P(μ) returned by ComPIDVarB and ComPIDVarE on MC dataset. For all particles identified by both variables, there was a muon identification consistency of 99.1%. 146
A.11 Comparison of P(μ) returned by ComPIDVarB and ComPIDVarF on MC dataset. For all particles identified by both variables, there was a muon identification consistency of 100%. 146
A.12 Comparison of P(μ) returned by ComPIDVarB and ComPIDVarG on MC dataset. For all particles identified by both variables, there was a muon identification consistency of 98.4%. 147
A.13 Comparison of P(μ) returned by ComPIDVarB and ComPIDVarH on MC dataset. For all particles identified by both variables, there was a muon identification consistency of 100%. 147
A.14 Comparison of P(μ) returned by ComPIDVarB and ComPIDVarI on MC dataset. For all particles identified by both variables, there was a muon identification consistency of 99.2%. 148
A.15 Comparison of P(μ) returned by ComPIDVarC and ComPIDVarD on MC dataset. For all particles identified by both variables, there was a muon identification consistency of 30.4%. 148
A.16 Comparison of P(μ) returned by ComPIDVarC and ComPIDVarE on MC dataset. For all particles identified by both variables, there was a muon identification consistency of 98.9%. 149
A.17 Comparison of P(μ) returned by ComPIDVarC and ComPIDVarF on MC dataset. For all particles identified by both variables, there was a muon identification consistency of 100%. 149
A.18 Comparison of P(μ) returned by ComPIDVarC and ComPIDVarG on MC dataset. For all particles identified by both variables, there was a muon identification consistency of 98.7%. 150

A.19 Comparison of P(μ) returned by ComPIDVarC and ComPIDVarH on MC dataset. For all particles identified by both variables, there was a muon identification consistency of 100%. 150
A.20 Comparison of P(μ) returned by ComPIDVarC and ComPIDVarI on MC dataset. For all particles identified by both variables, there was a muon identification consistency of 99.4%. 151
A.21 Comparison of P(μ) returned by ComPIDVarD and ComPIDVarE on MC dataset. For all particles identified by both variables, there was a muon identification consistency of 27.2%. 151
A.22 Comparison of P(μ) returned by ComPIDVarD and ComPIDVarF on MC dataset. For all particles identified by both variables, there was a muon identification consistency of 81.2%. 152
A.23 Comparison of P(μ) returned by ComPIDVarD and ComPIDVarG on MC dataset. For all particles identified by both variables, there was a muon identification consistency of 45.7%. 152
A.24 Comparison of P(μ) returned by ComPIDVarD and ComPIDVarH on MC dataset. For all particles identified by both variables, there was a muon identification consistency of 57.5%. 153
A.25 Comparison of P(μ) returned by ComPIDVarD and ComPIDVarI on MC dataset. For all particles identified by both variables, there was a muon identification consistency of 25.2%. 153
A.26 Comparison of P(μ) returned by ComPIDVarE and ComPIDVarF on MC dataset. For all particles identified by both variables, there was a muon identification consistency of 100%. 154
A.27 Comparison of P(μ) returned by ComPIDVarE and ComPIDVarG on MC dataset. For all particles identified by both variables, there was a muon identification consistency of 98.9%. 154
A.28 Comparison of P(μ) returned by ComPIDVarE and ComPIDVarH on MC dataset. For all particles identified by both variables, there was a muon identification consistency of 95.1%. 155
A.29 Comparison of P(μ) returned by ComPIDVarE and ComPIDVarI on MC dataset. For all particles identified by both variables, there was a muon identification consistency of 98.3%. 155
A.30 Comparison of P(μ) returned by ComPIDVarF and ComPIDVarG on MC dataset. For all particles identified by both variables, there was a muon identification consistency of 93.3%. 156

A.31 Comparison of P(μ) returned by ComPIDVarF and ComPIDVarH on MC dataset. For all particles identified by both variables, there was a muon identification consistency of 100%. 156
A.32 Comparison of P(μ) returned by ComPIDVarF and ComPIDVarI on MC dataset. For all particles identified by both variables, there was a muon identification consistency of 100%. 157
A.33 Comparison of P(μ) returned by ComPIDVarG and ComPIDVarH on MC dataset. For all particles identified by both variables, there was a muon identification consistency of 90.6%. 157
A.34 Comparison of P(μ) returned by ComPIDVarG and ComPIDVarI on MC dataset. For all particles identified by both variables, there was a muon identification consistency of 95.2%. 158
A.35 Comparison of P(μ) returned by ComPIDVarH and ComPIDVarI on MC dataset. For all particles identified by both variables, there was a muon identification consistency of 83.3%. 158
A.36 Comparison of P(μ) returned by ComPIDVarA and ComPIDVarC for LiH dataset. For all particles identified by both variables, there was a muon identification consistency of 98.6%. 159
A.37 Comparison of P(μ) returned by ComPIDVarA and ComPIDVarD for LiH dataset. For all particles identified by both variables, there was a muon identification consistency of 34.0%. 160
A.38 Comparison of P(μ) returned by ComPIDVarA and ComPIDVarE for LiH dataset. For all particles identified by both variables, there was a muon identification consistency of 78.2%. 160
A.39 Comparison of P(μ) returned by ComPIDVarA and ComPIDVarF for LiH dataset. For all particles identified by both variables, there was a muon identification consistency of 92.6%. 161
A.40 Comparison of P(μ) returned by ComPIDVarA and ComPIDVarG for LiH dataset. For all particles identified by both variables, there was a muon identification consistency of 98.2%. 161
A.41 Comparison of P(μ) returned by ComPIDVarA and ComPIDVarH for LiH dataset. For all particles identified by both variables, there was a muon identification consistency of 86.1%. 162
A.42 Comparison of P(μ) returned by ComPIDVarA and ComPIDVarI for LiH dataset. For all particles identified by both variables, there was a muon identification consistency of 81.9% 162

A.43 Comparison of P(μ) returned by ComPIDVarB and ComPIDVarC for LiH dataset. For all particles identified by both variables, there was a muon identification consistency of 97.8%. 163
A.44 Comparison of P(μ) returned by ComPIDVarB and ComPIDVarD for LiH dataset. For all particles identified by both variables, there was a muon identification consistency of 31.5%. 163
A.45 Comparison of P(μ) returned by ComPIDVarB and ComPIDVarE for LiH dataset. For all particles identified by both variables, there was a muon identification consistency of 78.8%. 164
A.46 Comparison of P(μ) returned by ComPIDVarB and ComPIDVarF for LiH dataset. For all particles identified by both variables, there was a muon identification consistency of 88.9%. 164
A.47 Comparison of P(μ) returned by ComPIDVarB and ComPIDVarG for LiH dataset. For all particles identified by both variables, there was a muon identification consistency of 97.0%. 165
A.48 Comparison of P(μ) returned by ComPIDVarB and ComPIDVarH for LiH dataset. For all particles identified by both variables, there was a muon identification consistency of 85.5%. 165
A.49 Comparison of P(μ) returned by ComPIDVarB and ComPIDVarI for LiH dataset. For all particles identified by both variables, there was a muon identification consistency of 81.3%. 166
A.50 Comparison of P(μ) returned by ComPIDVarC and ComPIDVarD for LiH dataset. For all particles identified by both variables, there was a muon identification consistency of 34.2%. 166
A.51 Comparison of P(μ) returned by ComPIDVarC and ComPIDVarE for LiH dataset. For all particles identified by both variables, there was a muon identification consistency of 71.9%. 167
A.52 Comparison of P(μ) returned by ComPIDVarC and ComPIDVarF for LiH dataset. For all particles identified by both variables, there was a muon identification consistency of 100%. 167
A.53 Comparison of P(μ) returned by ComPIDVarC and ComPIDVarG for LiH dataset. For all particles identified by both variables, there was a muon identification consistency of 95.6%. 168
A.54 Comparison of P(μ) returned by ComPIDVarC and ComPIDVarH for LiH dataset. For all particles identified by both variables, there was a muon identification consistency of 89.5%. 168

A.55 Comparison of P(μ) returned by ComPIDVarC and ComPIDVarI for LiH dataset. For all particles identified by both variables, there was a muon identification consistency of 82.0%. 169
A.56 Comparison of P(μ) returned by ComPIDVarD and ComPIDVar for LiH datasetE. For all particles identified by both variables, there was a muon identification consistency of 32.8%. 169
A.57 Comparison of P(μ) returned by ComPIDVarD and ComPIDVarF for LiH dataset. For all particles identified by both variables, there was a muon identification consistency of 93.6%. 170
A.58 Comparison of P(μ) returned by ComPIDVarD and ComPIDVarG for LiH dataset. For all particles identified by both variables, there was a muon identification consistency of 34.2%. 170
A.59 Comparison of P(μ) returned by ComPIDVarD and ComPIDVarH for LiH dataset. For all particles identified by both variables, there was a muon identification consistency of 36.5%. 171
A.60 Comparison of P(μ) returned by ComPIDVarD and ComPIDVarI for LiH dataset. For all particles identified by both variables, there was a muon identification consistency of 37.0%. 171
A.61 Comparison of P(μ) returned by ComPIDVarE and ComPIDVarF for LiH dataset. For all particles identified by both variables, there was a muon identification consistency of 30.8%. 172
A.62 Comparison of P(μ) returned by ComPIDVarE and ComPIDVarG for LiH dataset. For all particles identified by both variables, there was a muon identification consistency of 71.5%. 172
A.63 Comparison of P(μ) returned by ComPIDVarE and ComPIDVarH for LiH dataset. For all particles identified by both variables, there was a muon identification consistency of 64.4%. 173
A.64 Comparison of P(μ) returned by ComPIDVarE and ComPIDVarI for LiH dataset. For all particles identified by both variables, there was a muon identification consistency of 64.0%. 173
A.65 Comparison of P(μ) returned by ComPIDVarF and ComPIDVarG for LiH dataset. For all particles identified by both variables, there was a muon identification consistency of 65.8%. 174
A.66 Comparison of P(μ) returned by ComPIDVarF and ComPIDVarH for LiH dataset. For all particles identified by both variables, there was a muon identification consistency of 98.1%. 174

A.67 Comparison of P(μ) returned by ComPIDVarF and ComPIDVarI for LiH dataset. For all particles identified by both variables, there was a muon identification consistency of 83.7%. 175
A.68 Comparison of P(μ) returned by ComPIDVarG and ComPIDVarH for LiH dataset. For all particles identified by both variables, there was a muon identification consistency of 81.0%. 175
A.69 Comparison of P(μ) returned by ComPIDVarG and ComPIDVarI for LiH dataset. For all particles identified by both variables, there was a muon identification consistency of 82.6%. 176
A.70 Comparison of P(μ) returned by ComPIDVarH and ComPIDVarI for LiH dataset. For all particles identified by both variables, there was a muon identification consistency of 74.1%. 176
A.71 Comparison of P(μ) returned by PIDVarC and PIDVarD on MC dataset. For all particles identified by both variables, there was a muon identification consistency of 85.9%. 177
A.72 Comparison of P(μ) returned by PIDVarC and PIDVarE on MC dataset. For all particles identified by both variables, there was a muon identification consistency of 80.9%. 178
A.73 Comparison of P(μ) returned by PIDVarC and PIDVarG on MC dataset. For all particles identified by both variables, there was a muon identification consistency of 22.3%. 178
A.74 Comparison of P(μ) returned by PIDVarC and PIDVarH on MC dataset. For all particles identified by both variables, there was a muon identification consistency of 90.3%. 179
A.75 Comparison of P(μ) returned by PIDVarD and PIDVarE on MC dataset. For all particles identified by both variables, there was a muon identification consistency of 98.0%. 179
A.76 Comparison of P(μ) returned by PIDVarD and PIDVarF on MC dataset. For all particles identified by both variables, there was a muon identification consistency of 87.3%. 180
A.77 Comparison of P(μ) returned by PIDVarD and PIDVarG on MC dataset. For all particles identified by both variables, there was a muon identification consistency of 1.56%. 180
A.78 Comparison of P(μ) returned by PIDVarD and PIDVarH on MC dataset. For all particles identified by both variables, there was a muon identification consistency of 98.8%. 181

A.79 Comparison of P(μ) returned by PIDVarE and PIDVarF on MC dataset. For all particles identified by both variables, there was a muon identification consistency of 98.7%. 181
A.80 Comparison of P(μ) returned by PIDVarE and PIDVarG on MC dataset. For all particles identified by both variables, there was a muon identification consistency of 7.55%. 182
A.81 Comparison of P(μ) returned by PIDVarE and PIDVarH on MC dataset. For all particles identified by both variables, there was a muon identification consistency of 97.6%. 182
A.82 Comparison of P(μ) returned by PIDVarF and PIDVarG on MC dataset. For all particles identified by both variables, there was a muon identification consistency of 36.7%. 183
A.83 Comparison of P(μ) returned by PIDVarG and PIDVarH on MC dataset. For all particles identified by both variables, there was a muon identification consistency of 95.7%. 183

Acknowledgments

Firstly, it seems appropriate to thank my supervisor, Steve Boyd, for giving me the opportunity to actually pursue a PhD, and for the many useful conversations and pieces of advice he has given me whilst writing this thesis. And also for the chainsaw and the unicorn room. (For those confused by the reference, please be assured that no fictional creatures were harmed in the writing of this thesis).

I would like to express my sincere thanks to everyone I have worked with in the MICE collaboration. There are far too many people for me to name you all, but I have come to the end of this PhD having worked with, and often been helped by, many excellent people.

In particular I would like to thank the two Warwick post-docs we've had on MICE during this time; Ian Taylor, who provided excellent support and showed incredible patience in my early days of writing code, and Paolo Franchini, partly for his general kindness and confidence that I would reach this day, but mostly for letting me know that somewhere in the world there is a researcher who made the odd career jump to clown college, something I found oddly comforting to know. I would also like to thank Adam Dobbs and Durga Rajaram for their kindness and support while wrestling with the foibles of our software, Chris Rogers for both his computing and analysis support, and Victoria Blackmore for providing both great physics insight and great boardgames. Furthermore I would like to thank Melissa Uchida, who has given me a great deal of advice and support over the last few years. It is with great sadness that I realise I will never again have the chance to go into public places and truthfully declare her to be my MOM.

On a more personal note, I would like to thank my friends for their patience

and understanding during my PhD, especially during the writing up of this thesis. In particular I would like to thank Carrie and Elena for their support, oddly poetic in form, that has bookended this whole experience.

And finally I would like to thank my parents, who have supported and encouraged me in everything I have done, never questioning that I could achieve what I set my mind to, even when I questioned myself. Thank you.

Declarations

Chapter 1 is an amalgamation of material from the literature, publications and sources listed in the bibliography. Chapter 2 makes use of material from MICE publications and internal documents. Section 3.1 of Chapter 3 draws from internal documents and software descriptions in MICE. Section 3.2 and onwards is the sole work of the author. The work in Chapter 4 is based upon a method proposed by T. Carlisle in his PhD thesis, but all susbsequent work is that of the author. This thesis has not been submitted for a degree at another university.

Abstract

The Muon Ionisation Cooling experiment aims to measure the effect of passing through low Z materials on the emittance of muons. This process is dependent on energy loss and multiple scattering through the material, which is currently not well understood for muons, and so it is necessary to study these effects. These studies require muon samples with high purity, greater than 99.9% upstream of the MICE cooling channel, for which strong particle identification is required.

A Global Particle Identification software framework has been developed, its performance assessed, and then applied to both Monte Carlo and MICE data. Monte Carlo studies have shown that the software can achieve the required purity. An analysis of multiple scattering of muons through Lithium Hydride has also been presented, using a method designed for the presence of magnetic fields in the cooling channel. This has been applied for Monte Carlo input in both the presence and absence of fields, and for data taken in the absence of fields, which is all of the scattering data taken thus far in MICE. The results of these studies have been compared with both the Wentzel-VI model of scattering implemented in Geant4 and with the PDG approximation for multiple scattering, which has shown that Wentzel-VI underestimates the widths of the scattering distributions, while the PDG approximation overestimates their widths, in particular the width of the distributions of the 3D space angle.

Chapter 1

Introduction

The Standard Model of particle physics describes the fundamental constituents of matter (fermions), and the particles that mediate the interactions between them (bosons). Fermions are further divided between quarks and leptons, the properties of which are shown in Table 1.1. In the lepton sector the three charged leptons, the electron (e^-), muon (μ^-), and tauon (τ^-), each have a corresponding neutrino, (ν_e, ν_μ, ν_τ).

Discoveries made in recent decades, which will be discussed below, suggest that new physics could be found in the neutrino sector. To further our current knowledge of neutrino properties and to address some of the mysteries still surrounding neutrinos, more advanced facilities are required. One such proposed facility is the Neutrino Factory, which would deliver unparalleled precision and particle flux. However it presents a number of technical challenges, among them a requirement for cooling muon beams, which due to the short muon lifetime requires that a new cooling technique, ionisation cooling, be developed.

The Muon Ionisation Cooling Experiment (MICE) is a proof of principle experiment, based at the Rutherford Appleton Laboratory, UK, intended to demonstrate the feasibility of using ionisation cooling to provide the degree of emittance reduction required by a Neutrino Factory. Integral to this is an understanding of how muons interact with the cooling materials used, principally the effects of energy loss and multiple Coulomb scattering.

	Particle	Mass	Charge
Quarks	u	2.4 MeV/c^2	$\frac{2}{3}$
	d	4.8 MeV/c^2	$-\frac{1}{3}$
	c	1.27 GeV/c^2	$\frac{2}{3}$
	s	104 MeV/c^2	$-\frac{1}{3}$
	t	171.2 GeV/c^2	$\frac{2}{3}$
	b	4.2 GeV/c^2	$-\frac{1}{3}$
Leptons	e^-	0.511 MeV/c^2	-1
	μ^-	105.7 MeV/c^2	-1
	τ^-	1.777 GeV/c^2	-1
	ν_e	< 2.2 eV/c^2	0
	ν_μ	< 0.17 MeV/c^2	0
	ν_τ	< 15.5 MeV/c^2	0

Table 1.1: Fermion masses and electric charges

1.1 Neutrino Physics

1.1.1 Discovery

The neutrino was first postulated in 1930 by Wolgang Pauli, to account for the continuous energy spectrum measured in β decay. However it wasn't until 1956 that the (anti) electron neutrino $\bar{\nu_e}$ was first observed by Cowan and Reines at the Hanford reactor [1], using the interaction

$$\bar{\nu_e} + p \rightarrow n + e^+ \tag{1.1}$$

The muon neutrino $\bar{\nu_\mu}$ was found at the Brookhaven Alternating Gradient Sychrotron in 1962, produced by pion decay, and in 2000 the tau neutrino ν_τ was detected in the DONUT experiment at Fermilab [2].

1.1.2 Neutrino Flavour Oscillations

One of the most significant discoveries in particle physics in the last two decades was the discovery of neutrino flavour oscillations, which proved that neutrinos are not massless, contrary to what had been assumed by the Standard Model.

While the confirmation of neutrino oscillations is a relatively recent development, evidence of the phenomenon was first seen in the 1960s. The Homestake experiment [3], started in 1965, was designed to detect solar neutrinos. However there was a large discrepancy between the flux of neutrinos measured, and the flux

predicted by the Standard Solar Model. This became known as the Solar Neutrino Problem [5].

In addition to the Solar Neutrino Problem, another discrepancy between theory and experiment, the Atmospheric Neutrino Anomaly [4], indicated the possibility of neutrino flavour oscillations. Atmospheric neutrinos are produced when cosmic rays interact in the Earth's atmosphere. The neutrinos are produced from muon decay, the muons having been produced by the decays of pions, kaons, and other particles created in cosmic ray interactions [6]. Super Kamikande [7], built to detect atmospheric neutrinos, was one of the experiments to detect a deficit when compared to theoretical predictions, in the ratio of the muon neutrino rate to the electron neutrino rate. A dependence of the muon neutrino rate on the azimuthal angle was also observed. As the azimuthal angle of a neutrino entering the detector is a function of the distance travelled by the neutrino from it's source, this implied a dependence of the rate on the path length of the neutrino.

In order to establish if neutrino oscillations were indeed the cause of the observed deficits, the Sudbury Neutrino Observatory (SNO) [8] was built. SNO used a water Cherenkov detector filled with heavy water (D_2O), which was able to detect all three neutrino species via the neutral current interaction of the neutrino scattering inelastically with a deuterium nucleus, d, and as such measure the total neutrino rate.

$$\nu + d \rightarrow \nu + n + p \tag{1.2}$$

SNO was also able to measure the ν_e rate through elastic scattering

$$\nu_e + e^- \rightarrow \nu_e + e^- \tag{1.3}$$

and through the charged current interaction

$$\nu_e + d \rightarrow e^- + p + p \tag{1.4}$$

SNO measured an ν_e flux of $(1.76 \pm 0.01) \times 10^{-8} cm^{-2} s^{-1}$, and a total neutrino flux via the neutral current interaction of $(5.09 \pm 0.63) \times 10^{-8} cm^{-2} s^{-1}$, which is in excellent agreement with the Standard Solar Model prediction of $(5.05 \pm 1.01) \times 10^{-8} cm^{-2} s^{-1}$ [8], thus solving the Solar Neutrino Problem, and confirming the phenomenon of neutrino oscillations.

Theoretical Description of Neutrino Oscillations

Neutrino oscillations are able to occur because the three neutrino flavour eigenstates $|\nu_\alpha\rangle\,(\alpha = e, \mu, \tau)$ are not the same as the mass eigenstates $|\nu_k\rangle\,(k = 1, 2, 3)$. In fact, the two states can be considered to be a coherent superposition of one another [21]. For a unitary matrix, U, the flavour states can be related to the mass states by

$$|\nu_\alpha\rangle = \sum_k U_{\alpha k}\,|\nu_k\rangle \tag{1.5}$$

and the mass states can be written as

$$|\nu_k\rangle = \sum_\alpha U^*_{\alpha k}\,|\nu_\alpha\rangle \tag{1.6}$$

For a neutrino with 4-momentum $\mathrm{p_k} = (\mathrm{t}, \mathbf{p})$ and 4-space vector $\mathrm{x} = (\mathrm{t}, \mathbf{x})$, the propagation of the mass states is described by the time-dependent Schrödinger Equation

$$i\frac{\partial}{\partial t}\,|\nu_k(x,t)\rangle = E_k\,|\nu_k(x,t)\rangle \tag{1.7}$$

the solution to which is

$$|\nu_k(x,t)\rangle = e^{-i(E_k t - p_k x)}\,|\nu_k(0,0)\rangle = e^{-i\phi_k}\,|\nu_k(0,0)\rangle \tag{1.8}$$

where ϕ_k is the phase factor. Given that neutrinos are relativistic, $p >> m_k$ and $E \approx p$, the neutrino energy E_k can be expressed as

$$E_k = \sqrt{m_k^2 + p_k^2} \simeq p_k + \frac{m_k^2}{2p_k} \simeq E + \frac{m_k^2}{2E} \tag{1.9}$$

From Eqn. 1.5 and Eqn. 1.8, it follows that at a later space-time point (x,t) the neutrino flavour eigenstate is given by

$$\begin{aligned} |\nu_\alpha(x,t)\rangle &= \sum_k U_{\alpha k}\,|\nu_k(x,t)\rangle \\ &= \sum_k U_{\alpha k} e^{i\phi_k}\,|\nu_k(0,0)\rangle \\ &= \sum_k \sum_\beta U_{\alpha k} U^*_{\beta k} e^{i\phi_k}\,|\nu_\beta\rangle \end{aligned}$$

The existence of different, non-zero neutrino masses implies that the phase factor is different for different mass states, resulting in the flavour content of the final state

being different to that of the initial state. The transition amplitude for a change in flavour from $\nu_\alpha \to \nu_\beta$ is given by

$$A(\alpha \to \beta) = \sum_k U_{\alpha k} e^{i\phi_k} U^*_{\beta k} = \sum_k U_{\alpha k} e^{i(E_k t - p_k x)} U^*_{\beta k} \tag{1.10}$$

which, using Eqn. 1.9, can be rewritten as

$$A(\alpha \to \beta) = \sum_k U^*_{\beta k} U_{\alpha k} \exp\left(- i \frac{m_k^2}{2} \frac{L}{E} \right) \tag{1.11}$$

where L is the distance between the detector and the neutrino source.

The transition probability P is then given by

$$P(\alpha \to \beta) = |A(\alpha \to \beta)|^2 = |\sum_k U_{\alpha k} e^{i\phi_k} U^*_{\beta k}|^2 \tag{1.12}$$

For three neutrino flavours, Eqn. 1.12 can be written

$$P(\alpha \to \beta) = \delta_{\alpha\beta} - 4 \sum_{i>j=1} Re(K_{\alpha\beta,ij}) \sin^2 \left(\frac{\Delta m^2_{ij} L}{4E} \right) + 4 \sum_{i>j=1} Im(K_{\alpha\beta,ij}) \sin \left(\frac{\Delta m^2_{ij} L}{4E} \right) \cos \left(\frac{\Delta m^2_{ij} L}{4E} \right)$$

where $K_{\alpha\beta,ij} = U_{\alpha i} U^*_{\beta i} U^*_{\alpha j} U_{\beta j}$ and $\Delta m^2_{ij} = m^2_i - m^2_j$, as given in [6].

The matrix U is the Pontecorvo-Maka-Nakagawa-Sakata (PMNS) matrix, and is the equivalent of the quark sector CKM matrix for neutrinos, and is shown in Eqn. 1.13.

$$U = \begin{pmatrix} 1 & 0 & 0 \\ 0 & c_{23} & s_{23} \\ 0 & s_{23} & c_{23} \end{pmatrix} \times \begin{pmatrix} c_{13} & 0 & s_{13} e^{-i\delta} \\ 0 & 1 & 0 \\ -s_{13} e^{i\delta} & 0 & c_{13} \end{pmatrix} \times \begin{pmatrix} c_{12} & s_{12} & 0 \\ -s_{12} & c_{12} & 0 \\ 0 & 0 & 1 \end{pmatrix} \times \begin{pmatrix} 1 & 0 & 0 \\ 0 & e^{i\alpha} & 0 \\ 0 & 0 & e^{i\beta} \end{pmatrix} \tag{1.13}$$

where $s_{ij} = \sin(\theta_{ij})$ and $c_{ij} = \cos(\theta_{ij})$, δ is the CP violating Dirac phase, and α and β are Majorana phases (which are not relevant to neutrino oscillations). This representation of the matrix separates out the rotation matrices with respect to the individual mixing angles, θ_{12}, θ_{23}, and θ_{13}.

Dirac and Majorana neutrinos

To account for the existence of the neutrino masses, and for the currently undiscovered right (left) handed neutrino (anti-neutrino), two prominent but fundamentally different theories have been proposed. The first proposes that neutrinos are Dirac particles, with masses generated by the Higgs mechanism, and that right handed neutrinos do exist, but they interact with the Higgs boson extremely weakly, and do not interact at all with the other forces. An allternative theory is that neutrinos are Majorana particles (making the neutrino its own antiparticle), and that ν_L have small masses, supressed by ν_R having a very large mass, via the see-saw mechanism [9].

1.2 Current state of the field

The current focus of neutrino physics is the measurement of the PMNS mixing matrix parameters ($\theta_{13}, \theta_{23}, \theta_{12}$ and the CP-violating phase δ_{CP}), and measuring the neutrino masses and mass splittings Δm^2_{21} and Δm^2_{32}.

1.2.1 Measuring the absolute neutrino mass

β decay

β decay, having already provided the first evidence of the existence of the neutrino, is also the primary method by which the mass of the electron neutrino could be measured. The KATRIN experiment [10], currently being built, will study the energy spectra of electrons from β decay in tritium. The transition energy in the β decay of Tritium to Helium is shared between the electron and anti-neutrino. This energy is split between the kinetic energies and rest masses of the electron and neutrino. The effect of the rest mass of the neutrino on the kinetic energy of the electron is greatest at low energies (when the neutrino is non-relativistic) at the end of the electron energy spectrum, as shown in Figure 1.1, and so information about the neutrino mass is best gained from a precision measurement in this region. KATRIN aims to either directly measure the mass of the electron neutrino, if it is larger than 0.35 eV/c^2, or appoint an upper limit to the mass down to 0.2 eV/c^2, an order of magnitude improvement on the current limit of 2.2 eV/c^2 [11].

Neutrinoless double β decay ($0\nu\beta\beta$)

An observation of $0\nu\beta\beta$ decay would serve as both proof that neutrinos are Majorana particles, and as a measurement of the neutrino mass, as the rate of $0\nu\beta\beta$ decay

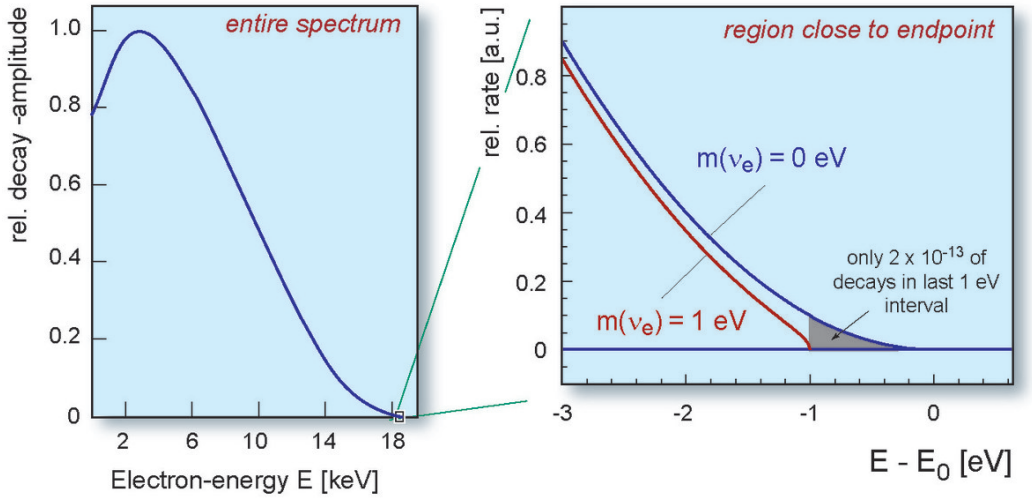

Figure 1.1: The relative decay amplitude for tritium, as a function of the electron energy, is shown in the left hand plot. The right hand plot shows the difference between the the electron and anti-neutrino energy, which can be measured in the high energy region in the tail of the electron energy distribution, where the neutrino is non-relativistic [11].

is dependent on the neutrino mass. Unlike standard double beta decay, where the nucleus emits two electrons and two antineutrinos, converting two neutrons to protons in the process, in neutrinoless double β decay, each emitted neutrino is absorbed by the other nucleon. The NEMO experiment, most recently NEMO III, searched for neutrinoless double β decay in a number of materials, but primarily in ^{100}Mo. Neutrinoless double β decay was not observed, but a limit on the Majorana neutrino mass in the range of $\langle m_\nu \rangle < 0.33 - 0.62$ eV was determined [12]. The next generation SuperNEMO experiment is currently in development, which aims to build a detector that will be sensitive to an effective neutrino mass of the order of 50 meV [13]. The SNO+ experiment [14], which reuses the SNO detector now filled with liquid scintillator, is also primarily intended to search for neutrinoless double beta decay, with an expected sensitivity in the range 55-133 meV.

1.2.2 Oscillation Experiments

MINOS/MINOS+

MINOS+ [15] is a continuation of the MINOS experiment with upgraded electronics. It is a long baseline experiment based at Fermilab, which uses neutrinos produced by the NuMI (Neutrinos at Main Injector) beamline. The neutrino flux and beam composition are measured by a near detector 1 km from the neutrino source. The far detector is 732 km away in the Soudan mine in Northern Minnesota. Both detectors use iron plates interspersed with scintillator planes, and they are also magnetised, which allows for ν_μ interactions to be distinguished from $\bar{\nu_\mu}$ interactions. The current best fit values obtained from MINOS and MINOS+ are $|\Delta m^2_{32}| = 2.37^{+0.11}_{-0.07} \times 10^{-3}$ eV^2 and $sin^2\theta_{23} = 0.43^{+0.19}_{-0.05}$ for an inverted hierarchy (see Section 1.2.3) [16].

NOνA

The NOνA (NuMI Off-Axis ν_e Appearance) experiment [17], as the name suggests, also uses NuMI as a neutrino source. It uses two segmented tracking calorimeters at 1 km and 810 km away from the source, both positioned off-axis from the beam. The first results from NOνA were released in 2015. In 2016, NOνA reported measurements of $\Delta m^2_{32} = 2.52^{+0.20}_{-0.18} \times 10^{-3}$ eV^2 and $0.38 < sin^2\theta_{23} < 0.65$ [18].

T2K

T2K (Tokai to Kamioka) [19] uses an off-axis muon neutrino beam produced at the J-PARC facility, directed at the Super-Kamiokande water Cherenkov detectior 295 km away. The ND280 near detector measures the neutrino flux and beam content 280 m from the source. The primary goal of T2K was to use ν_e appearance in a ν_μ beam to measure θ_{13}, with current results showing it to be non-zero and large. It has also produced the current best measurements of θ_{23} ($sin^2_{\theta_{23}} = 0.514^{+0.055}_{0.056}$ for the normal and $sin^2_{\theta_{23}} = 0.511 \pm 0.055$ for the inverted hierarchy) and $\Delta m^2_{32} = (2.51 \pm 0.10) \times 10^{-3}$eV^2 [20].

1.2.3 Status of measurements

The current best fit values for the neutrino oscillation parameters and the mass splittings are given in Table 1.2. The sign of $|\Delta m^2|$ (where $\Delta m^2 = m^2_3 - [m^2_2 + m^2_1]/2$) is unknown; as such the ordering of the neutrino masses, the mass hierarchy, is unknown. Either it will be a normal hierarchy ($m_1 < m_2 < m_3$) or an inverted hierarchy ($m_3 < m_1 < m_2$), as shown in Figure 1.2.

Parameter	best-fit ($\pm 1\sigma$)	3σ
Δm^2_{21} [10^{-5} eV^2]	$7.54^{+0.26}_{-0.22}$	$6.99 - 8.18$
$\lvert\Delta m^2\rvert$ [10^{-3} eV^2]	$2.43 \pm 0.06 (2.38 \pm 0.06)$	$2.23 - 2.61 (2.19 - 2.56)$
$\sin^2\theta_{12}$	0.308 ± 0.017	$0.259 - 0.359$
$\sin^2\theta_{23}$, $\Delta m^2 > 0$	$0.437^{+0.033}_{-0.023}$	$0.374 - 0.628$
$\sin^2\theta_{23}$, $\Delta m^2 < 0$	$0.455^{+0.039}_{-0.031}$	$0.380 - 0.641$
$\sin^2\theta_{13}$, $\Delta m^2 > 0$	$0.0234^{+0.0020}_{-0.0019}$	$0.0176 - 0.0295$
$\sin^2\theta_{13}$, $\Delta m^2 < 0$	$0.0240^{+0.0019}_{-0.0022}$	$0.0178 - 0.0298$
δ/π (2σ range quoted)	$1.39^{+0.38}_{-0.27}$ $(1.31^{+0.29}_{-0.33})$	(0.00 - 0.16) $\oplus$ (0.86 - 2.00) ((0.00 - 0.02) $\oplus$ (0.70 - 2.00))

Table 1.2: Current best-fit values and 3σ allowed ranges of the netrino oscillation parameters. The values (values in brackets) correspond to the normal (inverted) mass hierarchy. $\Delta m^2 = m_3^2 - (m_2^2 + m_1^2)/2$, and is greater than zero for the normal mass hierarchy, less than zero for the inverted hierarchy [21].

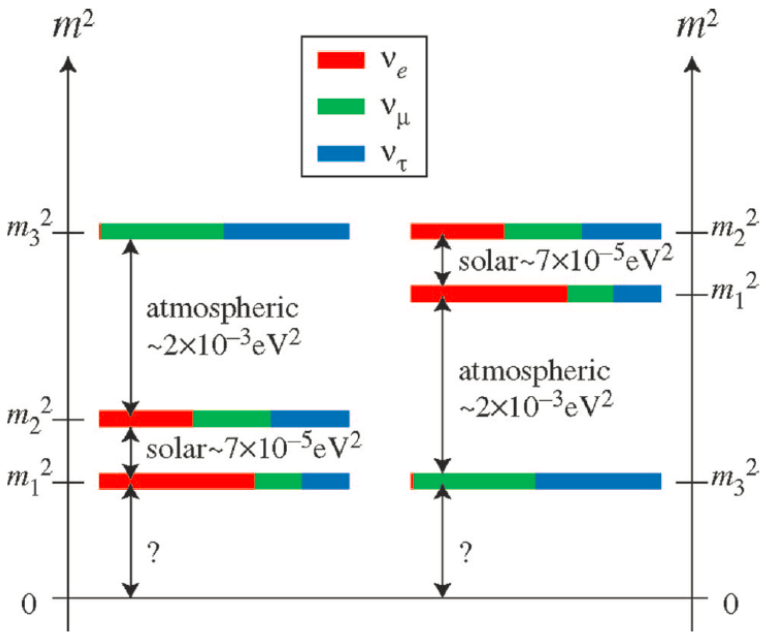

Figure 1.2: Neutrino mass eigenstates for the Normal (left) and Inverted (right) hierarchies [22].

Continuing and future experiments will seek to improve the precision on the mixing angles, determine the mass hierarchy, and measure δ_{CP}. The following sections will discuss the proposed future facilities and their physics reach.

1.2.4 Future Facilities

Three types of facilities have been proposed as the next generation of experiments; Super Beams and Beta Beams, outlined here, and the Neutrino Factory, which will be discussed in more detail in Section 1.3. A comparison of the physics reach of the three facilities is shown in Figure 1.3, from which it can be seen that the Neutrino Factory has the greatest reach across the parameter space, and has the greatest sensitivity to δ_{CP}. However the technical challenges involved in the Neutrino Factory compared to those for a Super Beam, as will be discussed below, means that to some people Super Beams present a more readily achievable near-future option.

Super Beams

In Super Beam experiments, neutrinos are produced by colliding a proton beam on a target to produce pions, which are then focussed using a magnetic horn into a decay channel, where they then decay to generate neutrinos. Advancements on current experiments, such as T2K, would involve using a high power (4 MW) beam of 5 GeV protons, to create a high intensity, high flux source of neutrinos. The technical challenges posed by such a beam centre on developing a proton driver that can deliver the desired power, and a target that can withstand thermal shock and will not suffer irradiation damage. These issues aside, next generation Super Beams still require far less R&D than other proposed facilities, and so are an attractive option for the near future, especially now θ_{13} has been found to be non-zero and quite large [23].

Beta Beams

In Beta Beams, the neutrino beam is generated by the decay of stored high energy radioactive ions. Two ion species are used, one which decays to produce ν_e, and another that produces $\bar{\nu_e}$, which would produce a very well defined neutrino beam. However, the difficulties involved in creating, accelerating and storing a sufficient flux of ions to achieve the sensitivity required from a future facility present a particular challenge to developing a Beta Beam experiment [23], with such a facility falling out of favour for next generation neutrino experiments.

1.3 Neutrino Factory

A neutrino factory, using muon beams, would be an ideal facility with which to study many areas of neutrino physics. Currently, in experiments such as T2K, neutrino

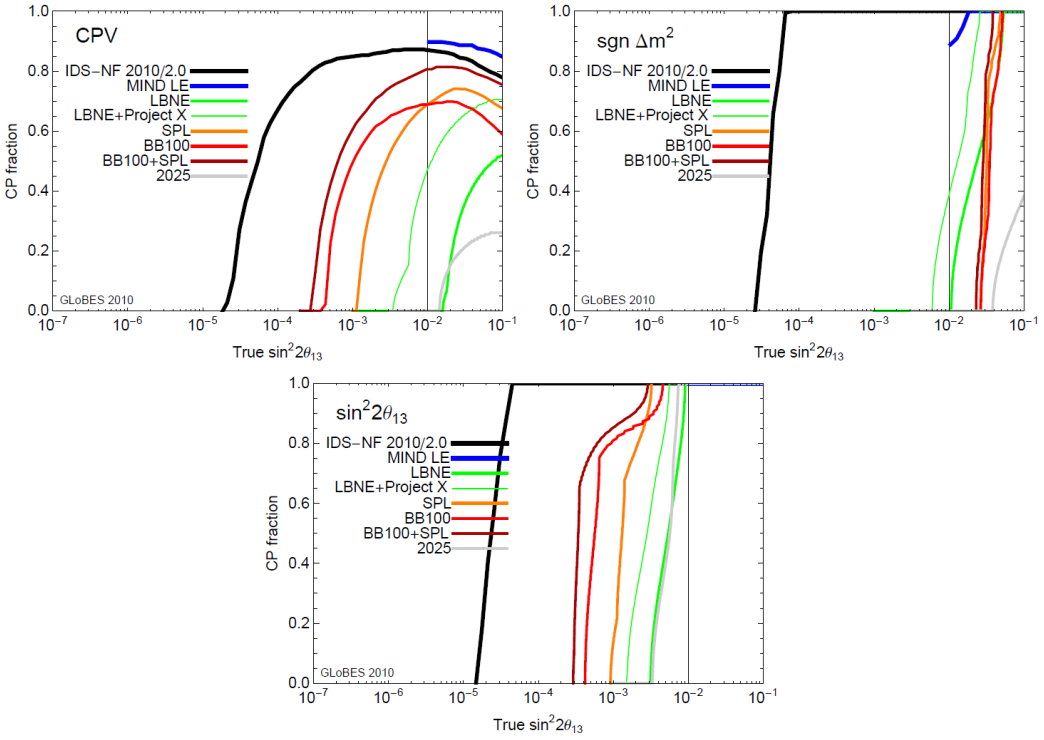

Figure 1.3: Physics reach of different potential facilities for the discovery of δ_{CP} (top left), the mass hierarchy (top right), and $\sin^2 2\theta_{13}$ (bottom). BB refers to β beams, SPL and LBNE are proposed Super Beam experiments, MIND LE is a low energy Neutrino Factory, IDS-NF is the International Design Study for the Neutrino Factory[24].

beams are produced from the decays of pions produced by high energy proton beams colliding with a target. There are, however, large uncertainties associated with the pion intensity of such a beam, and so there are large uncertainties in the flux of neutrinos produced by the beam, whereas it is possible to measure precisely the current of a monochromatic muon beam, and the physics process of muon decay is well understood. The use of a muon beam creates a neutrino beam with a known flavour composition and energy spectrum [25]. A further disadvantage to using neutrinos produced from pion decay is that a significant fraction of the original proton's energy is lost to pions that do not decay and to secondary hadrons, instead of being transferred to the neutrinos to be studied. Using muons in storage rings would have the advantage that all of the muons will eventually decay into neutrinos, which improves the understanding of the flux of neutrinos produced by the muons, and the number of muons produced would be proportional to the power of the proton

beam [24]. A muon beam could produce an intense, pure, high energy neutrino beam, ideal for precision studies of neutrino oscillations and CP-violation. It would also be sensitive to areas of new physics, such as sterile neutrinos [24].

In a neutrino factory, pions are produced by colliding a high power proton beam with a target, which then decay in flight to muons. These muons are captured and manipulated in 6-D phase space (x,y,z,p_x,p_y,p_z) to maximise the number of muons transported into the accelerator and storage ring where they will then decay into neutrinos [24]. The current design for the neutrino factory is shown in Figure 1.4, and Sections 1.3.1 - 1.3.6 detail the main components of the facility.

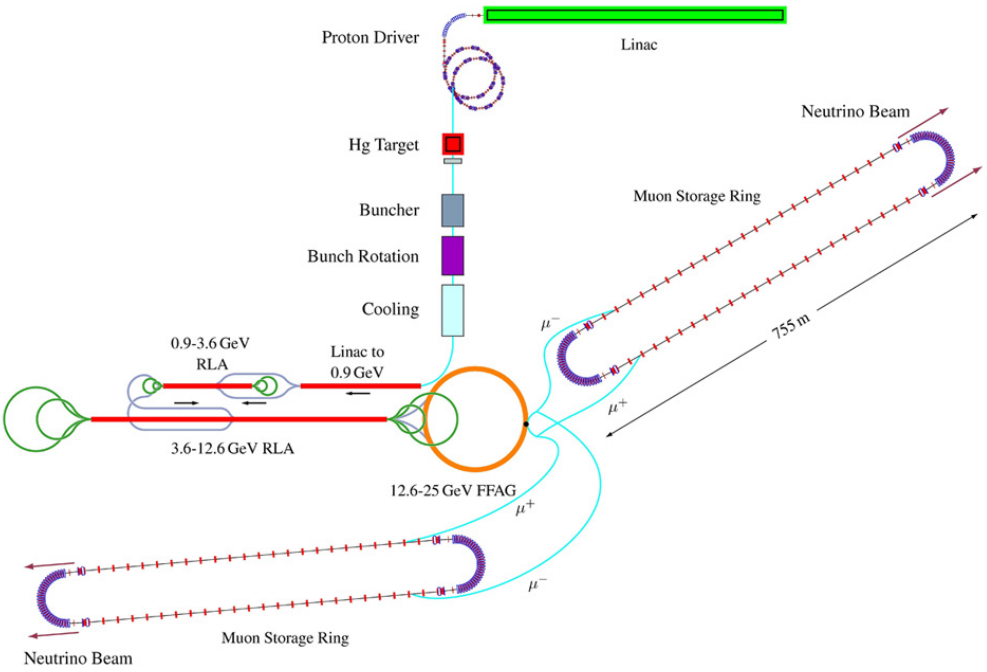

Figure 1.4: Neutrino Factory baseline schematic from the International Scoping Study for a Neutrino Factory. [24].

1.3.1 Proton Driver

The first stage of the neutrino factory is a proton beam. This new "proton driver" is required to deliver a 4 MW, 50 Hz proton beam to the target. Preliminary designs of the proton driver consist of an H^- ion source, a radio-frequency quadrupole to bunch and accelerate the ions, a chopper to produce bunch trains, and then an accelerator to achieve the required proton energy. The Front End Test Stand

(FETS) experiment [26] at Rutherford Appleton Laboratory is currently studying the design of such a system.

1.3.2 Target

One challenge facing the development of the neutrino factory is building a target that can withstand the power of the proton beam. One possible target design is the use of a liquid mercury jet, although other liquid metal jets and metal powder jets are also being considered [24]. The MERIT experiment [27] was a proof of principle experiment that demonstrated that a free mercury jet was a viable target system for use with a 4 MW beam.

1.3.3 Decay Channel, Buncher and Phase Rotation

The pions produced from the collision of the proton beam with the target are captured and transported through the decay channel where they decay into muons. RF cavities in the buncher section then form bunches from the muon beam. The bunches undergo a phase-energy rotation to give all of the bunches the same energy by decelerating the leading high energy bunches and accelerating the low energy bunches [24].

1.3.4 Cooling

The intended method of cooling is ionisation cooling, which will be explained in more detail in Section 1.5.

1.3.5 Acceleration

High acccelerating gradients are required by the neutrino factory due to the short muon lifetime. A combination of a linac system and a Fixed Field Alternating Gradient (FFAG) ring is proposed to accelerate the muons from their front end momentum of 230 MeV/c up to 25 GeV. An advantage of FFAG's is their large acceptance, as well as their ability to accelerate particles rapidly [24]. EMMA [28] was a proof of principle experiment based at Daresbury Laboratory that successfully demonstrated rapid and stable acceleration of electrons.

1.3.6 Storage Rings

The muons are then transported to storage rings where they decay into neutrinos. The storage rings would have long straight sections that pointed towards distant far

detectors. The design favoured for the neutrino factory is a racetrack design with two straight sections, one directing the neutrino beam to the far detector, and the other section would be for collimation [24].

1.4 Accelerator Physics

Before discussing ionisation cooling, it is useful to consider the accelerator concepts that describe the behaviour of particle beams; how these pertain to cooling, and the difficulties inherent in cooling muon beams, to better appreciate the necessity of developing a new technique.

1.4.1 Emittance

The emittance of a particle in a beam is a measure of how much the particle diverges from the ideal trajectory, and is denoted by ε. Particle beams in an accelerator can be considered as a cloud of points within a closed contour in phase space, with this contour usually taking the form of an ellipse with area $A = \pi\varepsilon$, and so $\varepsilon = A/\pi$, as shown in Figure 1.5. The 6-D phase space of a particle in a beam with the direction of the motion of the beam running along the z axis (in cartesian coordinates) is composed of the particle's transverse spatial coordinates, (x, y), the components of its transverse momenta (p_x, p_y), its longitudinal coordinates, z (the time, t, or the phase of the particle, ϕ, may also be used in place of z) and E, the energy of the particle [29]. The particle can also be described in trace space, which has coordinates (x, x', y, y', z, E), where:

$$x' = \frac{p_x}{p_z} = \frac{dx}{dz} \tag{1.14}$$

$$y' = \frac{p_y}{p_z} = \frac{dy}{dz} \tag{1.15}$$

The divergence of the particle away from the beam axis z is now given by x' and y', and the emittance can be expressed in terms of the volume of the trace space that the beam occupies:

$$\varepsilon = \frac{A}{\pi} = \frac{1}{\pi}\int y' dx \tag{1.16}$$

The equation of the ellipse, known as the Courant and Snyder invariant, is given by

$$\gamma(s)x^2 + 2\alpha(s)xx' + \beta(s)x'^2 = \varepsilon \tag{1.17}$$

where α, β and γ are the Twiss parameters that describe the shape and orientation of the ellipse [29]. Figure 1.5 shows the relationship between the emittance and the Twiss parameters. In this treatment, the emittance can be considered to be the area (divided by π) in the x, x' plane that the particles occupy. As the beam travels along the beamline, in the absence of acceleration, the area remains constant. This is a condition of the Liouville theorem, which states that volumes in phase space are invariant. While $\pi\varepsilon$ remains constant, the orientation and width of the beam can change. β is related to the width of the beam, as the half beam width is given by $\sqrt{\beta\varepsilon}$. γ is related to the divergence of the beam, and α described how strongly x and x' are correlated; if $\alpha > 0$, the beam is converging, if $\alpha < 0$ it is diverging, and if $\alpha = 0$ the beam size is at a minimum or maximum.

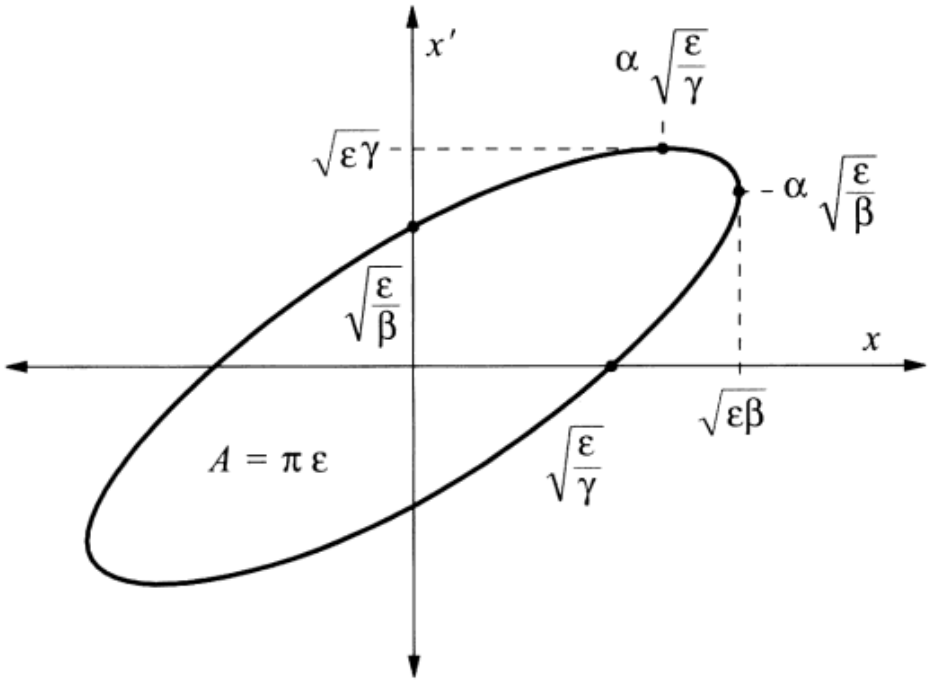

Figure 1.5: Plot of emittance, ε, in trace space, showing the relation to the Twiss parameters, α, β and γ. [30].

Emittance in MICE

The emittance as calculated in Eqn. 1.16 is not conserved during acceleration. As such it is necessary to define a quantity that is invariant under acceleration; the

normalised emittance, ϵ_n, which is given by

$$\epsilon_n = \gamma\beta\epsilon \tag{1.18}$$

where γ and β are the Lorentz factor and relativstic β (as opposed to the twiss parameters).

The emittances and other beam optics functions used in MICE are discussed fully in [31]. Quantities of note (taken from [31]) are:

- **Transverse Emittance**
  The transverse normalised emittance is

  $$\epsilon_\perp = \frac{\sqrt[4]{|\mathbf{V}|}}{m} \tag{1.19}$$

  where m is the muon mass, $\mathbf{V}$ is the covariance matrix of the transverse phase space variables (x, p_x, y, p_y) and $|\mathbf{V}|$ is the determinant of $\mathbf{V}$.

- **Longitudinal Emittance**
  The longitudinal normalised emittance is

  $$\epsilon_\parallel = \frac{\sqrt[2]{|\mathbf{V}|}}{m} \tag{1.20}$$

  where m is the muon mass and $\mathbf{V}$ is the covariance matrix of the longitudinal phase space variables (z, E).

- **6D Emittance**
  The 6D normalised emittance is

  $$\epsilon = \frac{\sqrt[6]{|\mathbf{V}|}}{m} \tag{1.21}$$

  where m is the muon mass and $\mathbf{V}$ is the covariance matrix of all of the phase space variables (x, p_x, y, p_y, z, E).

1.4.2 Traditional Cooling Methods

Prior to acceleration, the phase space that the muon beam occupies must be reduced so that it can pass through the aperture of the accelerating components, hence the requirement for cooling. Traditional methods of cooling include:

- **Stochastic Cooling**
  The transverse momentum of the beam is reduced by using a pickup to sample particle displacements in the beam, and a kicker magnet applies a correction to direct the particles back into the beam [32].

- **Electron Cooling**
  Used in ion accelerators to reduce beam emittance by overlapping a monochromatic electron beam with the ion beam, electrons are given a velocity equal to the average velocity of the ions in the beam, and the ions then lose energy via Coulomb scattering through the electrons, until a thermal equilibrium between the two beams is reached [33].

- **Adiabatic Damping**
  Electrons in a circular accelerator lose energy via synchrotron radiation, which has a cooling effect on the beam. However, given that the muon is far more massive than the electron, and so synchrotron radiation losses are smaller, this method is not suitable for muons.

Due to the short muon lifetime (2.2 μs), none of these methods can be used, as the time required for them to have the necessary cooling effect is too large compared to the lifetime of the muon, and so a novel approach is required. The alternative method of ionisation cooling has been proposed.

1.5 Ionisation Cooling

The muons used in MICE, and those that would be used in a Neutrino Factory, are tertiary particles produced via pion decay, the pions in turn having been created from a proton beam colliding with a target. This method of production results in a muon beam with high transverse and longitudinal emittances that need to be reduced (cooled).

Ionisation cooling involves passing the muon beam through an ionising material to reduce the total momentum, and then using RF cavities to restore the longitudinal component of the momentum. Figure 1.6 shows a diagram of the effect of these stages on the muons momentum.

Energy loss in the material reduces both the transverse and longitudinal momenta, and reacceleration in the longitudinal direction by the RF cavities results in a cooling of the beam. However multiple coulomb scattering also occurs in the material, which has a heating effect. The rate of change of the normalised emittance,

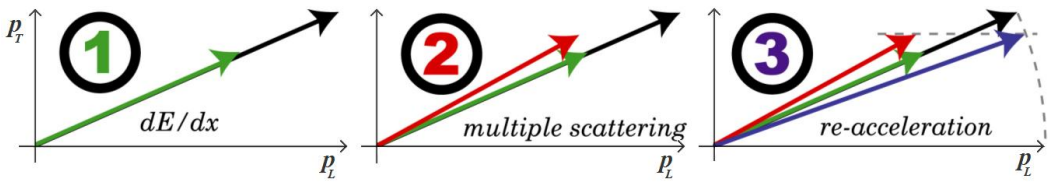

Figure 1.6: Changes to the transverse and longitudinal momentum due to energy loss (1) and multiple scattering (2) in the ionising material, and reacceleration (3) in the RF cavity.

$d\epsilon_N/dX$ is dependent on the degree of cooling and heating experienced by the beam, and is described by the Eqn. 1.22:

$$\frac{d\epsilon_N}{dX} \approx -\frac{\epsilon_N}{\beta^2 E_\mu}\left\langle\frac{dE}{dX}\right\rangle + \frac{\beta_t(13.6MeV)^2}{2\beta^3 E_\mu m_\mu X_0} \tag{1.22}$$

where X_0 is the radiation length in the medium, β_t is the betatron function, E_μ and m_μ are the energy and mass of the muons, and β is their velocity ($\beta = pc/E$). The negative term is the cooling term, and so describes the reduction of the emittance, whilst the positive term corresponds to the heating due to multiple scattering [25].

Due to the heating effect of multiple scattering, it is necessary to choose materials that have a low degree of scattering relative to the energy loss. As such, low Z materials are preferred. The cooling performance for several materials is shown in Figure 1.7.

When the cooling and heating terms in Eqn. 1.22 are equal, the emittance of the beam will be at an equilibrium emittance. If a beam with an emittance lower than the equilibrium emittance is passed through a material, then multiple scattering will dominate and heating will occur. As such it is not possible to reduce the emittance of a beam to less than the equilibrium emittance of a given material. For increasing Z, scattering in the material increases, which results in a higher equilibrium emittance.

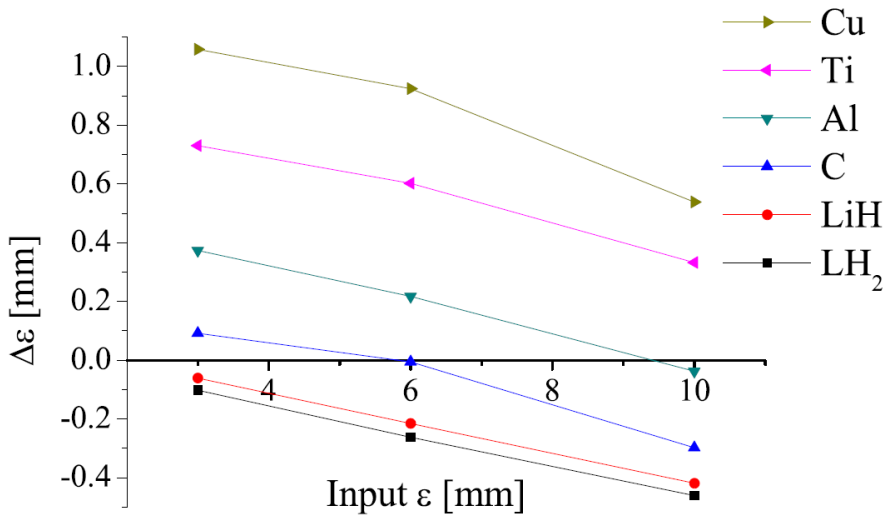

Figure 1.7: Simulated change in emittance $\Delta\varepsilon$ for several materials as a function of the nominal transverse emittance ε of the simulated beam, taken from [34].

Chapter 2

The Muon Ionisation Cooling Experiment

2.1 Introduction

The Muon Ionisation Cooling Experiment (MICE) is a proof of principle experiment, designed to demonstrate the feasibility of ionisation cooling in reducing the emittance of a muon beam for use in a Neutrino Factory or Muon Collider. The change in emittance across the cooling channel is measured by two scintillating fibre trackers, which can measure the normalised emittance reduction, ϵ_n, to a precision of 0.1%. It will study muon beams with input momenta between 140 MeV/c and 240 MeV/c, and emittances between 3-10 mm. In addition to the emittance measurements made by the trackers, particle identification (PID) detectors are used upstream and downstream of the cooling channel to identify contamination to the beam which would impact the emittance measurement.

The experiment is based at Rutherford Appleton Laboratory, UK, and generates a muon beam from the decays of pions produced by the introduction of a titanium target into the ISIS proton beam. MICE is being performed in three stages. The first stage, designated as Step I, consisted of the muon beamline and PID detectors and was used to characterise the beam. Step IV, shown in Figure 2.1, introduces an absorber module and the trackers. The final stage of the experiment, the Demonstration of Ionisation Cooling, shown in Figure 2.2, has several absorbers, and two radio-frequency (RF) cavities to re-accelerate the beam in the longitudinal direction.[1]

The following sections will describe the beamline (section 2.2) which supplies

[1] At the time of writing, the final design for the Demonstration of Ionisation Cooling is in flux.

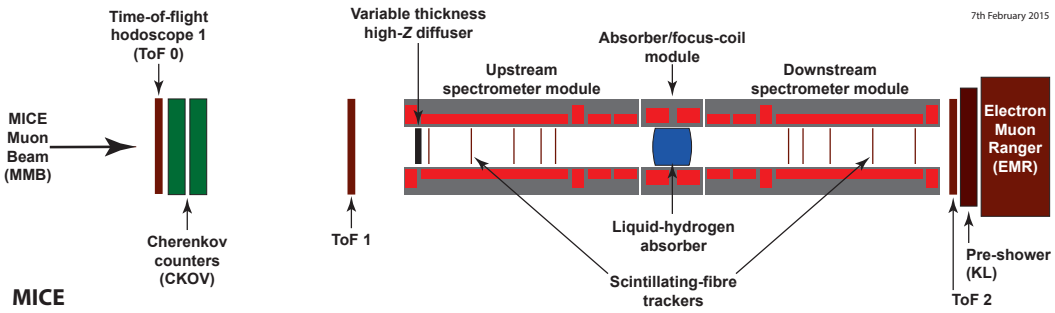

Figure 2.1: MICE Step IV layout. The muon beam enters from the left.

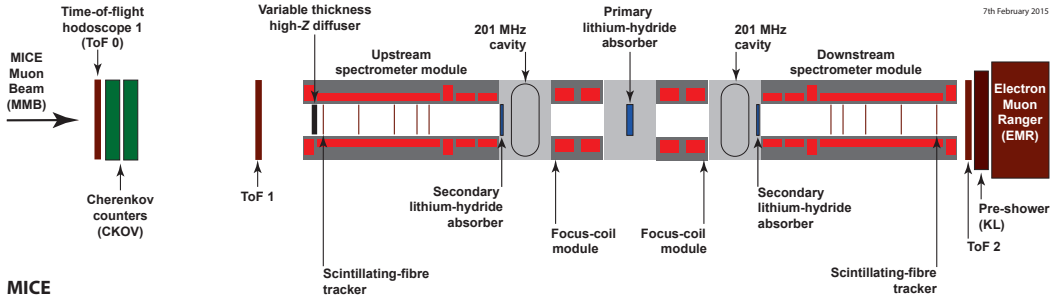

Figure 2.2: Demonstration of Ionisation Cooling layout. The muon beam enters from the left.

the muon beam for the experiment, the components of the MICE cooling channel at both Step IV and for the Demonstration of Ionisation Cooling (section 2.3), and a brief introduction to the detectors and MICE software will be given in sections 2.4 and 2.5.

2.2 Beamline

MICE runs parasitically off of the ISIS synchrotron, dipping a target into the proton beam, and extracting the resulting pions into the MICE beamline, allowing them to decay into the desired muons and transporting the beam to the cooling channel.

2.2.1 ISIS

ISIS is an 800 MeV proton synchrotron that produces beams of neutrons and muons. In the ISIS injector, H^- ions are accelerated by a radio frequency quadrupole, accelerating them into bunches 5ns long, with an energy of 665 keV, which is then increased to 70 MeV by a linac. The ions are then injected to the synchrotron, as

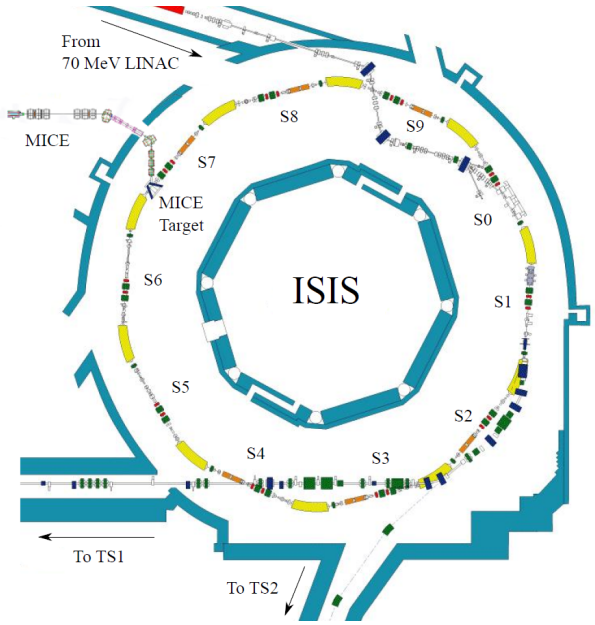

Figure 2.3: The position of the MICE target and beamline with respect to the ISIS synchrotron.

shown in Figure 2.3, and as the ions enter the synchrotron, they have their electrons removed, producing a beam of protons, which is then formed into two bunches and accelerated by RF cavities up to 800 MeV, with a repetition rate of 50 Hz. The beam is then extracted into two beamlines and collided with tungsten targets at Target Station 1 (TS1) and Target Station 2 (TS2) to produce neutron beams. A carbon target 20 m upstream of the TS1 neutron target is also used to produce polarised muons for muon spectroscopy.

2.2.2 Target

The MICE target is a titanium cylinder which is dipped into the ISIS proton beam at the end of the acceleration cycle. Figure 2.4 shows a schematic of the MICE target drive. Permanent magnets on the target shaft are accelerated by coils in the stator, and upper and lower bearings are used to maintain the correct postion of the shaft. The target drive is mounted within a frame which can be raised away from the ISIS beam, so that even if the target was then lowered, it would not reach the beam.

The target is driven into the beam pipe with an acceleration of 80g, just before the beam is extracted. The dip rate is approximately 1 Hz, and so MICE samples 1/50 ISIS pulses. The interaction of the target with the ISIS beam results in

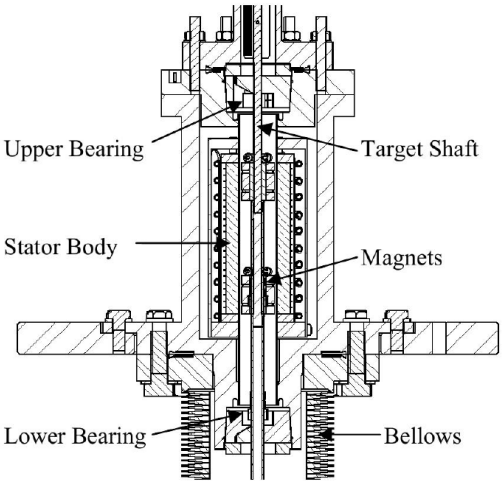

Figure 2.4: MICE target mechanism.

protons being lost from the beam, with the degree of beam loss being proportional to the dip depth. The higher this beam loss, the greater the particle rate achieved in MICE, however it also has the potential to disrupt the beam for other ISIS users, and beam loss within the synchrotron can result in radiation damage. Accordingly, a balance must be found between reasonable particle rates in MICE and an acceptable level of beam loss, which is carefully monitored by both ISIS beam loss monitors and the MICE Luminosity Monitor.

2.2.3 Beamline

Magnets

The layout of the beamline magnets is shown in Figure 2.5. The pions produced by inserting the target into the ISIS beam are captured by a quadrupole triplet (Q1-3) and transported to a dipole magnet, D1, which performs a momentum selection to obtain a pion beam with the desired momentum. The pions then travel through a 5 T decay solenoid, decaying into muons which are subject to a further momentum selection at the second dipole magnet, D2. Depending on the currents selected in D1 and D2, MICE can be operated in one of two modes. In muon mode the momentum selected at D2 is half that at D1, which selects backward-going muons in the pion rest frame, generating a muon beam with high purity. In pion mode the momentum selection at D2 is approximately the same as at D1, resulting in a beam containing a mixture of muons, pions and electrons, which is useful for the calibration of particle detectors, and also produces a greater flux of particles at TOF1. The beam is then

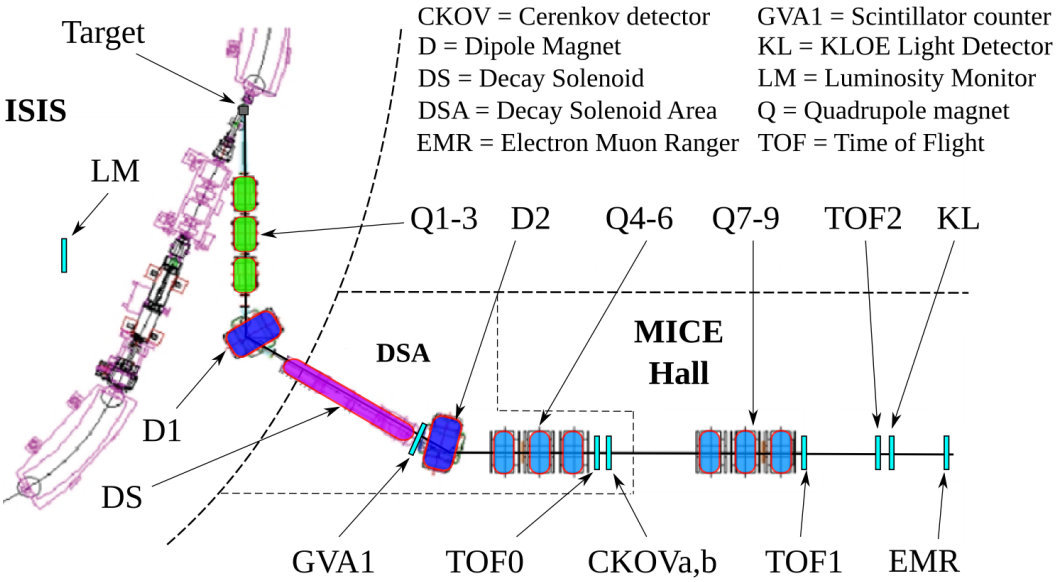

Figure 2.5: Step I configration of the MICE beamline and PID detectors. In the Step IV configuration, and for the Demonstration of Ionisation Cooling, the cooling channel will be between TOF1 and TOF2, with the other downstream detectors (KL and EMR) immediately downstream of TOF2. The distance between D2 and the EMR is approximately 21.5 metres.

transported via two further quadrupole triplets (Q4-6, Q7-9) to the MICE cooling channel.

Proton Absorber

When MICE is run in a positive beam mode, protons deflected from the ISIS beam can enter the MICE beamline. This results in an unwanted contamination to the beam which, while identifiable using time of flight information, is still a background that should be removed before reaching the upstream particle detectors.

Sheets of varying thicknesses (15 mm, 29 mm, 49 mm and 54 mm) of borated-polyethylene are used, in different combinations depending on the momentum settings of the beam, to remove the proton contamination, while allowing muons and pions to pass through. The proton absorber, shown in Figure 2.6, is pneumatically driven and can be operated remotely. It is situated between the decay solenoid and GVA1 scintillator counter.

Figure 2.6: Pneumatically operated proton absorber.

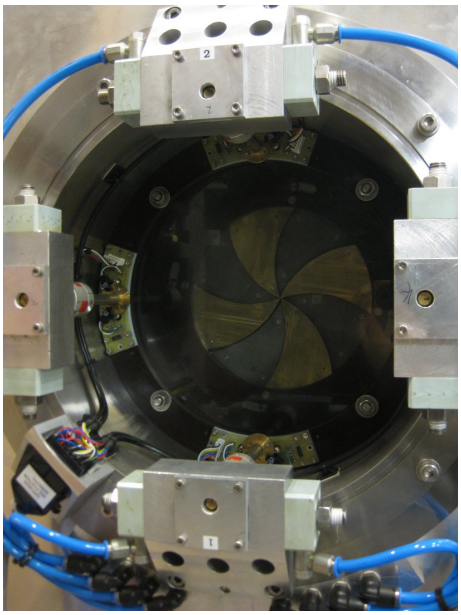

Figure 2.7: MICE diffuser installed within the upstream spectrometer solenoid.

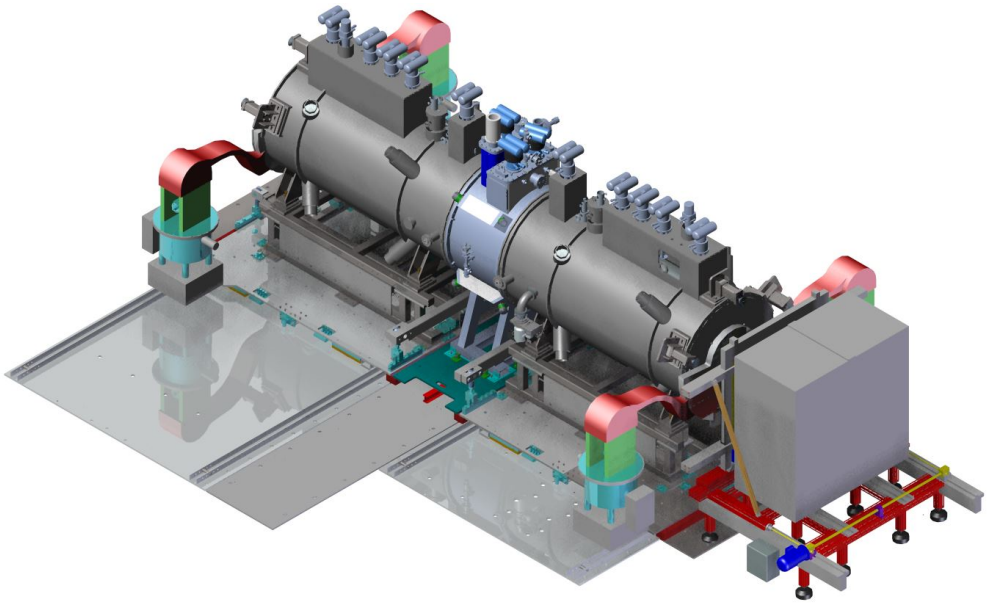

Figure 2.8: Rendering of the Step IV cooling channel.

Diffuser

The diffuser, Figure 2.7, is used to inflate the emittance of the beam, allowing for beams with different input emittances to be studied by MICE. Four irises (two of brass and two of tungsten) of different thicknesses can be used in different combinations to introduce up to 3 X_0 of material to the beam, in 0.2 X_0 intervals, increasing the emittance of the beam up to 10 mm. The diffuser is housed in the upstream spectrometer solenoid, upstream of the scintillating fibre tracker. As it must operate in the environment of the 4 T solenoid, electric motors cannot be used, and so the remotely operated irises are pneumtically actuated.

2.3 Cooling Channel

In Step IV, the cooling channel will consist of a single absorber module. A rendering of the channel, flanked upstream and downstream by the tracking spectrometers, is shown in Figure 2.8. In the Demonstration of Ionisation Cooling, a primary lithium hydride absorber will be used, with re-acceleration of the beam done using single RF cavities upstream and downstream of the absorber. Secondary absorbers will be used to provide screening between the RF and the spectrometer solenoids.

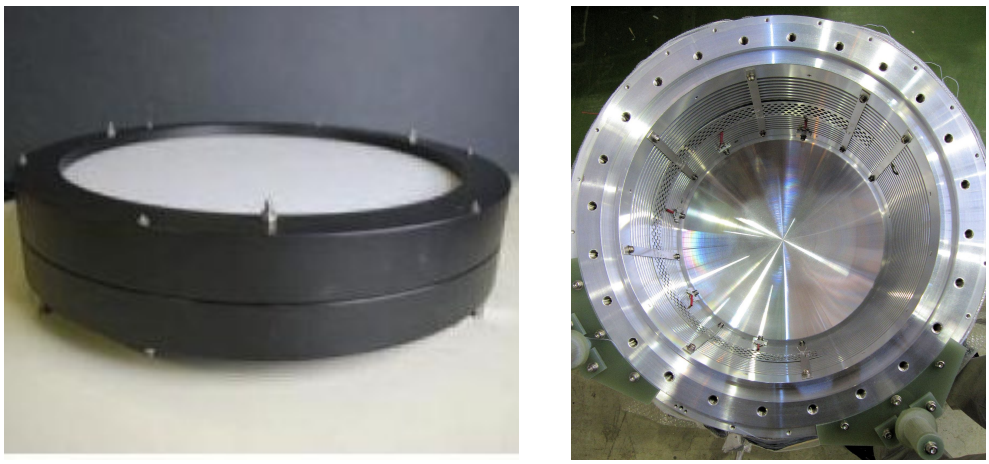

(a) LiH absorber (b) LH_2 vessel

Figure 2.9: The absorbers to be studied in Step IV

2.3.1 Absorber Focus Coil (AFC)

The absorber module used in Step IV will consist of an absorber housed within a focus coil, which constitutes an absorber focus coil (AFC) module. During the Demonstration of Ionisation Cooling, the focus coils will be placed upstream and downstream of the primary absorber.

Absorbers

The absorbers in MICE are used to produce the energy loss required for ionisation cooling. The materials to be studied are liquid hydrogen (LH_2) and lithium hydride (LiH). As described in Section 1.5, an ideal absorber material would allow for maximal cooling via energy loss, whilst keeping heating due to multiple scattering to a mimimum. This is best achieved by low Z materials, which is why LH_2 and LiH were selected for study.

The solid LiH absorber is a 65 mm thick disk, shown in Figure 2.17a. The LH_2 absorber is contained within a 21 litre aluminium vessel, shown in Figure 2.17b. Ultra thin aluminium windows mimise the amount of material the beam must pass through, thus minimising scattering. The material properties of both absorbers will be studied at Step IV.

Focus Coil (FC)

A FC module consists of two coils, and is used to focus the beam to maximise cooling. The coils can be operated in either solenoid mode (where the coils are operated with

Figure 2.10: Focus Coil.

the same polarity) or in flip mode (operated with opposite polarity). In solenoid mode, strong focussing fields can be achieved at lower currents than in flip mode. However for a lattice consisting of several focus coils, a cumulative growth in the kinetic angular momentum of the beam would occur if only coils in solenoid mode were used, resulting in a beam that is mismatched to the lattice. Alternating coils in solenoid mode with coils in flip mode would remove this net growth in angular momentum. Figure 2.10 shows the focus coil to be used in Step IV.

2.3.2 RF Cavities

During the Demonstration of Ionisation Cooling, as shown in Figure 2.2, the muon beam energy lost in the absorbers will be restored by two 201 MHz RF cavities, powered at 10.3 MV/m, which will reaccelerate the muons in the longitudinal direction. This will not restore the total energy lost in the absorbers, and so the different beam energies with and without RF will be compared to determine the feasibility of sustainable cooling if more RF cavities or a greater RF gradient were available. As ionisation cooling is a function of the particle energy, one would expect it to also be a function of the acceleration experienced by each particle. Muons in MICE are produced in spills, with no bunching, so to perform an analysis on a sample of muons approximating a real bunch, it is necessary to select them out by their RF transit phase. The cavity transit time can be inferred from the TOF transit time,

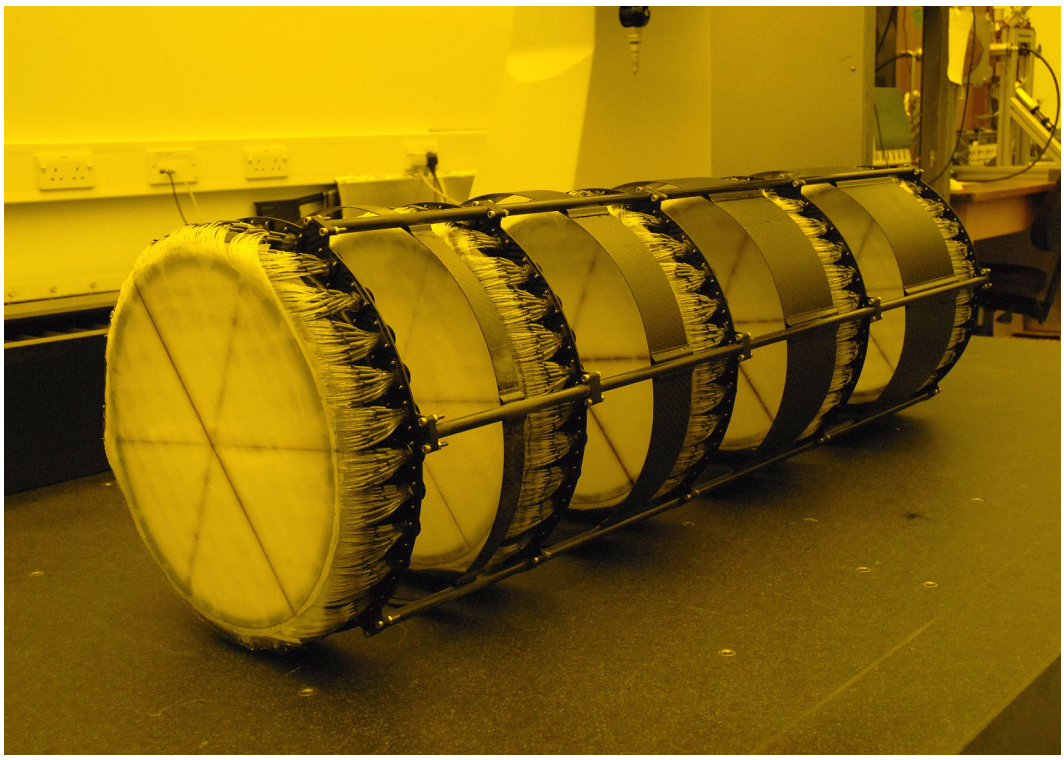

Figure 2.11: One of the MICE scintillating fibre trackers.

which has a resolution of ∼50ps, and the momentum measured in the tracker, which has a resolution of ∼3.5 MeV/c [35].

2.4 Overview of Detectors

As the muons used by MICE are created from pion decay, and can themselves decay into electrons, particle identification is required to detect contamination of the muon beam. MICE employs time of flight (TOF) and Cherenkov detectors, as well as calorimetry, to distinguish between particle types. Scintillating fibre trackers are used to measure the emittance of the beam upstream and downstream of the cooling channel, so the emittance change can be determined. The trackers also provide momentum information which can be used in PID routines.

2.4.1 Scintillating Fibre Trackers

The emittance measurement in MICE is performed by two scintillating fibre trackers, placed upstream and downstream of the cooling channel, which will allow for the change in emittance across the channel to be measured, with a precision of 0.1%.

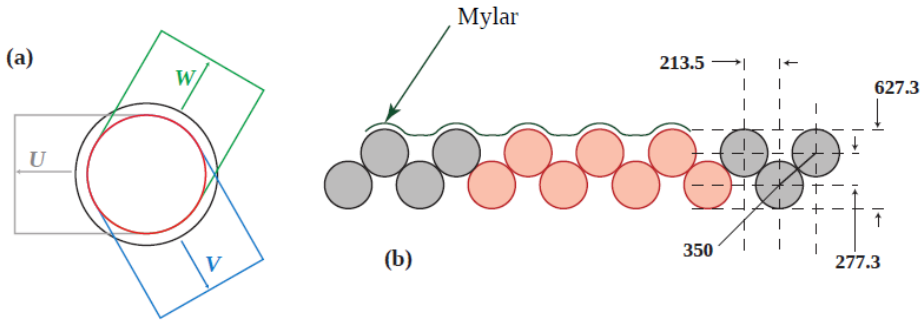

Figure 2.12: The arrangement of the doublet layers is shown in figure (a). The inner circle is the active area of the tracker; the outer is the solenoid bore. The doublet layer structure of the fibres is shown in (b) [36].

The trackers are housed within 4T solenoids, shown in Figure 2.13, inducing the helical motion of the incoming particle, from which the transverse position and momentum of the particle can be measured.

Each tracker consists of stations, as shown in Figure 2.11, which increase in separation along the beam axis. Each station is composed of three planes of scintilating fibres of diameter 350 μm, each orientated at 120° to each other, with the fibres arranged in a doublet structure. The orientation of the planes and the doublet layer structure are shown in Figure 2.12. Scintillation light produced when ionising radiation passes through the fibres is readout by visible light photon counters (VLPCs) [36].

The fibres are grouped into channels (seven fibres per channel). Within the tracker reconstruction, a hit in a single channel will result in a cluster being formed, with any adjacent hits being included in the cluster. Spacepoints in each plane are then formed from either two (doublet spacepoint) or three (triplet spacepoint) clusters. An algorithm to fit the spacepoints into straight or helical tracks is performed, before a Kalman Filter is applied, to account for multiple coulomb scattering and energy losses that occur within the tracker [36]. The position and momentum residuals for the Kalman fit are shown in Figure 2.14 and show that the RMS of the position resolution is less than the fibre thickness. The RMS of the transverse momentum measurements are 1 MeV/c, and 4 MeV/c for the longitudinal momentum, with an offset of 2 and 3.3 MeV/c for the upstream and downstream trackers respectively. The source of these offsets is currently unknown.

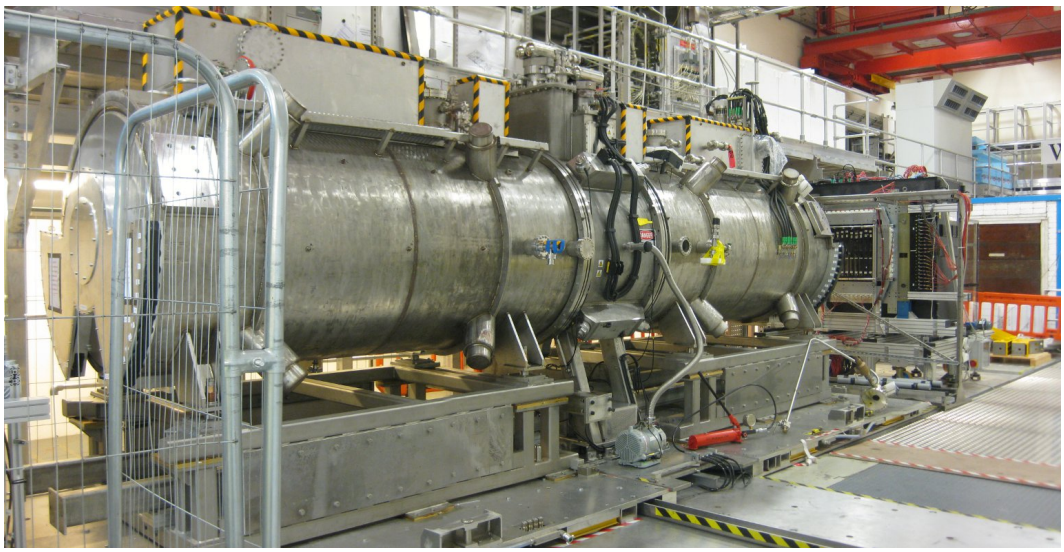

Figure 2.13: Spectrometer solenoids installed in the MICE hall. The focus coil module is between them.

2.4.2 PID Detectors

Time of Flight Detectors (TOF)

Three time of flight detectors, identified in Figure 2.5 as TOF 0, 1 and 2, serve several purposes. Their most important use is to provide particle identification information by measuring the time of flight between two TOF stations. They can also serve as an experimental trigger, and during Step I the first measurement of emittance was made using the TOFs. An example of the time of flight distributions between TOF0 and TOF1 during Step I is shown in Figure 2.15

The TOFs are composed of slabs of scintillating material arranged in two planes, orientated in X and Y. TOF0,1, and 2 have active areas of 40×40 cm^2, 42×42 cm^2, and 60×60 cm^2 respectively. The slabs in TOF0 are 4 cm wide, while the slabs of TOF1 and TOF2 are 6 cm wide [37]. respectively. The strip width is 4 cm for TOF0 and 6 cm for the other two stations. Readout is performed by photo-multiplier tubes (PMTs). TOF0,1, and 2 have timing resolutions of 51 ps, 58 ps and 52 ps respectively, consistent with design requirements. TOF0 and TOF1 are placed upstream of the cooling channel, and TOF2 is downstream of the channel, mounted in front of the KL, as shown in Figure 2.16.

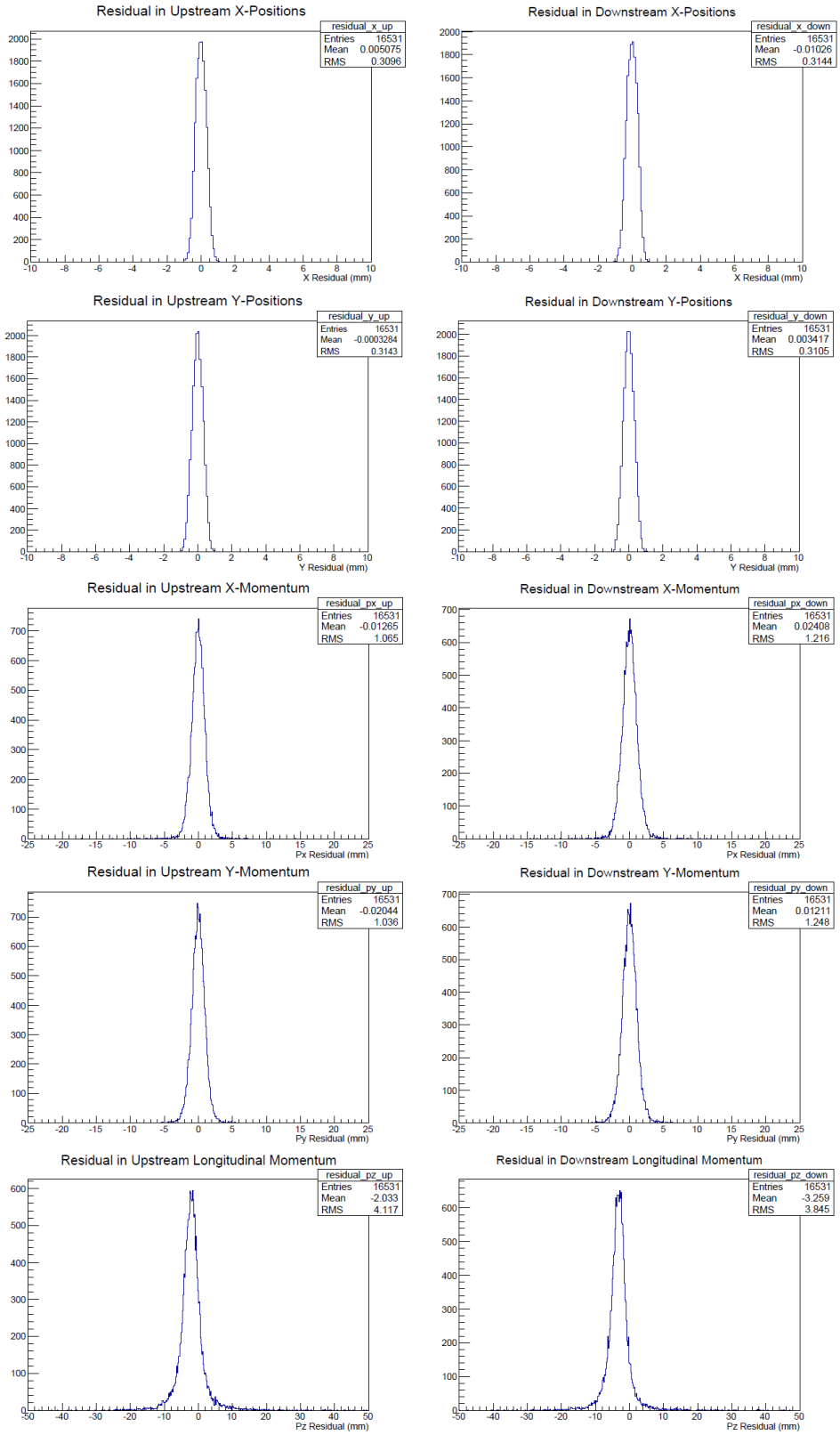

Figure 2.14: Residuals of track fit in the trackers for a 6 mm, 200 MeV/c beam, taken from [36].

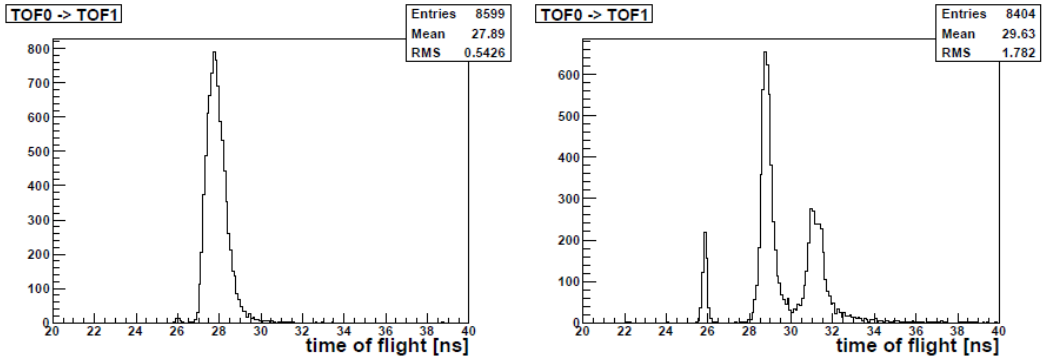

Figure 2.15: Time of flight between TOF0 and TOF1 for a muon beam (left) and pion beam (right) [38]. In the muon beam, a small electron peak can be seen at 26 ns, while the pion contamination of the beam is contained within the muon peak. For the pion beam, the electron, muon, and pion peaks are clearly separated, at 26, 29, and 31 ns respectively.

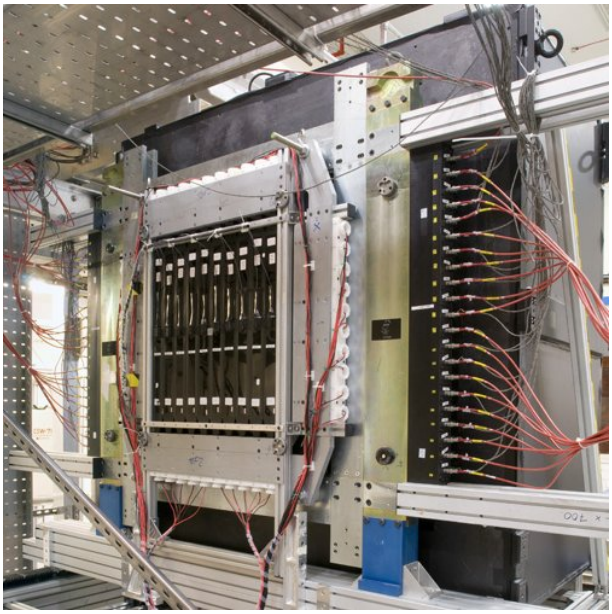

Figure 2.16: TOF2 in front of the KL.

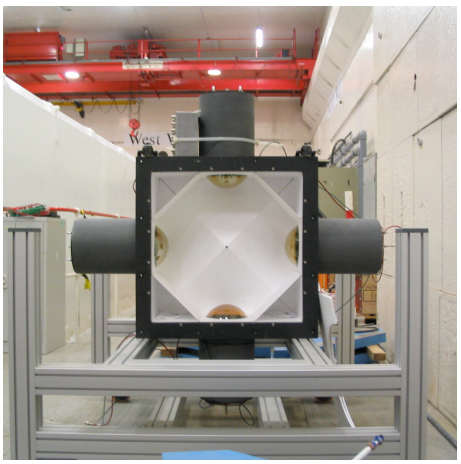

(a) Front view of one of the Cherenkov detectors.

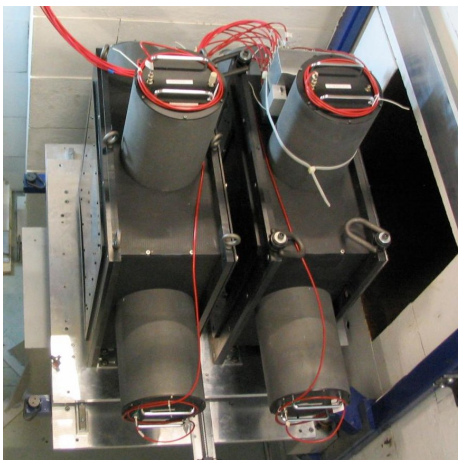

(b) Both Cherenkov detectors in place in the beamline.

Figure 2.17: Cherenkov detectors in MICE

Cherenkov Detectors

Cherenkov light is produced when a charged particle passes through a medium with a speed that is greater than the speed of light in that medium. In a Cherenkov detector, this light is then converted by a photomultiplier tube into an electrical signal that is proportional to the intensity of the light produced.

At higher momenta, muons and pions cannot be easily distinguished by their time of flight. MICE has two Cherenkov detectors (CkovA and CkovB) with different refractive indices (1.07 and 1.12 respectively), immediately downstream of TOF0, which can distinguish between particle types due to their different values of relativistic β.

The refractive indices of the Cherenkovs have been selected such that, for a 200 MeV/c beam, muons will produce a signal in CkovB, but not CkovA, and pions will produce no signal. For a 240 MeV/c beam, pions will produce a signal in CkovB, whereas muons will produce a signal in both detectors. At 140 MeV/c, neither muons or pions will produce a signal in the Cherenkovs, however TOF separation is sufficient at this lower momentum. Figure 2.18 shows the Cherenkov response with respect to the particle time of flight. The efficiencies of CkovA and CkovB are shown in Figure 2.19.

KLOE Light (KL) Calorimeter

The KLOE Light (KL) pre-shower calorimeter (based upon the KLOE calorimeter) mounted downstream of TOF2, is used to distinguish muons from decay electrons. It

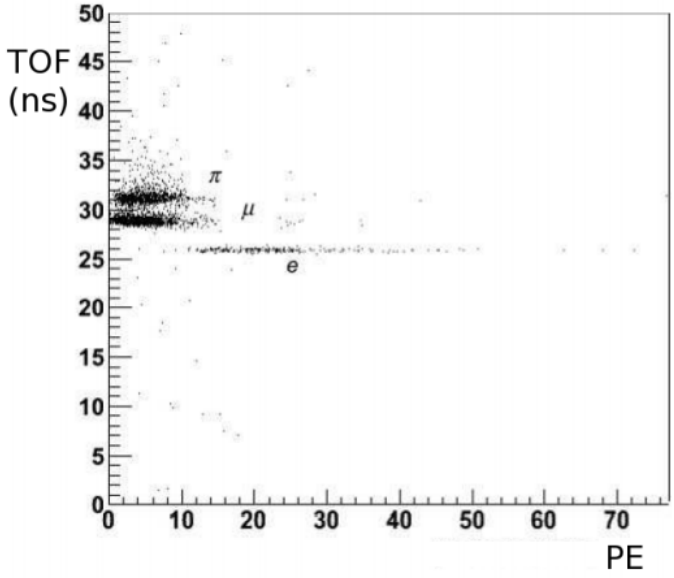

Figure 2.18: The number of photoelectrons produced in the Cherenkovs with respect to the time of flight. A clear separation between the different particle species can be seen [25].

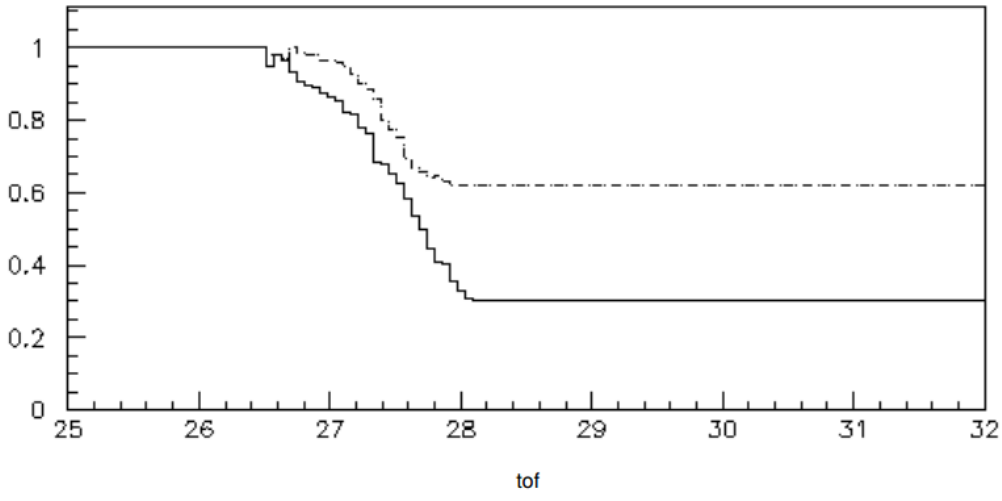

Figure 2.19: The efficiencies of CkovB (solid line) and CkovA (dashed line), as a function of the particle time of flight (in ns) [39].

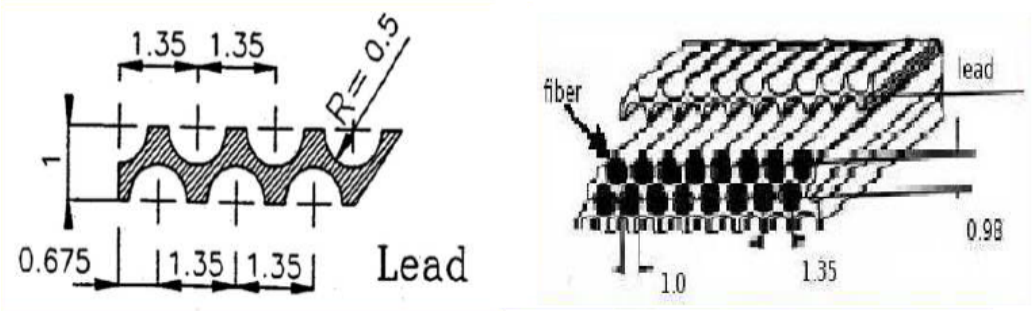

Figure 2.20: Layout of the KL extruded lead and fibres [38].

has an active volume of 93 x 93 x 4 cm^3 and is composed of 21 cells of scintillating fibres within extruded lead foils, shown in Figure 2.20, and scintillation light is readout by 42 Hamamatsu R1355 PMTs. Figure 2.21 shows an exploded view of the KL readout [38], while an exploded view of the KL assembly is shown in Figure 2.21. The signal from the PMTs is shaped and extended in time to match the sampling rate of flash ADCs. The measurement quantity of interest from the KL is the ADC charge product, which is the product of the digitised signals from either side of the cell, divided by their sum, and with a factor of 2 for normalisation, which is of more use than just the ADC charge as it compensates for light attenuation [25].

$$ADC_{prod} = 2 \times ADC_{left} \times ADC_{right}/(ADC_{left} + ADCright) \tag{2.1}$$

The response of the KL to muons, pions, and electrons of different momenta is shown in Figure 2.22.

Electron Muon Ranger (EMR)

The EMR is a totally active scintillator detector, that can distinguish between muons and electrons produced by muon decay in the channel, based upon the range of the particle in the detector, and the characteristics of the energy loss of the particle in the detector. Extruded triangular shaped scintillating plastic bars are arranged in a x-y geometry into 48 planes of 59 bars each. The scintillator light is carried by wavelength shifting fibres, and readout by multi-anode PMTs on both sides. Figure 2.24 shows the EMR in the MICE hall.

Muons and electrons have distinctively different behaviours in the EMR. A muon will leave a single track in the EMR before either stopping, decaying, or exiting the detector, whereas electrons will create an electromagnetic shower. Event displays of a muon track in the EMR are shown in Figure 2.25, and of a showering

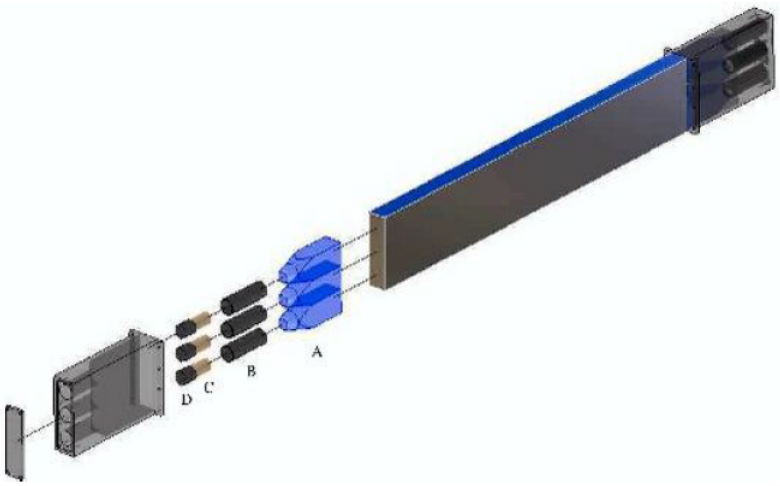

Figure 2.21: An exploded view of a single KL module (which contains 3 cells), with the light guides (A), metal shielding (B), PMTs (C) and voltage dividers (D) [25].

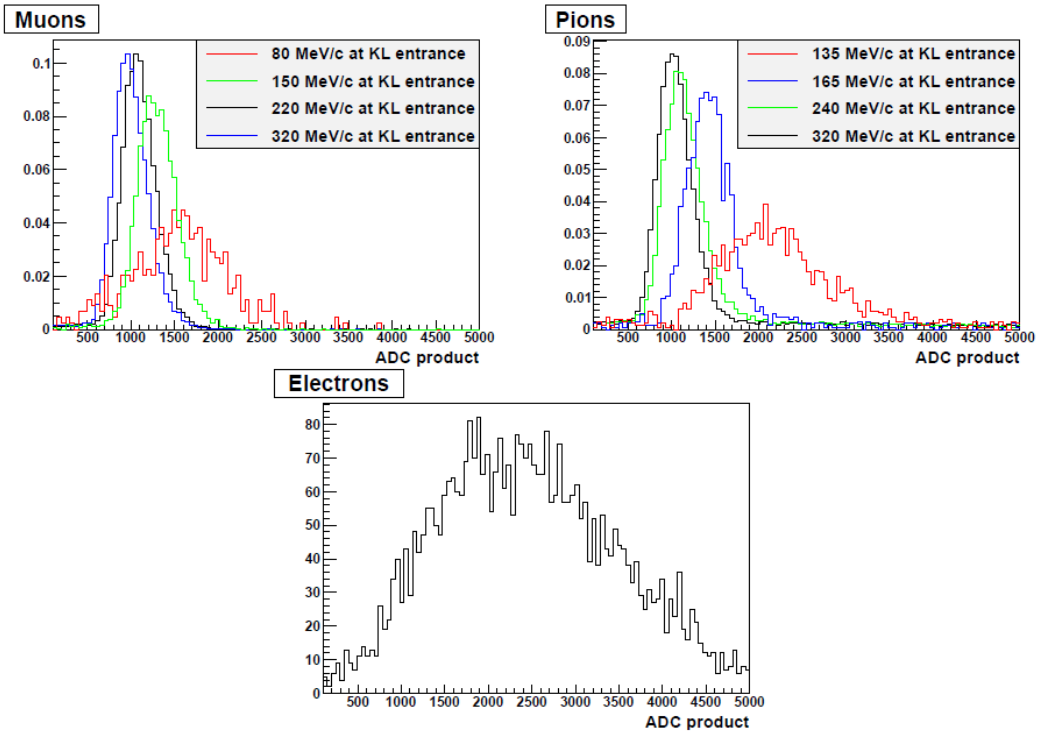

Figure 2.22: KL response for different muon and pion momenta, and for 80 MeV/c electrons, taken from [25].

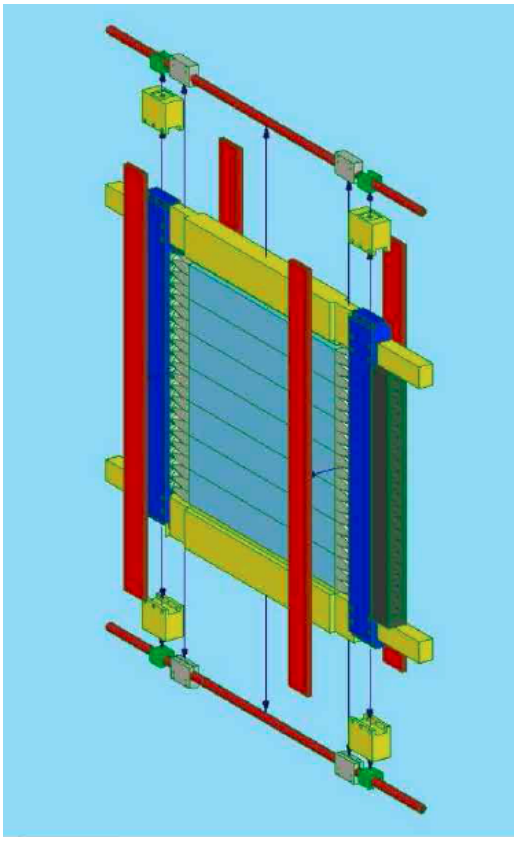

Figure 2.23: Exploded view of KL assembly. The seven strips in the centre contain the active cells. The red bars cover the light guides, the dark blue is the magnetic shielding for the PMTs, the green is the iron bars that house the PMT voltage dividers, and the mechanical support for the KL is in yellow [25].

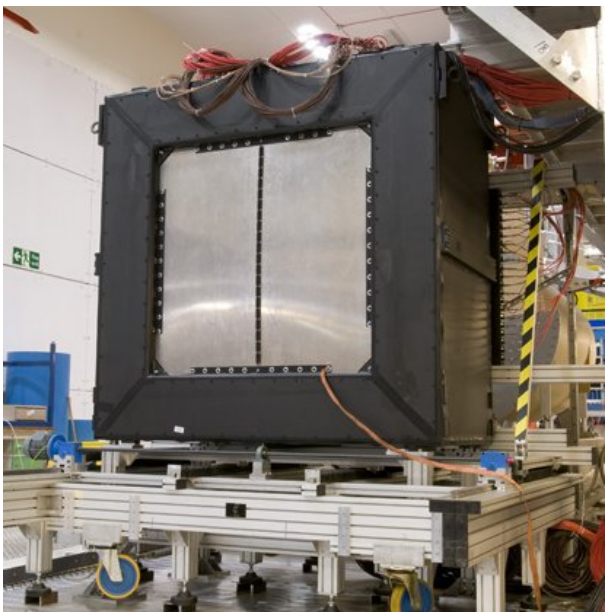

Figure 2.24: EMR detector.

electron in Figure 2.26. For a particle that stops in the EMR, it is also possible to determine the momentum of the particle, with a resolution of 3 MeV/c [40]

2.5 Software

The MICE Analysis User Software (MAUS) is used to perform the simulation, reconstruction (of both simulated and real data) and analysis for the experiment. It can also be run online during experimental running to monitor and provide diagnostics of the data taking. Whilst MAUS is primarily intended for use in MICE, the code can also be used for generic accelerator development.

MAUS is written in Python and C++. It has an Application Programmer Interface (API) framework that is built around the concept of modules. There are four types of module within MAUS, **Inputters**, **Mappers**, **Reducers** and **Outputters**. The principle event type used in MAUS is a spill. A single spill corresponds to the particles produced by a dip of the MICE target. The MAUS modules can be described in terms of how they work with spills:

1. **Inputters** instantiate a spill of data.

2. **Mappers** modify a single spill, and are used both in MC and reconstruction routines.

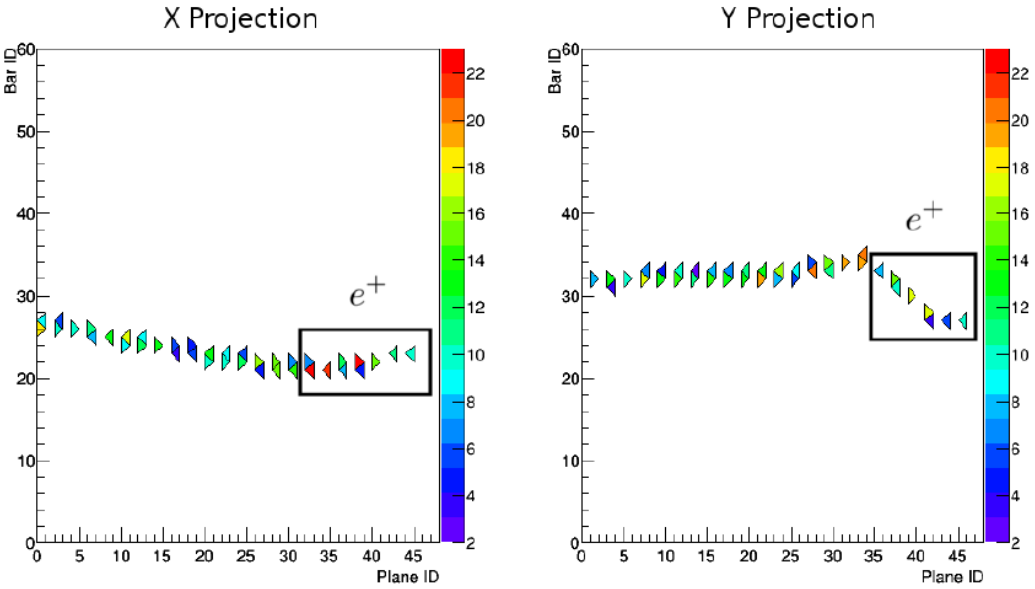

Figure 2.25: Event display of a muon decaying into a positron in the EMR [40].

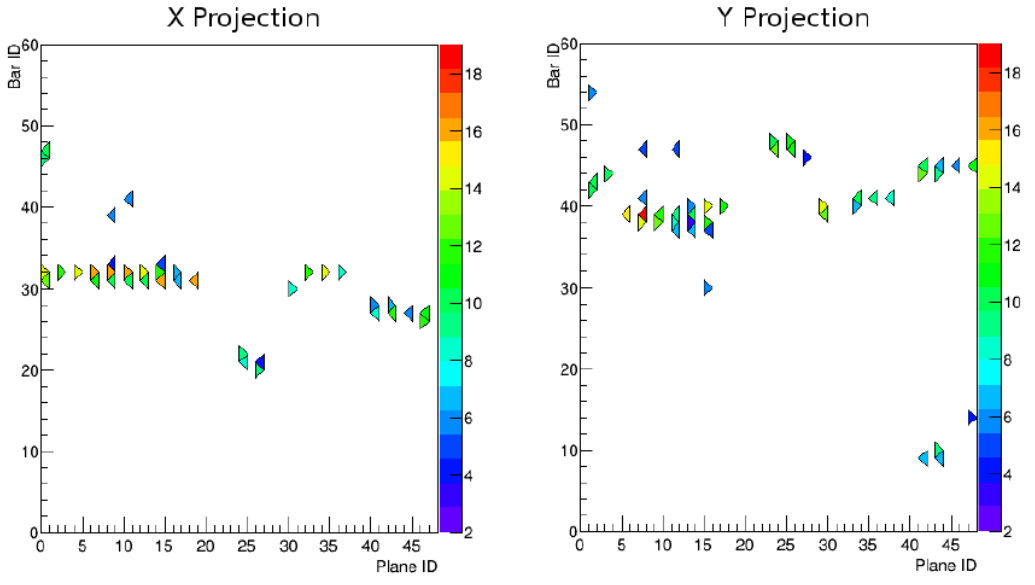

Figure 2.26: Event display of an electron shower in the EMR [40].

3. **Reducers** act on a collection of spills, and can be used to produce histograms based upon the data.

4. **Outputters** save the data.

MAUS data can be written as a binary ROOT object or as an ASCII JSON object, and routines exist to convert between the two.

MC simulation in MICE starts from D2. A G4Beamline file can be used as input, or an input beam can be generated by MAUS for a given beam definition. Particle tracking through the geometry of MICE is performed by Geant4 [41]. The geometries used in MAUS are stored in an online Configuration Database, provide the simulation with the descriptions of the physical volumes (detectors, magnets etc.) and magnetic fields in MICE. Digitization of the MC data allows the responses of the various detectors to be modelled, enabling MAUS to produce simulated detector responses identical in structure to real data.

Reconstruction in MAUS operates on both MC and real data identically. Reconstruction is performed for all MICE detectors, and will be discussed in more detail in Chapter 3.

Online reconstruction of data is used during data taking to provide a real time visualisation of detector performance using histograms.

2.6 Controls and Data Acquisition

MICE uses a controls and monitoring system based upon EPICS [42] (Experimental Physics and Industrial Control System) which is integrated with the DATE [43] (Data Acquisition and Test Environment) system, originally developed for the ALICE experiment.

2.6.1 Controls and Monitoring

Operation of MICE is handled largely by MICE Run Control. It integrates the controls and monitoring systems for the beamline, the particle detectors, the spectrometer solenoids and AFC, the hall environment, and the DAQ and electronics [42]. During operations, Run Control is used to configure the beamline elements for a given run setting (e.g. setting currents in beamline magnets), initiate and end data taking, and monitor the status of the experiment. At all times, Run Control monitors the environment in the MICE hall. In the event of issues with any of the systems Run Control monitors, an alert is issued via the Alarm Handler.

2.6.2 DAQ

The data acquisition system of MICE is required to be able to acquire data at a rate of 600 triggers per 1 ms spill. This means that the Front-End Electronics (FEE) must complete digitisation in less than 500 ns. The digitised data is stored in buffer memory, which is then read out and recorded in the 1 s before the arrival of the next spill [43]. VME FEE interface to Linux data acquisition PCs via an optical link. There is a single PC per VME crate, acting as the Local Data Concentrator (LDC) for the detector being read out. The spill information for all LDCs is then combined over a Local Area Network by the Global Data Concentrator, producing a final data file containing data from all detectors [43].

Chapter 3

Global Particle Identification

3.1 Introduction

Particle Identification (PID) is of great importance in MICE, as upstream of the cooling channel a muon sampling purity greater than 99.9% is desired. The Global PID framework within MAUS is designed to combine the information from the MICE detectors to provide a particle ID estimator for a global track (a track constructed from the individual detectors), and to provide values for the likelihoods of each potential particle species.

3.1.1 Global Reconstruction in MAUS

Global reconstruction in MAUS combines the data from across the experiment for each particle, and uses this to construct a global track, and where possible provides probabilities for the particle to have a given particle ID. Reconstruction upstream and downstream of the cooling channel is performed independently, so that the channel itself can be treated as a black box. However these upstream and downstream tracks can then be combined based upon the time of flight between TOF1 and TOF2.

The global data structure in MAUS is shown in Figure 3.1. Everything is contained within a GlobalEvent, which is itself contained within a ReconEvent, which corresponds to a single particle trigger. Within the global event there are primary chains, each primary chain specific to a single primary particle. When there is only one particle traversing the channel for a single trigger, the event will contain only one primary chain, but in cases where there are multiple particles per trigger (which should be rare in MICE) there will be multiple primary chains. The primary chains contain the global tracks and their constituent parts, trackpoints and

spacepoints. Trackpoints and spacepoints are similar objects, except trackpoints contain more information than spacepoints, and a trackpoint can be created from a spacepoint.

Global reconstruction can be considered to be performed in four stages, and each of these stages is performed by individual mappers. At each stage, the spacepoints, trackpoints and tracks are tagged with the name of the mapper that created them, so that they can be easily selected from the event when necessary.

MapCppGlobalReconImport This mapper imports the information from the detectors' local reconstructions into the global event. Depending on the output of the local reconstruction, the information may be imported as global spacepoints, trackpoints or tracks. Any quantities required for PID, such as the number of photoelectrons measured in the Cherenkov counters, is also carried forward into the event.

MapCppGlobalTrackMatching A 4th order Runge-Kutte (RK4) method is used to combine the output from MapCppGlobalReconImport into global tracks, which are tagged with the appropriate mapper name so that they can be selected from the global event by the PID. For each particle, tracks are formed upstream and downstream of the cooling channel independently. The RK4 algorithm is used to propagate tracks from the trackers, as these provide the most accurate position and momentum information, to the other detectors, and the position of these propagated hits is then compared to the position of the hits in the detectors given by their local reconstruction. If the positions of the propagated hit and the local reconstruction hit match within the acceptance (determined by the error on the local reconstruction measurement), then the detector hit is added to the global track. Because the RK4 requires a particle mass (and as such a particle ID), track matching is performed for all possible particle hypotheses ($\mu\pm$, $\pi\pm$, $e\pm$).

MapCppGlobalPID This mapper performs PID on the tracks that have been produced by the two preceding mappers, and if a particle ID is found, the track with that ID is passed on to the final global fitting mapper. The behaviour of this mapper will be discussed further later in this section.

MapCppGlobalTrackFitting Yet to be developed, but will likely use the same Kalman filter used in track fitting in the scintillating fibre trackers.

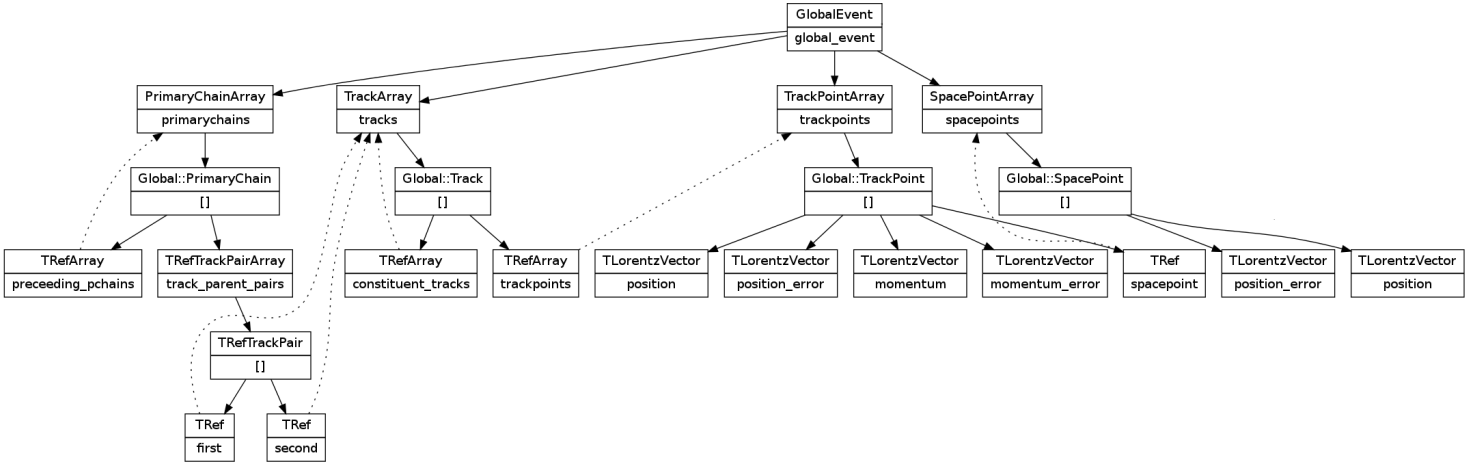

Figure 3.1: Structure of a global event in MAUS.

3.1.2 Datastructure Nomenclature

In both the local detector reconstructions and global reconstruction, the terms spacepoint, trackpoint, and track are used. However they are not consistently defined across the reconstructions. Their definitions for each detector will be outlined in Section 3.1.3. Their definitions within the global datastructure are:

- **Spacepoint:** A single measurement in a detector, with a 4D position (x,y,z,t).
- **Trackpoint:** A single point in 4D space with a momentum and associated errors. It may correspond to a spacepoint, or after track fitting to a projected point in space.
- **Track:** A collection of trackpoints, grouped by the global reconstruction, with an associated particle ID.

In the global reconstruction positions in space are given in terms of the global coordinate system (one that incorporates the whole experiment from D2 to the EMR) whereas in the local reconstructions initially reconstruct in a 'local' coordinate system which does not extend outside of the volume of the detector. These local positions are then converted to global positions in line with the global coordinate system.

3.1.3 Detectors

The detectors and their performance were discussed in detail in Chapter 2. This section will describe how the information from the detectors is incorporated into the global reconstruction.

Time of Flight detectors

The TOFs are composed of horizontal (x) and vertical (y) slabs of plastic scintillator. If a hit is recorded in both an x and y slab, then a TOF spacepoint is formed. The time, position (in global coordinates), and the errors on these values, are recorded, and this information is then retrieved by the global reconstruction at the importing stage, creating a global spacepoint for each TOF spacepoint. The positions are used during track matching and fitting, and the time of flight serves as both a valuable PID quantity, and also a means to connect upstream and downstream tracks by checking the TOF1-2 time of flight.

Cherenkovs

The number of photoelectrons measured for a single particle trigger are recorded together in a recon event, for both of the MICE Cherenkov detectors. No other information is provided that is of use to the global reconstruction. A single global spacepoint is produced for each cherenkov detector, and the number of photoelectrons is stored in that spacepoint.

Scintillating Fibre Trackers

A signal from a channel hit in the tracker is stored as a digit. Digits from adjacent channels, assumed to have come from the same particle, form a cluster. If clusters are found to intersect within at least two planes of the same station, these are reconstructed as a SciFi spacepoint, which has an associated x and y position, given by the cluster positions, and a z position, which is the z position of the station. Pattern recognition routines join together spacepoints in the tracker into either straight or helical tracks. A Kalman filter then creates trackpoints based upon the clusters that produced the spacepoints that feature in the pattern recognition track. These trackpoints have position and momentum information, with associated errors, and this information is retrieved by the global reconstruction at the importing stage, creating a global trackpoint for each SciFi trackpoint.

KL calorimeter

Hits in the KL are stored as cell hits, which provide a vertical position measurement with reasonable granularity, but due to the structure of the KL the horizontal position of the hit can only be known to be within the detector. Nonetheless, the KL reconstruction provides a global position, with errors, and the ADC charge and charge product for each hit, all of which is carried forward into the global event, with a global spacepoint produced for each KL cell hit.

EMR calorimeter

Plane hits in the EMR are used to form spacepoints, which are then fitted using a polynomial in the xz and yz planes to form a track, creating trackpoints from the spacepoints in the process. These tracks and trackpoints are imported into the global datastructure to be used by global track matching, as they have associated positions and errors. The EMR reconstruction also provides a number of self contained PID routines, which are very effective for separating out electrons, as is the purpose of the EMR. Two PID quantities that provide some degree of muon/pion separation

are the range of the particles in the EMR, and the density of plane hits, and so these are also used within the Global PID.

3.2 Global PID

Global PID in MAUS uses a framework built upon PID variables, discussed below, to determine the most likely particle ID (pid) of a global track, with an associated confidence level of the track having been produced by a given particle species. It also provides likelihoods (as log likelihoods) of the track having been produced by different particle species for the users reference.

3.2.1 Framework

The PID framework is based upon a library of PID variables; quantities that can distinguish between different particle species, e.g. time of flight. These variables are used in two ways. They can be used with Monte Carlo tracks to create probability density functions (PDFs) of their values for each particle species, and they can be used with tracks reconstructed from real data, calculating the value of each variable and comparing it to the corresponding PDFs for each pid, in order to find the likelihood of the track having a given pid.

PIDVariables

The information provided from the local reconstruction in each MICE detector is incorported into libraries of PID variables in MAUS. Currently there are two libraries of variables in MAUS, one for commissioning and one for Step IV running. These are detailed in Sections 3.3 and 3.4 respectively.

Each PID variable is represented by its own class, derived from a base class (PIDBase). This structure allows for new variables to be added easily into the framework when necessary. One (e.g. time of flight) and two (e.g. time of flight coupled with momentum) dimensional variables are currently in use, and so intermediate base classes are used (PIDBase1D and PIDBase2D) depending on the nature of the PID variable. The base classes contain functions to:

- Create PDFs of the variables.
- Create files and directories to store the PDFs.
- Populate the PDFs with the values of the variables (and perform any checks on the validity of the values).

- Calculate the PID variable value (a virtual function to be defined in each variable class)
- Perform the log-likelihood calculation for a global track.

Each class is named PIDVar$X$ (or ComPIDVar$X$ for commissioning PID variables), with X increasing alphabetically as variables are added. More descriptive variable names are set within the classes themselves, and this variable name is used in the file names of the PDFs. The PIDVar classes contain the functions to calculate the values of their variables, and in each class the range of allowed values can also be set.

PDF Production

The PDFs used by the PID are produced by **ReduceCppGlobalPID**. MAUS comes pre-packaged with a set of PDFs for common beam settings, but if a user has a non-standard beam that they would like to perform PID for, then that beam can be simulated and passed to the global reconstruction. The global tracks can then be processed by the reducer to create a directory that will correspond to the simulated particle hypothesis and the time at which the reducer was run, and within this directory will be files for each PID variable, each of which will contain the PDF for that variable and hypothesis.

Performing PID

PID is performed by **MapCppGlobalPID**. Track matching passes several potential tracks to the PID, each one reconstructed for a given particle hypothesis. The PID takes each track in turn, and determines the most likely pid for that track. This is done by:

1. Copying each track into a PID-Candidate track, and setting the pid of the copy to zero (undefined).
2. The log-likelihood, LL_X, for each potential pid hypothesis X, is calculated for the PID variables, as detailed in Section 3.2.2.
3. Each track has an associated PIDLogLPair object, which stores the log-likelihood for each particle hypothesis that the track was tested against.
4. Based on the log-likelihoods for i particle hypotheses, the confidence level

(CL_X) of the track having pid X is calculated by

$$CL_X = \frac{exp(LL_X)}{\sum_i exp(LL_i)} \times 100 \tag{3.1}$$

5. If the confidence level for one hypothesis is greater than the confidence levels of the other hypotheses by a user defined margin (confidence level cut), then the pid of the candidate track is set to that hypothesis.

   - If the track fails the confidence level cut, no identification is made. This would constitute a PID failure.

6. If the pid of the candidate track is the same as the pid of the track matching track from which it was copied, then that track is assumed to be the correct track, and is passed on to the global track fitting as a PID-Final track.

3.2.2 Log-Likelihoods

Comparisons of likelihoods for different particle hypotheses (as likelihood ratios) allows for strong discrimination between competing hypotheses. The use of log-likelihoods means that the differences of the log-likelihoods can be used, rather than the likelihood ratios.

For each PID variable, PDFs can be made for each potential particle hypothesis X_i. As the PDF is normalised, the integral over all entries of the histogram is unity. The likelihood that a particle hypothesis X_i produces a value v_k of the variable to be measured $L_k(v_k|X_i)$ is given by the number of entries in the histogram bin containing v_k. The likelihood that a collection of PID variable values $\vec{v}$ are produced due to a given particle hypothesis is given by

$$L(\vec{v}|X_i) = \prod_k L_k(v_k|X_i) \tag{3.2}$$

and the likelihood ratio between two particle hypotheses, r_{ij} is given by

$$r_{ij} = \frac{L(\vec{v}|X_i)}{L(\vec{v}|X_j)} \tag{3.3}$$

By using log-likelihoods, equation 3.2 can be re-written as

$$LL(\vec{v}|X_i) = \sum_k LL_k(v_k|X_i) \tag{3.4}$$

and the ratio of likelihoods given in equation 3.3 becomes a difference between log-likelihoods d_{ij},

$$d_{ij} = LL(\vec{v}|X_i) - LL(\vec{v}|X_j) \tag{3.5}$$

3.3 Commissioning PID

For the commissioning period of the MICE beamline and channel apparatus in preparation for Step IV, it was also desirable to perform reconstruction on a global level. During this period, as the spectrometer solenoids and focus coil were being installed and before they were trained, there were no fields in the channel, and so particles passing through the channel followed straight tracks. There was also no absorber material present in the channel. This means that the trackers were unable to provide a momentum measurement and so could not be used for PID. However the time of flight between TOF1 and TOF2 can compensate for this if used in conjunction with the other detector outputs. During commissioning of the experiment, and during global alignment studies of the detectors, there was not the same requirement of independence between upstream and downstream PID as there is during Step IV, and so cross channel measurements, including TOF1 to TOF2 time of flight were deemed reasonable.

3.3.1 Variables

The variables used during commissioning are summarised in Table 3.1, and examples of their probability density functions are shown in Figures 3.2 - 3.10 for a 200 MeV/c muon beam. The beam is designed to primarily consist of 200 MeV/c muons, but will have a small electron and pion contamination.

ComPIDVarA

The time of flight between TOF1 and TOF2, as shown in Figure 3.2 for a 200 MeV/c muon beam, provides excellent separation between electrons and muons/pions. For the example shown, it can be seen that by cutting on the time of flight at 32 ns when running PID, one would expect to obtain a largely pure muon sample (assuming that the MC is consistent with the data). However for lower momenta the separation of the muon and pion peaks would be less, and so the suitablility of this variable is dependent on the beam settings. Furthermore, for a muon beam, where there is a small amount of pion contamination, these pions would largely fall within the muon peak, and as such a TOF measurement alone may not be suitable for PID.

ComPIDVarB

Coupling the KL ADC charge product with the time of flight, as shown in Figure 3.3 for a 200 MeV/c muon beam, maintains the electron separation seen for just the time of flight measurement, and also allows for a cut to be placed not only on the time of flight, but also on the ADC charge product, which when trying to identify muons would remove some of the high energy pions that present with time of flights between 32 and 34 ns.

ComPIDVarC

The KL ADC charge alone, as shown in Figure 3.4 for a 200 MeV/c muon beam, does not allow for good separation between muons and pions, and in the muon/pion region, electrons would typically be mis-identified. However the variable is included in the framework should users wish to use it.

ComPIDVarD

The range of a particle in the EMR, as shown in Figure 3.5 for a 200 MeV/c muon beam, shows some separation between muons and pions, and demonstrates their limited penetration depth within the EMR.

ComPIDVarE

Coupling the EMR range with the time of flight, as shown in Figure 3.6 for a 200 MeV/c muon beam, maintains the electron separation seen for just the time of flight measurement, but also separates the muon and pion samples into distinct curves, with minimal overlap, allowing for greater purity in the PID measurement than with the EMR range alone.

ComPIDVarF

The density of plane hits in the EMR, as shown in Figure 3.7 for a 200 MeV/c muon beam does not show particularly good separation between particle species, except at plane densities greater than 95% where the populations of electrons and pions is very low. Between 80 and 95% the muon probability density is also higher than that for pions and electrons, however this region still has a reasonably large number of pions and electrons that would be misidentified as muons, and so for the sake of preserving the purity of the muon sample the ideal cut would be at 95%.

ComPIDVarG

Coupling the EMR plane density with the time of flight, as shown in Figure 3.8 for a 200 MeV/c muon beam, maintains the electron separation seen for just the time of flight measurement, and also improves the separation of the muon and pion samples, allowing for greater purity in the PID measurement than with the plane density alone.

ComPIDVarH

The number of photoelectrons produced in CkovA as a function of the time of flight, as shown in Figure 3.9 for a 200 MeV/c muon beam. Only electron and muon distributions are shown, with a clear separation between the distributions, as pions at this energy do not produce any Cherenkov light.

ComPIDVarI

The number of photoelectrons produced in CkovB as a function of the time of flight, as shown in Figure 3.10 for a 200 MeV/c muon beam. There is a clear separation between the electron and muon/pion distributions. There is a small region of overlap between the pions and muons, but in this region the probability density for pions is much higher than that for muons, which means that even without placing cuts on the time of flight/number of photoelectrons a largely pure muon sample should be obtained.

Class Name	Variable Name	Description
ComPIDVarA	diffTOF1TOF2	Time of flight between TOF1 and TOF2. Momentum dependent.
ComPIDVarB	KLChargevsDiffTOF1TOF2	KL ADC charge product and time of flight between TOF1 and TOF2. Time of flight reduces dependence of KL measurement on beam momentum.
ComPIDVarC	CommissioningKLADCChargeProduct	KL ADC charge product. Momentum dependent.
ComPIDVarD	CommissioningEMRrange	Range of particle in EMR. Momentum dependent.
ComPIDVarE	CommissioningEMRrangevsDiffTOF1TOF2	Range of particle in EMR and time of flight between TOF1 and TOF2. Time of flight reduces dependence of EMR measurement on beam momentum.
ComPIDVarF	CommissioningEMRdensity	EMR plane density. Momentum dependent.
ComPIDVarG	CommissioningEMRdensityvsDiffTOF1TOF2	EMR plane density and time of flight between TOF1 and TOF2. Time of flight reduces dependence of EMR measurement on beam momentum.
ComPIDVarH	CkovAvsDiffTOF1TOF2	Number of photoelectrons (pes) measured in CkovA and time of flight between TOF1 and TOF2.
ComPIDVarI	CkovBvsDiffTOF1TOF2	Number of photoelectrons (pes) measured in CkovB and time of flight between TOF1 and TOF2.

Table 3.1: Commissioning PID variables.

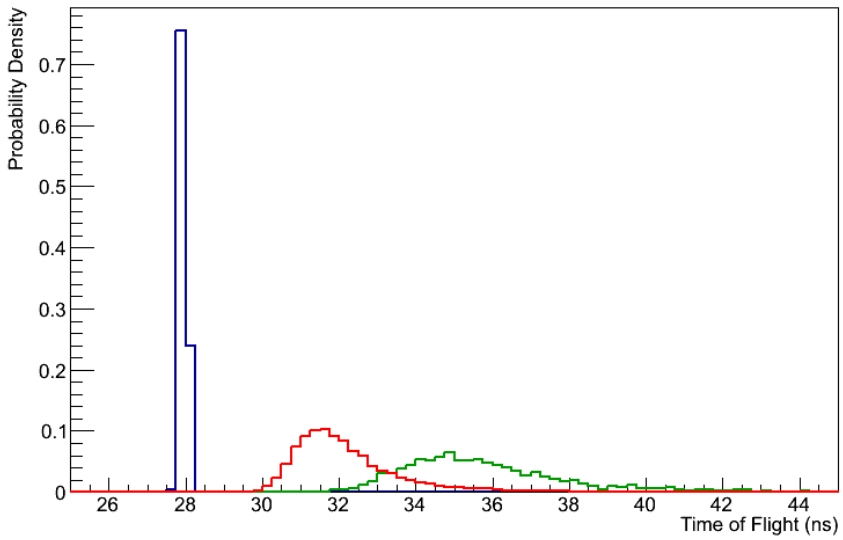

Figure 3.2: An example PDF, produced using ReduceCppGlobalPID, of ComPID-VarA. Shown are muons (red, peak at 32 ns), pions (green, peak at 35 ns) and electrons (blue, peak at 28 ns), for a simulated 200 MeV/c muon beam. As these distributions only include particles that make it through the entire channel, the electron distribution appears as a sharp monochromatic peak, as electrons that scatter out of the channel are omitted. While the pions contaminating the beam would initially have a higher momentum than the muons, the particles here have passed through both the diffuser and absorber in the channel, where the pions lose energy more quickly than the muons, resulting in the smeared distribution that peaks at a longer time of flight than if there were no material present.

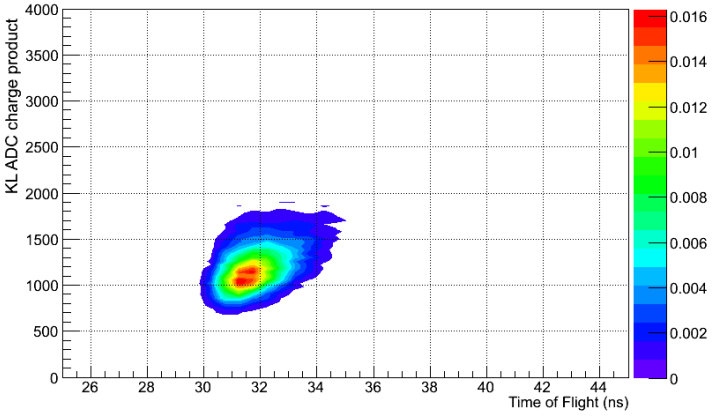

(a)

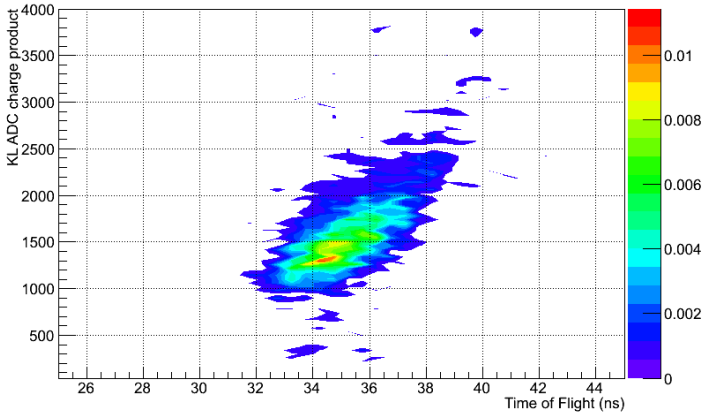

(b)

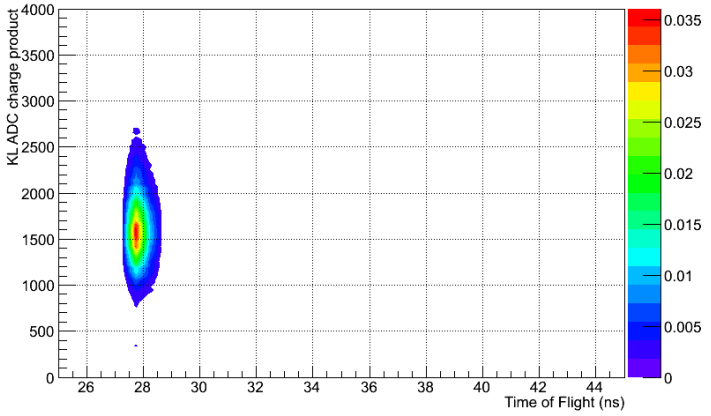

(c)

Figure 3.3: Example PDFs, produced using ReduceCppGlobalPID, of ComPIDVarB for muons (a), pions (b) and electrons (c), for a simulated 200 MeV/c muon beam. Compared to ComPIDVarC, as shown in Figure 3.4, it provides far better separation between particle types

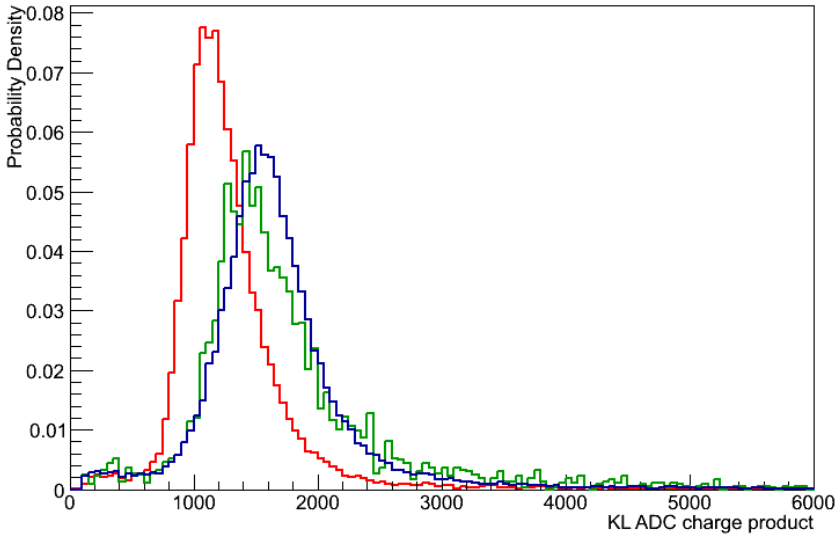

Figure 3.4: An example PDF, produced using ReduceCppGlobalPID, of ComPID-VarC. Shown are muons (red), pions (green) and electrons (blue), for a simulated 200 MeV/c muon beam.

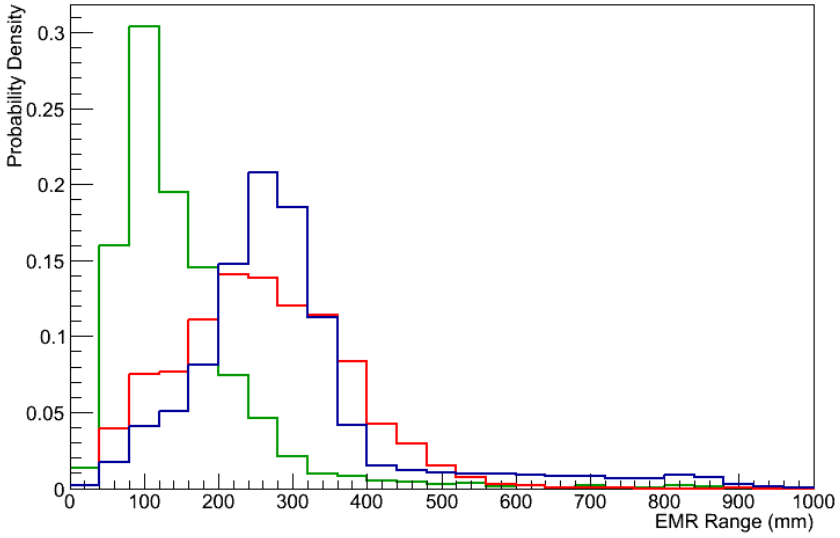

Figure 3.5: An example PDF, produced using ReduceCppGlobalPID, of ComPID-VarD. Shown are muons (red), pions (green) and electrons (blue), for a simulated 200 MeV/c muon beam.

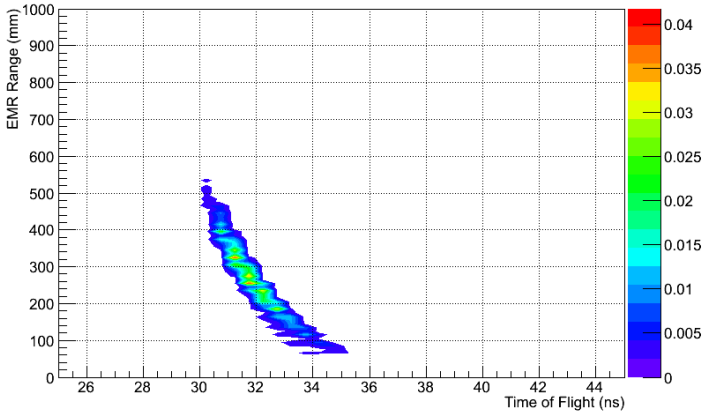

(a)

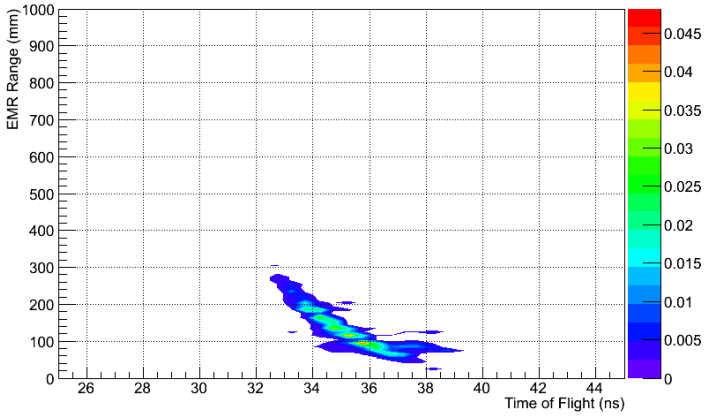

(b)

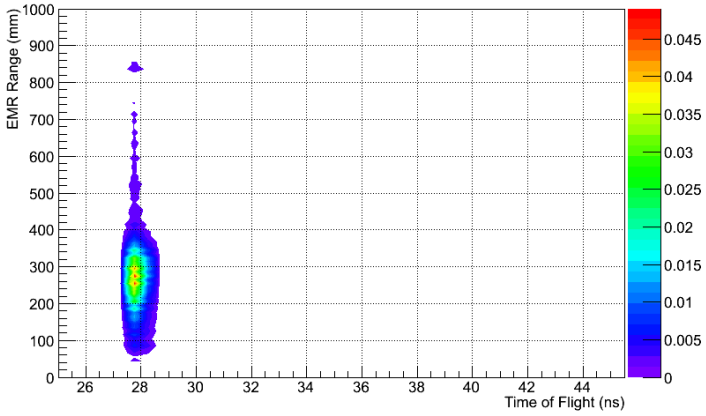

(c)

Figure 3.6: Example PDFs, produced using ReduceCppGlobalPID, of ComPIDVarE for muons (a), pions (b) and electrons (c), for a simulated 200 MeV/c muon beam.

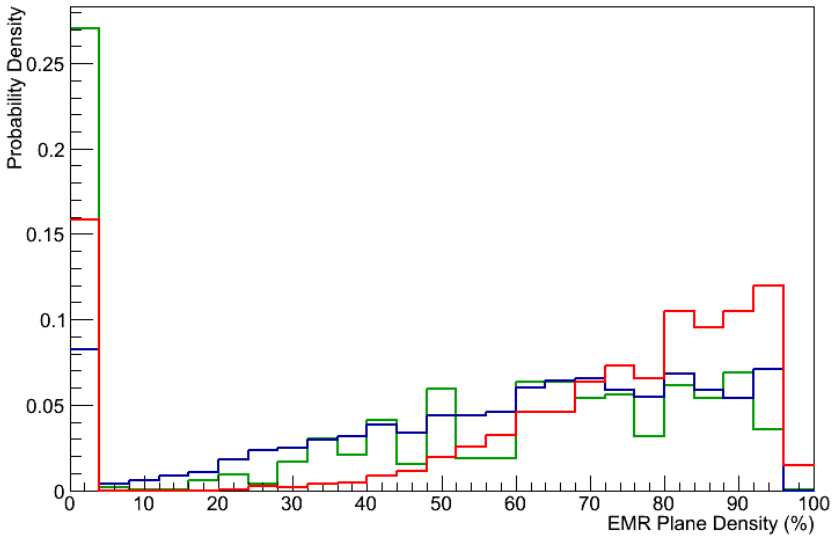

Figure 3.7: An example PDF, produced using ReduceCppGlobalPID, of ComPIDVarF. Shown are muons (red), pions (green) and electrons (blue), for a simulated 200 MeV/c muon beam.

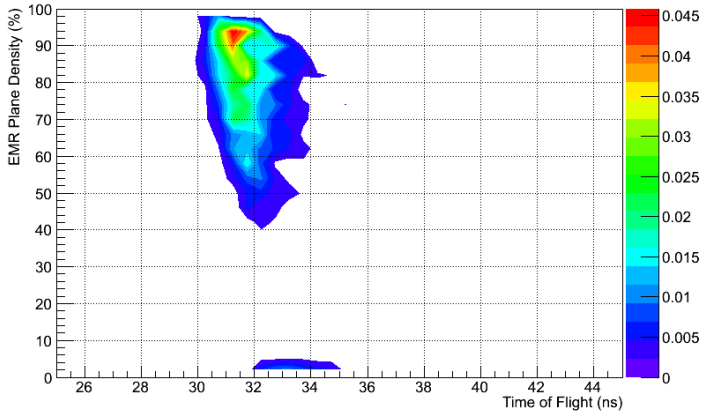

(a)

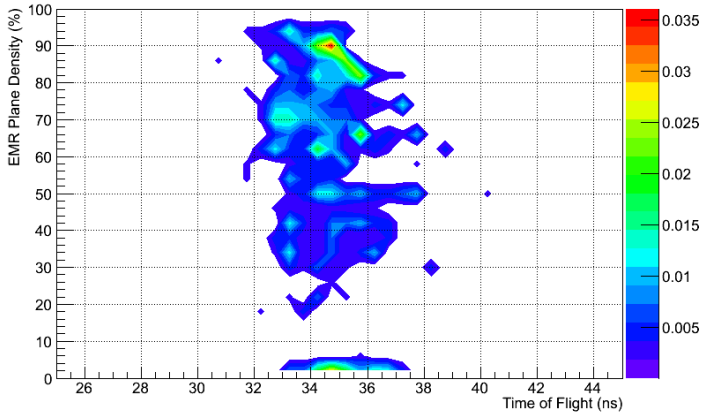

(b)

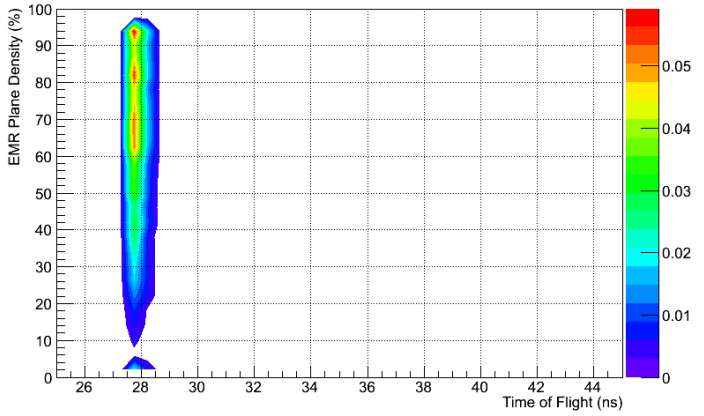

(c)

Figure 3.8: Example PDFs, produced using ReduceCppGlobalPID, of ComPIDVarG for muons (a), pions (b) and electrons (c), for a simulated 200 MeV/c muon beam.

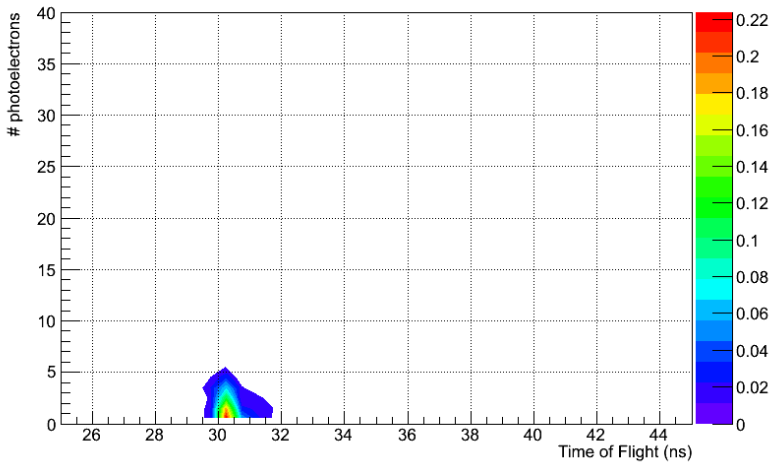

(a)

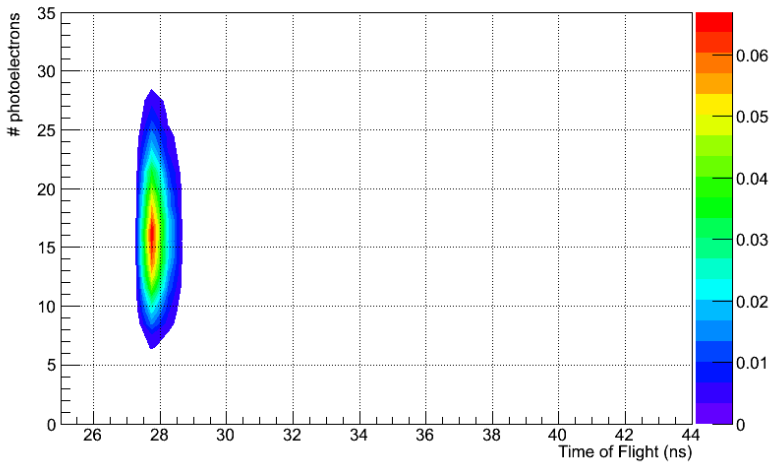

(b)

Figure 3.9: Example PDFs, produced using ReduceCppGlobalPID, of ComPIDVarH for muons (a) and electrons (b), for a simulated 200 MeV/c muon beam. Pions at this beam momentum setting do not produce a signal in Cherenkov A. The muon distribution here peaks at a lower time of flight than that shown for ComPIDVarA; this is due to only the higher momentum muons producing a signal in the detector.

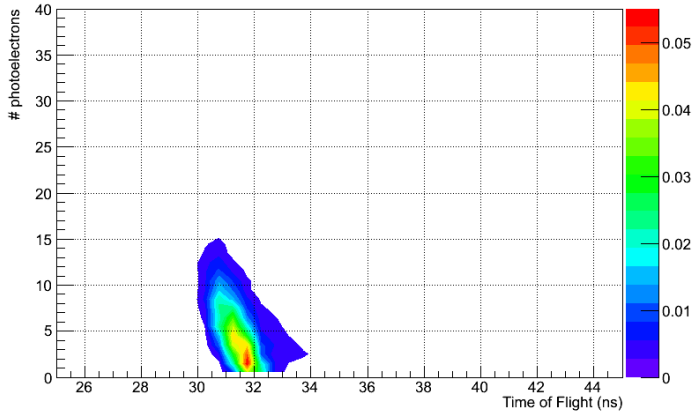

(a)

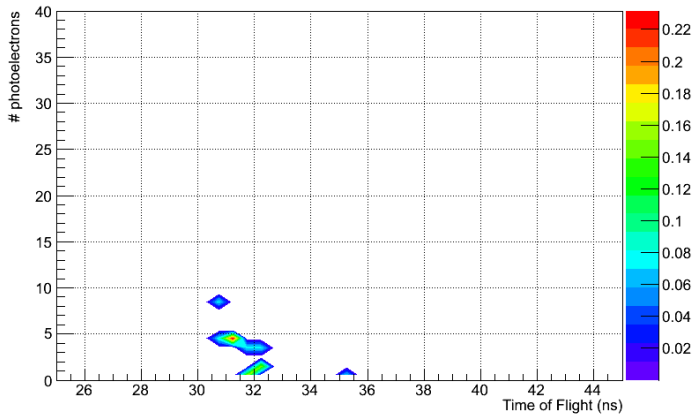

(b)

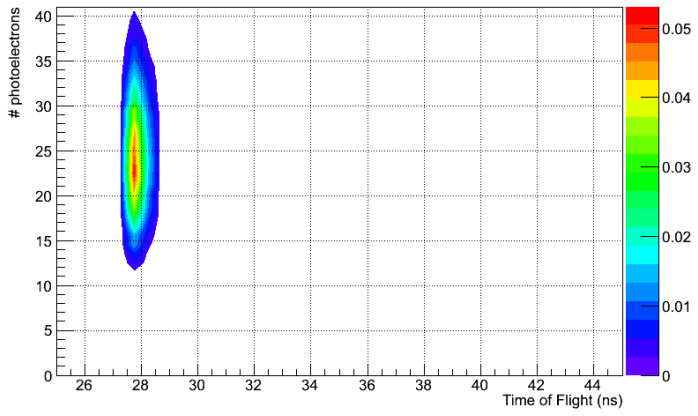

(c)

Figure 3.10: Example PDFs, produced using ReduceCppGlobalPID, of ComPIDVarI for muons (a), pions (b) and electrons (c), for a simulated 200 MeV/c muon beam.

3.4 PID at Step IV

During Step IV running, track reconstruction is performed independently upstream and downstream. Accordingly, it is necessary for the PID variables used at Step IV to be separated into upstream and downstream variables. This also means that the cooling channel itself can be treated as a black box.

3.4.1 Variables

The variables to be used during Step IV are outlined in Table 3.2, and examples of their probability density functions are shown in Figures 3.11 - 3.20, for a 200 MeV/c pion beam, which consists of a mixture of muons, pions and electrons, designed for a muon momentum of 200 MeV/c.

PIDVarA

Similar to ComPIDVarA, but for the time of flight between TOF0 and TOF1 (rather that TOF1 and TOF2), as shown in Figure 3.11 for a 200 MeV/c pion beam, provides excellent separation between electrons and muons/pions. The separation of the peaks is better than for ComPIDVarA as these particles have not passed through the diffuser or absorber, which would lead to some smearing of the time of flight peaks.

PIDVarB

Coupling the momentum measured in the upstream tracker with the time of flight, as shown in Figure 3.12 for a 200 MeV/c pion beam, distinctly separates out the muon, pion, and electron distributions, and so by placing cuts on both the time of flight and the momentum, one can acquire a muon sample with high purity. The further advantage of incorporationg the tracker momentum is that it removes the momentum dependence present in the time of flight distributions.

PIDVarC

Coupling the KL ADC charge product with the downstream tracker momentum, as shown in Figure 3.13 for a 200 MeV/c pion beam, provides some separation of muons and pions into bands, with a degree of overlap at higher values of the charge product, which can be cut on to obtain a greater muon purity. The electron distribution effectively creates a low background to the other two distributions, and could result in electrons being misidentified as muons/pions were this variable to be

used alone, however this can be mitigated by the use of multiple PID variables, as is the purpose of the Global PID.

PIDVarD

Same as ComPIDVarC, shown in Figure 3.14 for a 200 MeV/c pion beam.

PIDVarE

Same as ComPIDVarD, shown in Figure 3.15 for a 200 MeV/c pion beam.

PIDVarF

Coupling the EMR range with the downstream tracker momentum, as shown in Figure 3.16 for a 200 MeV/c pion beam, provides a good separation of muons and pions and electrons, and so should function well as a PID variable.

PIDVarG

Same as ComPIDVarF, shown in Figure 3.17 for a 200 MeV/c pion beam.

PIDVarH

Coupling the EMR plane density with the downstream tracker momentum, as shown in Figure 3.18 for a 200 MeV/c pion beam, separates out the electron distribution well. There is overlap between the muon and pion distributions between 180 and 200 MeV/c, and muons in this region would probably be misidentified as pions, however this is preferable to misidentifying pions as muons, which would reduce the muon sample purity, so this should still be an effective PID variable.

PIDVarI

The number of photoelectrons produced in CkovA as a function of the upstream tracker mometum, as shown in Figure 3.19 for a 200 MeV/c pion beam. Only the electron distributions is shown, as muons and pions at this energy do not produce any Cherenkov light.

PIDVarJ

The number of photoelectrons produced in CkovB as a function of the upstream tracker mometum, as shown in Figure 3.20 for a 200 MeV/c pion beam. Only

electron and muon distributions are shown, as pions at this energy do not produce any Cherenkov light. There is excellent separation between the two distributions.

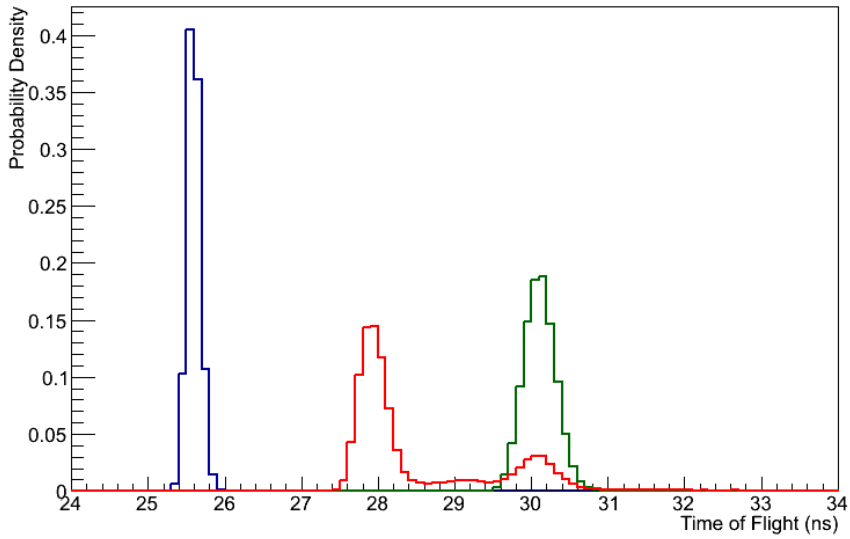

Figure 3.11: An example PDF, produced using ReduceCppGlobalPID, of PIDVarA. Shown are muons (red, larger peak at 28 ns, smaller peak at 30 ns), pions (green, peak at 30 ns) and electrons (blue, peak at 25.5 ns), for a simulated 200 MeV/c pion beam. The secondary muon peak contained within the pion peak is due to pions that decay in flight.

Class Name	Variable Name	Description
PIDVarA	diffTOF1TOF0	Time of flight between TOF1 and TOF0. Momentum dependent.
PIDVarB	diffTOF1TOF0vsUSTrackerMom	Time of flight between TOF1 and TOF0 and momentum measured in upstream tracker.
PIDVarC	KLChargeProdvsDSTrackerMom	KL ADC charge product and momentum measured in downstream tracker.
PIDVarD	KLADCChargeProduct	Same as ComPIDVarC.
PIDVarE	EMRrange	Same as ComPIDVarD
PIDVarF	EMRrangevsDSTrackerMom	Range of particle in EMR and momentum measured in downstream tracker.
PIDVarG	EMRdensity	Same as ComPIDVarF.
PIDVarH	EMRdensityvsDSTrackerMom	EMR plane density and momentum measured in downstream tracker.
PIDVarI	CkovAvsUSTrackerMom	Number of photoelectrons (pes) measured in CkovA and momentum measured in upstream tracker.
PIDVarJ	CkovBvsUSTrackerMom	Number of photoelectrons (pes) measured in CkovB and momentum measured in upstream tracker.

Table 3.2: Step IV PID variables.

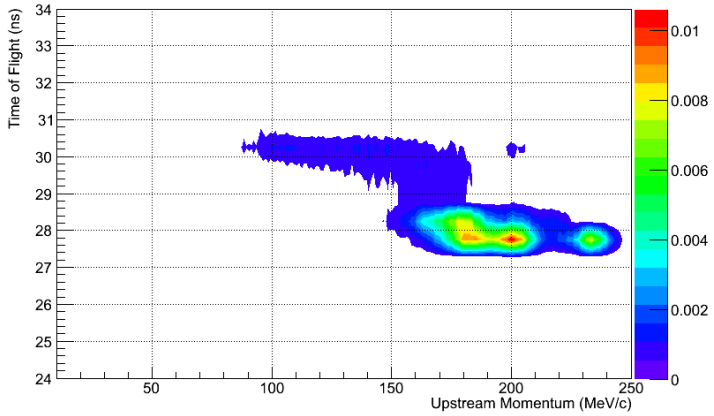

(a)

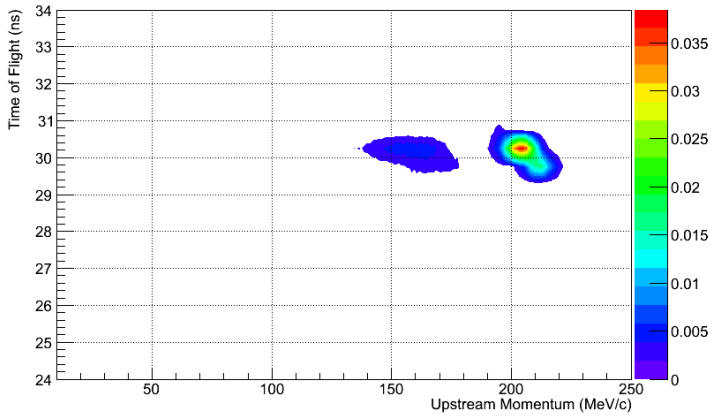

(b)

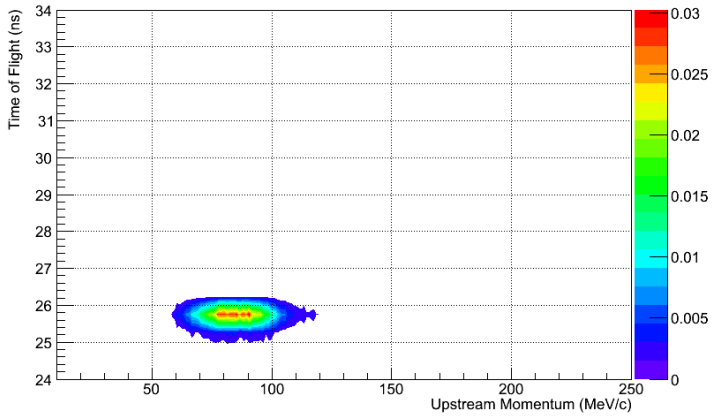

(c)

Figure 3.12: Example PDFs, produced using ReduceCppGlobalPID, of PIDVarB for muons (a), pions (b) and electrons (c), for a simulated 200 MeV/c pion beam.

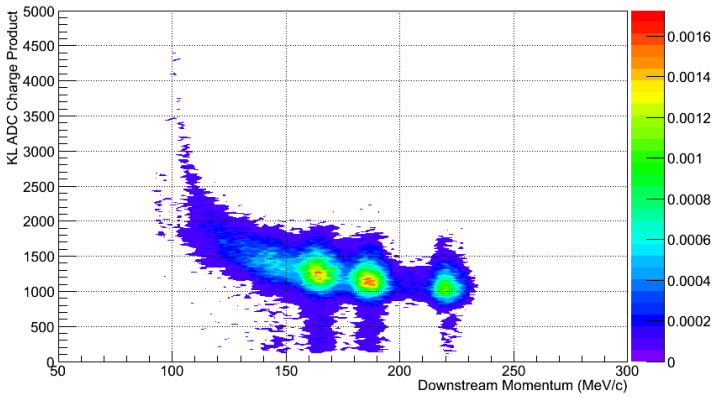

(a)

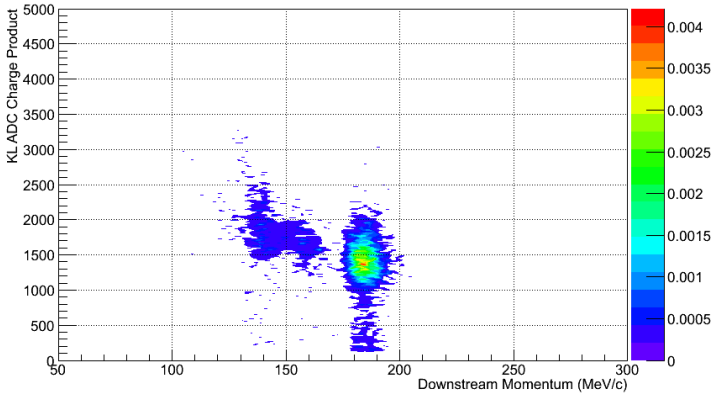

(b)

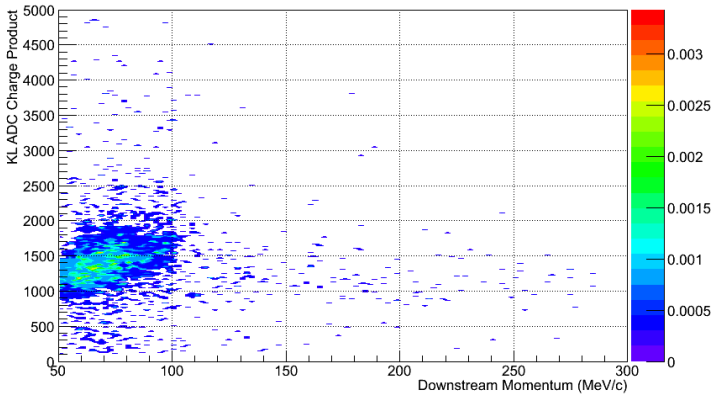

(c)

Figure 3.13: Example PDFs, produced using ReduceCppGlobalPID, of PIDVarC for muons (a), pions (b) and electrons (c), for a simulated 200 MeV/c pion beam.

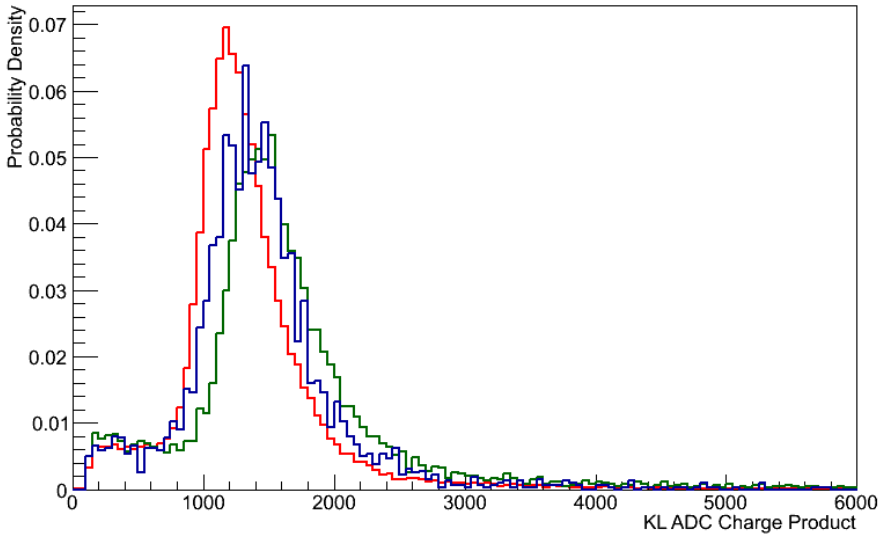

Figure 3.14: An example PDF, produced using ReduceCppGlobalPID, of PIDVarD. Shown are muons (red), pions (green) and electrons (blue), for a simulated 200 MeV/c pion beam.

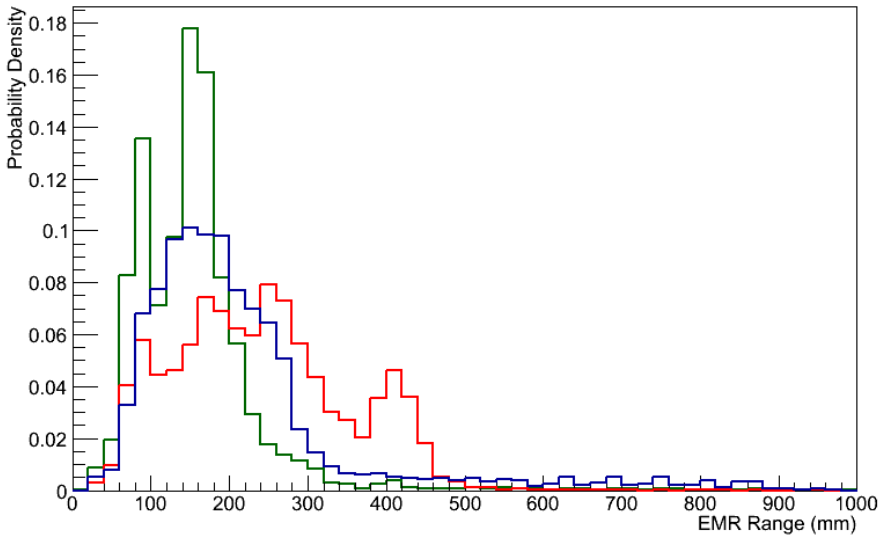

Figure 3.15: An example PDF, produced using ReduceCppGlobalPID, of PIDVarE. Shown are muons (red, peaks at 200 mm and 400 mm), pions (green, peaks at 100 mm and 200 mm) and electrons (blue, peak at 150 mm), for a simulated 200 MeV/c pion beam.

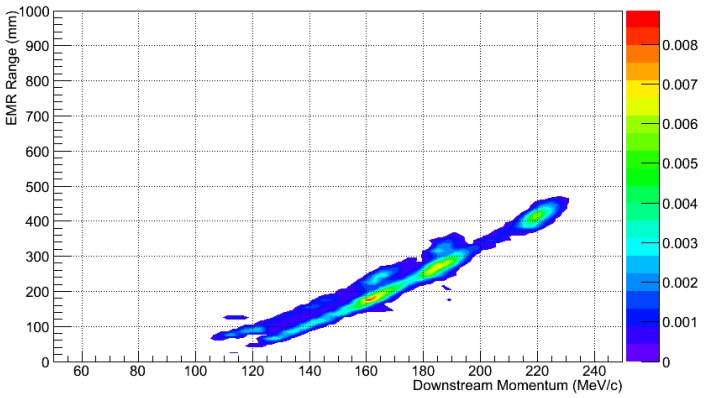

(a)

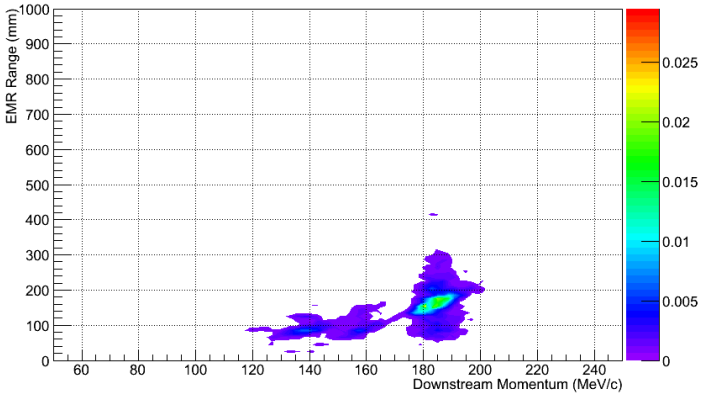

(b)

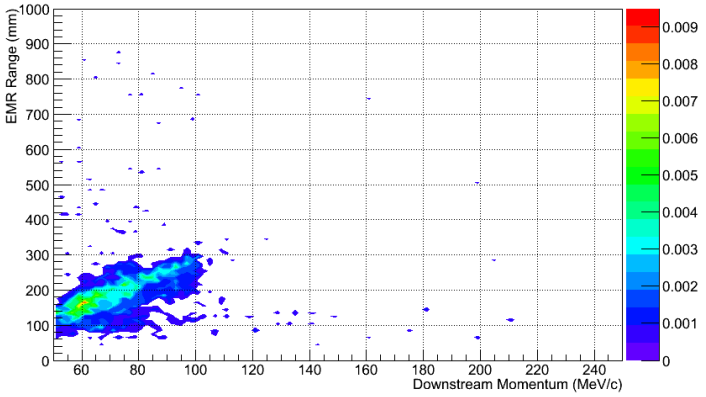

(c)

Figure 3.16: Example PDFs, produced using ReduceCppGlobalPID, of PIDVarF for muons (a), pions (b) and electrons (c), for a simulated 200 MeV/c pion beam.

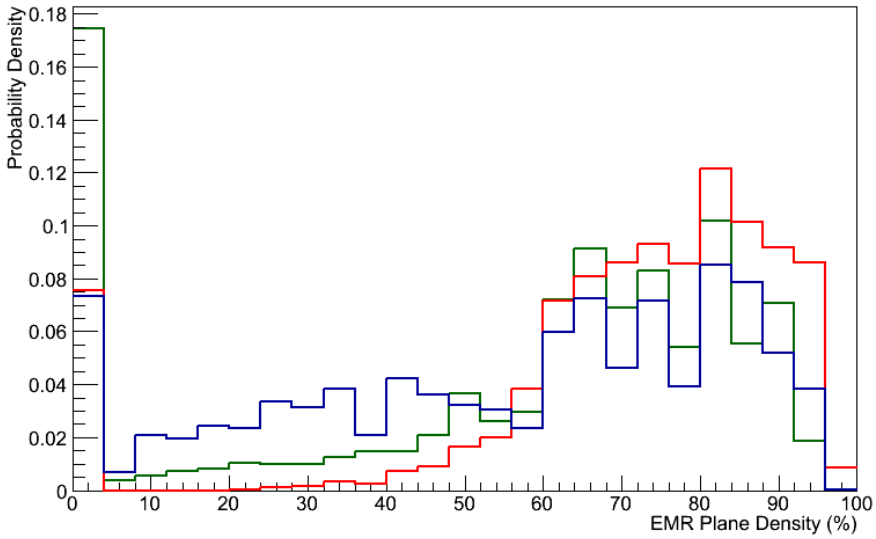

Figure 3.17: An example PDF, produced using ReduceCppGlobalPID, of PIDVarG. Shown are muons (red), pions (green) and electrons (blue), for a simulated 200 MeV/c pion beam.

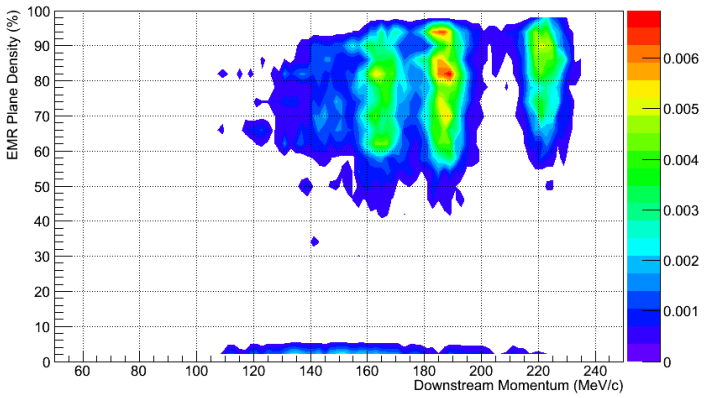

(a)

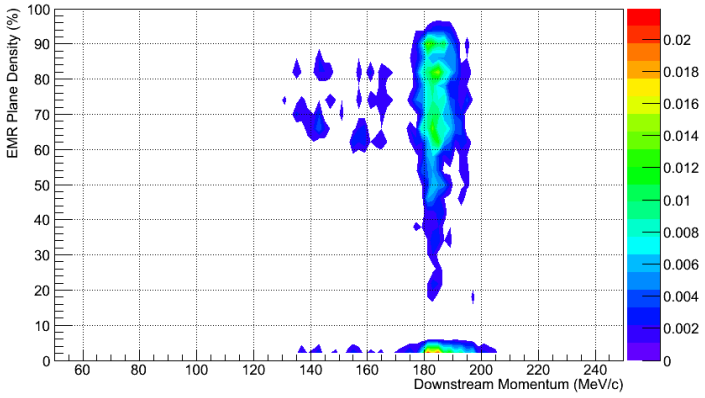

(b)

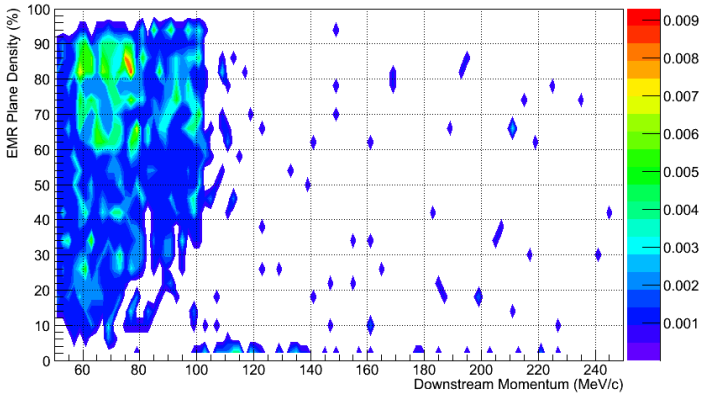

(c)

Figure 3.18: Example PDFs, produced using ReduceCppGlobalPID, of PIDVarH for muons (a), pions (b) and electrons (c), for a simulated 200 MeV/c pion beam.

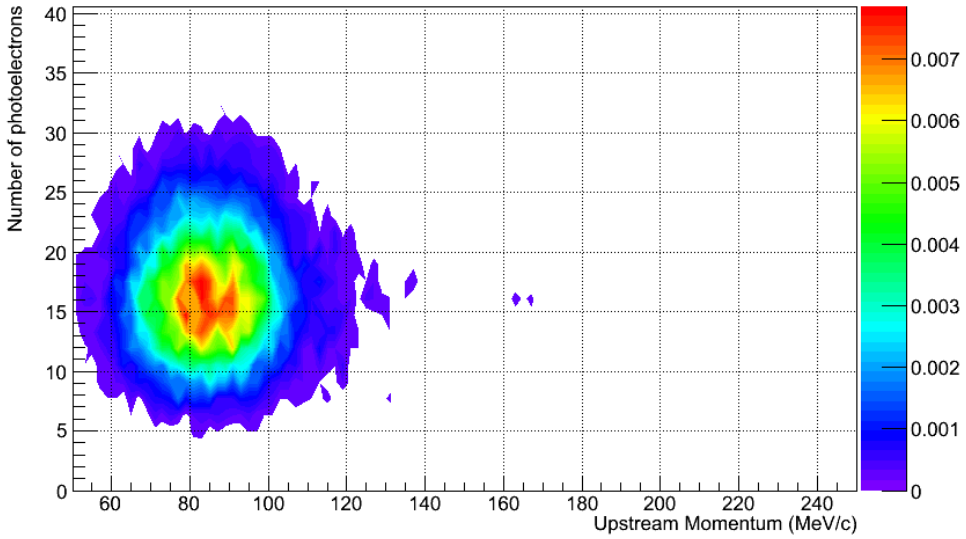

Figure 3.19: Example PDFs, produced using ReduceCppGlobalPID, of PIDVarI for electrons, for a simulated 200 MeV/c pion beam. For the momentum of this simulated beam muons and pions did not produce a signal in the detector.

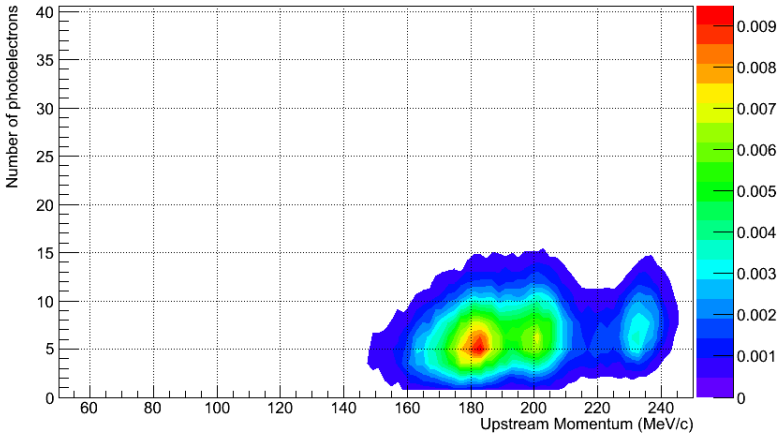

(a)

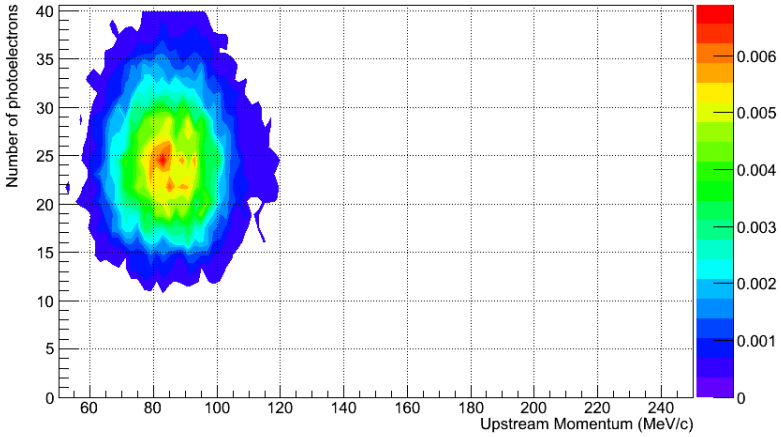

(b)

Figure 3.20: Example PDFs, produced using ReduceCppGlobalPID, of PIDVarJ for muons (a) and electrons (b), for a simulated 200 MeV/c pion beam. For the momentum of this simulated beam pions did not produce a signal in the detector.

3.5 Determining the performance of the Global PID

In some particle physics experiments, particle identification routines can be validated using test beams whose composition are well understood. As this is not possible for MICE, the validation of the Global PID will be performed by determining

1. The consistency of the variables with Monte Carlo (MC), as represented by efficiency/purity plots.

2. The consistency between the upstream variables, both on MC and real data, determined by the degree of agreement between the variables on a pid hypothesis.

3. The consistency between the downstream variables, both on MC and real data, determined by the degree of agreement between the varables on a pid hypothesis.

4. The consistency between upstream and downstream pid hypotheses.

3.5.1 Efficiency and Purity

The efficiency, ϵ_{PID} of the PID is given, from MC, by

$$\epsilon_{PID} = \frac{N_C}{N_S} \tag{3.6}$$

where N_C is the number of correctly identified tracks, and N_S is the number of "suitable" tracks, where $N_C \subseteq N_S$. Eqn. 3.6 can also be written as

$$\epsilon_{PID} = \frac{N_C}{N_{ID} + N_F} = \frac{N_C}{N_C + N_W + N_F} \tag{3.7}$$

where N_{ID} is the total number of identified tracks, N_W is the number of incorrectly identified tracks, and N_F is the number of tracks for which the PID failed to identify the track, despite it being suitable.
A suitable track is one that fulfills the criteria required to be able to perform PID on it (an unsuitable track may be missing detector information, or it may have been mis-reconstructed earlier in the processing chain). A PID failure may occur due to a user placing too strict a set of cuts on the allowed values of PID variables, or as mentioned previously a PID failure will occur if a track does not pass the

confidence level cut required to assign a PID. The binomial error on the efficiency, σ_ϵ, is calculated by

$$\sigma_\epsilon^2 = \frac{N_C(N_S - N_C)}{N_S^3} \tag{3.8}$$

The purity, ρ of the PID against MC is given by

$$\rho = \frac{N_C}{N_{ID}} = \frac{N_C}{N_C + N_W} \tag{3.9}$$

The error on the purity, σ_ρ, is calculated by

$$\sigma_\rho^2 = \left(\frac{N_W}{(N_C - N_W)^2}\right)^2 N_C + \left(\frac{-N_C}{(N_C - N_W)^2}\right)^2 N_W \tag{3.10}$$

The derivations of these error equations are given in [44].

3.5.2 Consistency between variables

To determine the consistency between two PID variables, the probabilities they return for a given track to be a muon are compared. The probabilities need not be identical; a positive correlation would indicate good agreement between the variables. A more quantitive measure of their consistency however is to measure what proportion of particles are identified as muons/not muons by both variables.

If one considers the possible outcomes of the PID to be μ and some *other* particle(s), then the probabilities returned by the PID would satisfy

$$P(\mu) + P(other) = 100\% \tag{3.11}$$

In the consistency studies, only tracks that have been identified by both variables are considered, so these tracks must have been identified with a probability that is greater than the probabilities of the other particles by at least the value of the confidence level cut (CL), so if for this example the particle was identified as a muon, then

$$P(\mu) > P(other) + CL \tag{3.12}$$

must be true. From Eqn. 3.11 it follows that for $CL = 10\%$, as was used for the performance studies, that the minimum value that $P(\mu)$ can take, while still definitely being identified as a μ, is greater than 45%, as for it to be identified as some *other* particle, $P(other)$ would have to be greater than 55% in order to satisfy the confidence level cut, which would violate Eqn. 3.11, and if $P(other) <$

55% then no identification would have been made as it would fail the confidence level cut. Therefore if two variables calculate a P(μ)>45% or P(μ)<45%, it would indicate that the variables are consistent. It should be noted though that it is possible for a particle with $40\% < P(\mu) < 45\%$ to also be identified as a muon, but cannot be guaranteed.

3.5.3 Performance of Commissioning PID

Efficiency/purity studies

For these studies, a 200 MeV/c muon beam was simulated, and PID performed by each variable class individually. Different efficiencies/purities are achieved by placing cuts on the allowed values of the variable and performing PID for these cuts in order to determine the optimal cut values that will return the best purity. For example, for ComPIDVarA, by cutting on the time of flight such that 27 ns $< t <$ 28.5 ns, one would expect to obtain a sample of muons with high purity, although the efficiency for all particle types would be reduced.

The results are shown in Figures 3.21 - 3.29, and the optimal settings are shown in Table 3.3. Each point on the efficiency/purity plots corresponds to a different cut setting. For each setting, both the overall particle identification efficiency (black squares) and the muon identification efficiency (red circles) have been calculated, as the muon efficiency is of particular interest, and in general more important than the overall efficiency.

With the exception of ComPIDVarD, all variables were able to achieve greater than 90% efficiency. The poor efficiency and purity returned by ComPIDVarD was to be expected, as it can be clearly seen from its PDF in Figure 3.5 that there is no real separation between particle species distributions for the range of particles in the EMR, with the muon peak being completely overlapped by the pion and electron peaks. The high optimal purity (99.2%) returned by ComPIDVarC would initially appear surprisingly high considering the poor peak separation for the KL ADC charge product as shown in Figure 3.4, with large portions of the pion and electron peaks being overlapped by the larger muon peak, however given the small pion/electron contamination found in a muon beam, this high purity is probably a result of the purity of the input beam, rather than due the discriminatory power of the variable itself. ComPIDVars A, B, E and G all performed very well, returning purities greater than 99%, indicating they would be very good PID variables. ComPIDVarF achieved a purity of 93.9%, however this required very tight cuts on the EMR plane density, resulting in very poor efficiency. This doesn't preclude the use

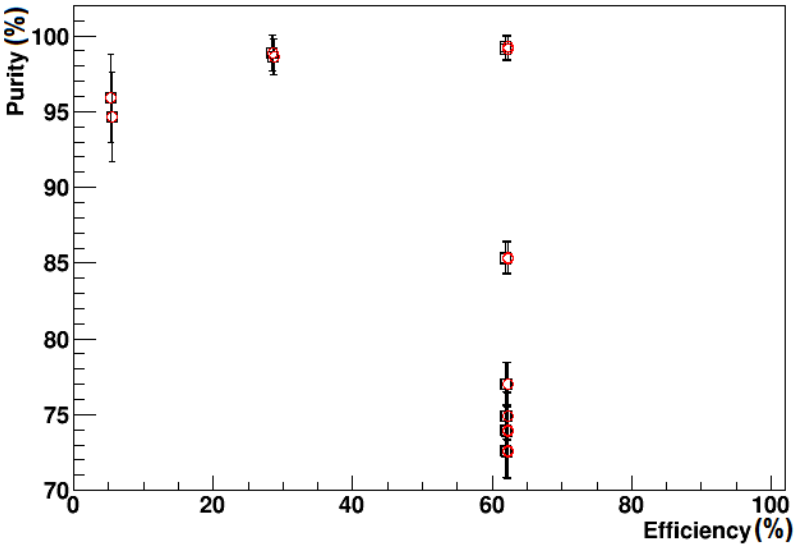

Figure 3.21: Efficiency/purity plot for ComPIDVarA. The black squares show the overall particle identification efficiency, the red circles show the muon identification efficiency. With this variable an identification purity of 99.3% can be achieved, with muon and overall efficiencies of 62.2% and 61.9% respectively.

of ComPIDVarF as a PID variable, as long as it is used in conjunction with other variables.

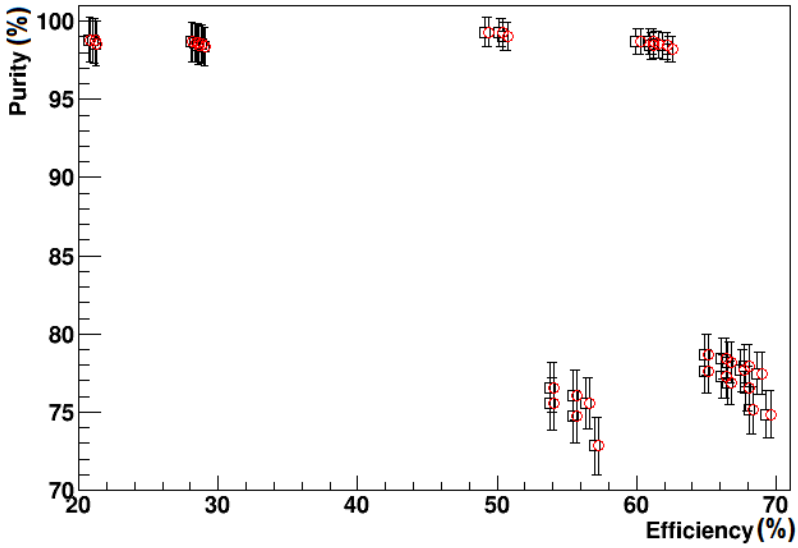

Figure 3.22: Efficiency/purity plot for ComPIDVarB. The optimal purity for this variable was found to be 99.3%, which corresponds to a muon efficiency of 50.4% and an overall identification efficiency of 50.1%

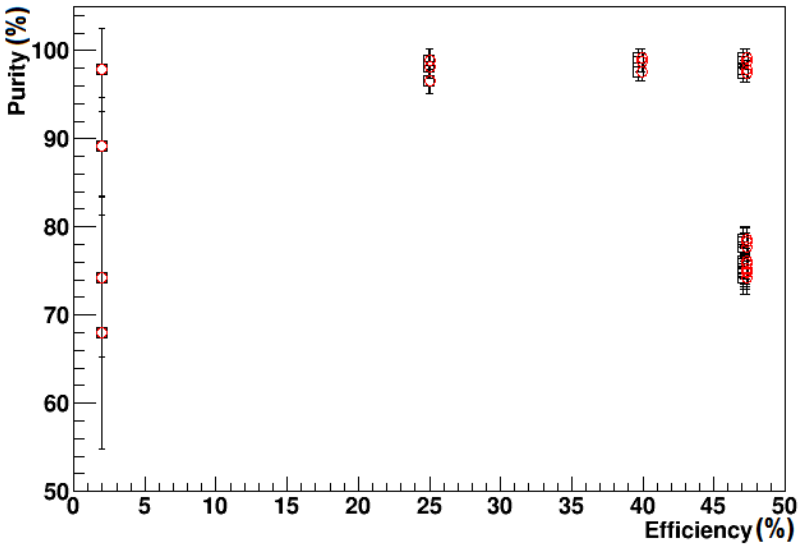

Figure 3.23: Efficiency/purity plot for ComPIDVarC. The optimal purity for this variable was found to be 99.2%, which corresponds to a muon finding efficiency of 47.3% and an overall identification efficiency of 47.0%

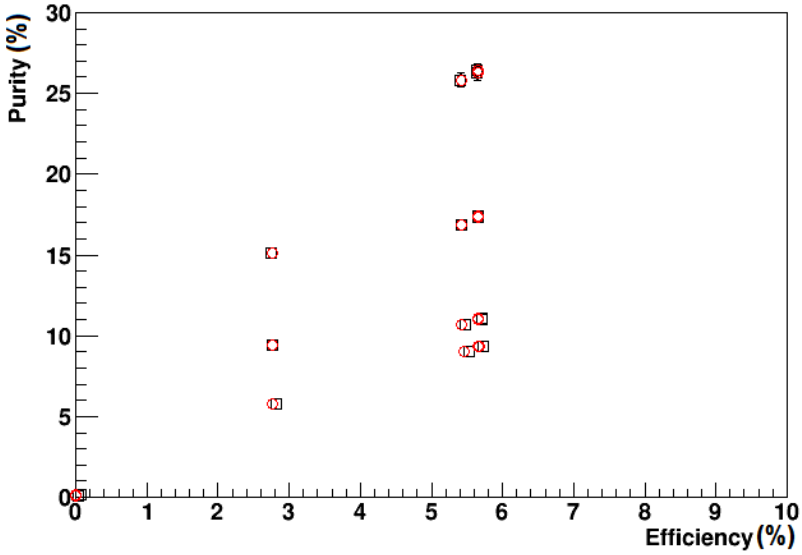

Figure 3.24: Efficiency/purity plot for ComPIDVarD. As can be seen, the EMR range alone cannot return either a reasonable purity or efficiency, making this variable clearly unsuitable for use in PID.

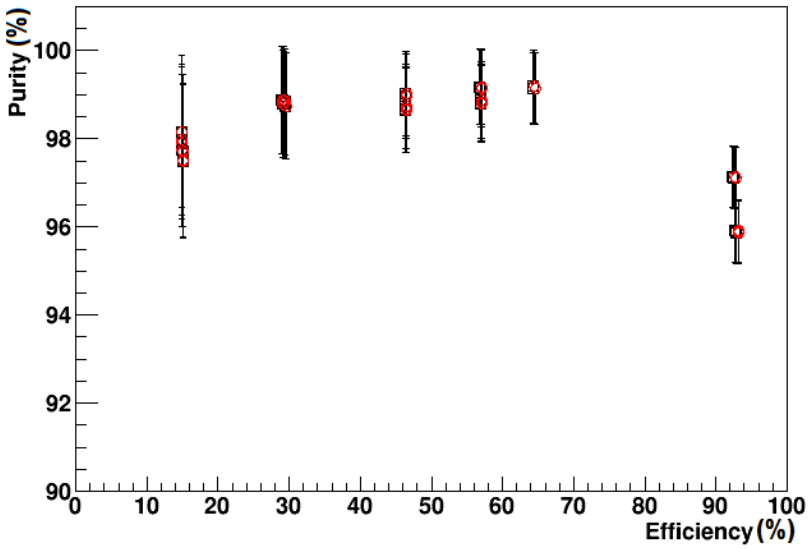

Figure 3.25: Efficiency/purity plot for ComPIDVarE. The optimal purity for this variable was found to be 99.2%, which corresponds to a muon finding efficiency of 64.5% and an overall identification efficiency of 64.2%

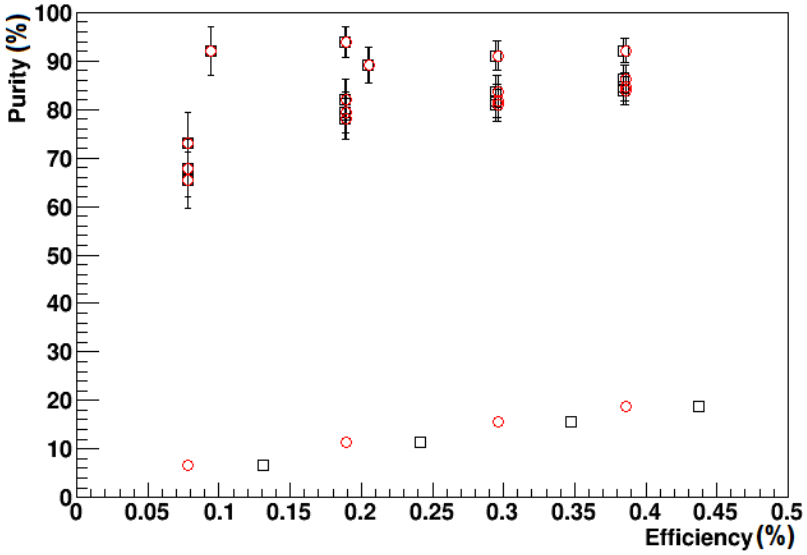

Figure 3.26: Efficiency/purity plot for ComPIDVarF. The optimal purity for this variable was found to be 93.9%, which corresponds to a muon finding efficiency of 0.189% and an overall identification efficiency of 0.188%, so while it is not an efficient variable, its inclusion in PID may be useful for a small number of tracks.

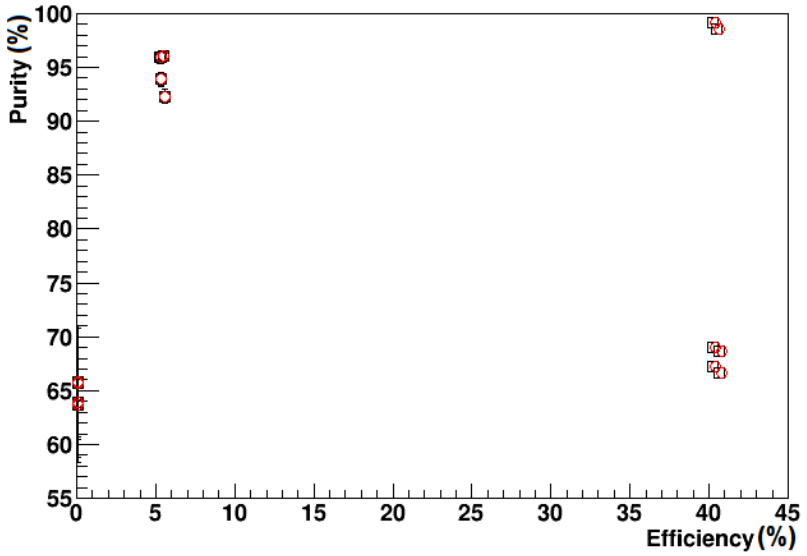

Figure 3.27: Efficiency/purity plot for ComPIDVarG. The optimal purity for this variable was found to be 99.2%, which corresponds to a muon finding efficiency of 40.4% and an overall identification efficiency of 40.2%

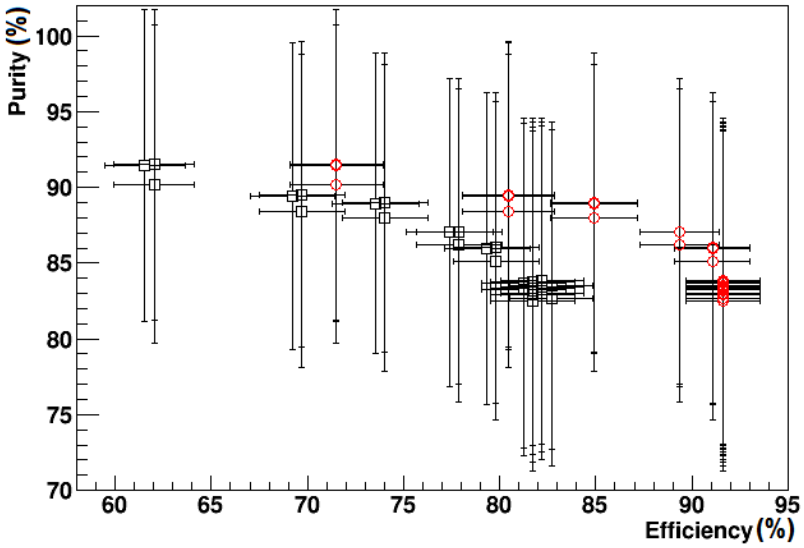

Figure 3.28: Efficiency/purity plot for ComPIDVarH. The optimal purity for this variable was found to be 91.5%, which corresponds to a muon finding efficiency of 71.5% and an overall identification efficiency of 62.0%. It should be noted that at this simulated beam momentum, there were only 208 tracks that produced signals in Cherenkov A and the time of flight detectors, hence the large error bars.

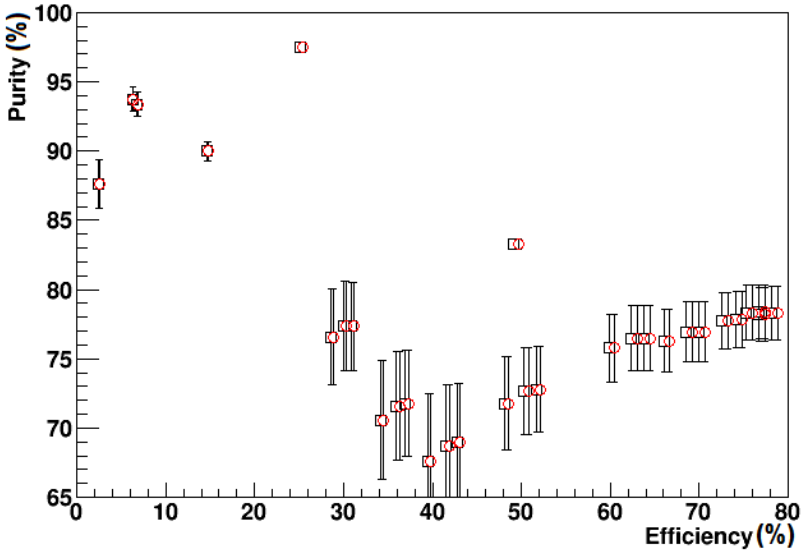

Figure 3.29: Efficiency/purity plot for ComPIDVarI. The optimal purity for this variable was found to be 97.5%, which corresponds to a muon finding efficiency of 25.5% and an overall identification efficiency of 25.2%.

	Optimal Setting			
	minX	maxX	minY	maxY
ComPIDVarA	26 ns	33 ns		
ComPIDVarB	26 ns	33 ns	600	2000
ComPIDVarC	600	1400		
ComPIDVarD	180 mm	600 mm		
ComPIDVarE	26 ns	35 ns	10 mm	1000 mm
ComPIDVarF	80%	90%		
ComPIDVarG	20 ns	33 ns	10%	100%
ComPIDVarH	26 ns	35 ns	0 pes	3 pes
ComPIDVarI	31 ns	40 ns	5 pes	140 pes

Table 3.3: Optimal settings for min/max values of commissioning PID variables based on efficiency/purity studies for a 3mm 200 MeV/c muon beam. One dimensional variables have only maximum and minimum X values, while two dimensional variables have both X and Y values.

Consistency between Commissioning PID variables

MC Consistency

As was done for the efficiency/purity studies, PID was performed by each variable class individually for the simulated 200 MeV/c muon beam. PID was performed once per variable, using the settings listed in Table 3.3. Following the procedure laid out in Section 3.5.2, plots comparing the variables were produced, showing the probability of a particle being a muon, P(μ), as determined by the variables being compared. The plot for ComPIDVarA and ComPIDVarB is included here as an example in Figure 3.30, and all of the other comparison plots can be found in Appendix A, in Figures A.1 - A.35. Table 3.4 lists the consistencies determined between all of the variables.

Figure 3.30 shows excellent consistency between ComPIDVarA and ComPIDVarB, as they agree on the identification of 99.5% of particles. This is shown by the fact that most of the points on the plot occupy the regions where either both variables return a P(μ) greater than 45%, or both variables return a P(μ) less than 45%, with only 0.5% of points falling outside of these regions. The red dotted lines indicate the edges of the regions, with the bottom left and top right quadrants being areas of agreement and the top left and bottom right being areas of disagreement between the variables.

With the exception of ComPIDVarD, which was established as an unreliable variable in Figure 3.24 due to it's low purity, there is excellent agreement between almost all variables, with many variables more than 99% consistent. ComPIDVarH

A	B	C	D	E	F	G	H	I
A	99.5%	99.1%	26.9%	99.6%	100%	99.2%	100%	99.3%
	B	99.2%	27.1%	99.1%	100%	98.4%	100%	99.2%
		C	30.4%	98.9%	100%	98.7%	100%	99.4%
			D	27.2%	81.2%	45.7%	57.5%	25.2%
				E	100%	98.9%	95.1%	98.3%
					F	93.3%	100%	100%
						G	90.6%	95.2%
							H	83.3%

Table 3.4: Consistency between ComPIDVars on MC.

and ComPIDVarF in some cases show 100% consistency with other variables, although this could be due to there being far fewer particles that both they and the variables they are being compared with managed to identify. Compared to the other consistency values, ComPIDVarH and ComPIDVarI have quite a low consistency at 83.3%, however this could again be due to the low number of tracks for which they both found a pid, as well as the fact that these variables had two of the lower purities.

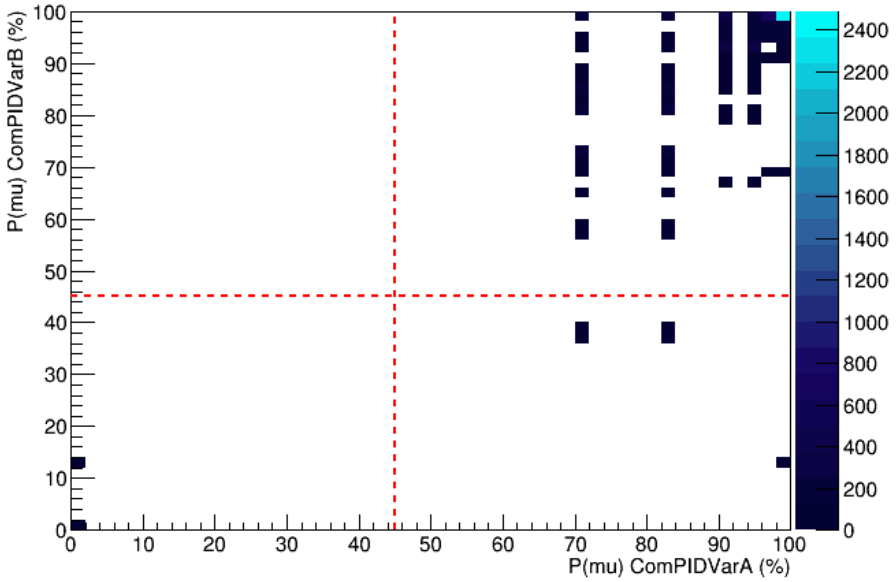

Figure 3.30: Comparison of P(μ) returned by ComPIDVarA and ComPIDVarB on MC dataset. For all particles identified by both variables, there was a muon identification consistency of 99.5%.

Data Consistency

For these studies, PID was performed by each variable class individually for the combined dataset from MICE runs 7834-7838, 7841-7843 (3 mm 200 MeV/c LiH data). Again, the plot for ComPIDVarA and ComPIDVarB is included here as an example in Figure 3.31, and all of the other comparison plots can be found in Appendix A, in Figures A.36 - A.70. Table 3.5 lists the consistencies determined between all of the variables.

Across most variables, there is a slight drop in consistency, which could be accounted for by variations between the data and MC. For ComPIDVarE there is a larger drop of 20%, and the consistency between all variables that include EMR input (ComPIDVars D, E, F and G) is unexpectedly rather poor, and warrants further investigation of the EMR reconstruction.

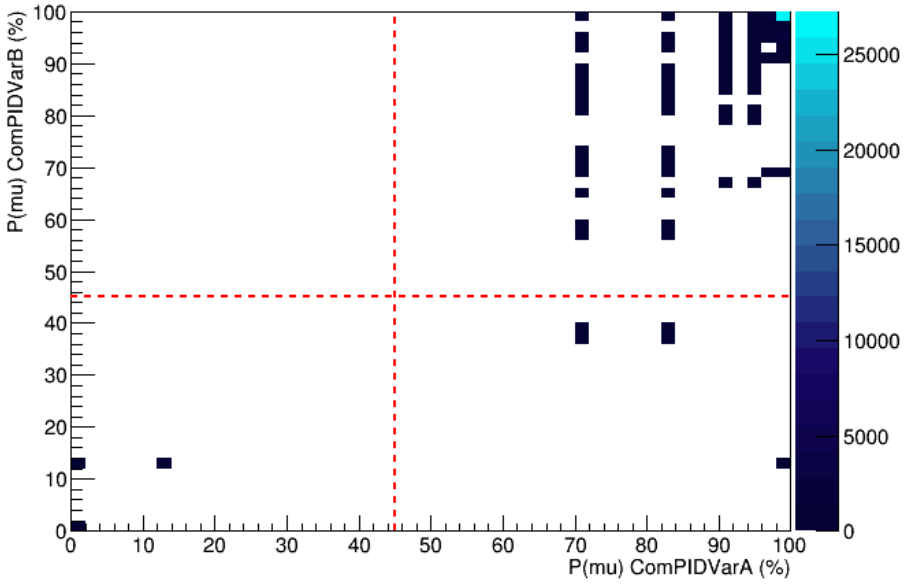

Figure 3.31: Comparison of P(μ) returned by ComPIDVarA and ComPIDVarB for LiH dataset. For all particles identified by both variables, there was a muon identification consistency of 99.0%.

A	B	C	D	E	F	G	H	I
A	99.0%	98.6%	34.0%	78.2%	92.6%	98.2%	86.1%	81.9%
	B	97.8%	31.5%	78.8%	88.9%	97.0%	85.5%	81.3%
		C	34.2%	71.9%	100%	95.6%	89.5%	82.0%
			D	32.8%	93.6%	34.2%	36.5%	37.0%
				E	30.8%	71.5%	64.4%	64.0%
					F	65.8%	98.1%	83.7%
						G	81.0%	82.6%
							H	74.1%

Table 3.5: Consistency between ComPIDVars on data.

3.5.4 Performance of Step IV PID

Efficiency and purity of Step IV PID variables

For these studies, PID was performed by each variable class individually for a simulated 200 MeV/c pion beam. The approach here is the same as that used for the commissioning variables.

The results are shown in Figures 3.32 - 3.40, and the optimal settings are shown in Table 3.6. PIDVarI is not shown in this study as the MC beam only produced 20 tracks that contained both CkovA and upstream tracker hits. Each point on the efficiency/purity plots corresponds to each cut setting. For each setting, both the overall particle identification efficiency (black squares) and the muon identification efficiency (red circles) have been calculated, as the muon efficiency is of particular interest, and in general more important than the overall efficiency.

The purities returned for the individual Step IV variables are lower than those returned for the commissioning variables, although a choice of settings was found that allowed PIDVarE (EMR range) to perform better than its commissioning counterpart by performing PID over the range occupied in the PDF (Figure 3.15) by the second muon peak at 400mm. The KL variables (PIDVarC and PIDVarD) performed far less well than their commissioning counterparts, due to the higher pion content of this beam than for the muon beam used in the commissioning studies.

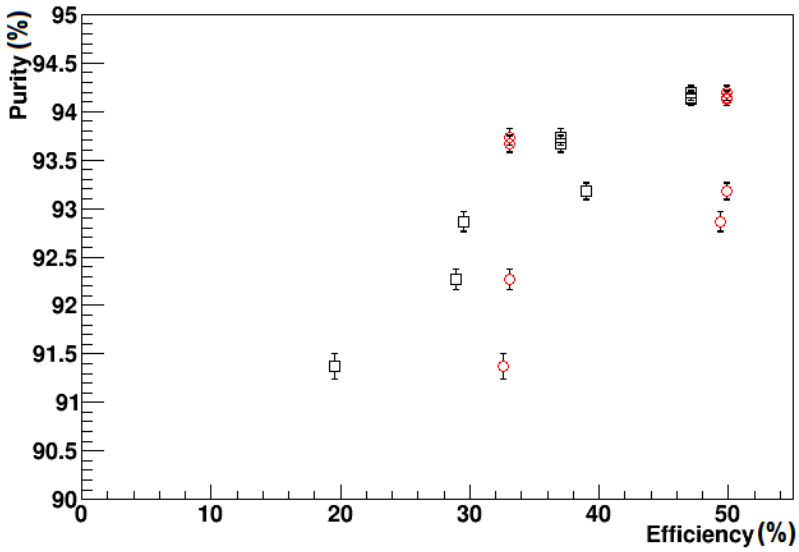

Figure 3.32: Efficiency/purity plot for PIDVarA. With this variable an identification purity of 94.2% has been achieved, with muon and overall efficiencies of 49.9% and 47.1% respectively.

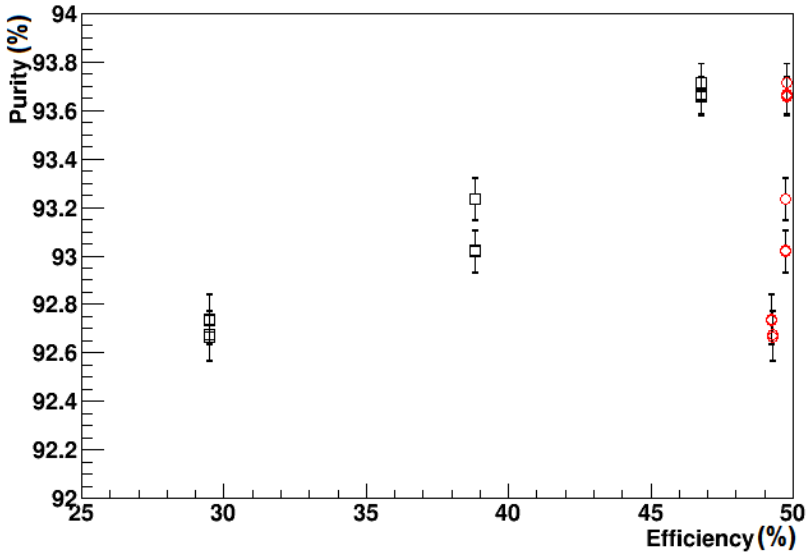

Figure 3.33: Efficiency/purity plot for PIDVarB. The optimal purity for this variable was found to be 94.1%, which corresponds to a muon efficiency of 49.7% and an overall identification efficiency of 46.7%.

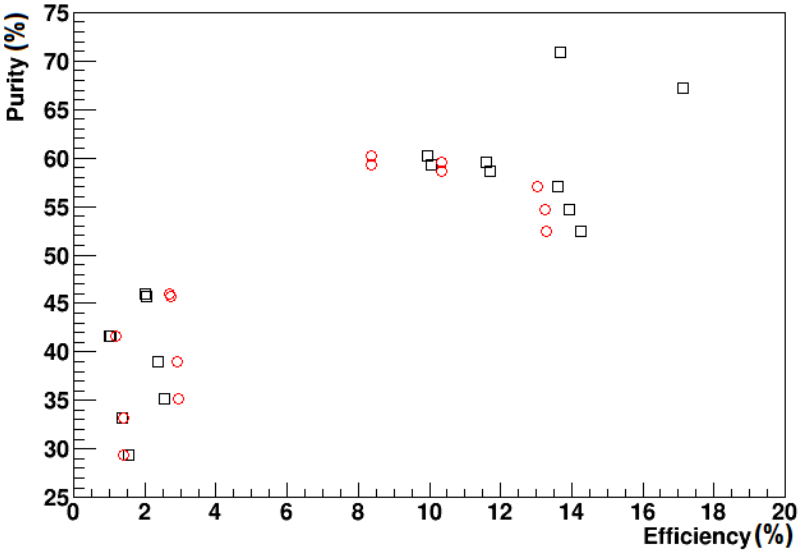

Figure 3.34: Efficiency/purity plot for PIDVarC. The optimal purity for this variable was found to be 70.9%, which corresponds to a muon finding efficiency of 21.7% and an overall identification efficiency of 13.7%.

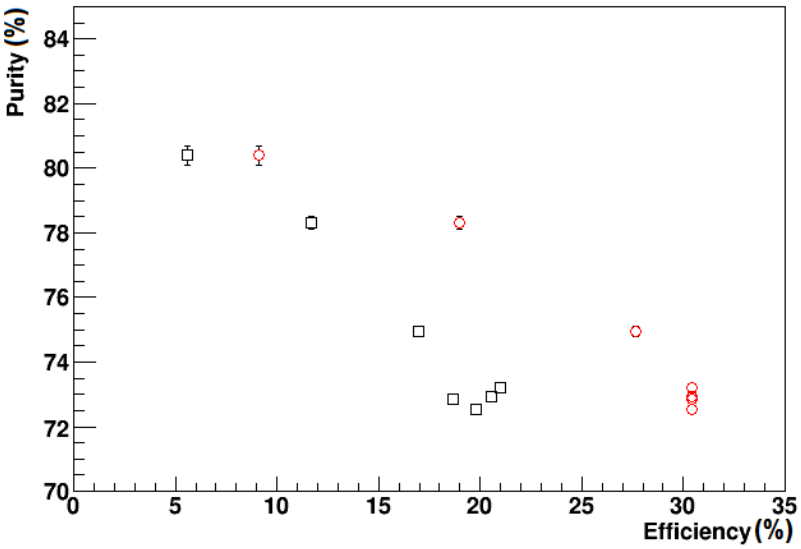

Figure 3.35: Efficiency/purity plot for PIDVarD. The optimal purity for this variable was found to be 80.4%, which corresponds to a muon finding efficiency of 9.09% and an overall identification efficiency of 5.58%.

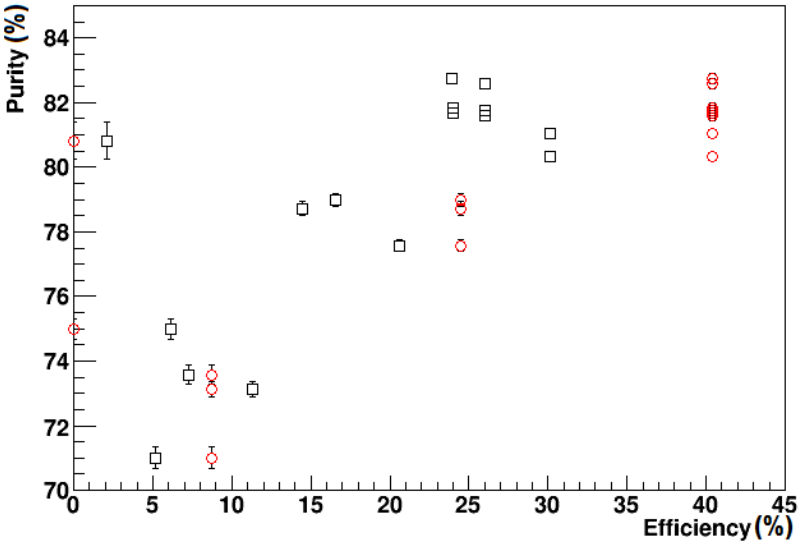

Figure 3.36: Efficiency/purity plot for PIDVarE. The optimal purity for this variable was found to be 82.7%, which corresponds to a muon finding efficiency of 40.4% and an overall identification efficiency of 24.0%.

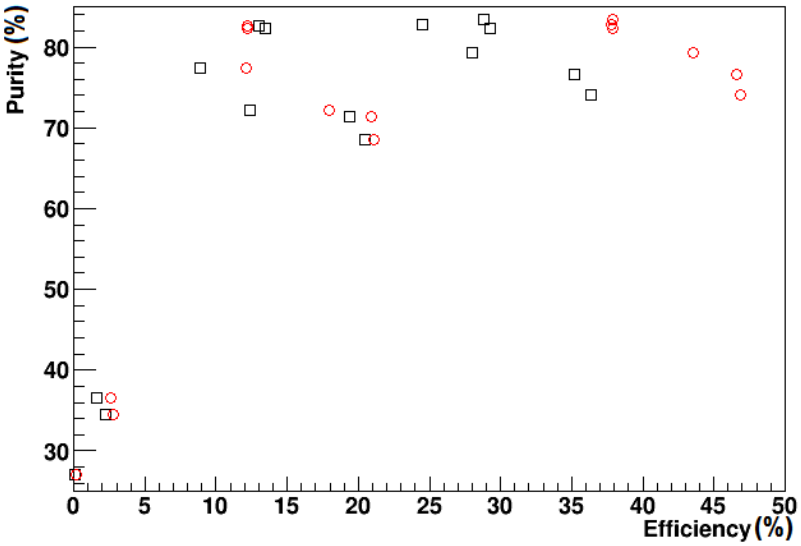

Figure 3.37: Efficiency/purity plot for PIDVarF. The optimal purity for this variable was found to be 83.5%, which corresponds to a muon finding efficiency of 37.9% and an overall identification efficiency of 28.8%.

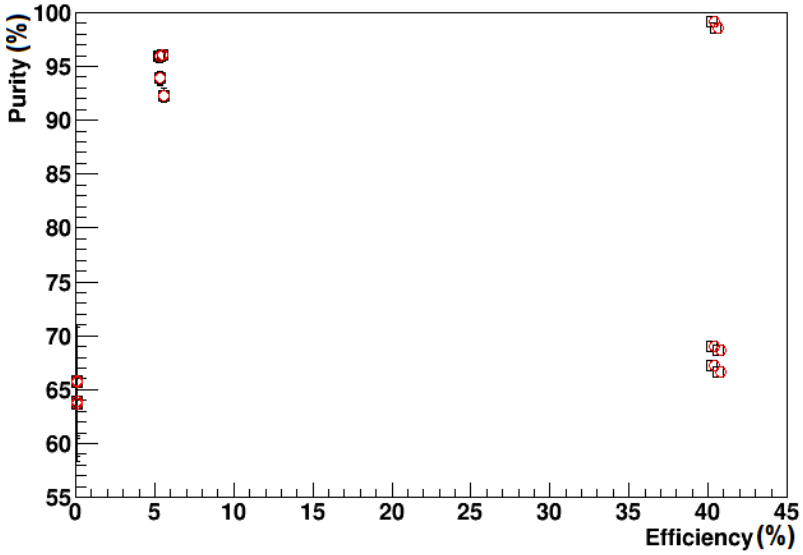

Figure 3.38: Efficiency/purity plot for PIDVarG. The optimal purity for this variable was found to be 43.0%, which corresponds to a muon finding efficiency of 0.261% and an overall identification efficiency of 0.155%.

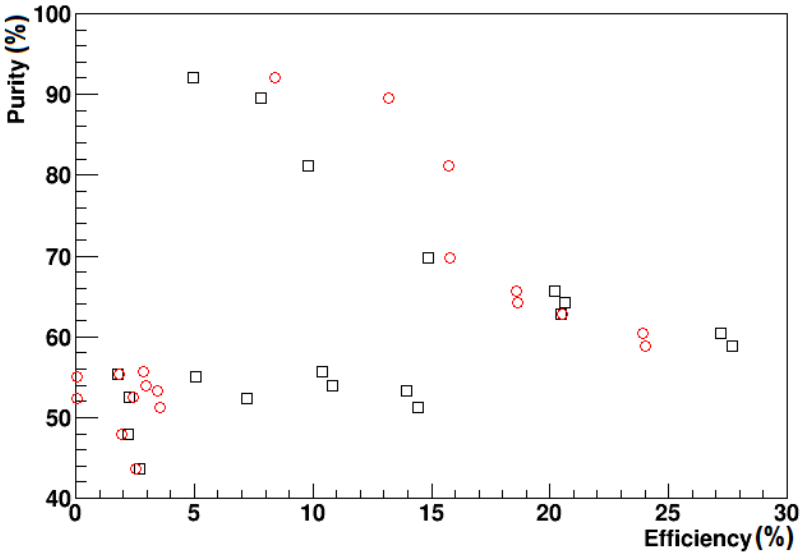

Figure 3.39: Efficiency/purity plot for PIDVarH. The optimal purity for this variable was found to be 92.0%, which corresponds to a muon finding efficiency of 8.39% and an overall identification efficiency of 4.97%.

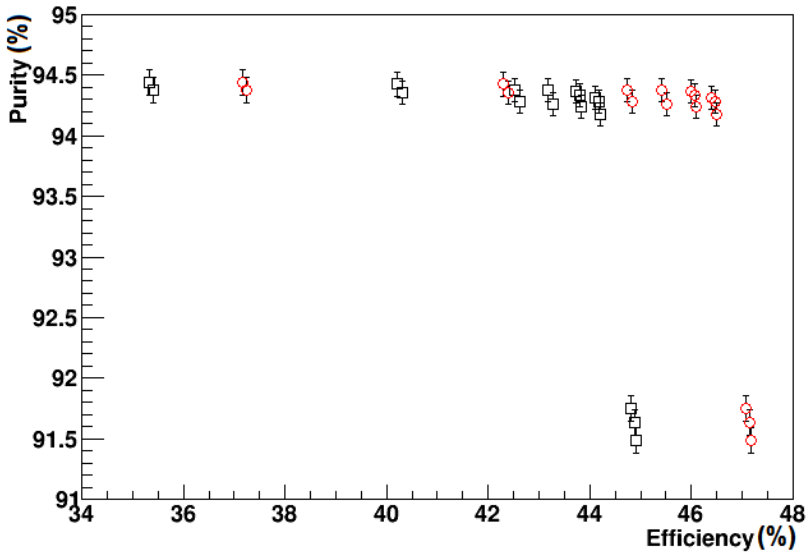

Figure 3.40: Efficiency/purity plot for PIDVarJ. The optimal purity for this variable was found to be 94.4%, which corresponds to a muon finding efficiency of 37.2% and an overall identification efficiency of 35.3%.

	Optimal Setting			
	minX	maxX	minY	maxY
PIDVarA	27 ns	31 ns		
PIDVarB	120 MeV/c	250 MeV/c	25 ns	31 ns
PIDVarC	200 MeV/c	350 MeV/c	0	8000
PIDVarD	0	1000		
PIDVarE	180 mm	500 mm		
PIDVarF	185 MeV/c	350 MeV/c	100 mm	1000 mm
PIDVarG	20%	100%		
PIDVarH	210 MeV/c	350 MeV/c	10%	100%
PIDVarI				
PIDVarJ	150 MeV/c	350 MeV/c	0 pes	8 pes

Table 3.6: Optimal settings for min/max values of Step IV PID variables based on efficiency/purity studies for a 6 mm 200 MeV/c pion beam. One dimensional variables have only maximum and minimum X values, while two dimensional variables have both X and Y values. No settings are given for PIDVarI as at the momentum studied the sample only contained 20 tracks that produced hits in CkovA and the trackers.

Consistency between Upstream Step IV PID variables

Following the same approach as used for the commissioning variables, except considering upstream and downstream variables separately, PID was performed by each upstream variable class individually for the simulated 200 MeV/c pion beam. PID was performed once per variable, using the settings listed in Table 3.6. Figures 3.41 - 3.43 show the probability of a particle being a muon, P(μ), as determined by the variables being compared. Table 3.7 lists the consistencies determined between the variables. As for the efficiency/purity studies, PIDVarI is omitted due to the low number of suitable tracks.

Comparison of the three upstream variables shows excellent consistency, suggesting all three would be suitable for use in PID, although this is not immediately obvious just by studying Figure 3.41. While it would appear that there are a high number of points on the plot that fall in the regions where PIDVarA and PIDVarB disagree on the muon identification, this is actually because the very high density of points in the regions of agreement cannot be easily seen by eye due to the degree of overlap. In fact PIDVarA and PIDVarB agreed on the identifiaction of 98.9% of particles.

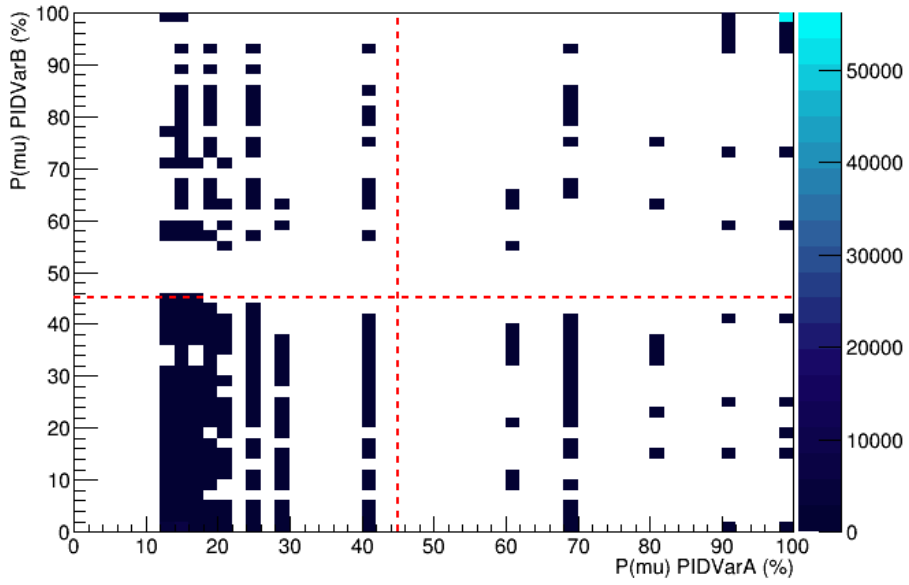

Figure 3.41: Comparison of P(μ) returned by PIDVarA and PIDVarB on MC dataset. For all particles identified by both variables, there was a muon identification consistency of 98.9%.

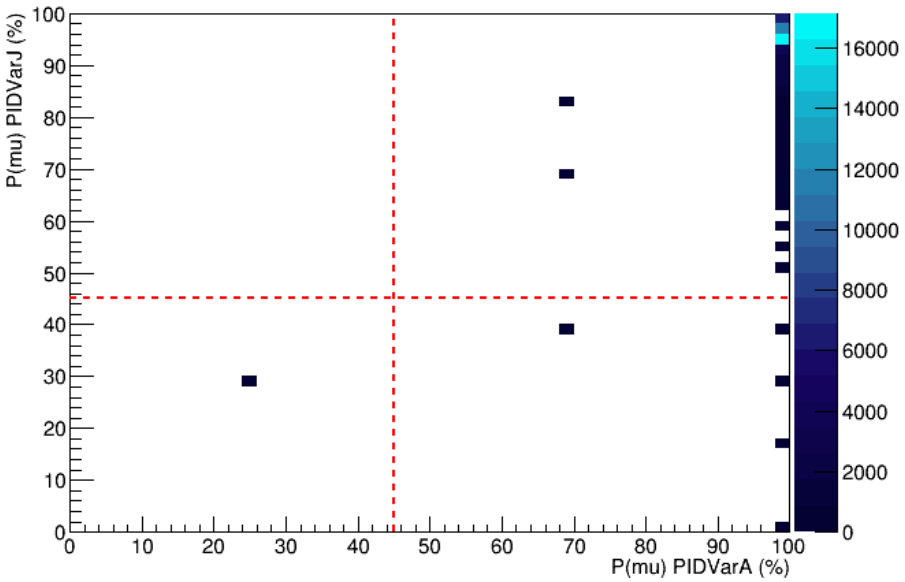

Figure 3.42: Comparison of P(μ) returned by PIDVarA and PIDVarJ on MC dataset. For all particles identified by both variables, there was a muon identification consistency of 99.3%.

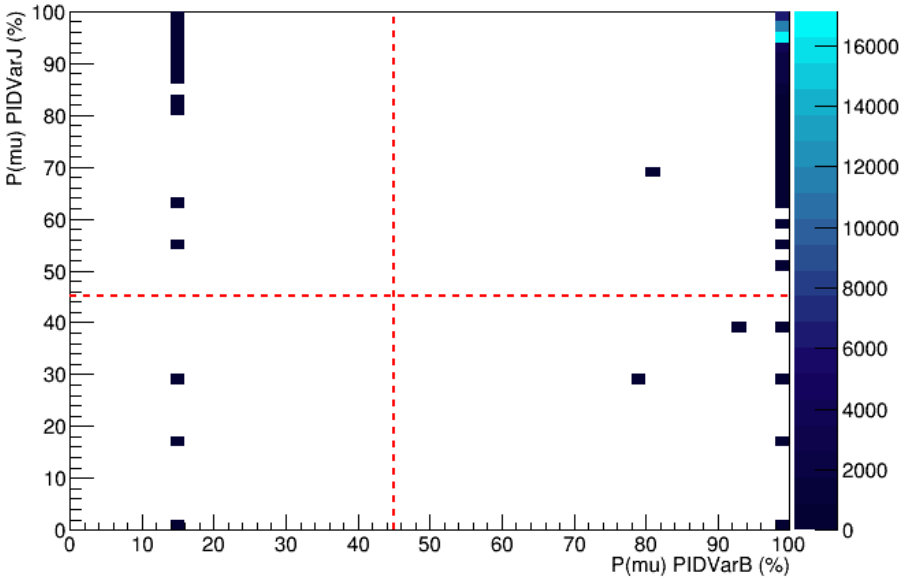

Figure 3.43: Comparison of P(μ) returned by PIDVarB and PIDVarJ on MC dataset. For all particles identified by both variables, there was a muon identification consistency of 99.8%.

A	B	I	J
A	98.9%		99.3%
	B		99.8%
		I	

Table 3.7: Consistency between upstream PIDVars for MC.

Consistency between Downstream Step IV PID variables

PID was performed by each downstream variable class individually for the simulated 200 MeV/c pion beam. PID was performed once per variable, using the settings listed in Table 3.6. All of the comparison plots can be found in Appendix A, in Figures A.71 - A.83. Table 3.8 lists the consistencies determined between the variables. For comparisons of PIDVarC with PIDVarF and PIDVarF with PIDVarH no plots are shown as there were no particles within the sample identified by both variables.

PIDVars E, F and H show good consistency on MC. PIDVars C and D are less good, which is to be expected given their poorer purities from the studies above. And the consistency of PIDVarG is very poor, which correlates with its poor purity performance.

C	D	E	F	G	H
C	85.9%	80.9%		22.3%	90.3%
	D	98.0%	87.3%	1.56%	98.8%
		E	98.7%	7.55%	97.6%
			F	36.7%	
				G	95.7%

Table 3.8: Consistency between downstream PIDVars for MC.

Consistency between Downstream and Upstream PID

Upstream PID was performed using variables A, B and J, and downstream PID was performed using variables E, F and H, for 200 MeV/c pion beam, using the settings listed in Table 3.6. These variables were selected due to their performance in the purity and consistency studies. Figure 3.44 shows the probability of a particle being a muon, P(μ), as determined upstream and downstream.

The muon identification consistency between upstream and downstream was 89.9% overall, with 2.28% of particles identified as muons upstream being identified

as not-muons downstream, and 7.83% of particles identified as muons downstream being identified as not-muons upstream.

The distance between the upstream and downstream tracker reference planes in the cooling channel is 3.77m. Over this distance, with no acceleration applied, one would expect 0.2% of 200 MeV/c muons to decay, and 20.9% of pions to decay.

The decay of muons across the channel would not wholly account for 2.28% of inconsistency between muons upstream not being identified as muons downstream. However an inconsistency of the order 2% is not itself inconsistent with the consistencies between the individual variables used in this case, which range between 97.6% and 99.8%.

The decay of pions across the channel could account for the 7.83% inconsistency between muons downstream not being identified as muons upstream, with the difference between 7.83% and 20.9% being accounted for by particles that did not get identified both upstream and downstream, and so not being included in this consistency study. Given that Table 3.11 shows a 35% reduction in the number of tracks suitable for PID between upstream and downstream, and less than half as many tracks being identified downstream as were identified upstream, this is a likely source of the difference.

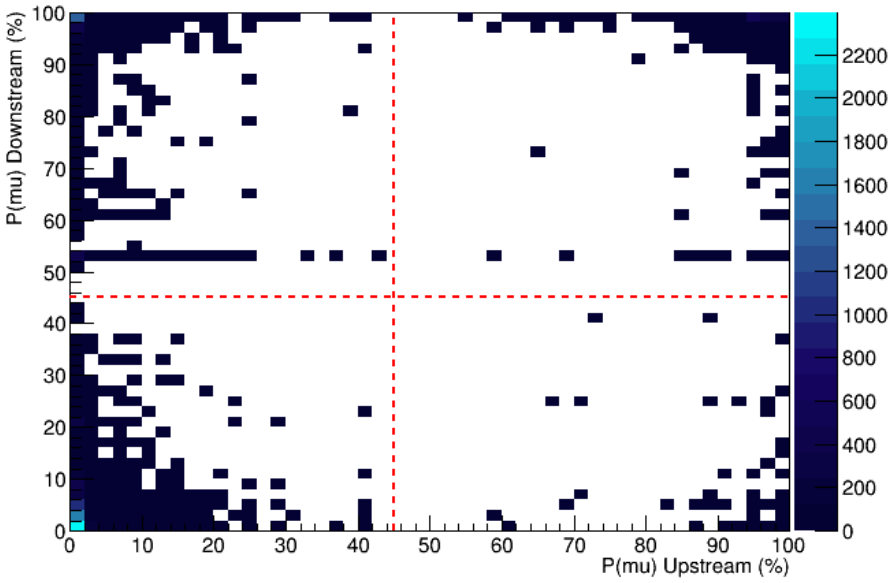

Figure 3.44: Comparison of P(μ) returned by upstream PID and downstream PID on MC dataset. Though not easily seen due to the density of points around (0,0) and (100,100), there was a muon identification consistency of 89.9%.

3.6 Results of Commissioning PID

Using the optimal settings from Table 3.3, PID was run on both the simulated and real data sets. All commissioning variables other than ComPIDVarD were used, as they performed well for both purity and consistency.

Tracks from TrackMatching that had been reconstructed through the cooling channel were selected to be studied. The confidence level cut of 10% as used in the performance studies was kept. The number of each particle species identified was counted. As the through tracks are constructed based upon the TOF1 - TOF2 time of flight, all tracks used had at least enough information to be identified by ComPIDVarA, and so all through tracks are suitable tracks for the PID.

3.6.1 For MC data set

The results of the commissioning PID on the 200 MeV/c muon beam are shown in Table 3.9. 85.1% of suitable tracks were assigned a pid, with the other 14.9% of tracks failing the confidence level cut. The purity of the muon sample obtained from the PID can be demonstrated by plottling the log-likelihoods returned by the PID for MC muons that were identified as muons and those returned by pions and positrons misidentifed as muons, as shown in Figure 3.45. It can be seen from this that the muon sample returned by the PID contained 22283 correctly identified muons, 22 pions misidentified as a muon, and 1 positron misidentified as a muon, which corresponds to a muon a purity of 99.9%, thus meeting the purity requirements of MICE.

	Through PID
# suitable tracks	23636
# identified	22707
# muons	22306
# pions	385
# positrons	16
# failed	929

Table 3.9: Results of PID for a MC 200 MeV/c, 3 mm muon beam.

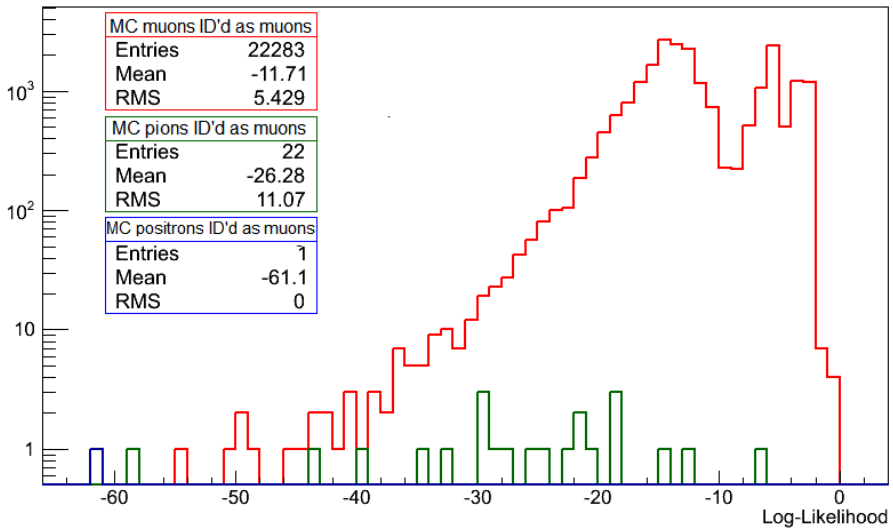

Figure 3.45: The log-likelihoods returned by the PID for MC muons (red), pions (green) and positrons (blue) that were identifed as muons.

3.6.2 For real data

The same settings were used for PID on data as were used for the MC. Table 3.10 shows the results of running PID on the individual MICE runs and the combined totals. Figure 3.46 shows the the identification efficiency of the PID on data, with an average of 92.8% of tracks being identified.

	Run #								
	07834	07835	07836	07837	07838	07841	07842	07843	Total
# suitable tracks	1140	10648	9957	9912	10875	3349	1957	9126	56964
# identified	1084	10104	9427	9377	10375	3192	1852	8682	54093
# muons	1013	9591	8952	8879	9816	3023	1736	8241	51251
# pions	64	452	418	448	498	154	102	389	2525
# positrons	7	61	57	50	39	15	14	52	295
# failed	56	544	530	535	500	157	105	444	2871

Table 3.10: Results of PID for all 200 MeV/c muon LiH runs.

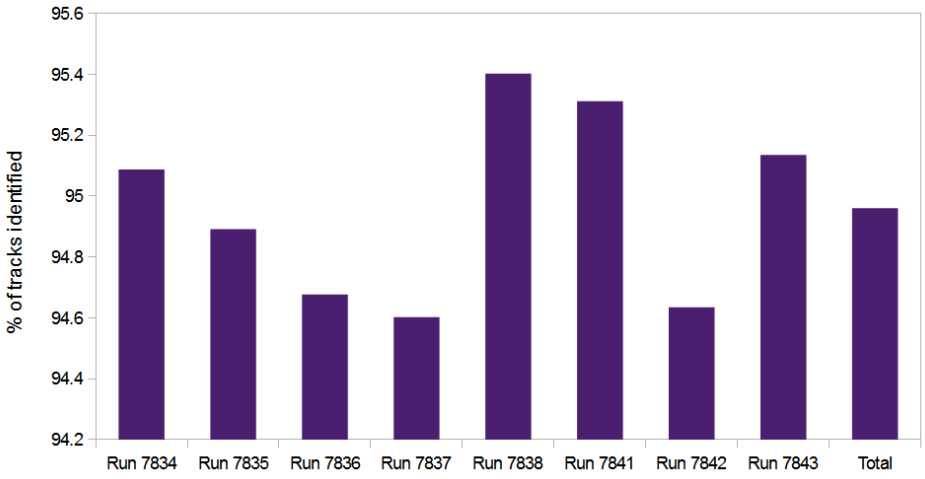

Figure 3.46: Percentage of tracks identified for all LiH data runs.

3.7 Results of Step IV PID for MC dataset

Using the optimal settings from Table 3.6, upstream and downstream PID was run separately on the 6 mm 200 MeV/c MC sample used previously. The upstream variables used were PIDVarA, PIDVarB and PIDVarJ. The downstream variables used were PIDVarE, PIDVarF and PIDVarH.

Tracks from TrackMatching that had been reconstructed through the cooling channel were selected to be studied. The confidence level cut of 10% as used in the performance studies was kept.

The results of the upstream and downstream PID are shown in Table 3.11. 98.8% of suitable tracks upstream were identified, and 73.0% of suitable tracks downstream were identified. Given the stronger performance of the upstream variables seen in the studies above, this disparity in efficiency is understandable, as it is necessary to use much stricter variable cut settings to achieve an acceptable degree of purity in the downstream muon sample. The discrepancy between the number of suitable upstream tracks and downstream tracks is due to particles lost from the beam before reaching the EMR. Higher numbers of muons were identified than any other particle because the PID variable cut settings were tuned to maximise muon purity and efficiency.

As with the commissioning PID, the purity of the muon sample obtained from the upstream and downstream PID can be demonstrated by plottling the log-likelihoods returned by the PID for MC muons that were identified as muons and those returned by muons misidentifed as pions and positrons, as shown in Figure

3.47 for the upstream PID and Figure 3.48 for the downstream PID. It can be seen from this that the muon sample returned by the upstream PID has a purity greater than 99.9% (60689 muons correctly identified, 25 pions and 17 positrons misidentified as muons), thus meeting the purity requirements of MICE, however downstream the purity is 97.4% (34124 muons correctly identified, 893 pions and 9 positrons misidentified as muons).

	Upstream PID	Downstream PID
# suitable tracks	92875	60487
# identified	91733	44183
# muons	60731	35026
# pions	31000	7619
# positrons	2	1537
# failed	1142	16304

Table 3.11: Results of PID for a 200 MeV/c, 6 mm pion beam.

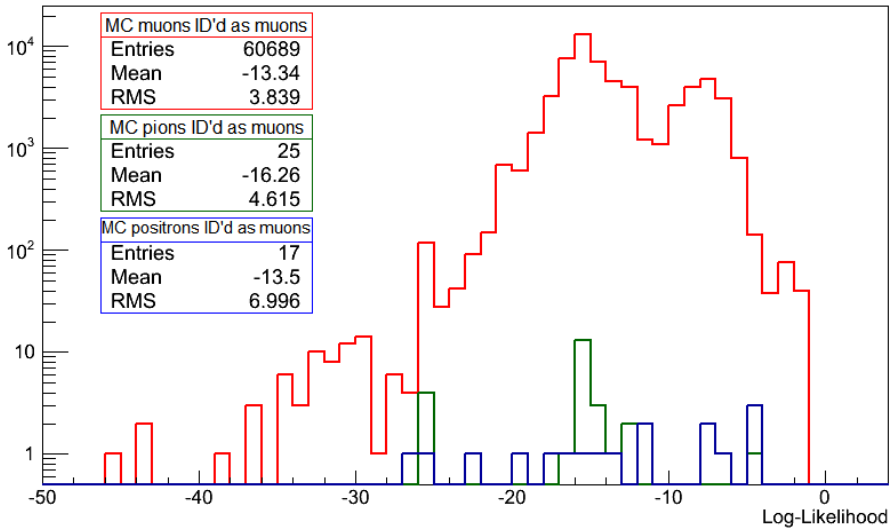

Figure 3.47: The log-likelihoods returned by the upstream PID for MC muons (red), pions (green) and positrons (blue) that were identifed as muons.

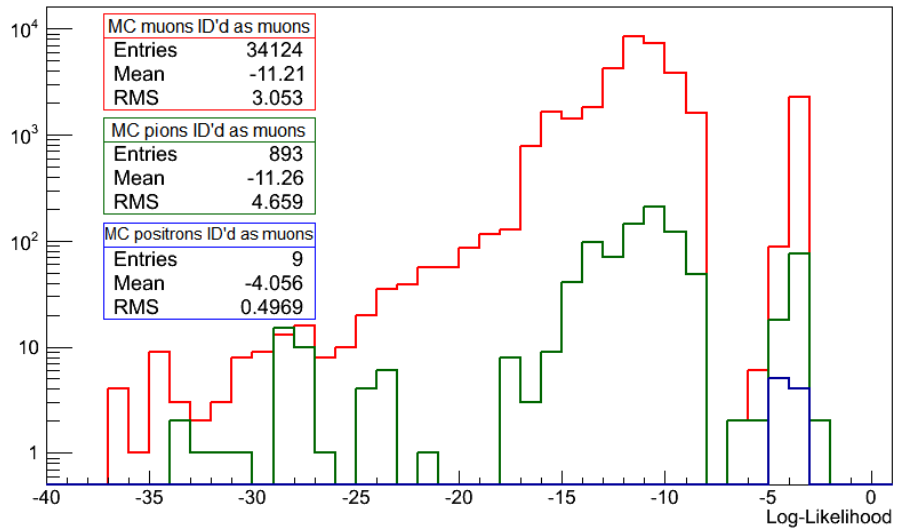

Figure 3.48: The log-likelihoods returned by the downstream PID for MC muons (red), pions (green) and positrons (blue) that were identifed as muons.

3.8 Conclusions

Strong particle identification in MICE is essential due to the desired muon purity upstream of the cooling channel of 99.9%. The Global PID framework was developed in MAUS to provide a method of particle identification that incorporated information from all of the MAUS detectors. This information was combined into different libraries of PID variables, for use on both commissioning and Step IV data. Studies of the efficiency and purity of individual variables and of the consistency between the variables was performed, in order to determine the best settings to use when performing PID, for a 3 mm, 200 MeV/c commissioning muon beam (for MC and data) and on an MC 6 mm, 200 MeV/c Step IV pion beam. Using these settings, the PID was able to select out muon samples with 99.9% purity for both the commissioning beam and for the upstream muon selection of the Step IV beam, meeting the requirements of the PID. Although the same stringent purity requirement isn't placed on the downstream PID, which returned a 97.4% pure muon sample, work could continue in this area to improve the discriminatory strength of the downstream variables.

Chapter 4

Measurement of Multiple Scattering in LiH

4.1 Introduction

As discussed in Section 1.5, the two processes that determine the effectiveness of ionisation cooling are multiple Coulomb scattering and energy loss. This section will focus on the theory of multiple scattering of muons and studies of how this may be measured in MICE. Some discussion of energy loss of muons through materials can be found in [45].

4.1.1 Multiple Coulomb Scattering

As a charged particle travels through a material, it undergoes multiple small-angle scatters. For all but low Z materials, most of these scatters are due to Coulomb scattering from nuclei [45]. However at low Z, especially for hydrogen, where the nuclear and electron potentials have the same magnitude, scattering with electrons becomes important [53].

Theory

The scattering of charged particles due to the Coulomb force was first discovered by Geiger, Marsden and Rutherford beginning in 1909, when they studied the elastic scattering of alpha particles incident on a thin gold foil [54]. For a single Coulomb scatter, a particle travelling towards an atom is deflected by the Coulomb forces, changing it's direction by an angle θ_C. However, for a particle travelling through a material, it will undergo multiple scatters, producing a net scattering effect, as shown in Figure 4.1, where θ_{plane} is the resultant two dimensional projected angle of

the particle leaving the material, s_{plane} is the effective path the particle would have followed had it experienced a single deflection upon entering the material, equivalent to the effect of the multiple deflections it experienced, Ψ_{plane} is the distance between the particle's initial trajectory and s_{plane} within the material, and y_{plane} is the distance between the particle's initial trajectory it's scattered position upon exiting the material.

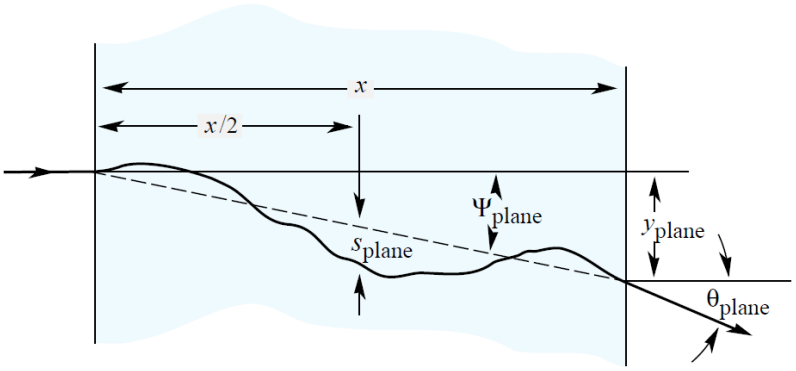

Figure 4.1: Contributions of multiple single scatters in material to θ_{plane}. Image taken from [45].

Models of Multiple Scattering

A number of theories describe charged particle scattering in a Coulomb field. Moliére theory [47] is widely used in implementations of scattering computations. It only includes interactions with the nucleus, and the scattering distribution is proportional to Z^2. Bethe expanded Moliére theory [48], replacing Z^2 with the $Z \times (Z+1)$ to also incorporate the electronic charge, which would be valid if the cross sections were the same for nucleus and electron scatters [49]. Geant4, which is used for simulation of physics processes in MAUS, does not use the Moliére theory, instead it uses the Wentzel-VI model, which combines both multiple and single scattering models [46]. As will be discussed in Section 4.1.2, neither the Moliére or Bethe models are particularly successful at estimating scattering in low Z materials. Geant4 was also used to study MuScat data, although at that time the default implementation of multiple scattering was different to that used now. A new model, ELMS [50], which considers both energy loss and multiple scattering has been developed, however ELMS uses numerical integration, which is time consuming, and is currently only implemented for hydrogen.

The Particle Data Group (PDG) formula [45] for multiple scattering is based

on Moliére theory, which describes the scattering distribution as approximately Gaussian for small angles, but for larger angles the behaviour is like Rutherford scattering. The PDG defines the scattering angle θ_0 as

$$\theta_0 = \theta_{plane}^{rms} = \frac{1}{\sqrt{2}}\theta_{space}^{rms} \tag{4.1}$$

where θ_{plane}^{rms} and θ_{space}^{rms} are the projected and 3D space angles respectively. Based upon the Gaussian approximation, the scattering angle is then calculated by

$$\theta_0 \approx \frac{13.6MeV}{\beta p_\mu} z\sqrt{x/X_0}\Big[1 + 0.038\ln(x/X_0)\Big] \tag{4.2}$$

where β is the velocity of the particle, p_μ is the momentum, z is the charge number of the particle, and x/X_0 is the thickness of the scattering medium in radiation lengths [45].

4.1.2 MuScat

As has been discussed previously in this thesis, muon cooling will play an essential role in the development of a muon collider facility, and given the importance of scattering in the cooling equation, it is necessary to understand how muons interact with different materials. However, prior to 2003, no relevant scattering experiments with muons had been performed. In 2003, the MuScat experiment [51] measured the scattering of 172 MeV/c muons through Li, Be, CH_2, C, Al, Fe and H_2. The experiment ran on the M20 muon beamline at TRIUMF. As shown in Figure 4.2, lead collimators were used to produce a narrow collinear muon beam. A wheel with the target materials, or a LH_2 vessel, was placed in the beam. This was then followed by a scintillating fibre tracker, which measured the particle distribution after scattering, trigger scintillators (which provided time of flight measurements), and the TINA (TRIUMF Iodide of Sodium) calorimeter [51].

MuScat was able to confirm what had first been observed in [52]; that Moliére does not accurately describe low Z materials in the tails of the scattering distributions. This is shown in Figure 4.3, which shows the the scattering angle distribution measured for 109 mm of LH_2, compared to simulation in Geant4, ELMS, and the predictions from (Z^2), and the Bethe adaptation of Moliére ($Z \times (Z+1)$). As can be seen from the figure, neither of the Moliére models accurately describes the data, while the Urban model used in Geant4 predicts too much scattering. The ELMS model shows good agreement, except at the highest scattering angles [51].

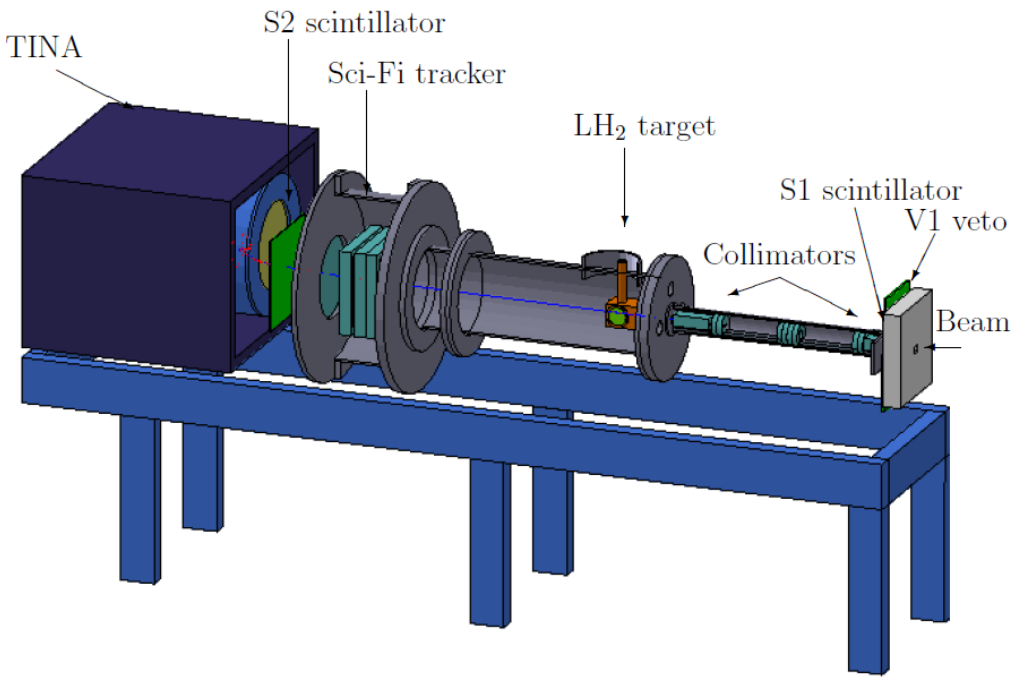

Figure 4.2: GEANT4 rendering of MuScat apparatus [51].

4.1.3 Multiple Coulomb Scattering in MICE

The cooling equation given by Eqn. 1.22 actually incorporates the scattering formula in Eqn. 4.2 (ignoring the logarithmic term). Eqn. 1.22 can be rewritten, independently of this approximation, as

$$\frac{d\epsilon_N}{dX} = -\frac{\epsilon_N}{\beta^2 E_\mu}\left\langle\frac{dE}{dX}\right\rangle + \frac{\beta_t p_\mu}{2m_\mu}\frac{d\theta_0^2}{dX} \tag{4.3}$$

Using an approximation of the scattering in the cooling equation limits the accuracy to which MICE can measure the emittance change. Accordingly, it is necessary to accurately measure multiple Coulomb scattering for the MICE absorbers which, being low Z materials, have been shown to disagree.

As was described in Section 2.3.1, MICE has two absorbers; a 65 mm LiH disk, and liquid hydrogen, which is housed in a vessel with two pairs of thin Al absorber windows that would also contribute to scattering, as would the Al helium windows around the trackers. The absorber windows are 0.180 mm on axis, however the thickness increases with the radius, as shown in Figure 4.4, which also shows the contribution to the scattering for a single window, calculated using Eqn. 4.2.

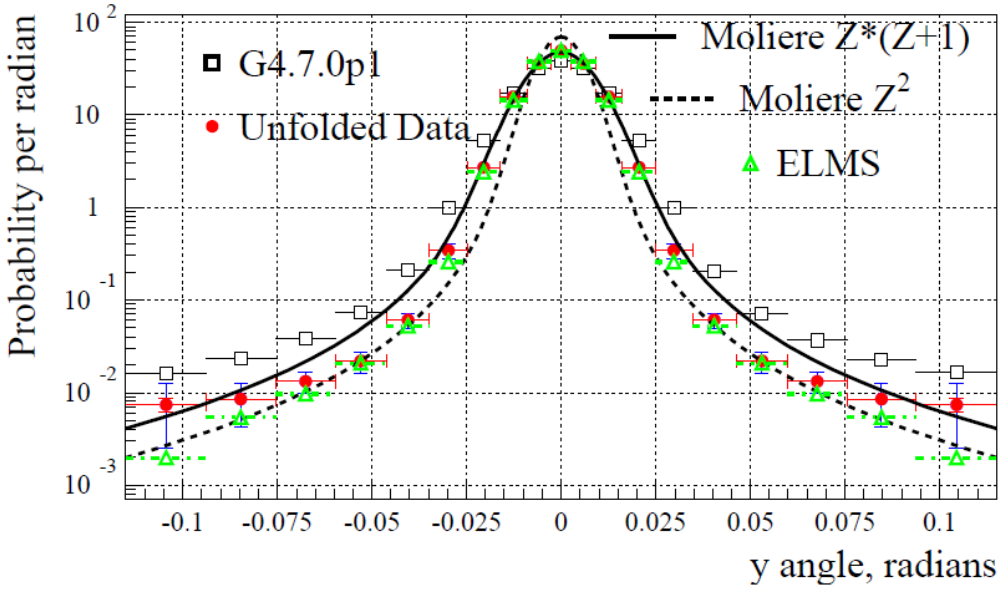

Figure 4.3: MuScat results for the projected scattering angle distribution in data and simulation for 109 mm of LH_2, taken from [51].

	LiH	Absorber Windows	Helium Windows	Helium
θ_0 (mrad)	17.5	6.80-48.8	11.4	0.0511

Table 4.1: Scattering contributions from materials in the MICE channel. The combined thickness of four absorber windows increases from 0.72 to 36 mm as the distance from the beam centre increases, hence the range given for scattering due to the absorber.

The contributions of the materials in the cooling channel as well as of the LiH absorber, as calculated by Eqn. 4.2, are shown in Table 4.1. A range is given for the contribution from the four absorber windows, due to the radial dependence.

The effect on the scattering measurement due to scattering in the scintillating fibres of the tracker planes themselves is minimised by the fact that only the measured position and momentum from the planes of the upstream and downstream trackers closest to the absorber are used to determine the scattering angle, so scattering in the other planes is less influential than it would be for a measurement that relied on the whole track within the trackers.

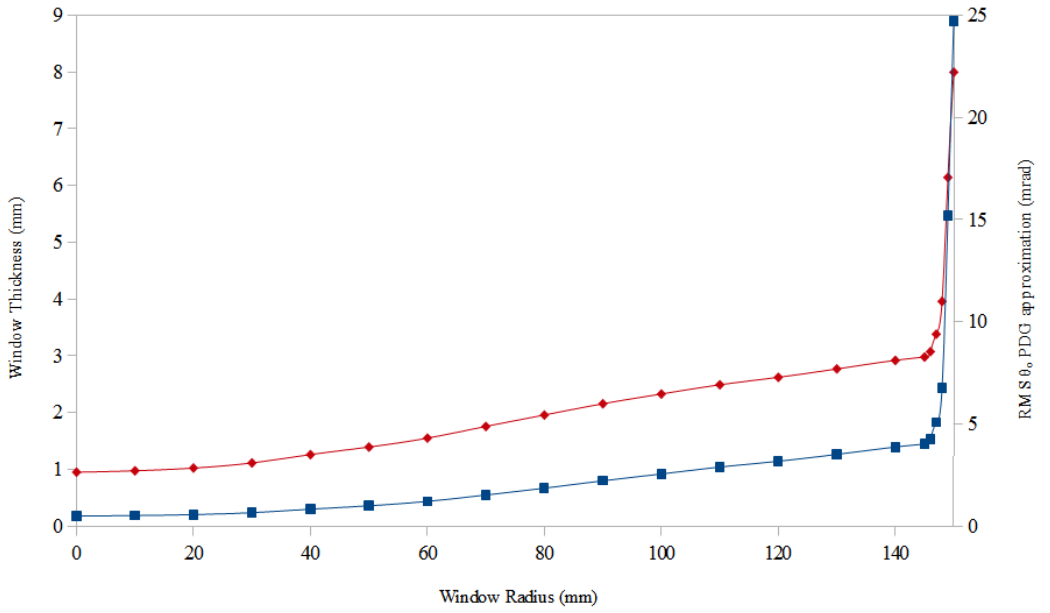

Figure 4.4: The thickness of a single absorber window as a function of radius (blue), and the corresponding RMS scattering angle (red). Thickness/radius values taken from [61].

4.2 Description of field on measurement

The approach taken here is based upon the Monte-Carlo studies performed in [53], expanded to include tracker reconstruction, which was unavailable at the time, and continued through the deconvolution process.

Step IV of MICE is designed with magnetic fields across the cooling channel. Particles passing through the fields of the spectrometer solenoids create helical tracks in the scintillating fibre trackers. The structure of the trackers, and their reconstruction capabilities, is discussed in section 2.4.1. Whereas for a particle travelling in a straight line along the beam axis it would be sufficient to calculate the angle between the upstream and downstream momentum vectors, the helical motion of the particle in the fields means that this isn't possible, and so an alternative method is required, which is illustrated in Figure 4.5.

1. The momentum vector $\vec{p}$ of a muon measured in the downstream plane of the upstream tracker is propagated downstream through the fields using MAUS, to predict its momentum vector $\vec{p'}$ at the downstream face of the absorber in the absence of scattering.

2. The momentum vector $\vec{q}$ of the same muon measured in the upstream plane

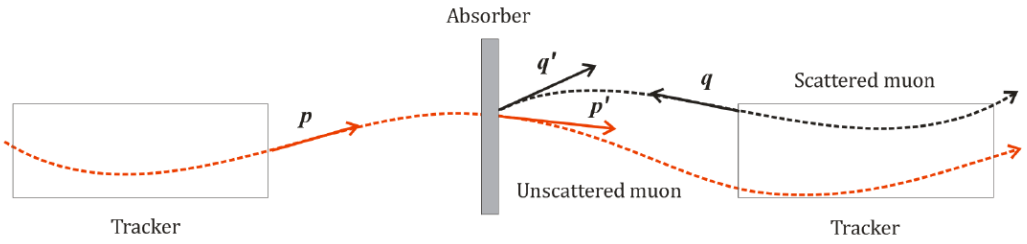

Figure 4.5: Scattering measurement method for a particle in the presence of magnetic fields, taken from [53].

of the downstream tracker is then propagated upstream through the fields, to predict its momentum vector $\vec{q'}$ at the downstream face of the absorber.

3. The three dimensional scattering angle is then calculated by

$$\theta = \arccos \frac{\vec{p'} \cdot \vec{q'}}{|\vec{p'}||\vec{q'}|} \tag{4.4}$$

The two dimensional scattering angles, for particles that do not diverge greatly from the beam axis, are given by

$$\theta_{x,y} = \frac{p'_{x,y}}{p'_z} - \frac{q'_{x,y}}{q'_z} \tag{4.5}$$

4.2.1 Application of Field-On Method to Field-Off Data

As previously stated, Step IV of MICE is designed with two spectrometer solenoids operating upstream and downstream of the cooling channel. However, due to damage sustained by one of the spectrometers that then necessitated a redesign of the quench protection and detection systems of the magnets before they could be used, at the time of writing scattering data has only been taken for a field off measurement. Accordingly, the following sections present an analysis of this data with the field on method, and then a Monte Carlo study of the method where fields are present.

4.2.2 Comparison of Raw Scattering Distributions for Monte Carlo and Reconstructed Monte Carlo

The first stage of this study is to establish the effects of the detector response on the resolution of the measurement, by performing Monte Carlo simulations of

both the empty absorber and LiH cases, and comparing the Monte Carlo scattering distributions with the reconstructed Monte Carlo distributions.

These simulations were performed using particle beams that were generated from G4Beamline input, transported through the beamline to the channel. For the field off studies 200 MeV/c muon beams were simulated, while for the field on studies 200 MeV/c pion beams were used. The pion beam was chosen as this actually has an improved muon rate compared to the muon beam. However field off data has already been taken with a muon beam, hence the difference. The LiH Monte Carlo datasets used in these studies are the same as those studied in Chapter 3.

For the raw scattering distributions, the only deliberate selection of particles was by particle id, selecting out muons. However, by the nature of how the global reconstruction works, when a through going track is reconstructed it must at least have produced hits in TOF1 and TOF2. As such any particles that would produce hits in the upstream tracker, but then scatter out of the beam before the downstream tracker, are already omitted from the sample. This results in a loss of approximately 10% of the particles that would have made it to the downstream tracker but not TOF2. The same TOF1/TOF2 hit requirement is placed on the muons in the Monte Carlo beam, to ensure consistency. The use of through going tracks for the field off study is necessary due to the time of flight between TOF1 and TOF2 being integral to the Global PID, and for consistency between the field on/field off measurements, through going tracks are also used for the field on measurement.

The simulated beam configurations were:

1. Empty absorber, no fields in cooling channel magnets.
2. LiH absorber, no fields in cooling channel magnets.
3. Empty absorber, fields in cooling channel magnets.
4. LiH absorber, fields in cooling channel magnets.

The raw space angle and projected angle distributions for the different configurations are shown in Figures 4.7 - 4.10, and the RMS angles are summarised in Table 4.2. The table also shows the degree of corrections (how much unfolding is required to compensate for the tracker resolution, given by Recon^2 - MC^2 = Correction^2) required to obtain the truth from the reconstructed distributions.

	RMS θ_{3D} (mrad)			RMS θ_x (mrad)		
	MC	Recon	Correction	MC	Recon	Correction
Field-Off Empty	18.7	18.9	2.74	19.8	20.5	5.31
Field-Off LiH	18.8	19.4	4.79	25.5	26.2	6.02
Field-On Empty	5.68	16.3	15.3	6.20	17.9	16.8
Field-On LiH	12.9	19.4	14.5	18.0	25.2	17.6

Table 4.2: Projected and space angles for Monte Carlo and reconstructed Monte Carlo distributions for field-on and field-off measurements, with estimates for the corrections required.

As can be seen in Table 4.2, the projected angle of a reconstructed field-on track scattering through LiH is 34% larger than the truth value, and for the case of an empty absorber the reconstructed angle is almost three times the truth angle, which shows that a large degree of unfolding is required to account for the resolution of the tracker reconstruction. For field-off tracks, the difference between truth and reconstructed truth is much smaller, so the requirement for unfolding is less.

While both Monte Carlo beams are designed with beam momenta of 200 MeV/c at the absorber, the field off beam actually has a lower momentum (discussed further in Section 4.2.5). Accordingly the muon scattering distributions of the two beams are not directly comparable. Furthermore, due to the lack of focussing in the field off case, the beam is much wider at the absorber, and the particles further from the beam axis will pass through a greater thickness of Aluminium from the absorber windows downstream of the absorber as the beam diverges, further increasing the measured distributions of both the empty and LiH configurations, which will further contribute to the larger RMS angles shown in the table for the field off angles. The differences between the beam distributions for field on and field off tracks is shown in Figure 4.6. Furthermore, for the field on case, the focussing effects of the fields may in fact 'correct' for the scattering in the windows, reducing their contributions to the scattering angle measured at the absorber.

The general agreement between the reconstructed and truth angular distributions as shown in Figure 4.8 indicates that the straight track (field off) tracker reconstruction is very reliable, with the width of the reconstructed distribution being solely due to the scattering in the materials and not any smearing due to the resolution of the reconstruction.

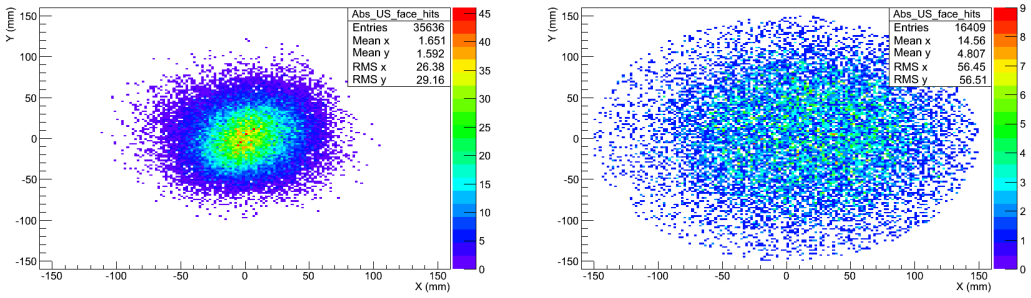

(a) (b)

Figure 4.6: The beam distribution at the upstream absorber face for the field on (a) and field off (b) beams.

θ_X Offset for Field-On Measurement

As can be seen in Figure 4.9b and Figure 4.10b there is an offset between the θ_X distributions for Monte Carlo and reconstructed Monte Carlo. This same offset is not seen for θ_Y. The source of this asymmetry can be determined by considering Eqn. 4.5 and the reconstructed momentum residuals of the particles and the momentum residuals once propagated, as shown in Figure 4.11.

From Eqn. 4.5 it can be seen that if p'_x is overestimated (and/or q'_x is underestimated) then θ_x will be overestimated.

While the reconstructed p_y is overestimated upstream, the propagation reduces the offset for p'_y. Meanwhile downstream q_y is also overestimated, and the propagation increases the offset for q'_y. This actually results in the effects of these two offsets almost cancelling out (as the mean overestimate for p'_y is -0.6252 MeV/c and for q'_y is -0.7236).

The reconstructed p_x is overestimated upstream, and the propagation increases the offset for p'_x to -1.111 MeV/c. Meanwhile downstream q_x is underestimated, with the propagation reducing the offset for q'_x to near zero. This systematic overestimation of p'_x would account for the systematic offset seen for θ_X. The source of the momentum residual offsets is still under investigation.

4.2.3 Measurement Procedure

The aim of this analysis is to perform a measurement of the multiple scattering of muons through the MICE LiH absorber, and to compare this measurement with existing scattering models, principally with scattering in Geant4, as this effects the analysis and reconstruction of MICE data, and with the PDG approximation, due

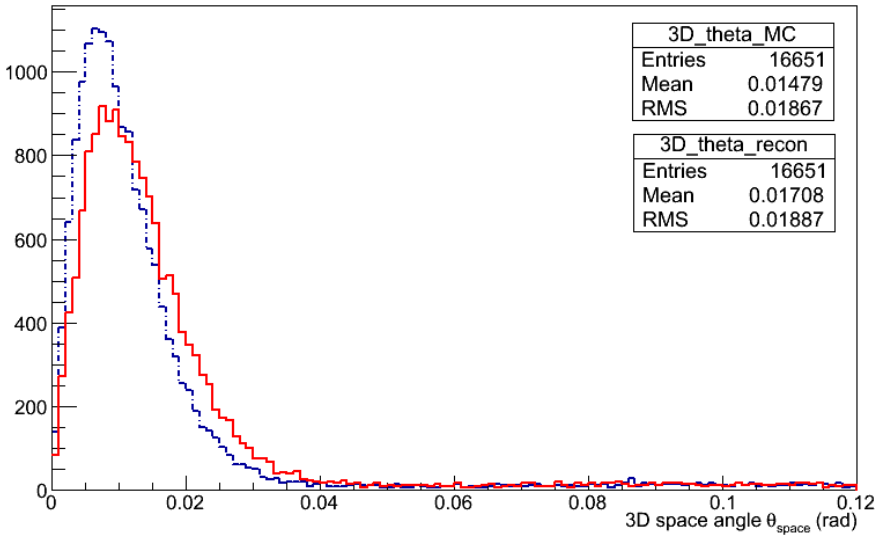

(a)

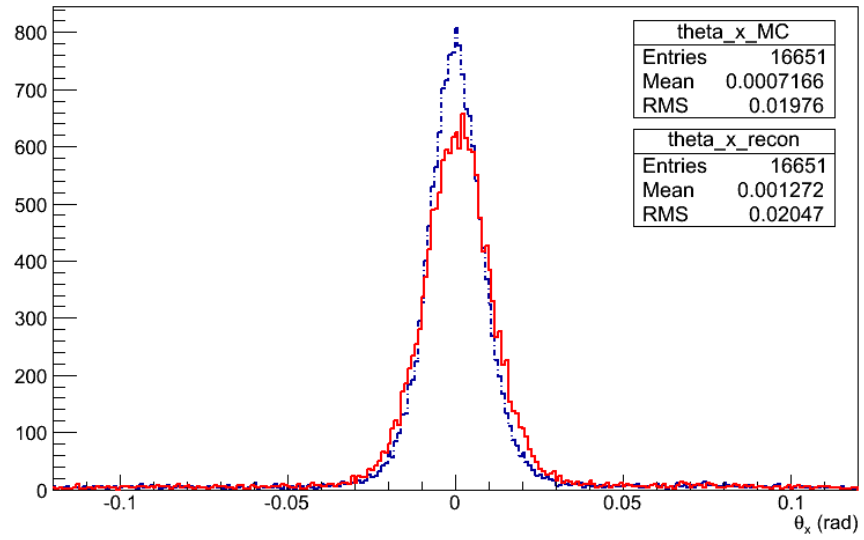

(b)

Figure 4.7: Monte Carlo (blue dashed line) and reconstructed Monte Carlo (red line) scattering distributions for an empty channel in the absence of magnetic fields.

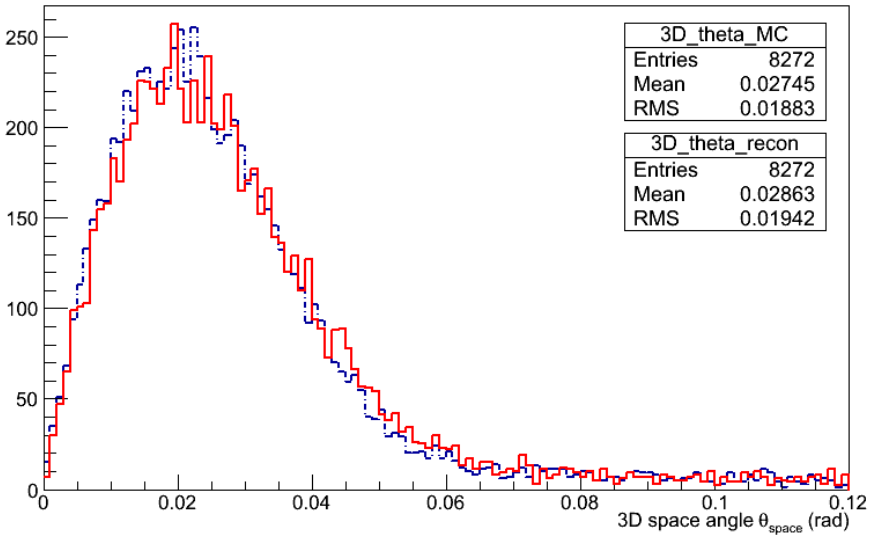

(a)

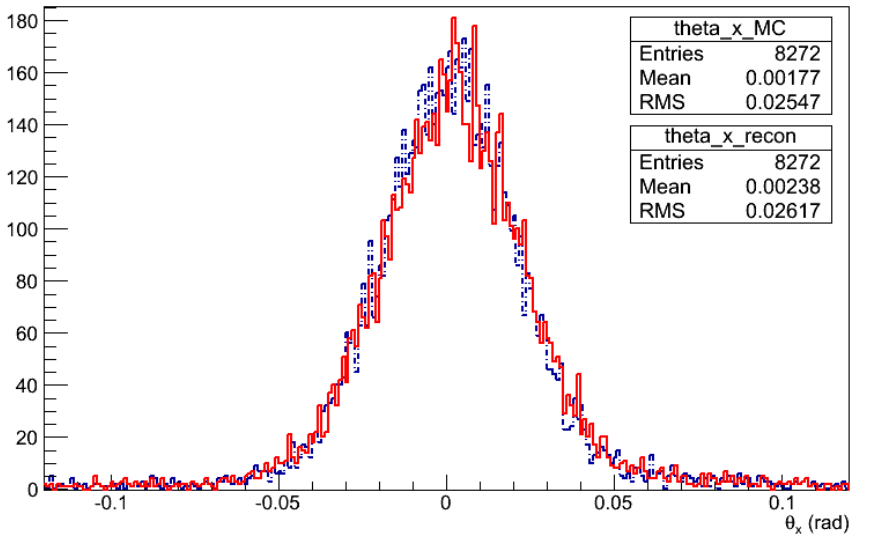

(b)

Figure 4.8: Monte Carlo (blue dashed line) and reconstructed Monte Carlo (red line) scattering distributions for a LiH absorber in the absence of magnetic fields.

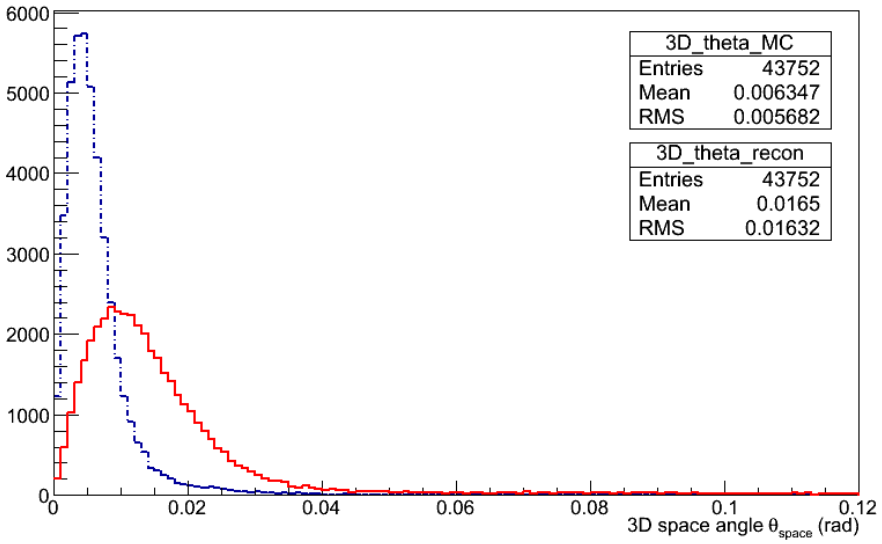

(a)

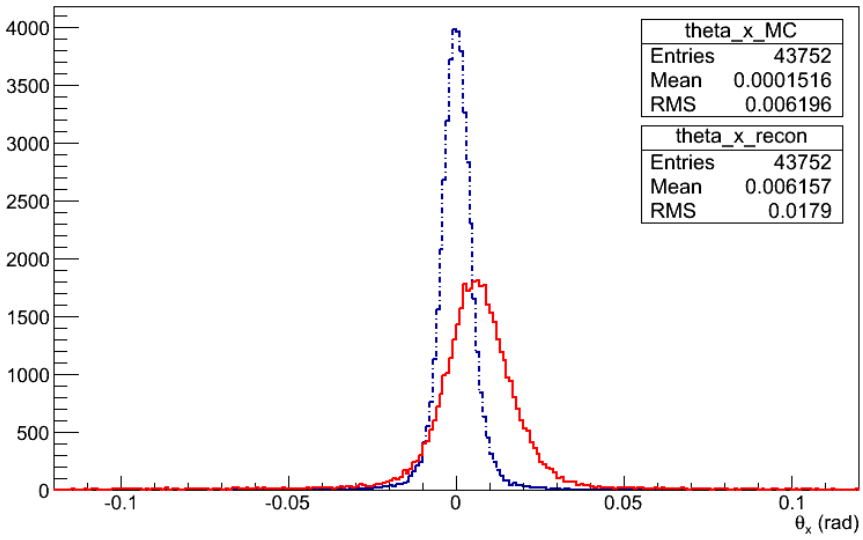

(b)

Figure 4.9: Monte Carlo (blue dashed line) and reconstructed Monte Carlo (red line) scattering distributions for an empty channel in the presence of magnetic fields.

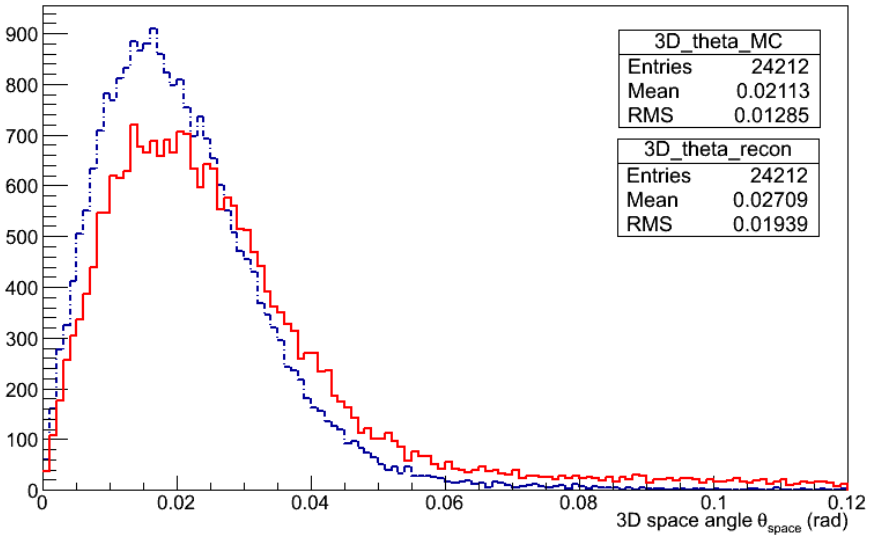

(a)

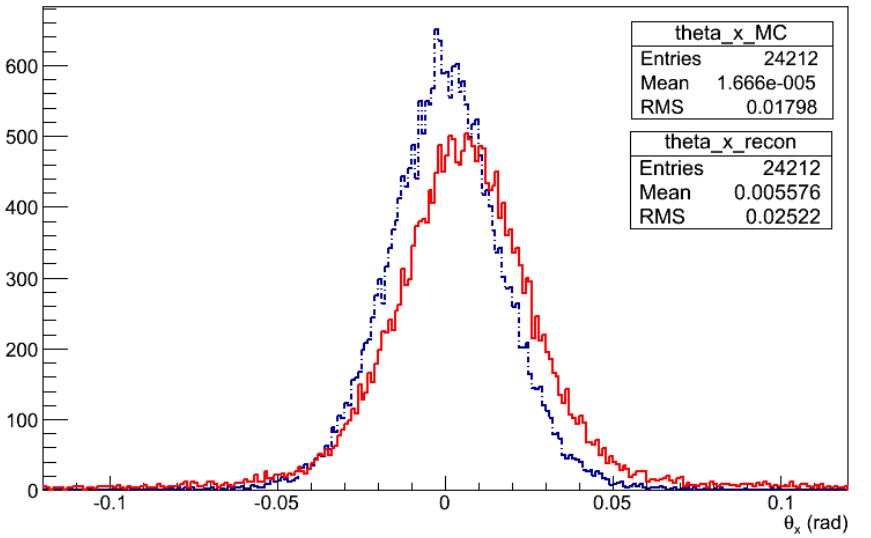

(b)

Figure 4.10: Monte Carlo (blue dashed line) and reconstructed Monte Carlo (red line) scattering distributions for a LiH absorber in the presence of magnetic fields.

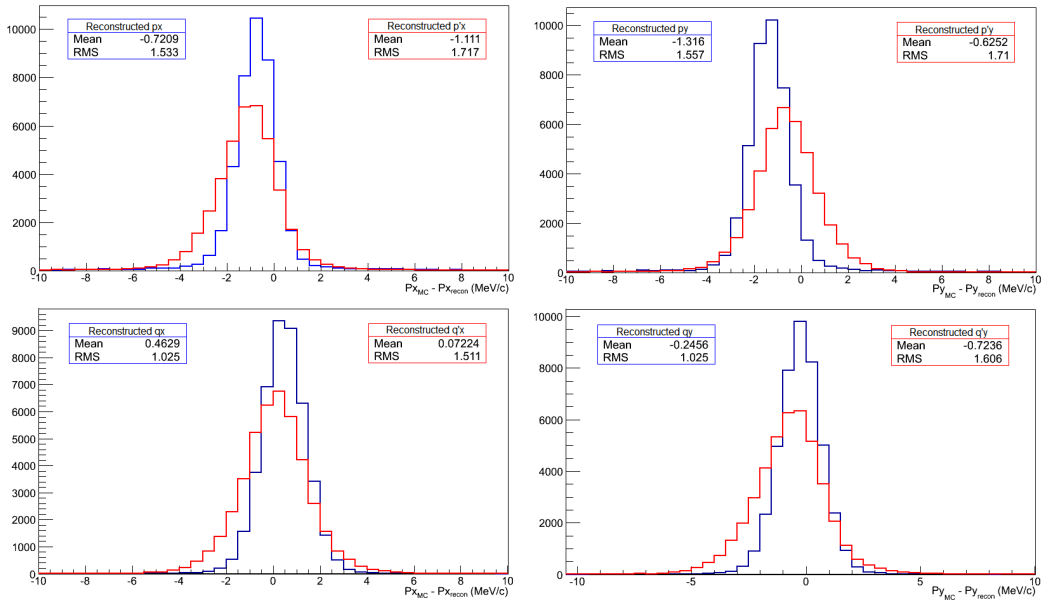

Figure 4.11: Residuals of the reconstructed transverse momentum components and their residuals after propagation through the fields, for an empty absorber.

to its inclusion in the MICE cooling equation.

The general approach will be to take MICE data (or reconstructed simulations where no data is available), calculate the scattering angles, and unfold these with respect to simulations of the same beam using MAUS (which uses Geant4). This procedure should return the "true" distributions of the scattering angles, with statistical errors. The systematic errors will be determined by performing the analysis under different conditions and measuring the effect this has on the scattering distributions. The errors will be combined in quadrature and then the final results will be compared with the expected values from scattering models, to determine their validity.

4.2.4 Unfolding Methods

Unfolding (or deconvolution) can be used to extract a quantity of interest from a measured distribution, removing the effects due to detector resolution. Several unfolding methods are implemented in ROOT within the RooUnfold package [55]. The two most frequently used methods are based upon Bayesian statistics [56] and singular value decomposition (SVD) [57].

Both methods use Monte Carlo truth to model how a given reconstructed

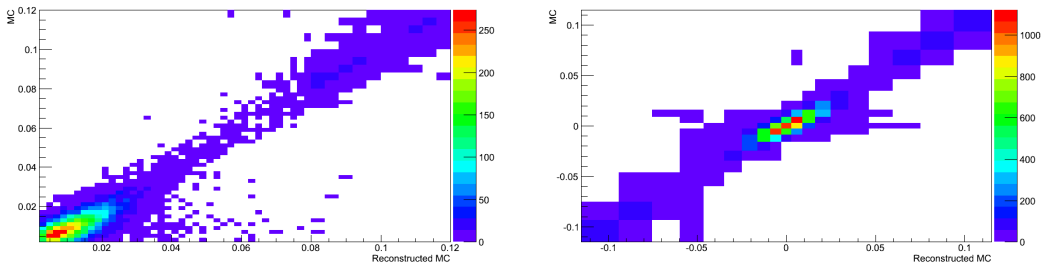

(a) Response for 3D space angle θ_{space}. (b) Response for projected space angle θ_x.

Figure 4.12: Response objects for the projected and space scattering angles (shown are the response objects for field-off empty absorber configuration).

quantity is correlated with the true value of the quantity, via a response matrix, with the quantities of interest here being the space and projected scattering angles. There is negligible dependence on the validity of the scattering model in the simulation here, as the measurements used to calculate the scattering angles are taken from the upstream and downstream tracker reference planes, and so are unaffected by prior scattering that may have occurred in the trackers. Figure 4.12 shows examples of the reponse matrices (as 2D histograms) for the projected and space scattering angles.

Both unfolding methods are iterative methods that require a regularisation parameter, *kreg*, which determines how much weight is placed on the data. The larger the value of *kreg*, the greater the weight of the data. Bayesian deconvolution is used by a number of particle physics experiments, with the value of *kreg* chosen to be the lowest value at which the χ^2 becomes constant. However questions have been raised about the validity of this method for choosing *kreg* [59], due to an emphasis on choosing the value of *kreg* that simply minimises the statistical errors, without any further (or mathematically rigorous) justfication for this choice. Accordingly the unfolding method that will be used here will be SVD unfolding.

SVD Unfolding

What follows is a summary of the full description presented in [57] and [58].

Consider a matrix $\hat{A}_{ij}$ (the 'response matrix') that simulates a detector response to a Monte Carlo sample, such that the probability that an event in the true bin j is measured in bin i is given by

$$\sum_j \hat{A}_{ij} x_j^{ini} = b_i^{ini} \tag{4.6}$$

where x_j^{ini} is the vector of truth values, and b_i^{ini} is the vector of measured (reconstructed from the truth) values. The purpose of the unfolding is to obtain x by solving $\hat{A}x = b$. This is not immediately straight forward as b will have associated errors, and the accuracy of $\hat{A}$ will be limited by statistics and inaccuracies in the detector simulation. The problem is approached using SVD. The $m \times n$ matrix A is factorised in the form

$$A = USV^T \tag{4.7}$$

where U is an $m \times m$ orthogonal matrix, V is an $n \times n$ orthogonal matrix, and S is an $m \times n$ diagonal matrix that satisfies

$$S_{ij} = 0 \text{ for } i \neq j, S_{ii} \equiv s_i \geq 0 \tag{4.8}$$

where s_i are the singular values of A. $\hat{A}x = b$ is then diagonalised by introducing new rotated vectors z and d:

$$\begin{aligned} USV^T x = b \Rightarrow z \equiv V^T x \ , \ d \equiv U^T b, \\ s_i z_i = d_i \Rightarrow z_i = \frac{d_i}{s_i} \Rightarrow x = Vz \end{aligned} \tag{4.9}$$

The matrix A and it's unknowns are then rescaled by multiplying A_{ij} by x_j^{ini}. New unknowns are defined by $w_j = x_j / x_j^{ini}$. Dividing each equation by the error Δb_i, such that now $\hat{A}x = b$ can be rewritten

$$\sum_j \tilde{A}_{ij} w_j = \tilde{b}_i \tag{4.10}$$

where the covariance matrix of $\tilde{b}_i$ is equal to the unit matrix, and w_i are defined relative to the Monte Carlo distribution, such that if $w_i = 1$ then the unfolded x would be the same as the truth. SVD is now used to solve the rescaled system:

$$\begin{aligned} \tilde{A}w = \tilde{b} \Rightarrow \tilde{A}USV^T \Rightarrow USV^T w = \tilde{b} \Rightarrow z \equiv V^T w, d \equiv U^T \tilde{b} \\ s_i z_i = d_i \Rightarrow z_i = \frac{d_i}{s_i} \Rightarrow w = Vz \end{aligned} \tag{4.11}$$

The d_i are independent and have errors ± 1. By plotting the values of d_i for all vector elements (or bins if using histograms) the value of i at which d_i becomes insignificant can be seen, as the value will fall below the independent error of ± 1. The exact solution to this system of equations is equivalent to minimising χ^2:

$$\chi^2 \equiv (\tilde{A}w - \tilde{b})^T (\tilde{A}w - \tilde{b}) \tag{4.12}$$

However in this situation it is hard to control bias, and so the condition is introduced that the solution is smooth, by introducing an extra term:

$$\chi^2 \equiv (\tilde{A}w - \tilde{b})^T(\tilde{A}w - \tilde{b}) + \tau(Cq)^T Cw \tag{4.13}$$

Cw is chosen such that

$$(Cw)^T Cw = \Sigma[(w_{i+1} - w_i) - (w_i - w_{i-1})]^2 \tag{4.14}$$

This produces a new linear system

$$\begin{bmatrix} \tilde{A} \\ \sqrt{\tau} \cdot C \end{bmatrix} w = \begin{bmatrix} \tilde{b} \\ 0 \end{bmatrix}. \tag{4.15}$$

Where τ is the regularisation parameter. For $\tau = 0$, Eqn. 4.15 is the same as Eqn. 4.10 and can be solved by SVD. However, for $\tau \neq 0$ the solution is given by

$$z_i^{(\tau)} = \frac{d_i}{s_i} . \frac{s_i^2}{s_i^2 + \tau} \tag{4.16}$$

The value of τ to be chosen, that will remove wildly oscillating contributions should be $\tau \simeq s_k^2$ where k is the index of the last significant d, found as mentioned above by plotting the values of d_i.

4.2.5 Systematics

The potential sources of systematic uncertainties are introduced here, and their effects on the scattering measurements will be studied in more detail for each configuration in their individual sections.

PID

Tracking through fields is reliant on particle mass and a muon is assumed. As such impurities in the beam will result in errors in the scattering distributions. An estimate for the systematic error due to these impurities can be obtained by re-running the analysis with less stringent PID settings, resulting in a less pure muon sample, and then comparing the resulting differences between the bin contents in the scattering distributions.

Density of LiH

The density of the LiH used in MICE was studied in [60], and measured to be 0.65 ± 0.16 gcm^{-3}, which is an uncertainty of 24.6%. A change in density is equivalent to a change in thickness of the absorber (while keeping the density constant) so the degree of uncertainty this introduces can be found by re-running the Monte Carlo simulations and analysis with a 24.6% increase and decrease in the absorber thickness, taking the error to be half of the difference between the maximum and minimum scattering values.

Kalman Scattering

As the momentum vectors at the trackers used for the analysis are determined by a Kalman fit, which itself uses the Highland formula to account for scattering in the fibres of the tracker. It was necessary to determine if this would effect the scattering measurement. This has been done by halving the radiation length used by the Kalman, which would increase the scattering angle obtained from the Highland formula, and performing again the simulations from Section 4.2.2. Doing so resulted in no change in the raw reconstructed scattering distributions, and so this is not a source of systematic uncertainty.

Time of Flight Selection

This is of particular importance for the field off measurement, as the Kalman fitter in the tracker reconstruction cannot reconstruct p_z, and so a default value is assumed. This default value should be matched to the equivalent time of flight of the particles. Although both the data and field off Monte Carlo particles are meant to have a nominal momentum of 200 MeV/c at the absorber, and so should have similar time of flight distributions, there is actually a discrepancy, as shown in Figure 4.13, with an offset between the data and Monte Carlo peaks greater than 1 ns.

Accordingly, it is necessary to select out a particular TOF range, and find the new default value of the momentum to be used by Kalman. A plot of time of flight against the true momentum in the upstream tracker is shown in Figure 4.14, from which it can be seen that a default value of 175 MeV/c should be used, as the majority of muons in the Monte Carlo have momenta around this value, which would correspond to a time of flight of 32.5 ns.

The systematic error due to the time of flight is then calculated in much the same way as that for the LiH density, by increasing/decreasing the time of flight window, and then taking the error to be half of the difference between the maximum

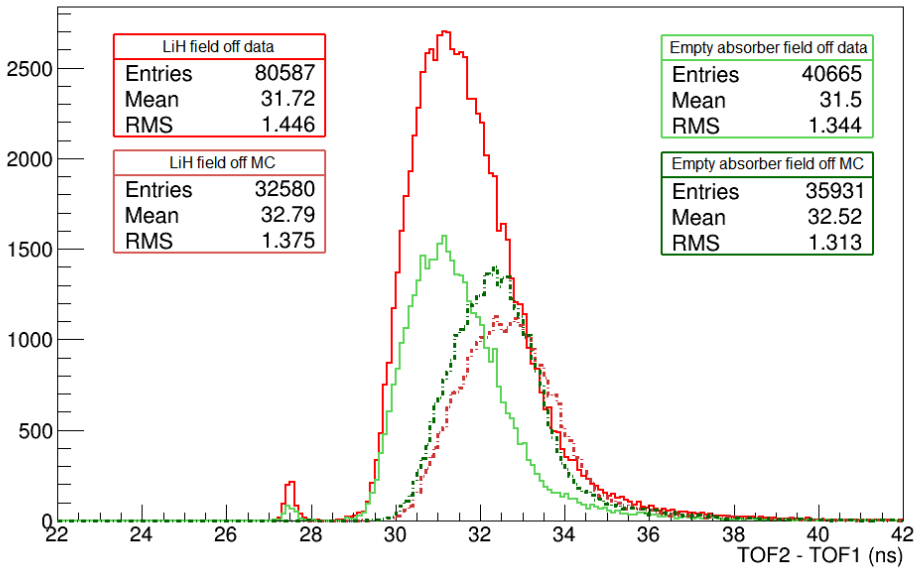

Figure 4.13: Time of flight distributions for the 200 MeV/c muon beams, for data (solid lines) and MC (dashed lines).

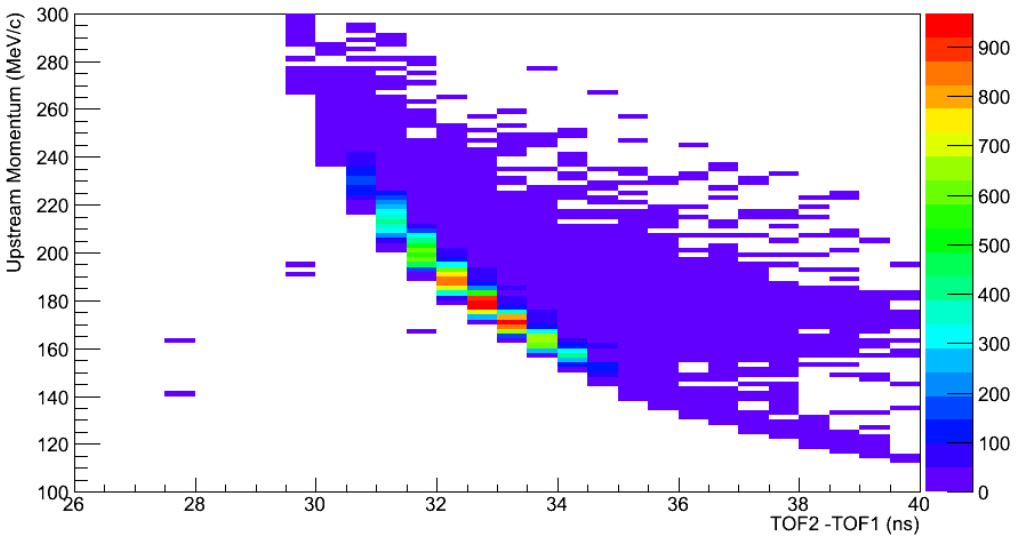

Figure 4.14: Time of flight vs the upstream tracker momentum, for the Monte Carlo muon beams.

and minimum scattering values. The TOF resolution is 60 ps, however for this study we will purposefully overestimate the effect of this on the measured time of flight, and so the time of flight window will be increased/decreased by 120 ps.

Scraping of Particles in the Channel

Particles that scrape the edges of the channel and then scatter back into the beam could affect the scattering measurements. However this can be avoided in the propagation step, as a maximum radius for the propagated particles particles can be set, such that particles that would scrape the edges are omitted from the sample. Performing the simulations with and without the maximum propagation radius shows no change in the number of particles, so this apparently does not remove any particles from the sample, which is likely due to another condition placed on the beam that it must pass through the radius of the absorber, which is 150mm, and so any particles that pass through the absorber are unlikely to scatter away from the beam centre and back in before reaching the absorber.

4.2.6 Predictions of θ_0 and θ_{3D} from PDG Equations

Before continuing, it is useful to note what the predicted values for the RMS of the scattering distributions would be based upon Eqn. 4.1 and Eqn. 4.2. These are shown in Table 4.3 for 200 MeV/c helical tracks and 175 MeV/c straight tracks. For the sake of these estimates, the thickness of the absorber windows is assumed to be the minimal value (0.18 mm), which should make these predictions too small, as not enough aluminium is included. However comparing the values in Table 4.3 with the truth values from Table 4.2 for the raw distributions shows that the PDG equations overestimates the RMS values of θ_{3D}^{RMS}, which Eqn. 4.1 shows should be larger than θ_0^{RMS}, but this is not seen in the Monte Carlo, which shows that the PDG approximation and the Wentzel-VI scattering model in Geant4 are inconsistent. While some difference between the PDG prediction and the truth values for the helical distributions from Wentzel can be accounted for by corrections to the particle path due to the fields in the channel (as can also be done for θ_0^{RMS}), the same argument cannot hold for the PDG prediction of θ_{3D}^{RMS} for field off scattering through LiH, for which the PDG prediction is almost twice the value obtained from the Wentzel model. The apparent underestimation here of θ_0^{RMS} for straight, field off tracks can be accounted for by the minimal window width used in the calculation.

	PDG θ_{3D}^{RMS} (mrad)	PDG θ_{0}^{RMS} (mrad)
Straight MC empty	19.5	13.8
Straight MC LiH	33.7	23.8
Helical MC empty	16.5	11.7
Helical MC LiH	28.5	20.2

Table 4.3: Predicted values of θ_0^{RMS} and θ_{3D}^{RMS} for helical (200 MeV/c) and straight (175 MeV/c) tracks for an empty and a LiH absorber.

4.3 Field-Off Measurement

4.3.1 Particle selection

As mentioned above, for the field off measurement the tracker reconstruction cannot reconstruct the longitudinal momentum, and so a default value is used. Because of the distributions shown in Figure 4.13, a time of flight window of 30-36 ns was used, to coincide with the Monte Carlo peaks. A narrower window could not be used as this would reduce the statistics of the sample too dramatically. The same window was used for both Monte Carlo and data beams.

4.3.2 Systematics

The effect of the sources of systematic errors on the RMS of the scattering distributions are summarised here. More detailed information, on a bin-by-bin basis, is given in the tables in Appendix B.

The thickness of the LiH and the time of flight windows were varied as described in Section 4.2.5. The PID settings were releaxed such that the allowed ranges of the PID variable values were set to their maximum, and the analysis performed again. The change in PID settings resulted in a reduction in muon purity of 0.0139%, and a loss in the muon sample size of 11% for the Monte Carlo beam. The systematic errors due to these changes are shown in Table 4.4 and Table 4.5 for straight Monte Carlo and data tracks respectively, and combined in quadrature to give the combined error.

4.3.3 Analysis

Presented below are the results of performing the unfolding on the reconstructed distributions. The distributions of the scattering angles are shown in Figures 4.15 - 4.20. Tables 4.6 - 4.12 summarise the RMS values of the scattering distributions. The errors quoted are systematic and statistical combined. Across all plots, the

	θ_X Sys. error (mrad)		θ_Y Sys. error (mrad)		θ_{3D} Sys. error (mrad)	
Source of error	Straight MC empty	Straight MC LiH	Straight MC empty	Straight MC LiH	Straight MC empty	Straight MC LiH
TOF	0.025	0.040	0.040	0.15	0.0085	0.0050
LiH density		0.090		0.065		0.15
PID	0.45	0.28	0.48	0.50	0.18	0.090
Combined error	0.45	0.30	0.48	0.53	0.18	0.18

Table 4.4: Summary of systematic errors for both an empty and LiH absorber, for straight MC tracks.

	θ_X Sys. error (mrad)		θ_Y Sys. error (mrad)		θ_{3D} Sys. error (mrad)	
Source of error	Data empty	Data LiH	Data empty	Data LiH	Data empty	Data LiH
TOF	0.075	0.090	0.080	0.085	0.026	0.015
PID	0.060	0.0050	0.040	0.010	0.055	0.050
Combined error	0.096	0.090	0.089	0.086	0.061	0.052

Table 4.5: Summary of systematic errors for both an empty and LiH absorber for data.

reconstructed (data or MC) distributions are represented by red triangles, the unfolded distributions by blue squares, and the Monte Carlo distribution by empty circles.

As discussed previously, the unfolding of data is done using the SVD method in RooUnfold. As this requires a training sample with which to fill the response matrices that is statistically and systematically independent of the data being unfolded, the same Monte Carlo input that was used in Chapter 3 to produce the probability density functions for the PID was used as the training sample, as the Monte Carlo settings were tuned to match the beam to be studied. The only time response matrices from the MC samples to be unfolded were used was to check that it was possible to recover the MC distributions by unfolding against their own response matrices.

Empty Absorber, MC data

The RMS of the scattering angle distributions for straight MC tracks through an empty absorber are summarised in Table 4.6, and the distributions are shown in Figure 4.15. The results are broken down by bin in Table B.4 for the projected angles and in Table B.7 for θ_{3D} in Appendix B.

From both the table and the figure, it can be seen that the unfolding of the reconstructed Monte Carlo, against a statistically and systematically independent training sample, has successfully removed the effects of the measurement resolution, returning a distribution that is in excellent agreement with the Monte Carlo distributions.

	θ_{3D}^{RMS} (mrad)	θ_{X}^{RMS} (mrad)	θ_{Y}^{RMS} (mrad)
Reconstructed	8.09 ± 0.19	13.3 ± 0.46	13.7 ± 0.48
Unfolded	8.01 ± 0.19	11.9 ± 0.46	12.3 ± 0.48
Monte Carlo	8.01 ± 0.05	11.9 ± 0.1	12.3 ± 0.1

Table 4.6: Summary of scattering distributions for an empty channel in the absence of fields for reconstructed MC and unfolded distributions, and for Monte Carlo truth. Systematic and statistical errors combined for reconstructed and unfolded results, statistical only for Monte Carlo.

LiH Absorber, MC data

The RMS of the scattering angle distributions for straight MC tracks through a LiH absorber are summarised in Table 4.7, and the distributions are shown in Figure

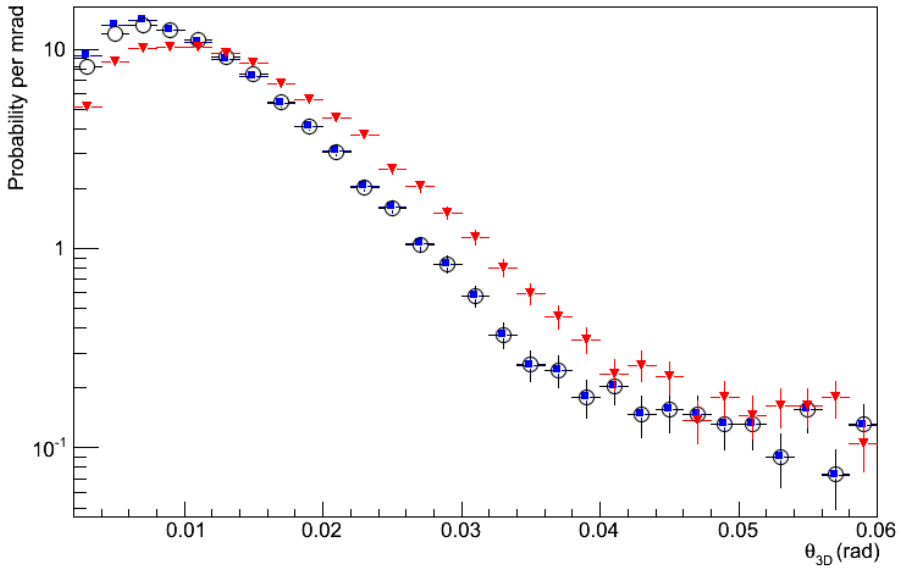

(a) 3D space angle

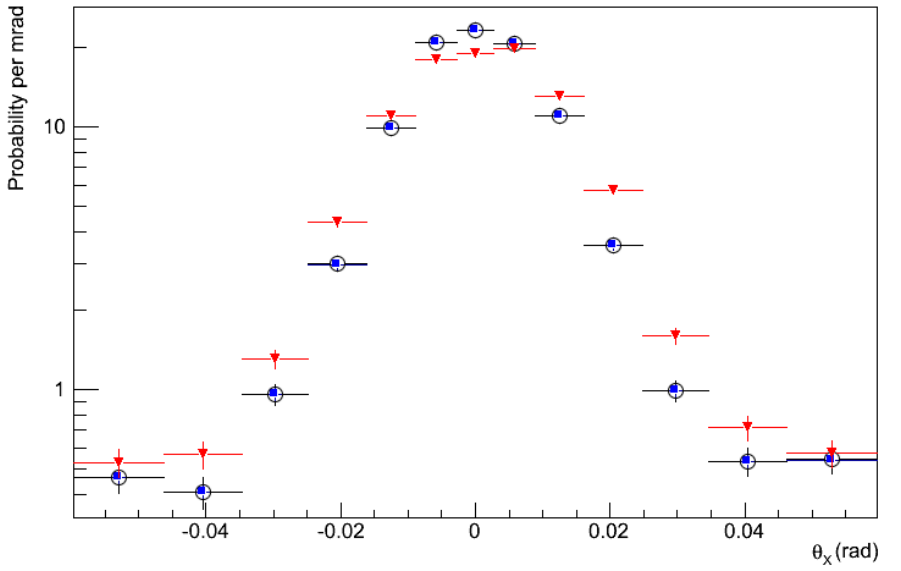

(b) Projected angle

Figure 4.15: Reconstructed MC (red triangles), unfolded (blue quares) and Monte Carlo (empty circles) distributions of the 3D space and projected scattering angles, for an empty channel in the absence of fields. Only statistical errors shown.

4.16. The results are broken down by bin in Table B.10 for the projected angles and in Table B.14 for θ_{3D} in Appendix B.

The RMS values of the distributions given in Table 4.7 indicate that the unfolding of the reconstructed Monte Carlo has successfully removed the effects of the measurement resolution, returning a distribution that is in excellent agreement with the Monte Carlo distributions. However it should be noted that in Figure 4.16, at angles less than 0.01 mrad, the agreement does worsen slightly, although the unfolded and Monte Carlo points do agree within errors.

	θ_{3D}^{RMS} (mrad)	θ_{X}^{RMS} (mrad)	θ_{Y}^{RMS} (mrad)
Reconstructed	12.9 ± 0.2	20.1 ± 0.3	20.0 ± 0.3
Unfolded	12.5 ± 0.2	21.0 ± 0.1	20.8 ± 0.2
Monte Carlo	12.5 ± 0.1	21.0 ± 0.1	20.8 ± 0.2

Table 4.7: Summary of scattering distributions for a LiH absorber in the absence of fields for reconstructed and unfolded distributions, and for Monte Carlo truth. Systematic and statistical errors combined for reconstructed and unfolded results, statistical only for Monte Carlo.

Conclusions

The field off Monte Carlo studies have shown that the measurement and unfolding methods used are effective at removing the effects of the measurement resolution from the reconstructed distributions, returning 'true' distributions that are in excellent agreement with the Monte Carlo upon which the reconstruction was performed. The use of a statistically and systematically independent training sample in the unfolding ensures that the unfolding procedure is robust. The performance of the procedure demonstrates its validity for use when unfolding real data distributions.

It is also clear from comparing Table 4.6 and Table 4.7 with Table 4.3 that the the PDG equation overestimates the RMS values of both the projected and space scattering angles.

Empty Absorber, data

The data distributions were unfolded using the same training sample and unfolding settings as was used to unfold the Monte Carlo data. The RMS of the scattering angle distributions for data tracks through an empty absorber are summarised in Table 4.8, and the distributions are shown in Figure 4.17. The Monte Carlo distributions for the same beam are shown for comparison. The results are broken down

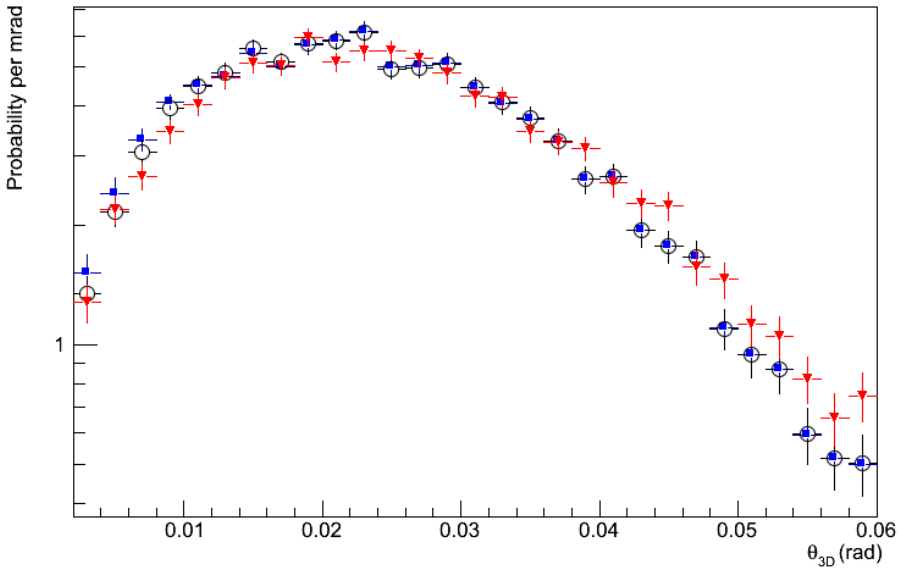

(a) 3D space angle

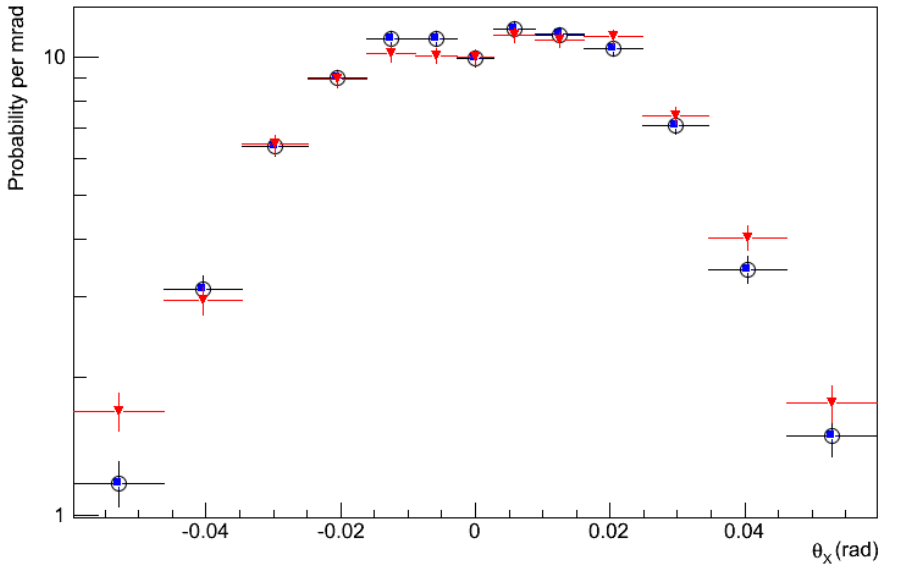

(b) Projected angle

Figure 4.16: Reconstructed MC (red triangles), unfolded (blue squares) and MC (empty circles) distributions of the 3D space and projected scattering angles, for the LiH absorber in the absence of fields. Only statistical errors shown.

by bin in Table B.4 for the projected angles and in Table B.7 for θ_{3D} in Appendix B.

At small angles (less than 0.03 mrad) there is reasonably good agreement between the unfolded distribution and the distribution of the Geant4 simulation of the same beam for $\theta^R_{3D}MS$. Beyond that however the distributions start to diverge, with the Wentzel-VI model underestimating the population at larger angles, and from Table 4.8 it can be seen that the scattering distibution of the unfolded data is wider than the distribution of the model.

This underestimation of scattering in the tails in MC compared to that measured for the data is also seen in Figure 4.17b. This is the opposite of what was seen in MuScat, where they found that the Urban scattering implementation in Geant4 tended to overestimate the population of the tails. A possible reason for this contradiction is due to the change in scattering models used. Back when MuScat published [51], the Urban scattering model was based on Lewis theory, whereas now Wentzel-VI is specifically designed for the simulation of muons and hadrons and combines multiple scattering and single scatters [46].

The values of θ^{RMS}_X and θ^{RMS}_Y are close to those predicted by the PDG equation, although θ^{RMS}_{3D} continues to be much smaller than predicted.

	θ^{RMS}_{3D} (mrad)	θ^{RMS}_X (mrad)	θ^{RMS}_Y (mrad)
Reconstructed	9.45 ± 0.09	14.5 ± 0.1	14.7 ± 0.1
Unfolded	8.42 ± 0.09	13.1 ± 0.1	13.5 ± 0.1
Monte Carlo	8.01 ± 0.05	11.9 ± 0.1	12.3 ± 0.1

Table 4.8: Summary of scattering distributions for an empty absorber in the absence of fields for data and unfolded distributions. Systematic and statistical errors combined for reconstructed and unfolded results, statistical only for Monte Carlo.

LiH Absorber, data

The RMS of the scattering angle distributions for data tracks through a LiH absorber are summarised in Table 4.9, and the distributions are shown in Figure 4.18. The Monte Carlo distributions for the same beam are shown for comparison. The results are broken down by bin in Table B.10 for the projected angles and in Table B.14 for θ_{3D} in Appendix B. As with the Figure 4.18a, below 0.01 mrad, for θ^{RMS}_{3D} the Monte Carlo underestimates the population at smaller angles (although still within errors). It also underestimates the populations above 0.05 mrad. Figure 4.18b also shows discrepancies between the data and Monte Carlo distributions. There appears

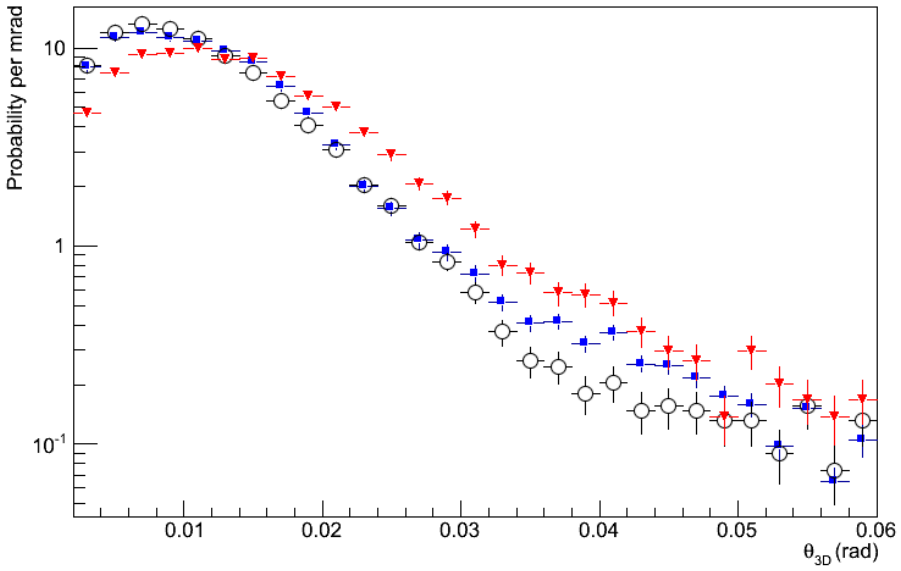

(a) 3D space angle

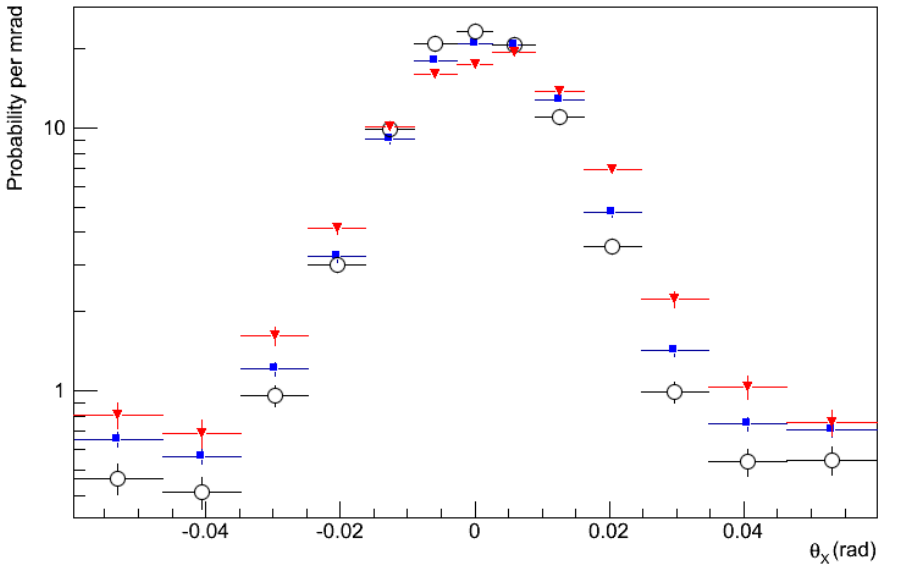

(b) Projected angle

Figure 4.17: Raw data (red triangles), unfolded (blue squares) and MC (empty circles) distributions of the 3D space and projected scattering angles, for an empty channel in the absence of fields. Only statistical errors shown.

to be a slight postive offset between the data and the Monte Carlo, as at angles less than 0.011 the Monte Carlo overestimates the population of the angular bins, and above 0.011 it underestimates the populations. The widths of the data distributions are again larger than those from the Wentzel-VI model. And again, all of the RMS values are overestimated by the PDG equation.

	θ_{3D}^{RMS} (mrad)	θ_{X}^{RMS} (mrad)	θ_{Y}^{RMS} (mrad)
Reconstructed	13.1 ± 0.2	22.0 ± 0.2	21.9 ± 0.1
Unfolded	12.9 ± 0.2	21.4 ± 0.2	21.4 ± 0.1
Monte Carlo	12.5 ± 0.1	21.0 ± 0.1	20.8 ± 0.2

Table 4.9: Summary of scattering distributions for a LiH absorber in the absence of fields for data and unfolded distributions. Systematic and statistical errors combined for reconstructed and unfolded results, statistical only for Monte Carlo.

Conclusions

The scattering angle distributions for straight track data taken by the MICE experiment for both empty and LiH configurations have been unfolded using the previously validated procedure. This has shown that the scattering distributions in the data are wider than those obtained from simulation with Wentzel-VI in MAUS, and has further shown that the PDG equation overestimates the widths of the scattering distributions.

4.4 Field-On Measurement

4.4.1 Systematics

The effect of the sources of systematic errors on the RMS of the scattering distributions are summarised here. More detailed information, on a bin-by-bin basis, is given in the tables in Appendix B.

As with the field off measurement, the thickness of the LiH was varied as described in Section 4.2.5. The PID settings were releaxed such that the allowed ranges of the PID variable values were set to their maximum, and the analysis performed again. The change in PID settings resulted in a reduction in muon purity upstream of 0.02% and downstream of 3.6%. The systematic errors due to these changes are show in Table 4.10 and combined in quadrature to give the combined error.

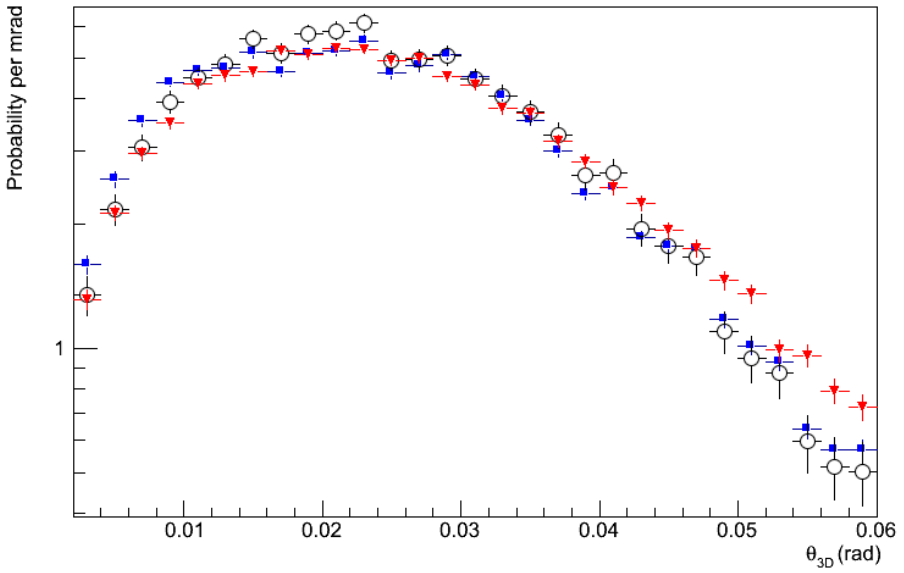

(a) 3D space angle

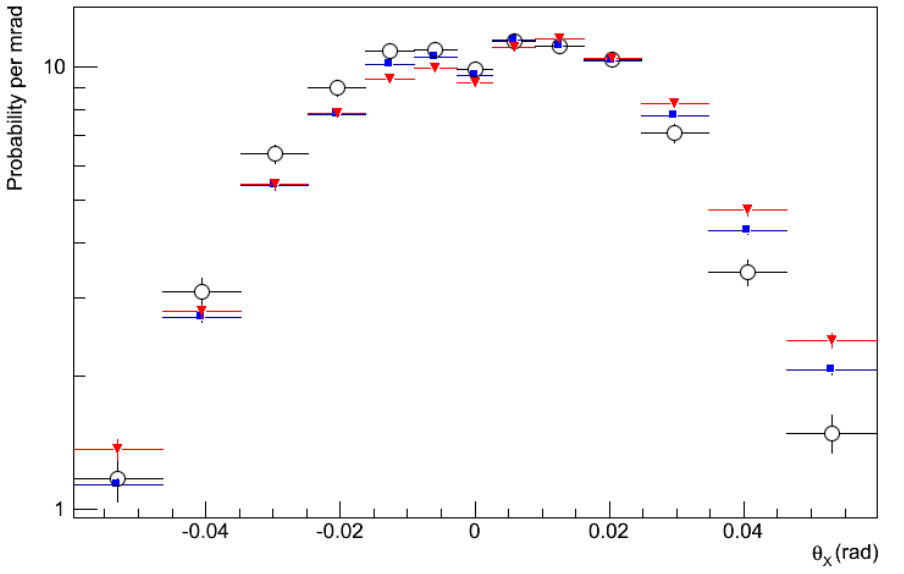

(b) Projected angle

Figure 4.18: Raw data (red triangles), unfolded (blue squares) and MC (empty circles) distributions of the 3D space and projected scattering angles, for a LiH absorber in the absence of fields. Only statistical errors shown.

	θ_X Sys. error (mrad)		θ_Y Sys. error (mrad)		θ_{3D} Sys. error (mrad)	
Source of error	Helical MC empty	Helical MC LiH	Helical MC empty	Helical MC LiH	Helical MC empty	Helical MC LiH
LiH density		0.045		0.030		0.055
PID	0.0060	0.010	0.0060	0.010	0.0060	0.0010
Combined error	0.0060	0.046	0.006	0.032	0.0060	0.055

Table 4.10: Summary of systematic errors for both an empty and LiH absorber, for helical MC tracks.

4.4.2 Analysis

Empty Absorber, MC data

The RMS of the scattering angle distributions for helical MC tracks through an empty absorber are summarised in Table 4.11, and the distributions are shown in Figure 4.19. The results are broken down by bin in Table B.17 for the projected angles and in Table B.20 for θ_{3D} in Appendix B.

From both the table and the figure, it can be seen that the unfolding of the reconstructed Monte Carlo has successfully removed the effects of the measurement resolution, and for θ_X has removed the systematic offset, returning a distribution that is in excellent agreement with the Monte Carlo distributions.

	θ_{3D}^{RMS} (mrad)	θ_{X}^{RMS} (mrad)	θ_{Y}^{RMS} (mrad)
Reconstructed	9.03 ± 0.03	12.6 ± 0.1	12.5 ± 0.1
Unfolded	5.18 ± 0.17	6.31 ± 0.15	6.34 ± 0.19
Monte Carlo	5.18 ± 0.02	6.31 ± 0.02	6.34 ± 0.02

Table 4.11: Summary of scattering distributions for an empty channel in the presence of fields. Systematic and statistical errors combined for reconstructed and unfolded results, statistical only for Monte Carlo.

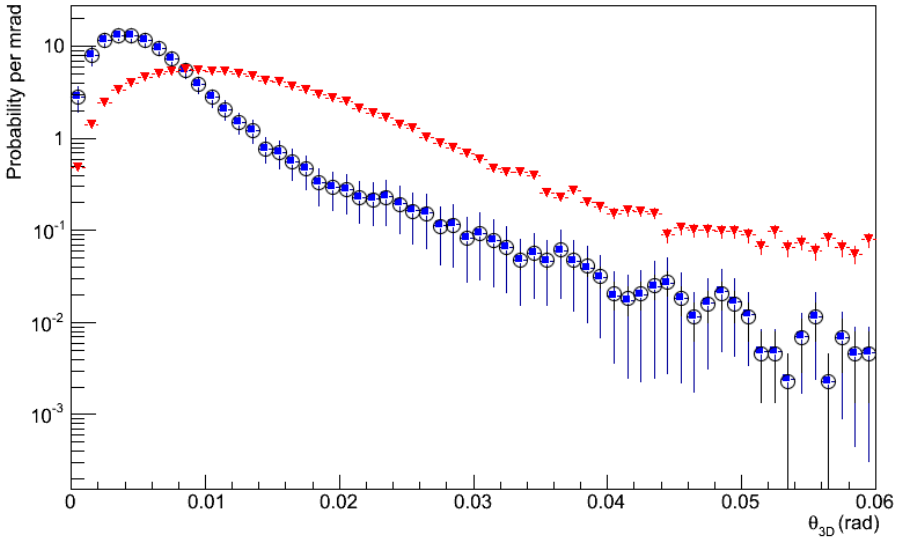

(a) 3D space angle

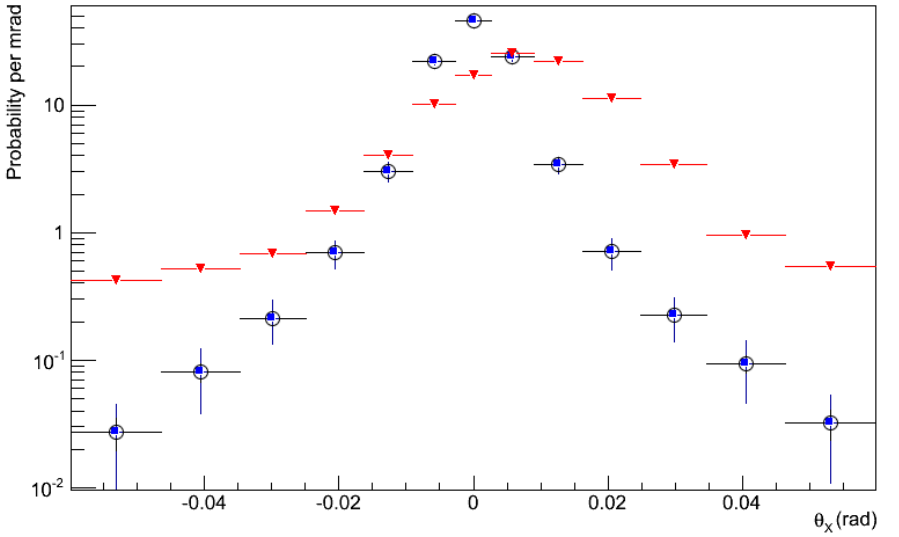

(b) Projected angle

Figure 4.19: Reconstructed MC (red triangles), unfolded (blue squares) and MC (empty circles) distributions of the 3D space and projected scattering angles, for a LiH absorber in the presence of fields. Only statistical errors shown.

	θ_{3D}^{RMS} (mrad)	θ_{X}^{RMS} (mrad)	θ_{Y}^{RMS} (mrad)
Reconstructed	12.5 ± 0.1	20.1 ± 0.1	20.0 ± 0.1
Unfolded	11.2 ± 0.1	17.3 ± 0.1	17.3 ± 0.1
Monte Carlo	11.2 ± 0.1	17.3 ± 0.1	17.3 ± 0.1

Table 4.12: Summary of scattering distributions for a LiH absorber in the presence of fields. Systematic and statistical errors combined for reconstructed and unfolded results, statistical only for Monte Carlo.

LiH Absorber, MC data

The RMS of the scattering angle distributions for helical MC tracks through a LiH absorber are summarised in Table 4.12, and the distributions are shown in Figure 4.20. The results are broken down by bin in Table B.23 for the projected angles and in Table B.26 for θ_{3D} in Appendix B.

From both the table and the figure, it can be seen that the unfolding of the reconstructed Monte Carlo has successfully removed the effects of the measurement resolution, and for θ_X has removed the systematic offset, returning a distribution that is in excellent agreement with the Monte Carlo distributions.

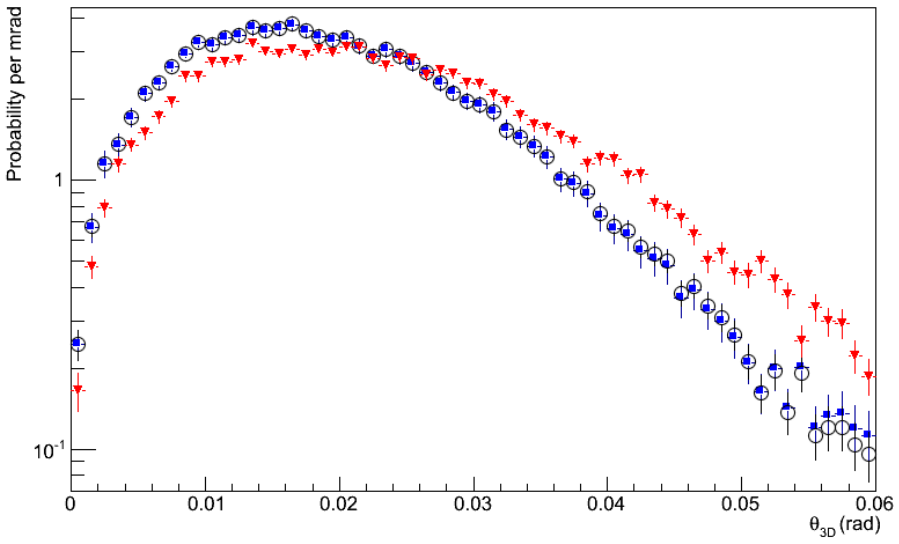

(a) 3D space angle

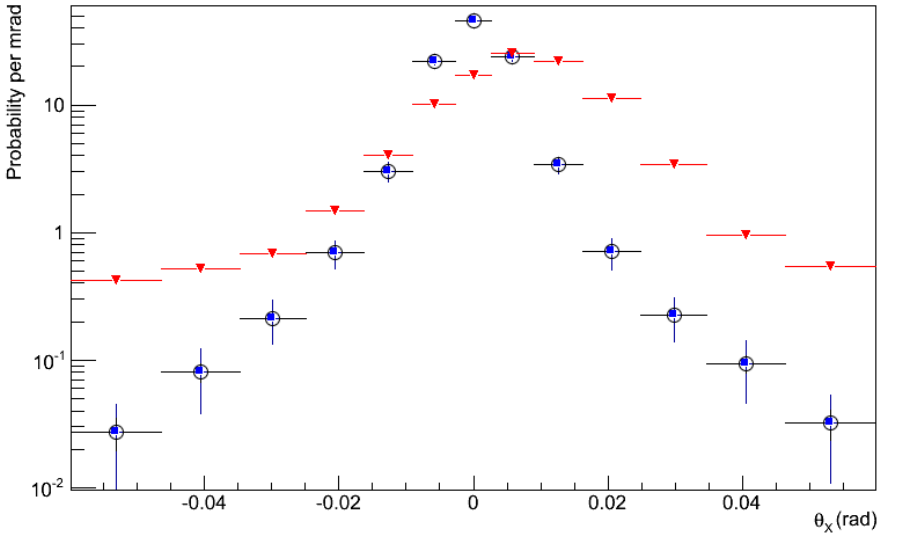

(b) Projected angle

Figure 4.20: Reconstructed MC (red triangles), unfolded (blue squares) and MC (empty circles) distributions of the 3D space and projected scattering angles, for the LiH absorber in the presence of fields. Only statistical errors shown.

Conclusions

As for the field off studies, the field on Monte Carlo studies have shown that the measurement and unfolding methods used are effective at removing the effects of the measurement resolution, and also the systematic offset in θ_X from the reconstructed distributions. It has again been shown in Table 4.6 and Table 4.7 that the the PDG equation overestimates the RMS values of both the projected and space scattering angles.

4.5 Conclusions

An analysis of multiple scattering in MICE has been presented. While the technique itself is intended for use in the presence of magnetic fields in the cooling channel, due to no field on data being available, the procedure has been tested on field off data, and the efficacy of the SVD unfolding has been verified.

The purpose of this analysis was to perform a measurement of the multiple scattering of muons through the MICE LiH absorber, and to compare this measurement with the Wentzel-VI implementation of scattering in Geant4, which effects the analysis and reconstruction of MICE data, and with the PDG approximation, which is integral to the MICE cooling equation.

It has been shown for both unfolded reconstructed Monte Carlo and unfolded data that the PDG approximation overestimates the RMS of the scattering distributions. Conversely, it has also been shown that the Wentzel model underestimates the width of the scattering distributions, in contrast to the results seen in MuScat, which saw an excess of events when using Geant4 with the Lewis based Urban model of multiple scattering.

The immediate next step in this analysis would be to study the field-on data once it has been taken. Another potential area for futher study would be to investigate the discrepancy between the Lewis and Wentzel-VI implementations of multiple scattering in Geant4 in how they describe the behaviour in the tails of the scattering distributions.

Chapter 5

Conclusions

The Muon Ionisation Cooling Experiment (MICE) is a proof of principle experiment, designed to demonstrate and make a measurement of the emittance change of muons due to ionisation cooling through low Z materials, which is an integral technology for the development of a future Neutrino Factory.

Ionisation cooling is influenced by two processes as the muon passes through material; energy loss, which contributes to the cooling of the beam, and multiple Coulomb scattering, which causes heating of the beam. These two processes are represented in the ionisation cooling equation, Eqn. 1.22, described in Section 1.5. The form of the multiple scattering term is based upon an approximation given by the Particle Data Group (PDG), which itself is based upon the Moliere model of scattering, and has not previously been validated for muons. The Wentzel-VI multiple scattering implementation in Geant4 is responsible for modelling scattering in MICE simulations, but this too has not been validated for muons, as MuScat, the only experiment to study the scattering of muons prior to MICE, used an earlier version of Geant4 which used a different implementation of scattering. Accordingly it is necessary to determine the validity of the current implementation of scattering. This is the subject of Chapter 4.

In Chapter 4, the scattering of muons through Lithium Hydride was studied, using an approach designed for use in the case where there are magnetic fields in the cooling channel. This was applied to both field-on Monte Carlo data, and field-off Monte Carlo and real MICE data, which is the only scattering data to have been taken at the time of writing. These studies showed that the PDG approximation is in disagreement with both the scattering models used in the simulation and with the real data itself, which would make it unsuitable for use in the cooling equation. However the actual measurement of emittance (and thus emittance change)

in MICE is independent of the cooling equation, and so this disagreement does not interfere with the measurement MICE aims to make. The studies also showed that Wentzel-VI underestimates the scattering in MICE, contrary to what was seen in MuScat, as Wentzel-VI underestimates the population of events in the tails of the projected scattering angle distributions, which the older scattering implementation overestimated, which is an area that warrants further study.

Given that the aim of MICE is to measure the emittance change in muons, robust and effective particle identification routines are required to minimise contamination of the measurement sample. MICE requires a muon sample purity of greater than 99.9% upstream of the cooling channel. Chapter 3 details the development, validation and use of a Global Particle Identification framework that has been developed for use in the MICE software, for both field off and field on data. Monte Carlo studies have established that the framework is able to achieve the required purity for both the field off case, and for the field on case upstream of the channel, and shown that while the downstream particle identification is still reasonable, there is scope to improve the downstream purity.

Appendix A

Global PID Consistency Plots

A.1 Commissioning Variable Consistency Plots (Monte Carlo)

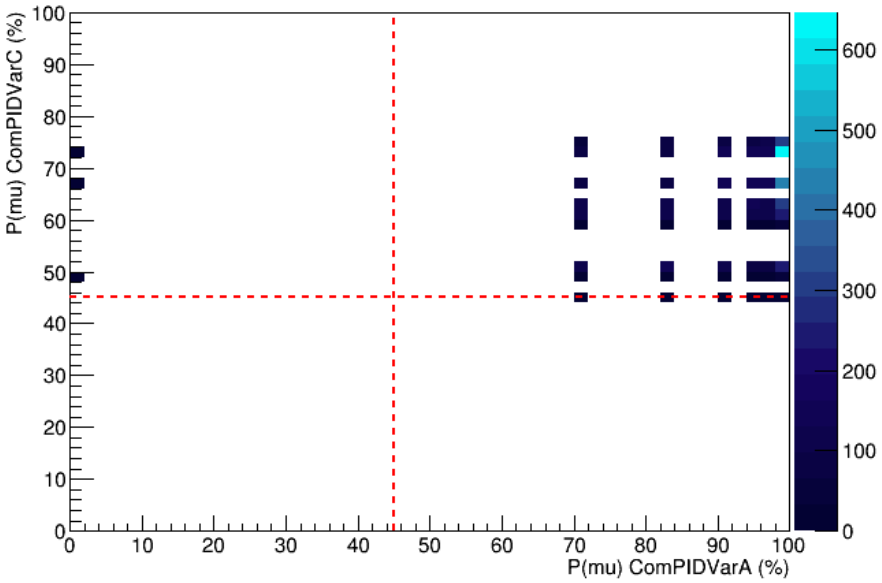

Figure A.1: Comparison of P(μ) returned by ComPIDVarA and ComPIDVarC on MC dataset. For all particles identified by both variables, there was a muon identification consistency of 99.1%.

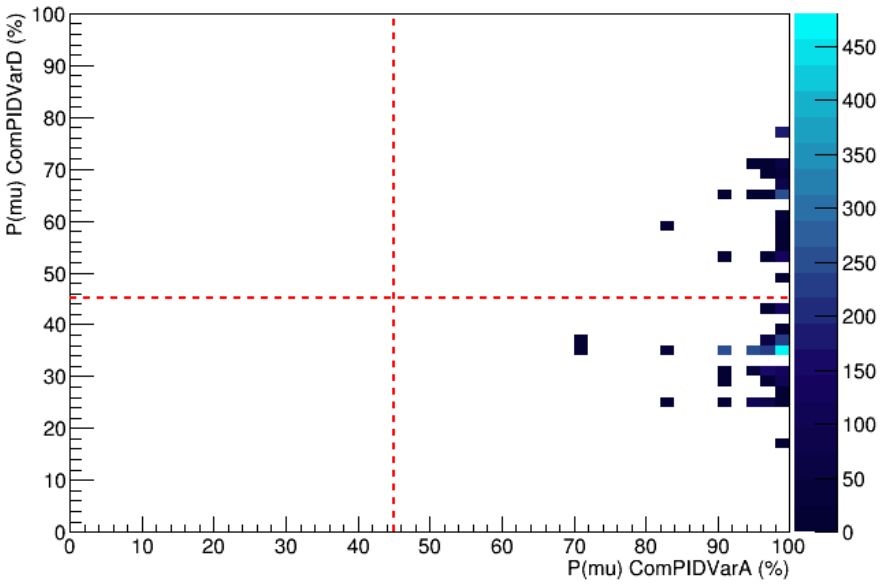

Figure A.2: Comparison of P(μ) returned by ComPIDVarA and ComPIDVarD on MC dataset. For all particles identified by both variables, there was a muon identification consistency of 26.9%.

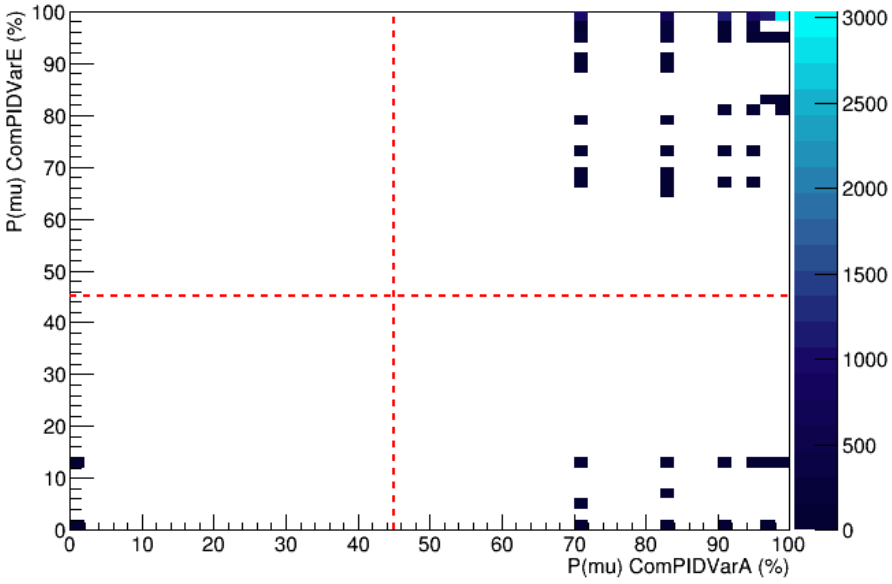

Figure A.3: Comparison of P(μ) returned by ComPIDVarA and ComPIDVarE on MC dataset. For all particles identified by both variables, there was a muon identification consistency of 99.6%.

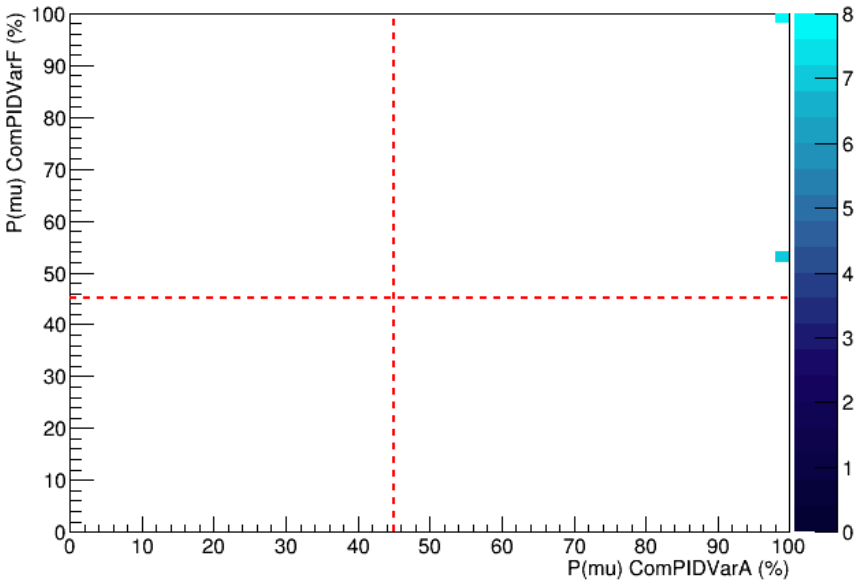

Figure A.4: Comparison of P(μ) returned by ComPIDVarA and ComPIDVarF on MC dataset. For all particles identified by both variables, there was a muon identification consistency of 100%.

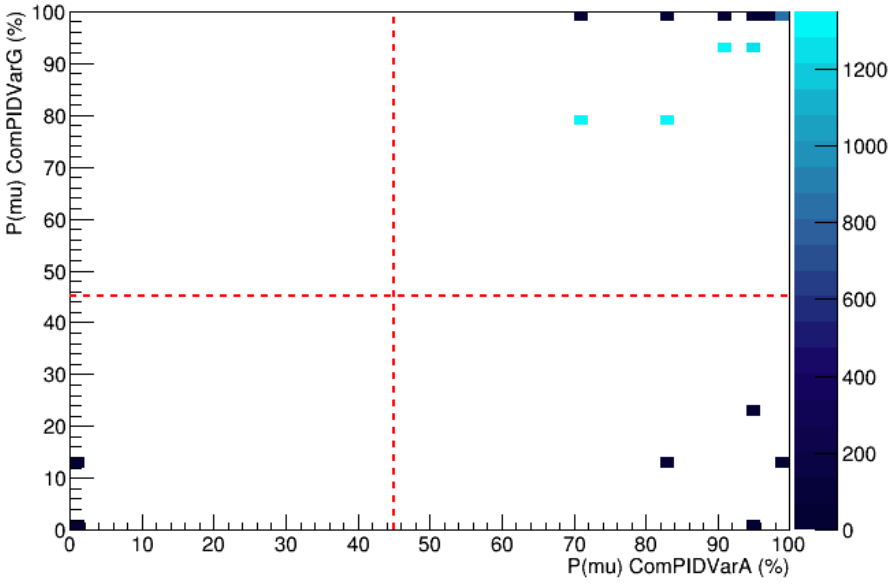

Figure A.5: Comparison of P(μ) returned by ComPIDVarA and ComPIDVarG on MC dataset. For all particles identified by both variables, there was a muon identification consistency of 99.2%.

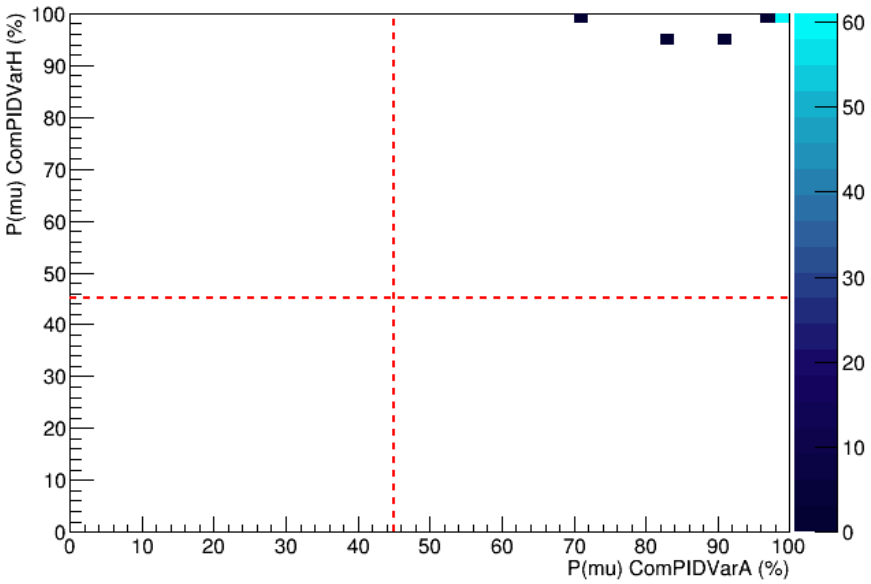

Figure A.6: Comparison of P(μ) returned by ComPIDVarA and ComPIDVarH on MC dataset. For all particles identified by both variables, there was a muon identification consistency of 100%.

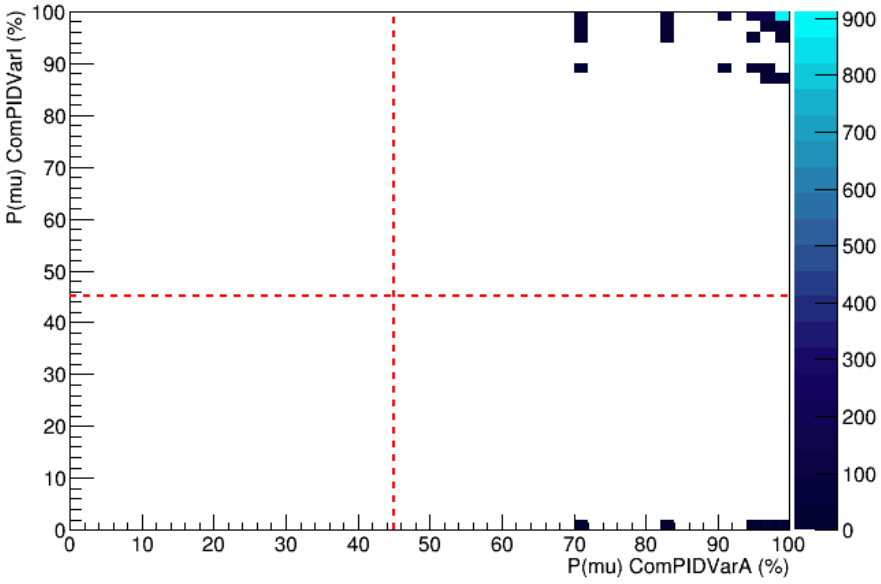

Figure A.7: Comparison of P(μ) returned by ComPIDVarA and ComPIDVarI on MC dataset. For all particles identified by both variables, there was a muon identification consistency of 99.3%

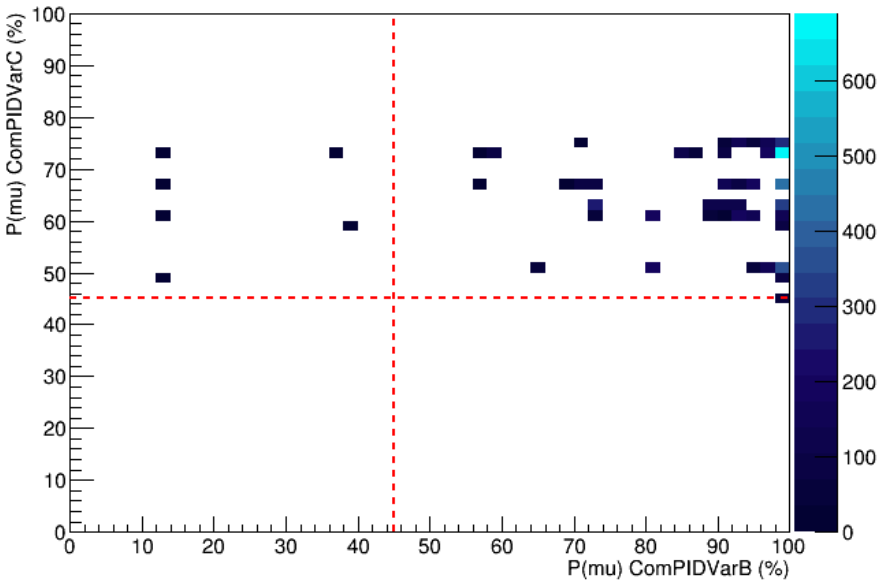

Figure A.8: Comparison of P(μ) returned by ComPIDVarB and ComPIDVarC on MC dataset. For all particles identified by both variables, there was a muon identification consistency of 99.2%.

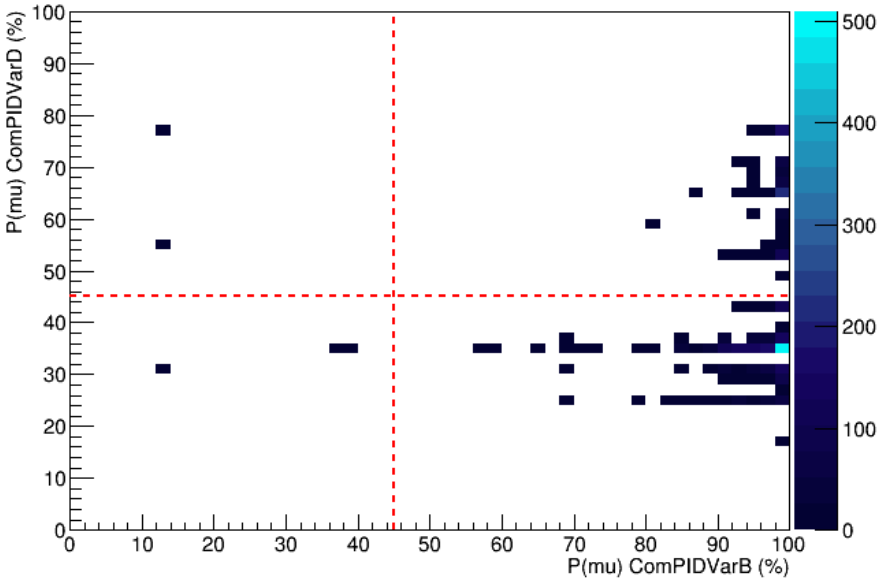

Figure A.9: Comparison of P(μ) returned by ComPIDVarB and ComPIDVarD on MC dataset. For all particles identified by both variables, there was a muon identification consistency of 27.1%.

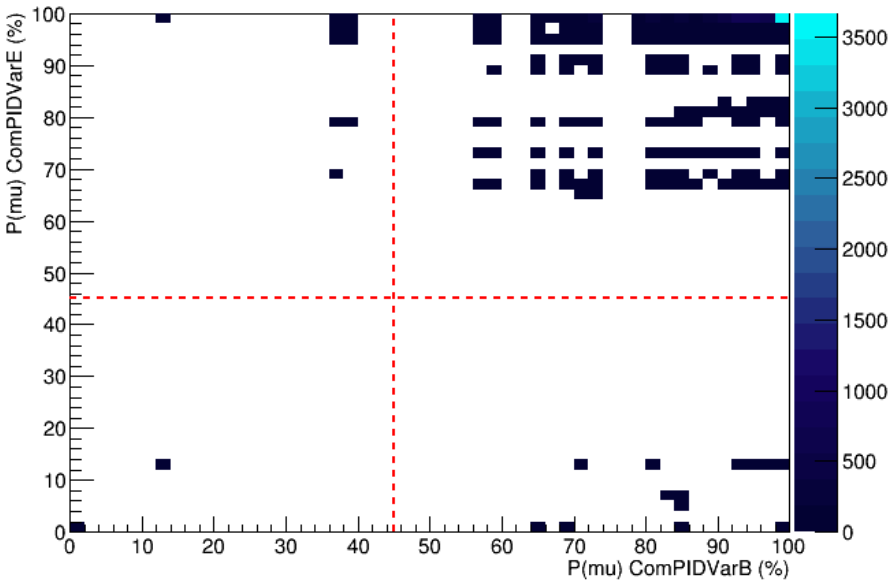

Figure A.10: Comparison of P(μ) returned by ComPIDVarB and ComPIDVarE on MC dataset. For all particles identified by both variables, there was a muon identification consistency of 99.1%.

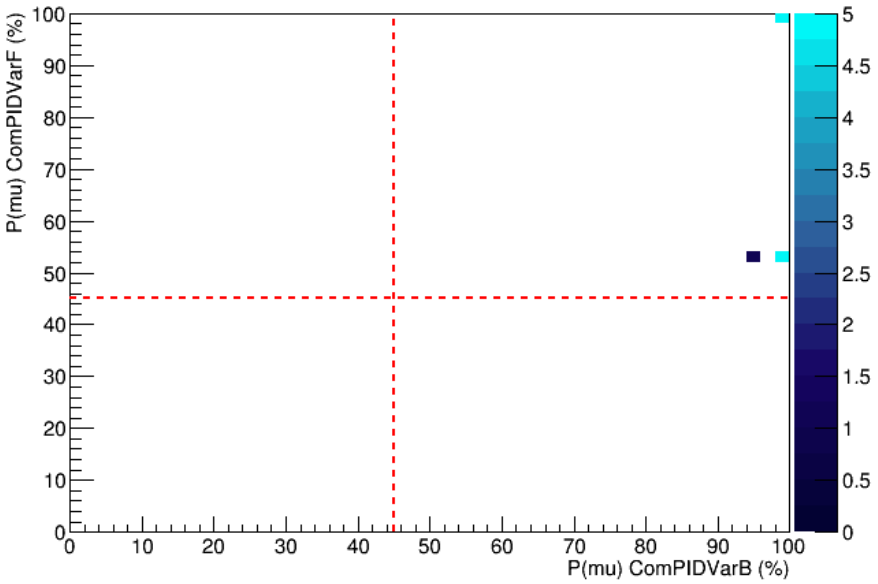

Figure A.11: Comparison of P(μ) returned by ComPIDVarB and ComPIDVarF on MC dataset. For all particles identified by both variables, there was a muon identification consistency of 100%.

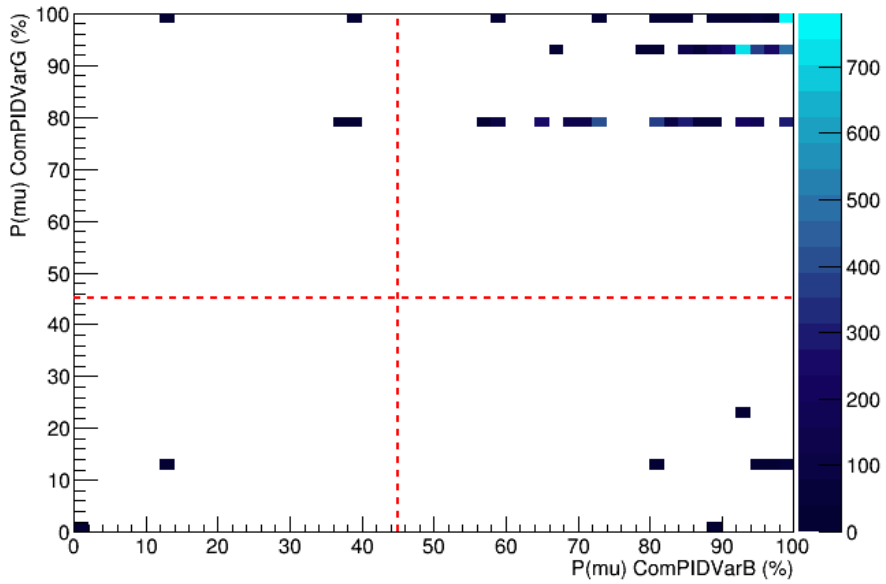

Figure A.12: Comparison of P(μ) returned by ComPIDVarB and ComPIDVarG on MC dataset. For all particles identified by both variables, there was a muon identification consistency of 98.4%.

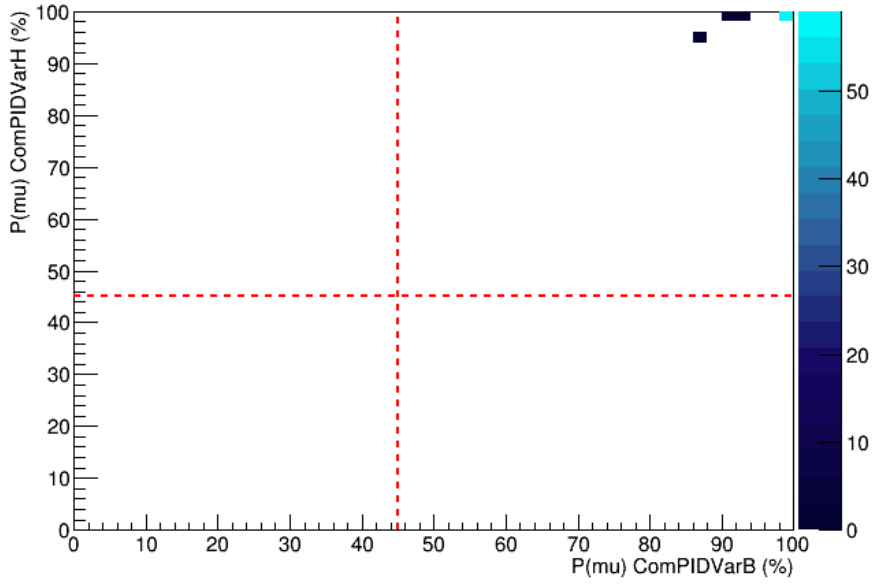

Figure A.13: Comparison of P(μ) returned by ComPIDVarB and ComPIDVarH on MC dataset. For all particles identified by both variables, there was a muon identification consistency of 100%.

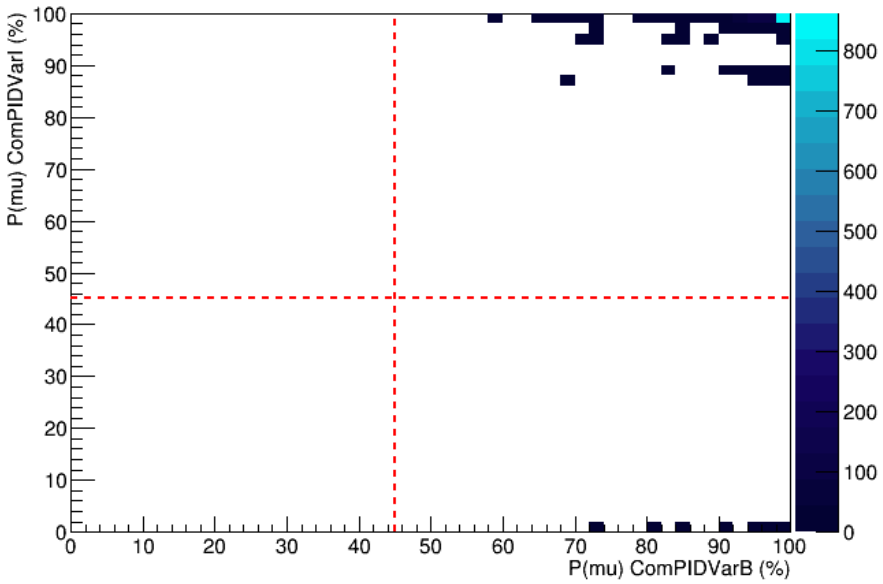

Figure A.14: Comparison of P(μ) returned by ComPIDVarB and ComPIDVarI on MC dataset. For all particles identified by both variables, there was a muon identification consistency of 99.2%.

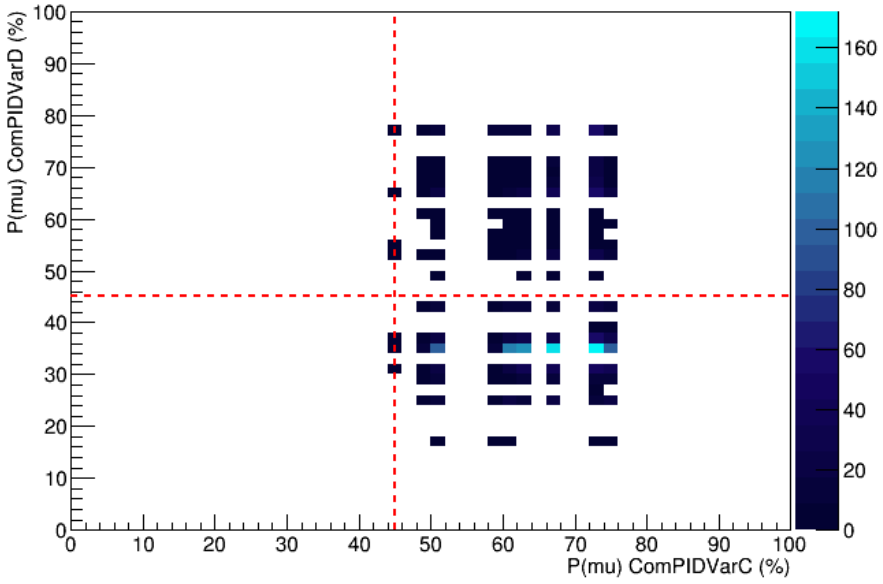

Figure A.15: Comparison of P(μ) returned by ComPIDVarC and ComPIDVarD on MC dataset. For all particles identified by both variables, there was a muon identification consistency of 30.4%.

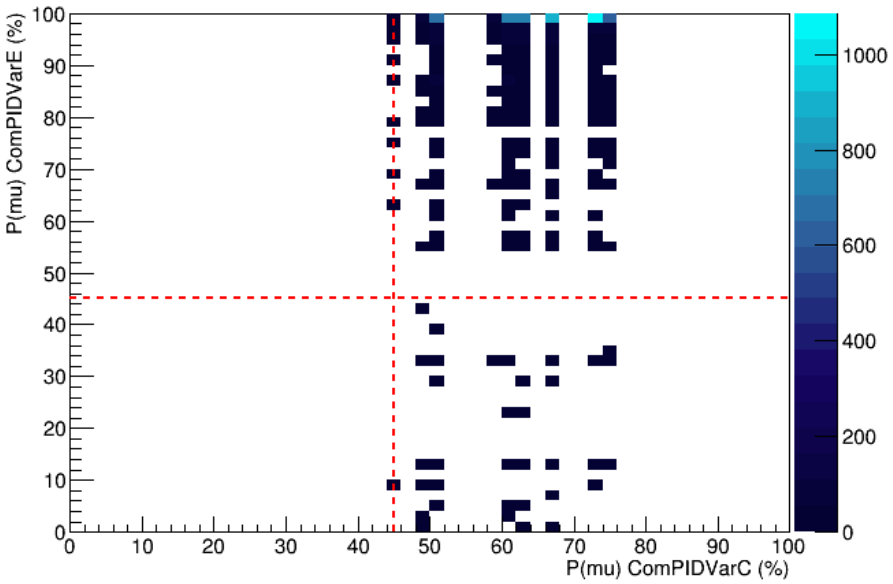

Figure A.16: Comparison of P(μ) returned by ComPIDVarC and ComPIDVarE on MC dataset. For all particles identified by both variables, there was a muon identification consistency of 98.9%.

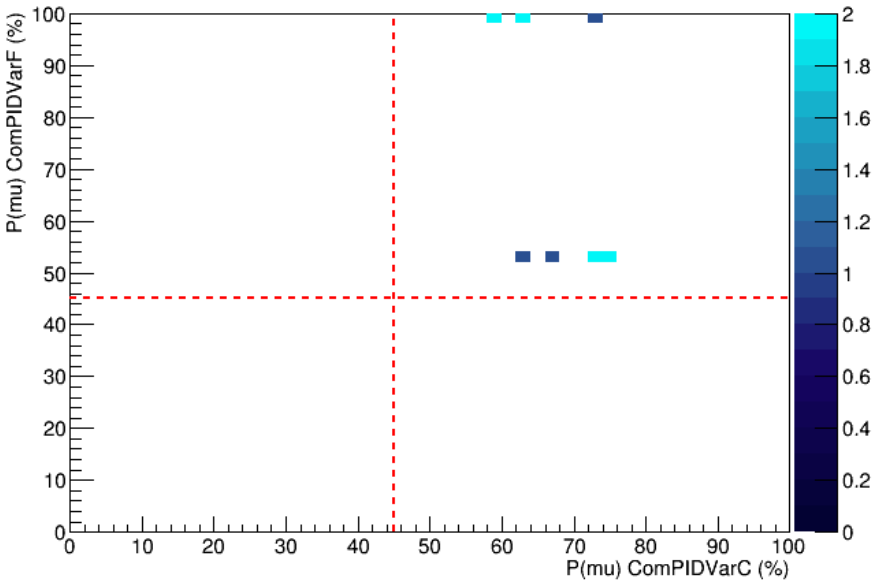

Figure A.17: Comparison of P(μ) returned by ComPIDVarC and ComPIDVarF on MC dataset. For all particles identified by both variables, there was a muon identification consistency of 100%.

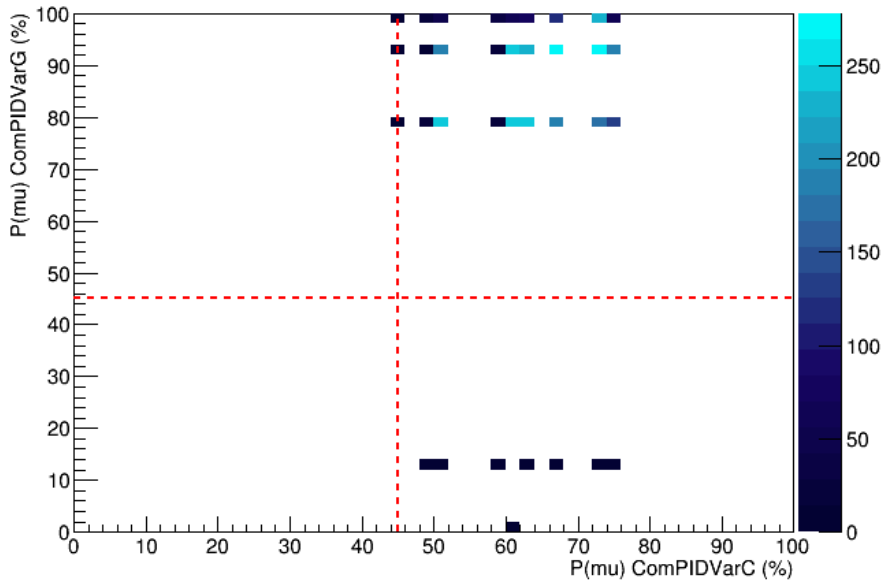

Figure A.18: Comparison of P(μ) returned by ComPIDVarC and ComPIDVarG on MC dataset. For all particles identified by both variables, there was a muon identification consistency of 98.7%.

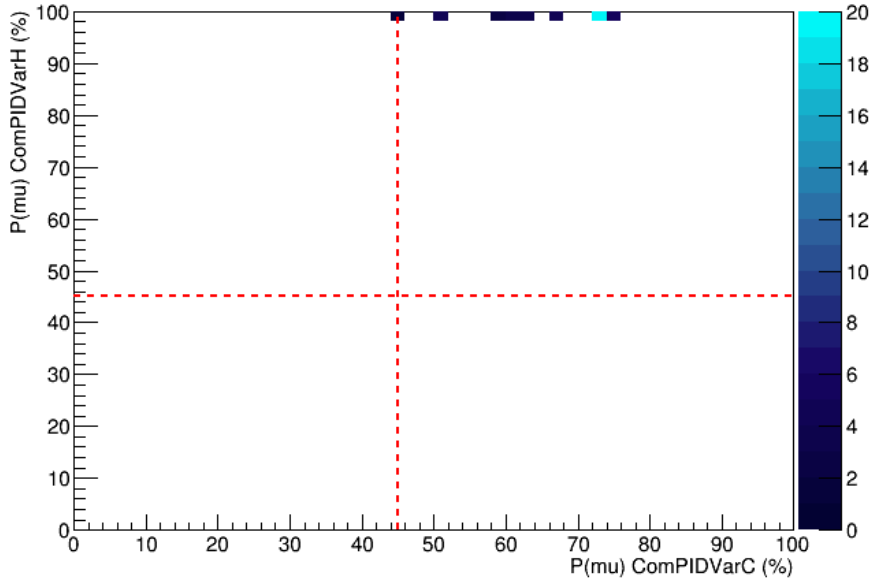

Figure A.19: Comparison of P(μ) returned by ComPIDVarC and ComPIDVarH on MC dataset. For all particles identified by both variables, there was a muon identification consistency of 100%.

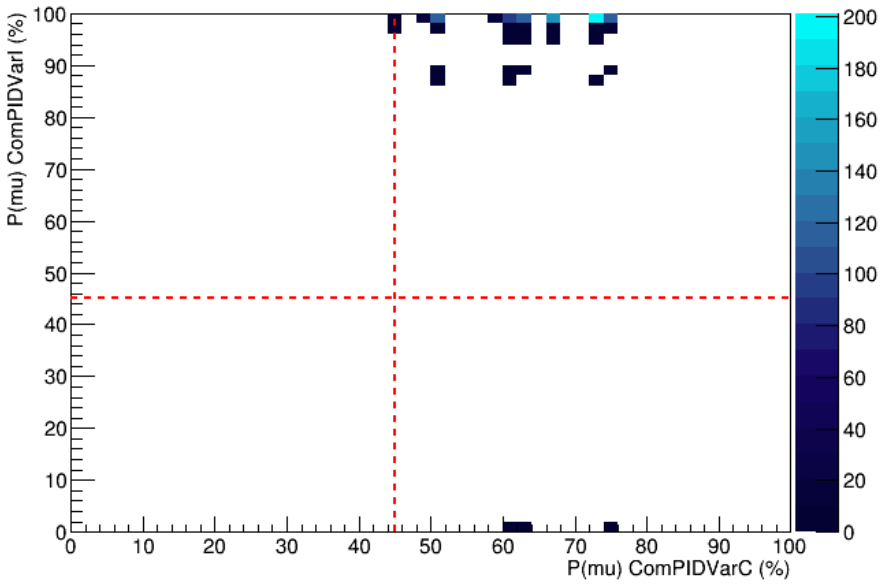

Figure A.20: Comparison of P(μ) returned by ComPIDVarC and ComPIDVarI on MC dataset. For all particles identified by both variables, there was a muon identification consistency of 99.4%.

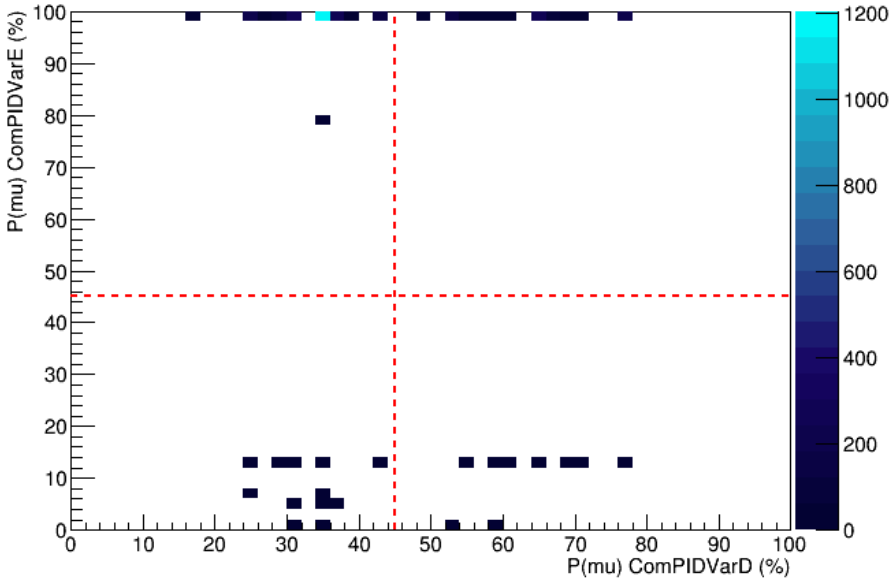

Figure A.21: Comparison of P(μ) returned by ComPIDVarD and ComPIDVarE on MC dataset. For all particles identified by both variables, there was a muon identification consistency of 27.2%.

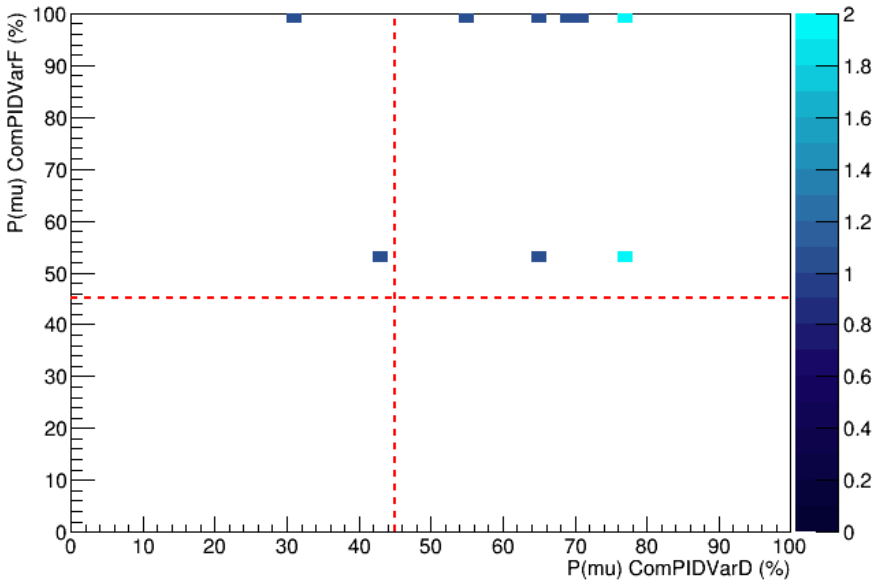

Figure A.22: Comparison of P(μ) returned by ComPIDVarD and ComPIDVarF on MC dataset. For all particles identified by both variables, there was a muon identification consistency of 81.2%.

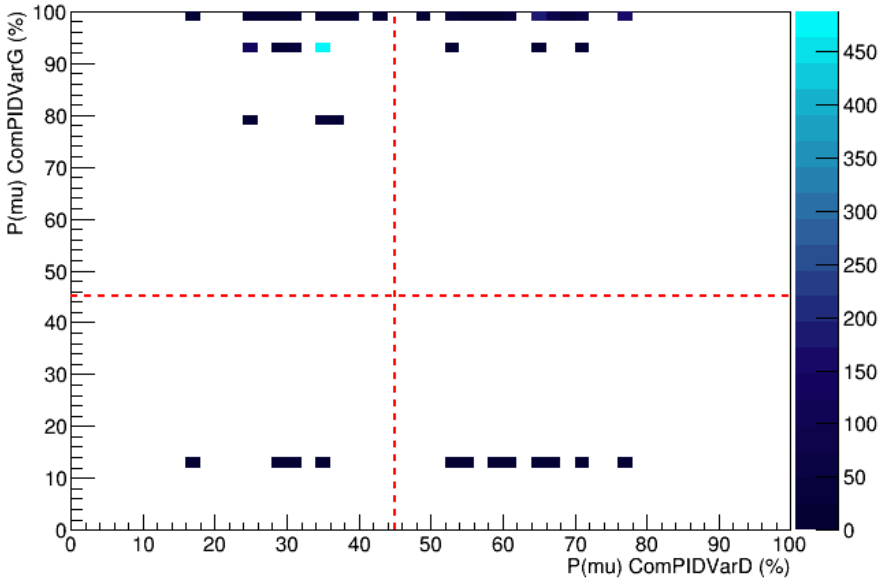

Figure A.23: Comparison of P(μ) returned by ComPIDVarD and ComPIDVarG on MC dataset. For all particles identified by both variables, there was a muon identification consistency of 45.7%.

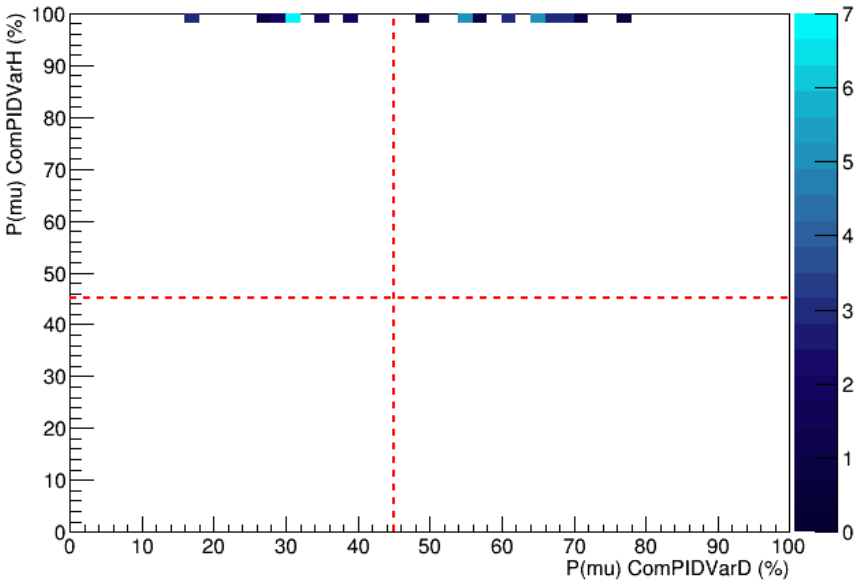

Figure A.24: Comparison of P(μ) returned by ComPIDVarD and ComPIDVarH on MC dataset. For all particles identified by both variables, there was a muon identification consistency of 57.5%.

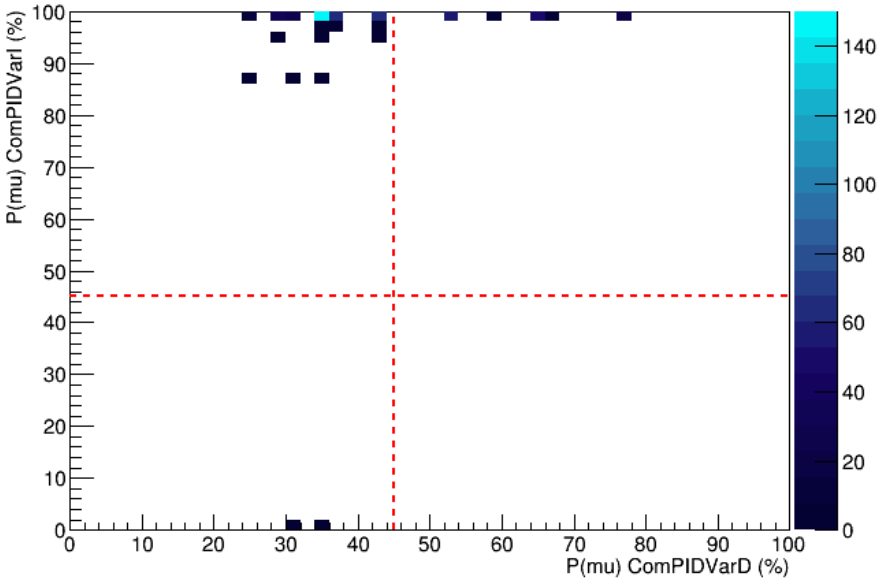

Figure A.25: Comparison of P(μ) returned by ComPIDVarD and ComPIDVarI on MC dataset. For all particles identified by both variables, there was a muon identification consistency of 25.2%.

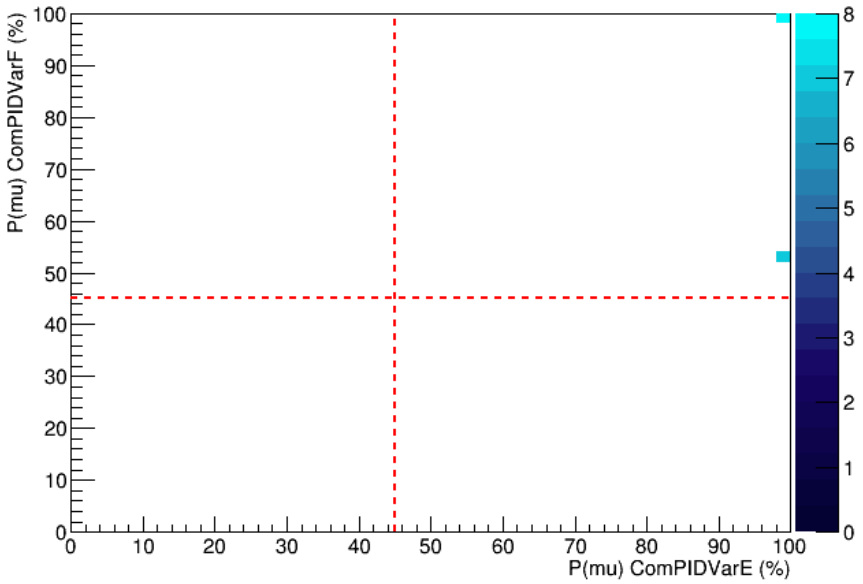

Figure A.26: Comparison of P(μ) returned by ComPIDVarE and ComPIDVarF on MC dataset. For all particles identified by both variables, there was a muon identification consistency of 100%.

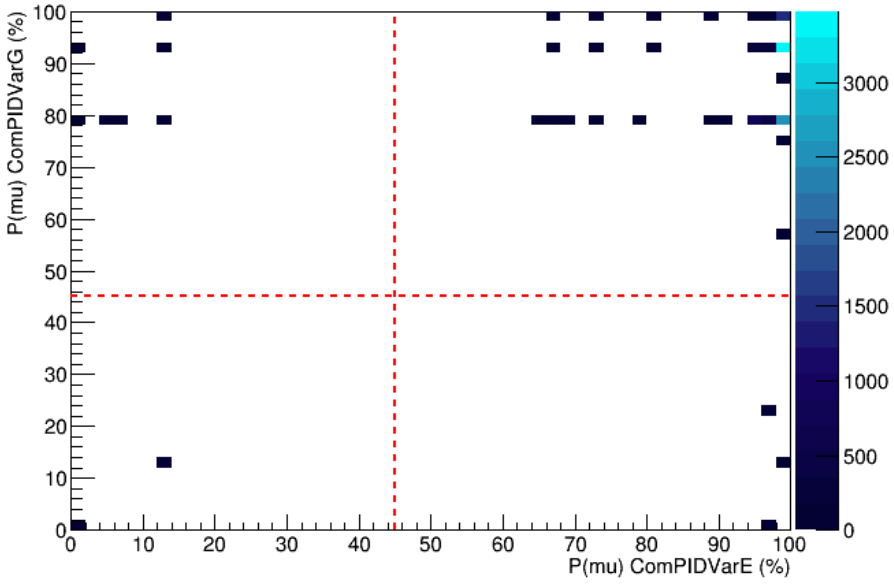

Figure A.27: Comparison of P(μ) returned by ComPIDVarE and ComPIDVarG on MC dataset. For all particles identified by both variables, there was a muon identification consistency of 98.9%.

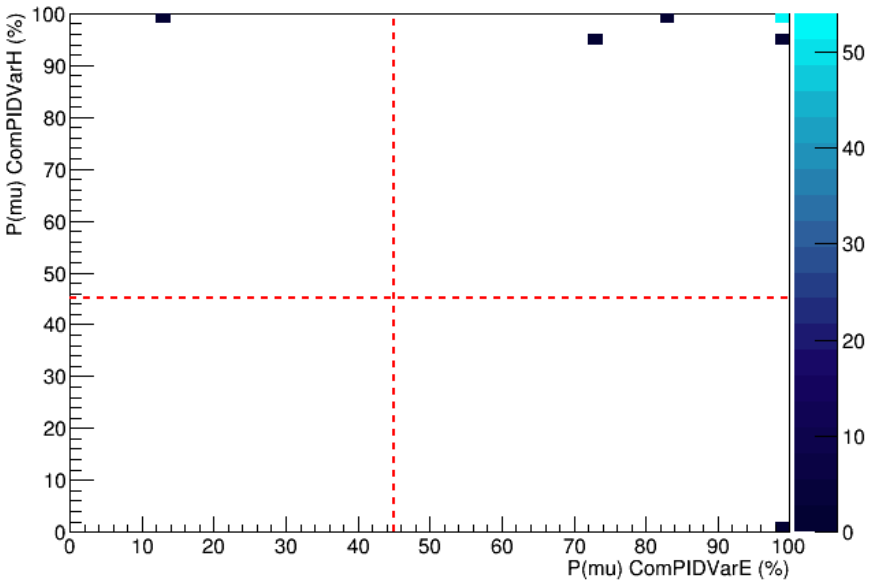

Figure A.28: Comparison of P(μ) returned by ComPIDVarE and ComPIDVarH on MC dataset. For all particles identified by both variables, there was a muon identification consistency of 95.1%.

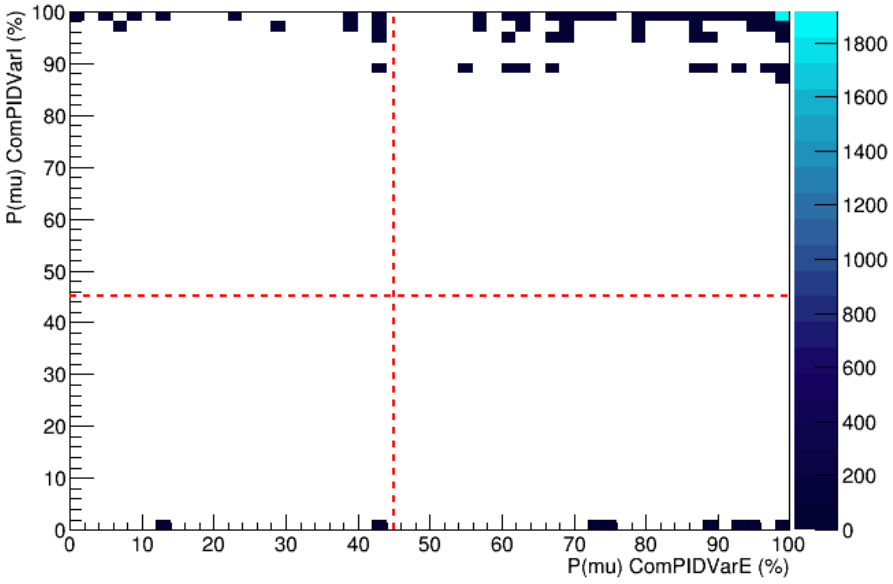

Figure A.29: Comparison of P(μ) returned by ComPIDVarE and ComPIDVarI on MC dataset. For all particles identified by both variables, there was a muon identification consistency of 98.3%.

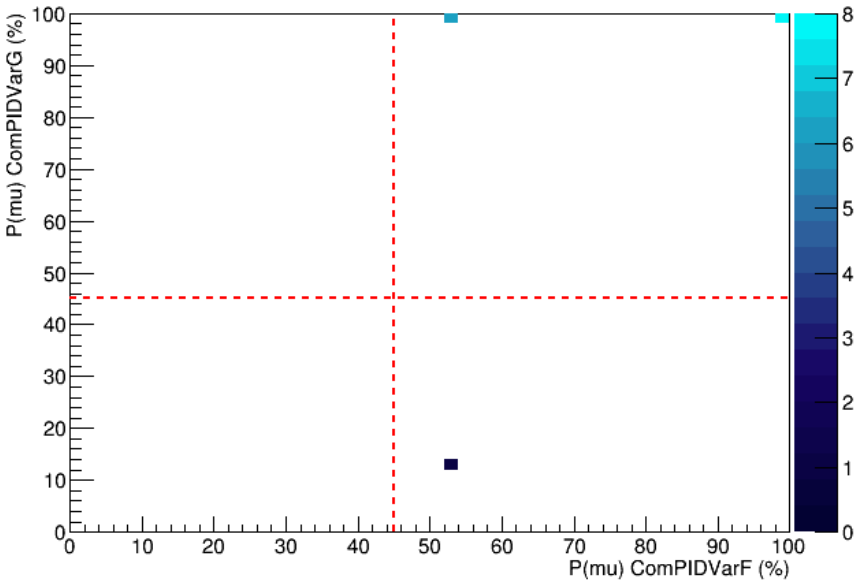

Figure A.30: Comparison of P(μ) returned by ComPIDVarF and ComPIDVarG on MC dataset. For all particles identified by both variables, there was a muon identification consistency of 93.3%.

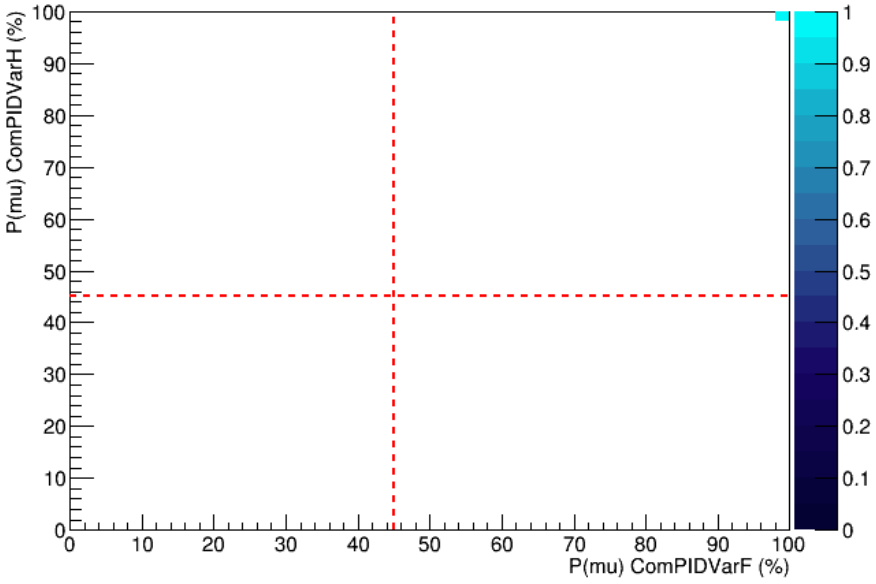

Figure A.31: Comparison of P(μ) returned by ComPIDVarF and ComPIDVarH on MC dataset. For all particles identified by both variables, there was a muon identification consistency of 100%.

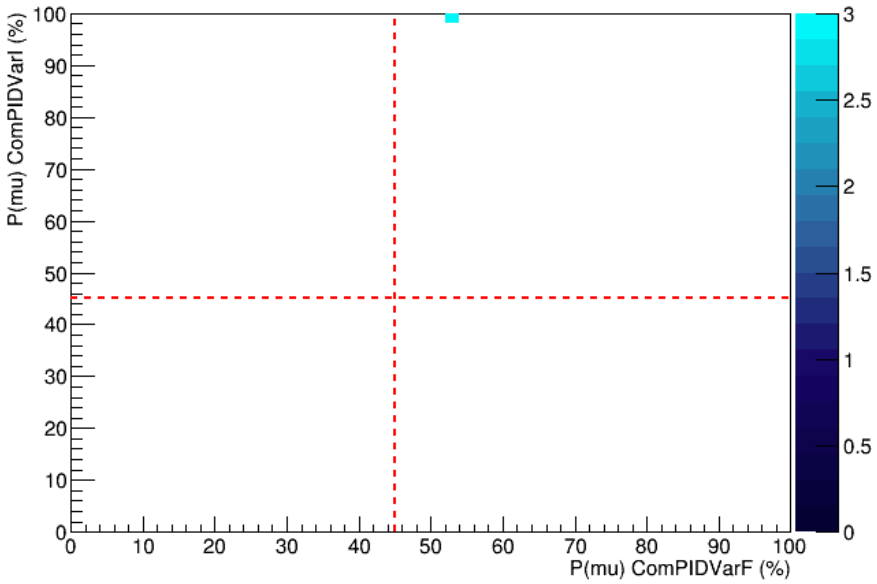

Figure A.32: Comparison of P(μ) returned by ComPIDVarF and ComPIDVarI on MC dataset. For all particles identified by both variables, there was a muon identification consistency of 100%.

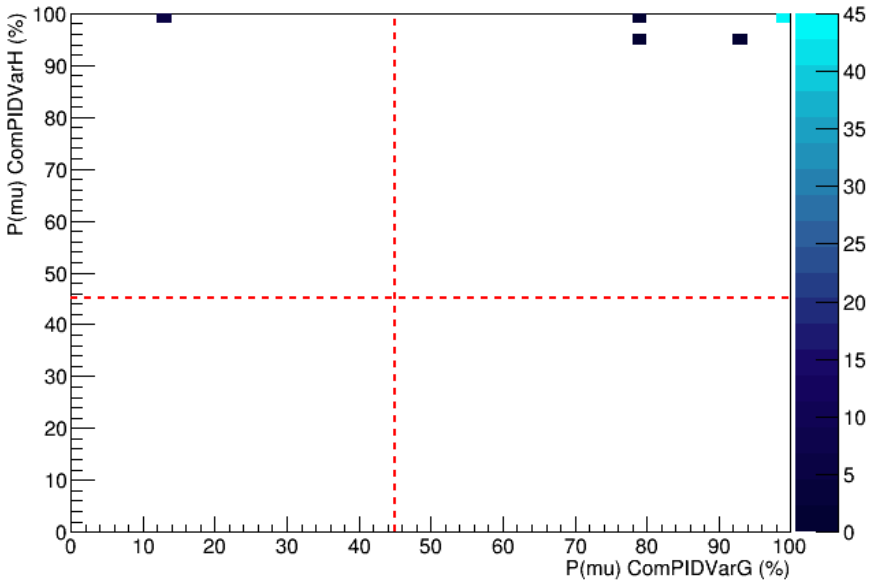

Figure A.33: Comparison of P(μ) returned by ComPIDVarG and ComPIDVarH on MC dataset. For all particles identified by both variables, there was a muon identification consistency of 90.6%.

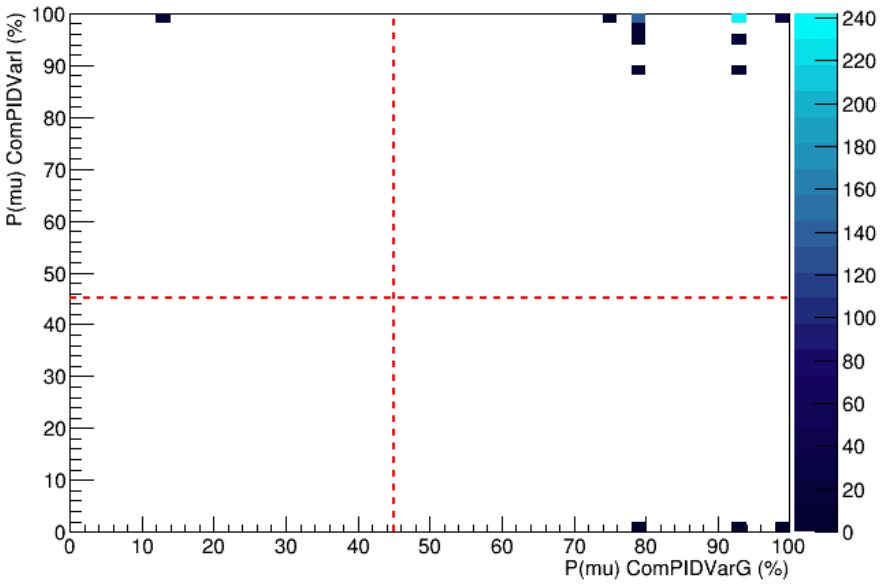

Figure A.34: Comparison of P(μ) returned by ComPIDVarG and ComPIDVarI on MC dataset. For all particles identified by both variables, there was a muon identification consistency of 95.2%.

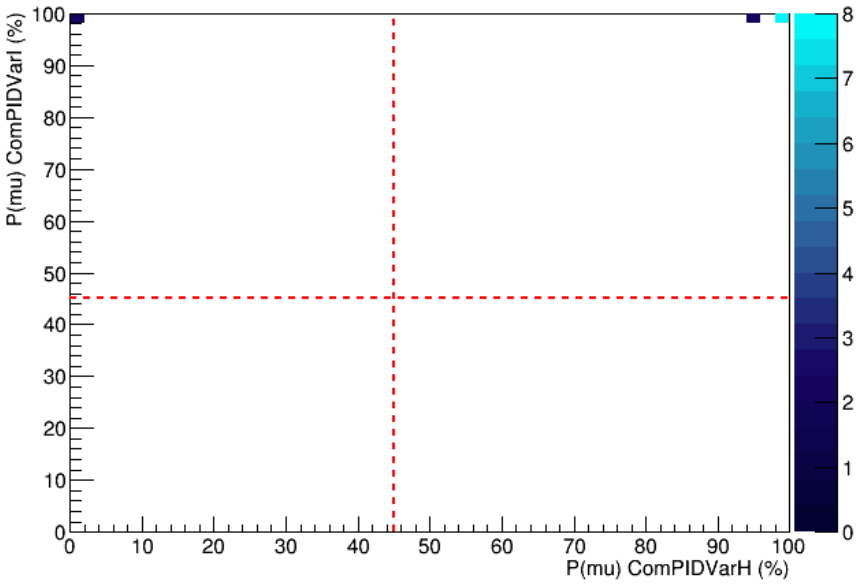

Figure A.35: Comparison of P(μ) returned by ComPIDVarH and ComPIDVarI on MC dataset. For all particles identified by both variables, there was a muon identification consistency of 83.3%.

A.2 Commissioning Variable Consistency Plots (Data)

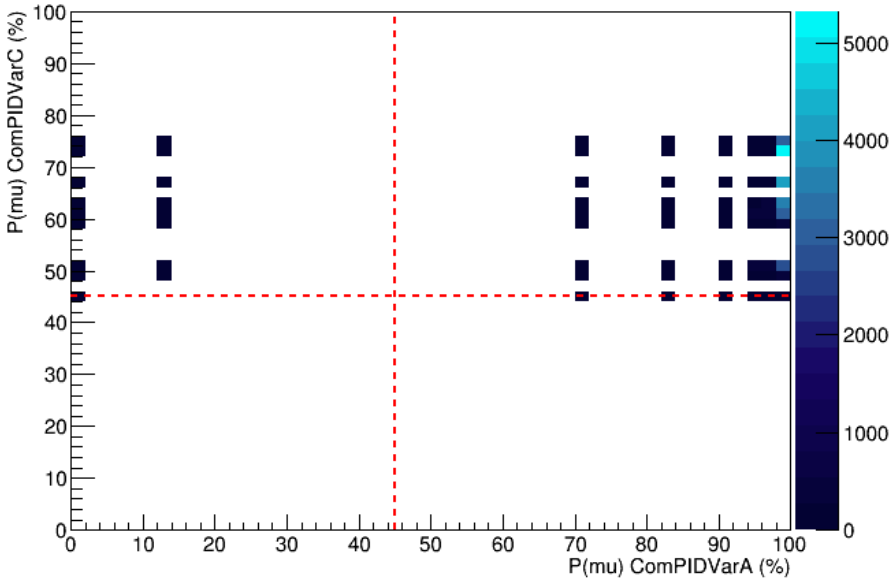

Figure A.36: Comparison of P(μ) returned by ComPIDVarA and ComPIDVarC for LiH dataset. For all particles identified by both variables, there was a muon identification consistency of 98.6%.

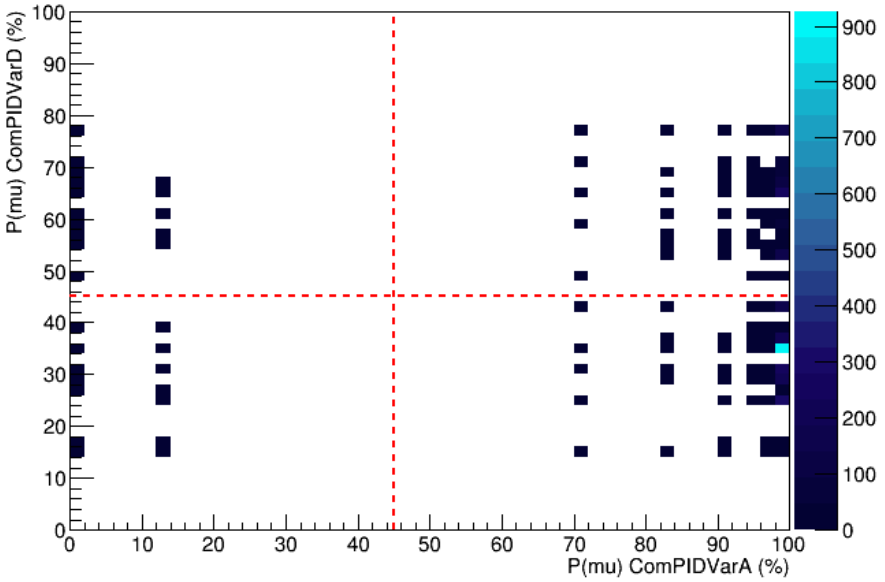

Figure A.37: Comparison of P(μ) returned by ComPIDVarA and ComPIDVarD for LiH dataset. For all particles identified by both variables, there was a muon identification consistency of 34.0%.

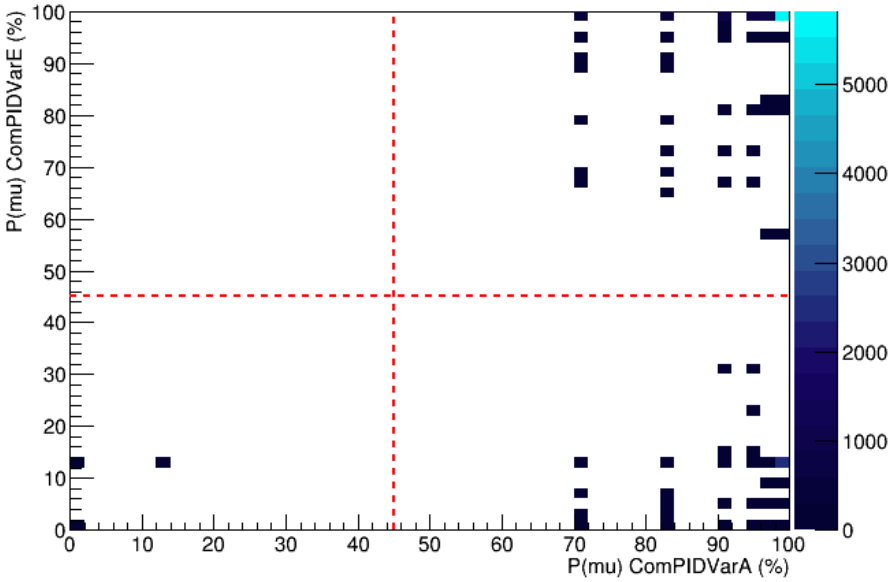

Figure A.38: Comparison of P(μ) returned by ComPIDVarA and ComPIDVarE for LiH dataset. For all particles identified by both variables, there was a muon identification consistency of 78.2%.

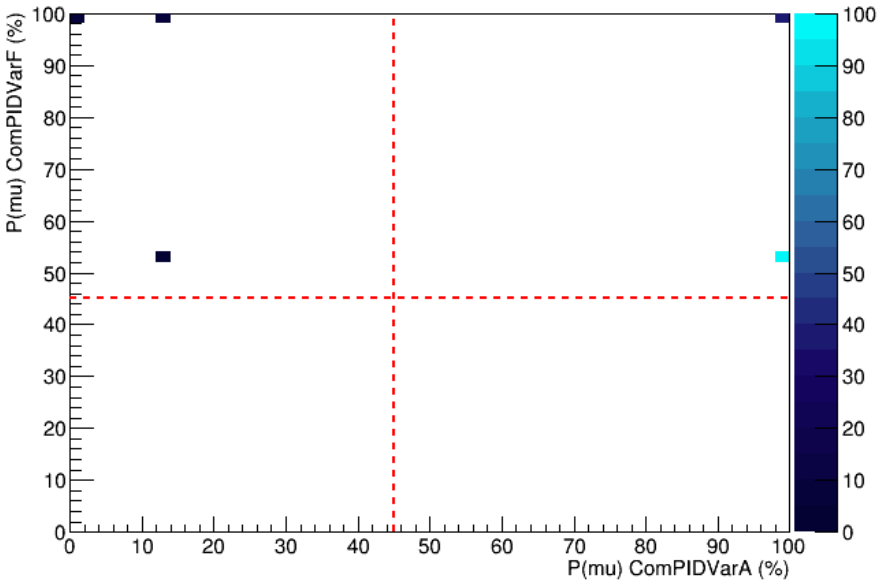

Figure A.39: Comparison of P(μ) returned by ComPIDVarA and ComPIDVarF for LiH dataset. For all particles identified by both variables, there was a muon identification consistency of 92.6%.

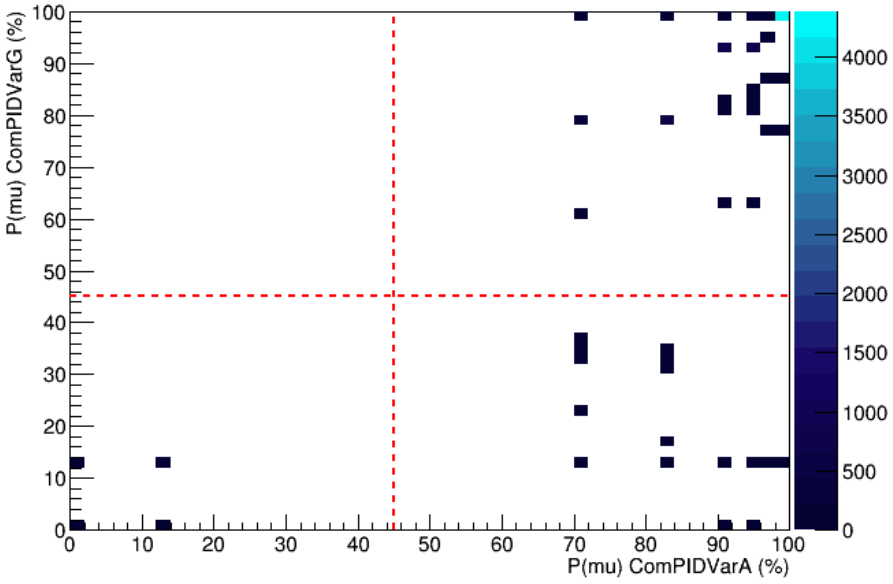

Figure A.40: Comparison of P(μ) returned by ComPIDVarA and ComPIDVarG for LiH dataset. For all particles identified by both variables, there was a muon identification consistency of 98.2%.

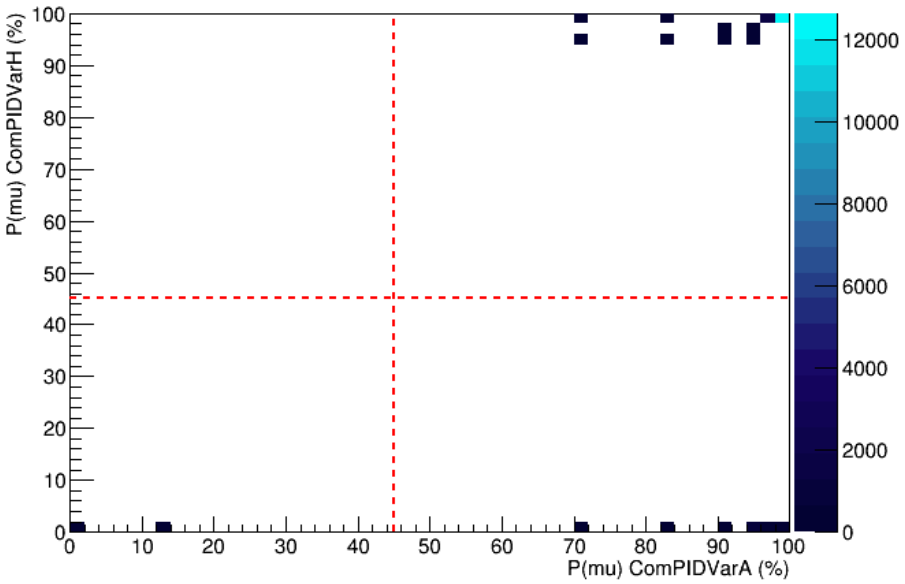

Figure A.41: Comparison of P(μ) returned by ComPIDVarA and ComPIDVarH for LiH dataset. For all particles identified by both variables, there was a muon identification consistency of 86.1%.

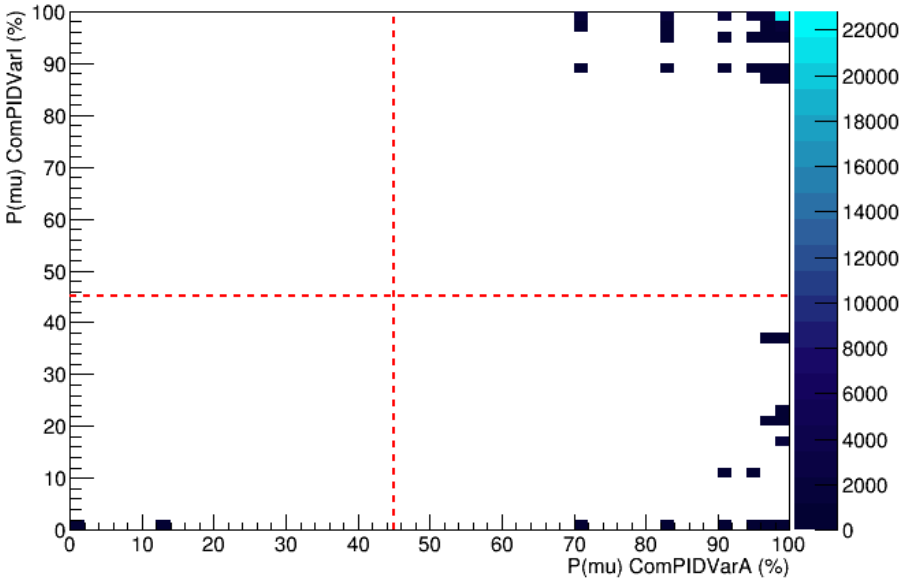

Figure A.42: Comparison of P(μ) returned by ComPIDVarA and ComPIDVarI for LiH dataset. For all particles identified by both variables, there was a muon identification consistency of 81.9%

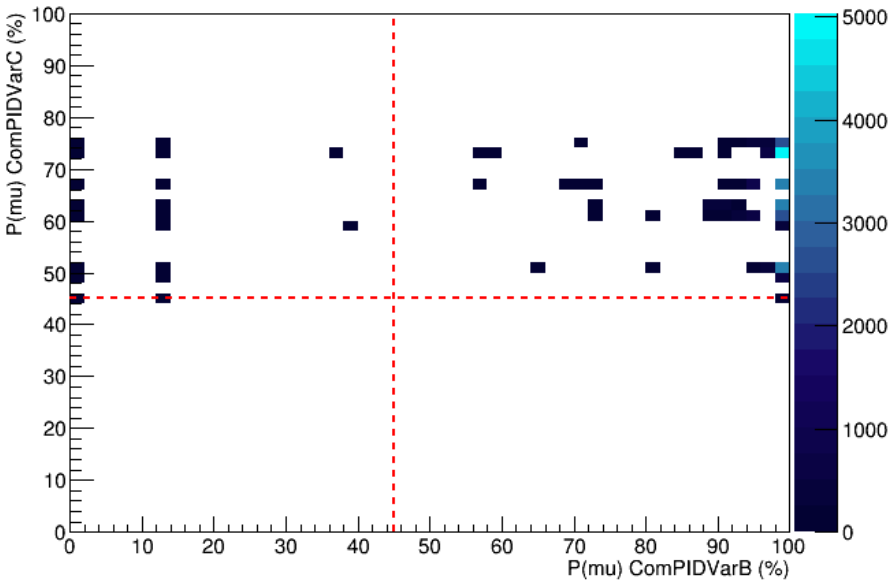

Figure A.43: Comparison of P(μ) returned by ComPIDVarB and ComPIDVarC for LiH dataset. For all particles identified by both variables, there was a muon identification consistency of 97.8%.

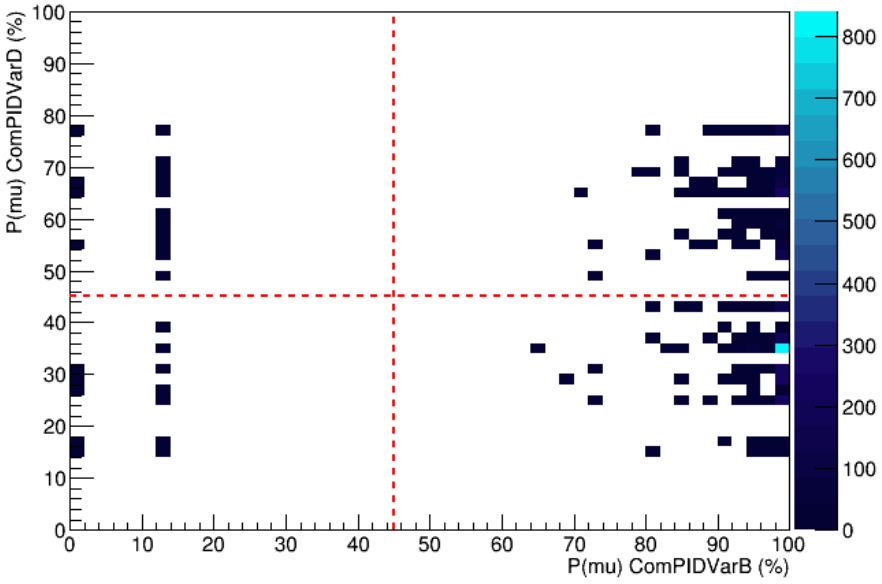

Figure A.44: Comparison of P(μ) returned by ComPIDVarB and ComPIDVarD for LiH dataset. For all particles identified by both variables, there was a muon identification consistency of 31.5%.

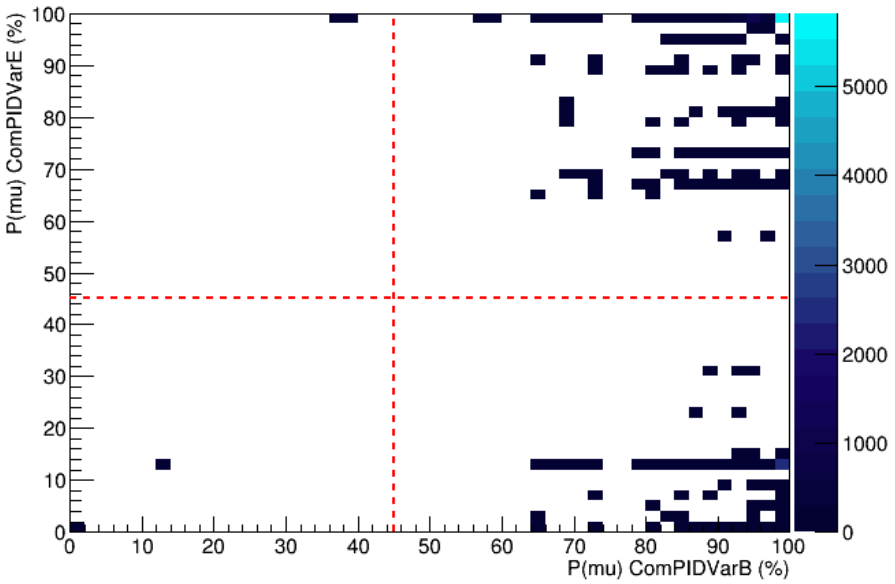

Figure A.45: Comparison of P(μ) returned by ComPIDVarB and ComPIDVarE for LiH dataset. For all particles identified by both variables, there was a muon identification consistency of 78.8%.

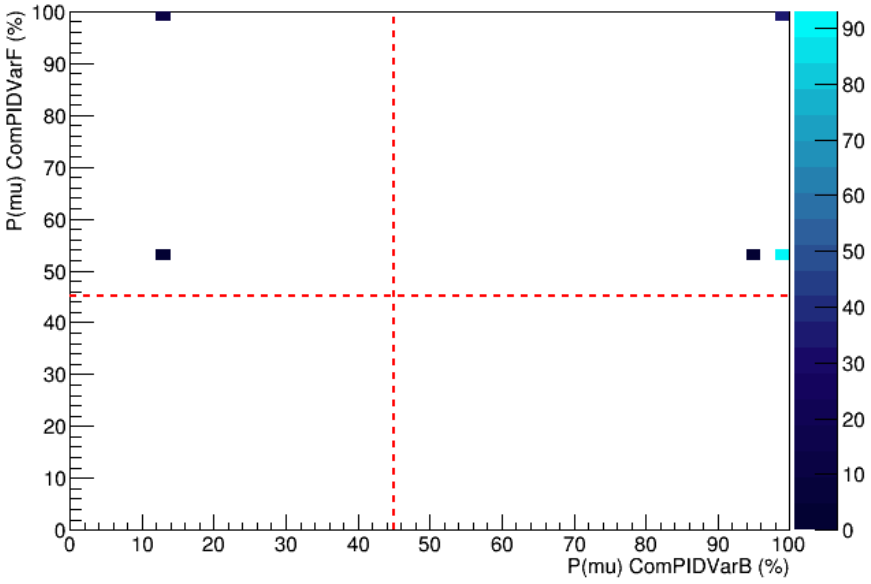

Figure A.46: Comparison of P(μ) returned by ComPIDVarB and ComPIDVarF for LiH dataset. For all particles identified by both variables, there was a muon identification consistency of 88.9%.

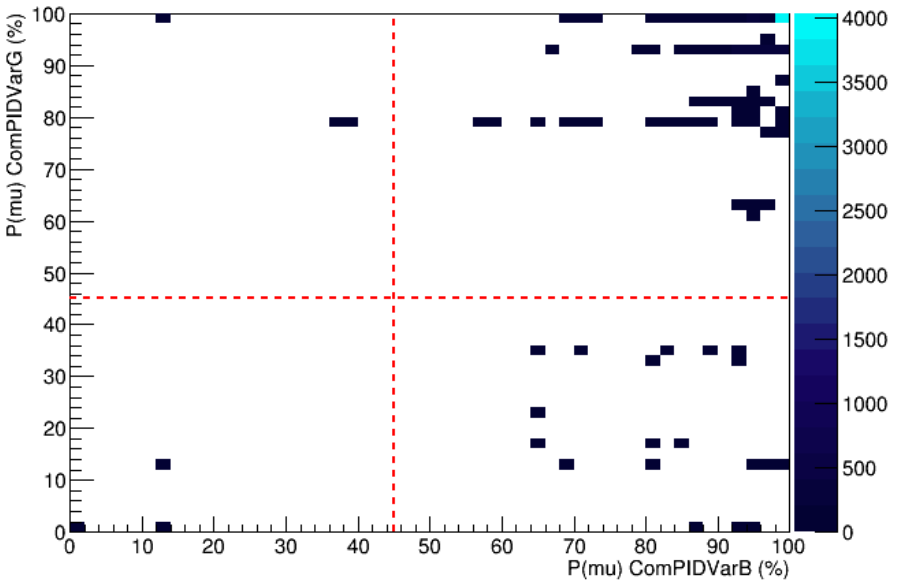

Figure A.47: Comparison of P(μ) returned by ComPIDVarB and ComPIDVarG for LiH dataset. For all particles identified by both variables, there was a muon identification consistency of 97.0%.

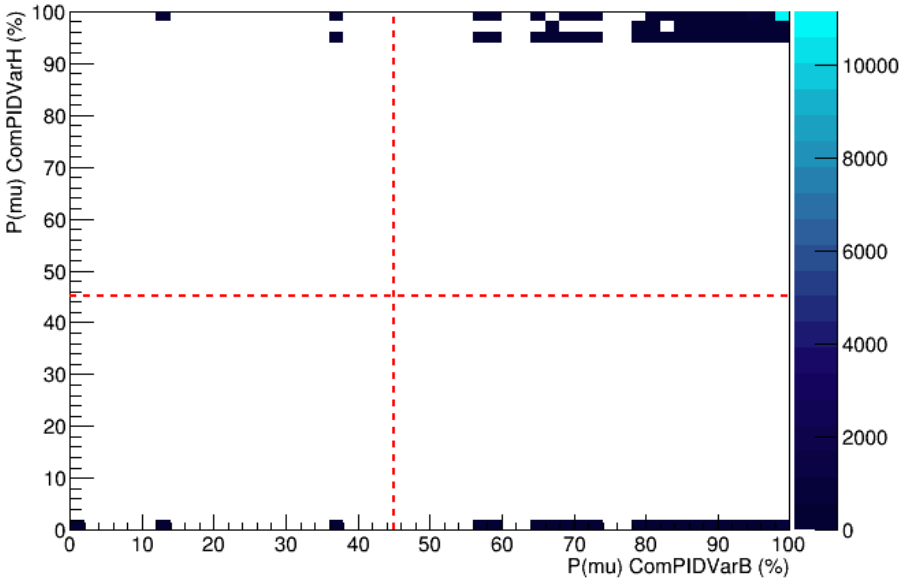

Figure A.48: Comparison of P(μ) returned by ComPIDVarB and ComPIDVarH for LiH dataset. For all particles identified by both variables, there was a muon identification consistency of 85.5%.

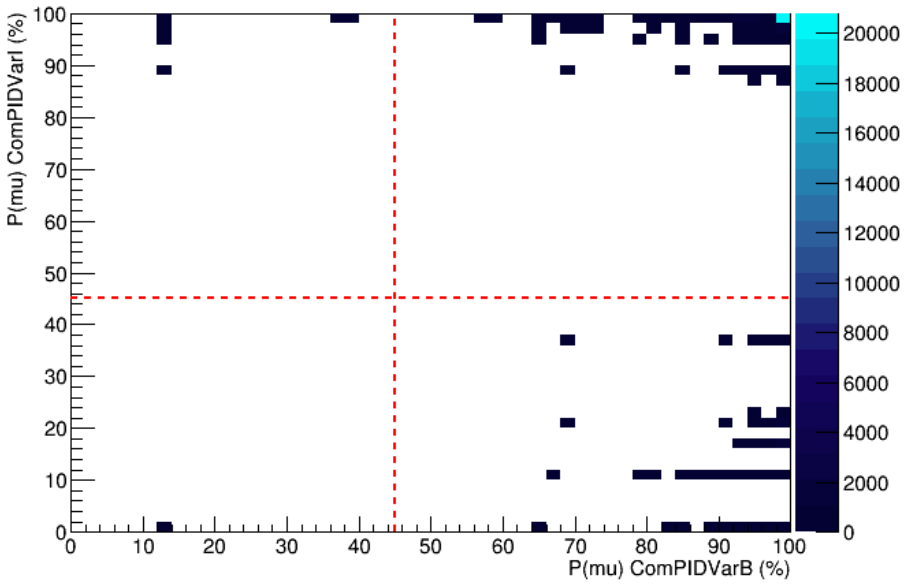

Figure A.49: Comparison of P(μ) returned by ComPIDVarB and ComPIDVarI for LiH dataset. For all particles identified by both variables, there was a muon identification consistency of 81.3%.

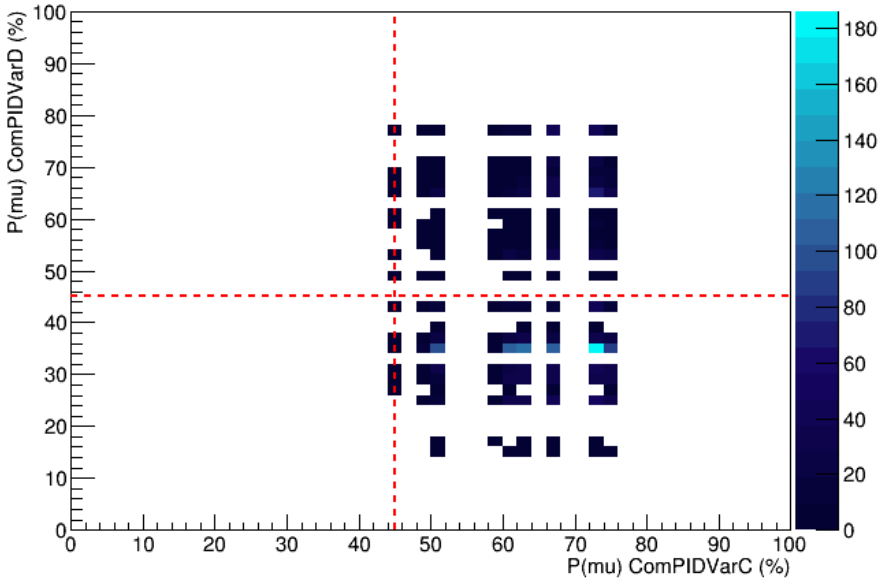

Figure A.50: Comparison of P(μ) returned by ComPIDVarC and ComPIDVarD for LiH dataset. For all particles identified by both variables, there was a muon identification consistency of 34.2%.

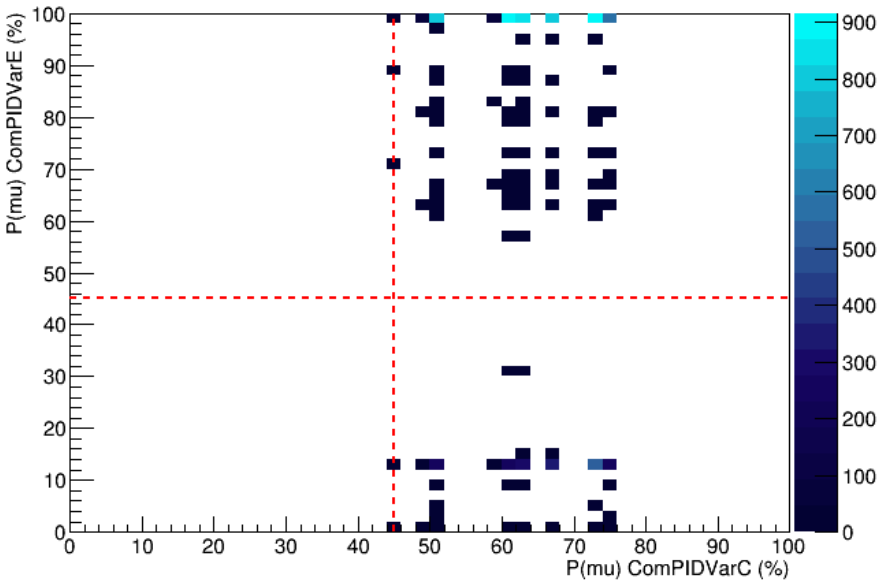

Figure A.51: Comparison of P(μ) returned by ComPIDVarC and ComPIDVarE for LiH dataset. For all particles identified by both variables, there was a muon identification consistency of 71.9%.

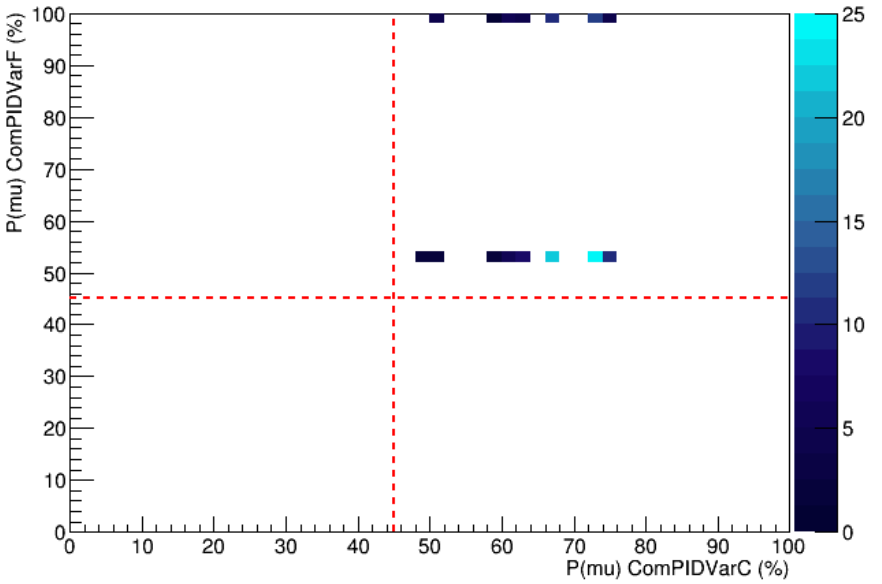

Figure A.52: Comparison of P(μ) returned by ComPIDVarC and ComPIDVarF for LiH dataset. For all particles identified by both variables, there was a muon identification consistency of 100%.

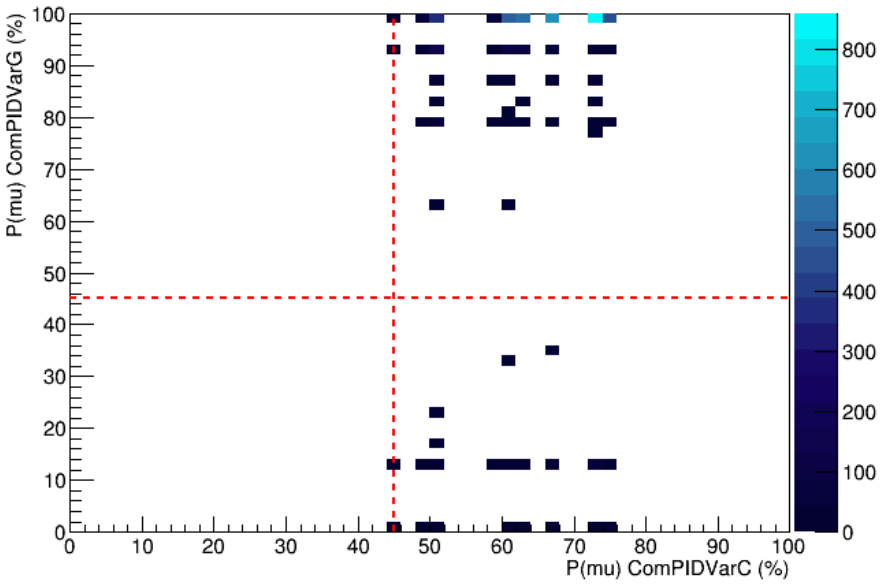

Figure A.53: Comparison of P(μ) returned by ComPIDVarC and ComPIDVarG for LiH dataset. For all particles identified by both variables, there was a muon identification consistency of 95.6%.

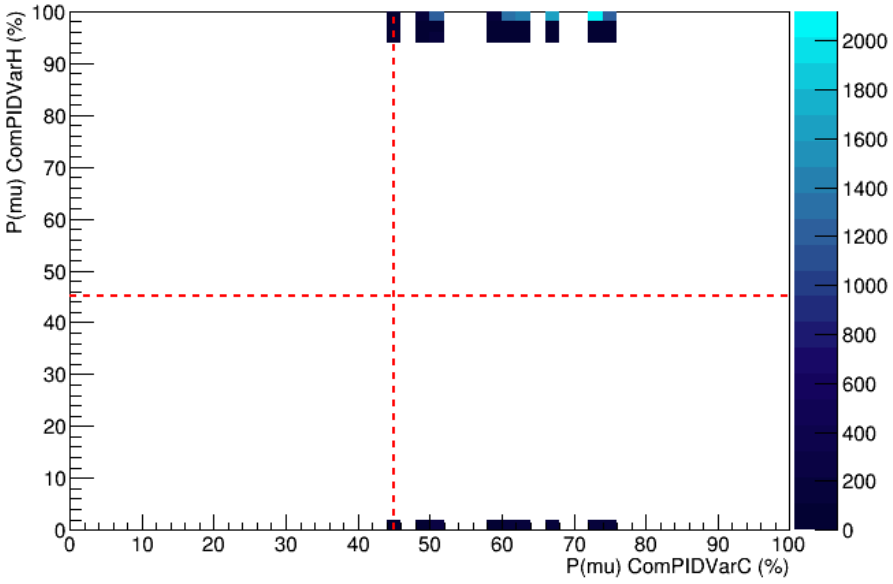

Figure A.54: Comparison of P(μ) returned by ComPIDVarC and ComPIDVarH for LiH dataset. For all particles identified by both variables, there was a muon identification consistency of 89.5%.

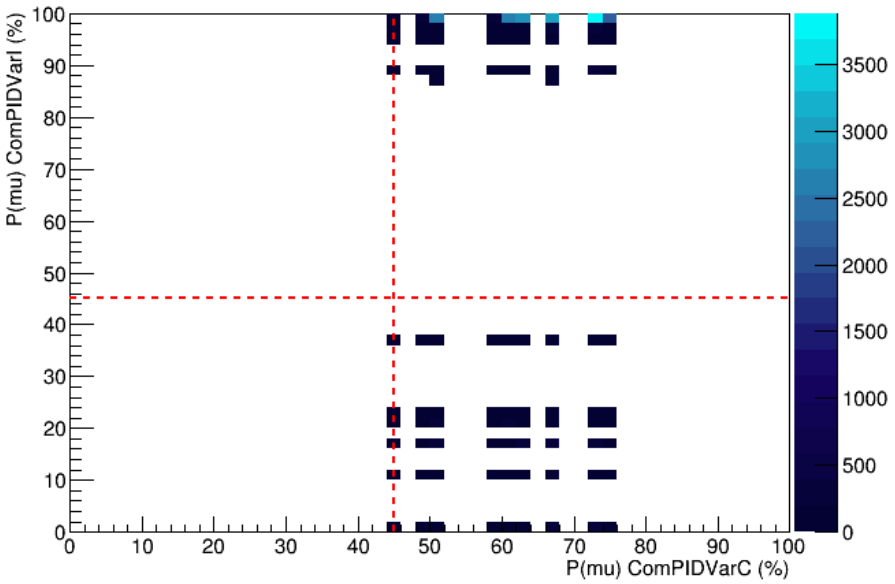

Figure A.55: Comparison of P(μ) returned by ComPIDVarC and ComPIDVarI for LiH dataset. For all particles identified by both variables, there was a muon identification consistency of 82.0%.

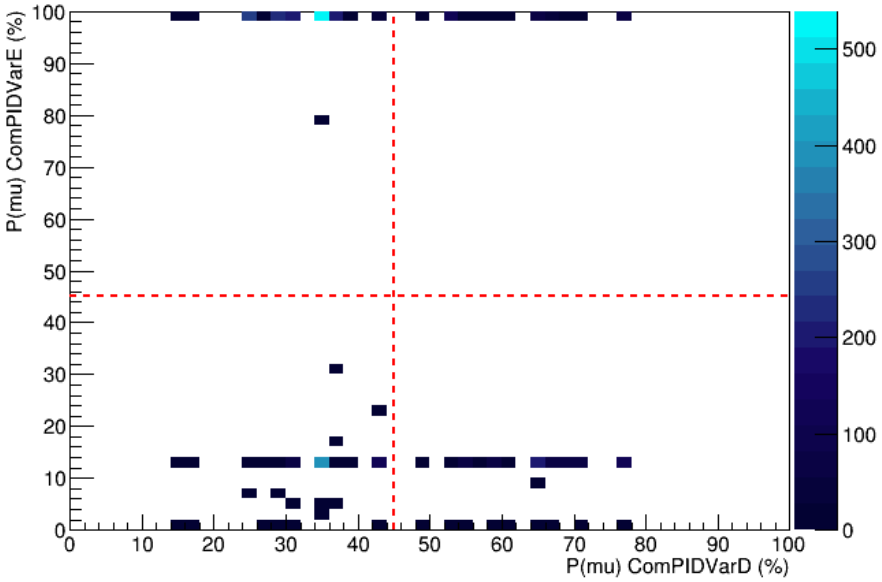

Figure A.56: Comparison of P(μ) returned by ComPIDVarD and ComPIDVar for LiH datasetE. For all particles identified by both variables, there was a muon identification consistency of 32.8%.

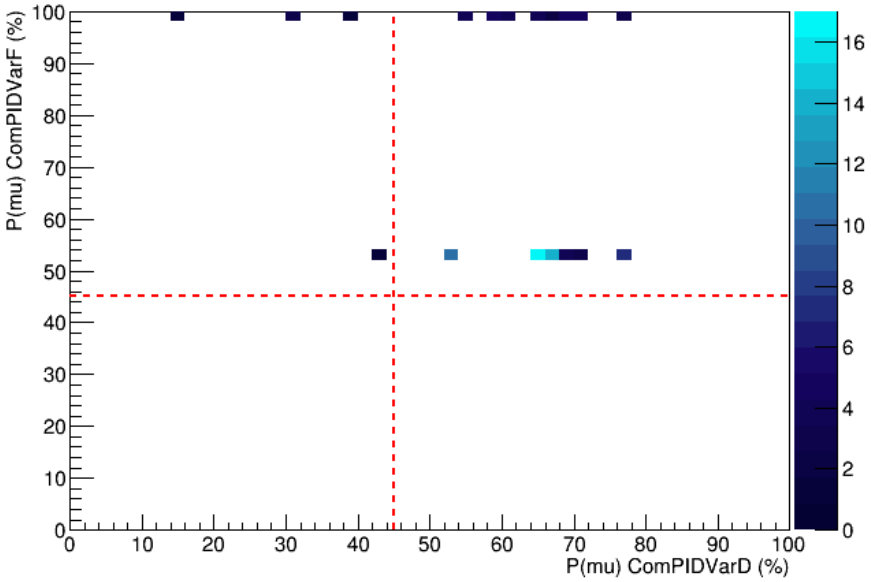

Figure A.57: Comparison of P(μ) returned by ComPIDVarD and ComPIDVarF for LiH dataset. For all particles identified by both variables, there was a muon identification consistency of 93.6%.

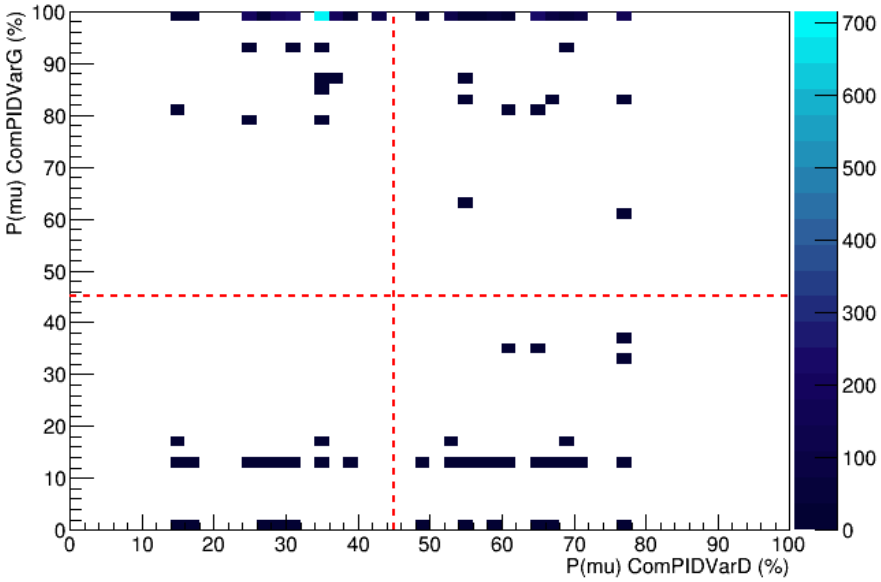

Figure A.58: Comparison of P(μ) returned by ComPIDVarD and ComPIDVarG for LiH dataset. For all particles identified by both variables, there was a muon identification consistency of 34.2%.

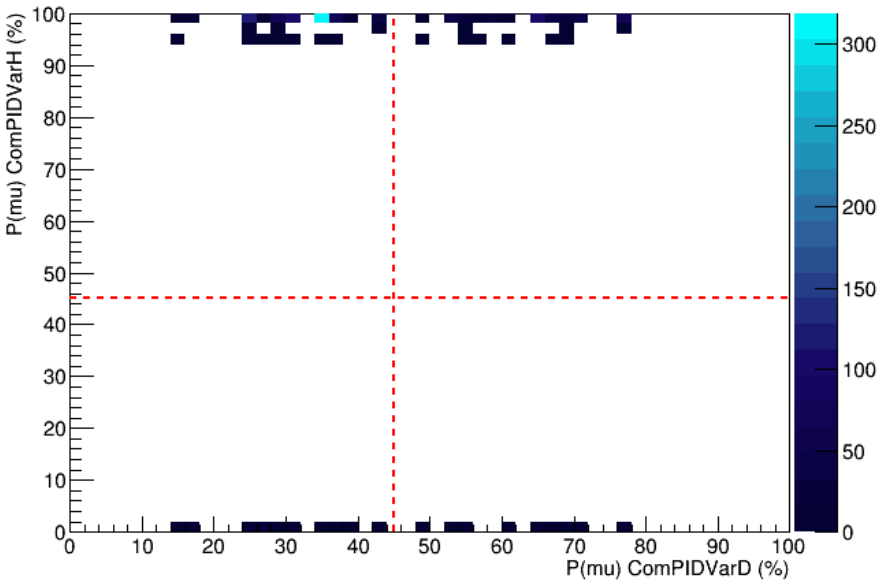

Figure A.59: Comparison of P(μ) returned by ComPIDVarD and ComPIDVarH for LiH dataset. For all particles identified by both variables, there was a muon identification consistency of 36.5%.

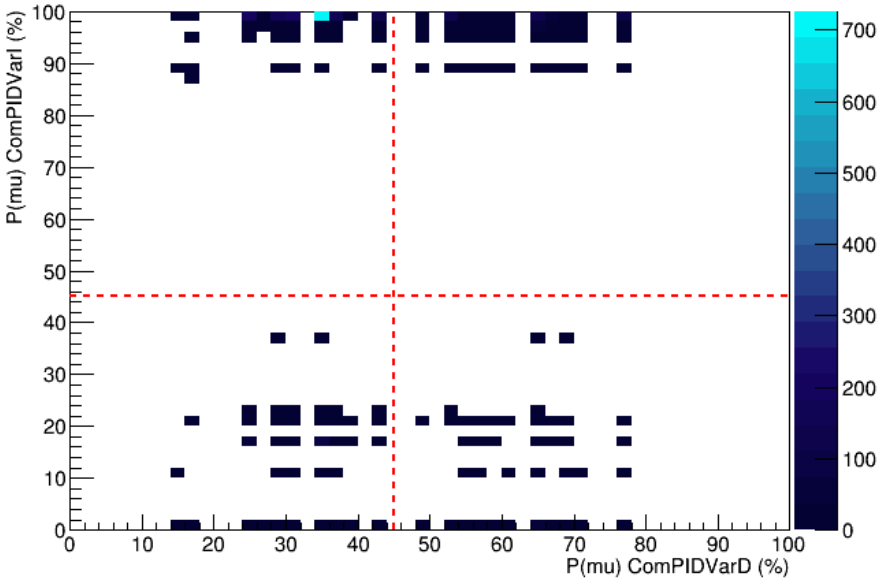

Figure A.60: Comparison of P(μ) returned by ComPIDVarD and ComPIDVarI for LiH dataset. For all particles identified by both variables, there was a muon identification consistency of 37.0%.

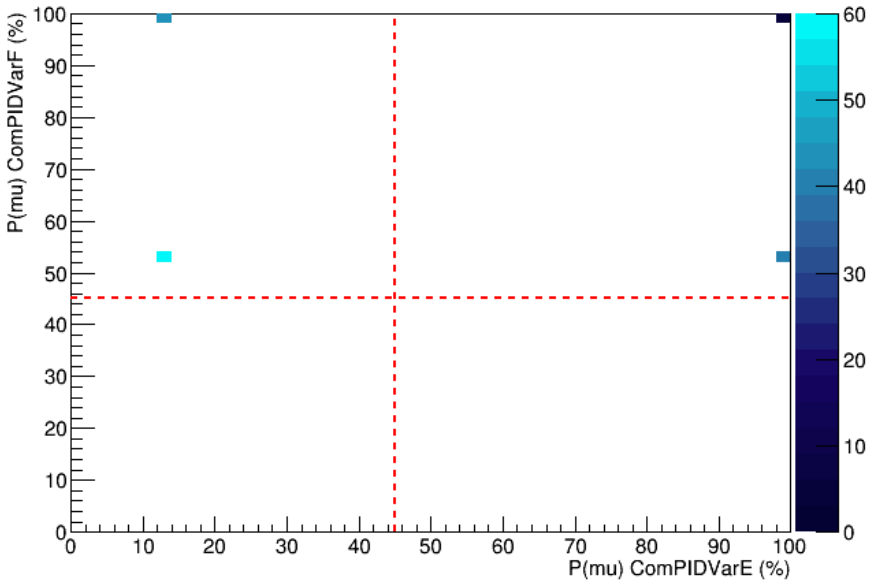

Figure A.61: Comparison of P(μ) returned by ComPIDVarE and ComPIDVarF for LiH dataset. For all particles identified by both variables, there was a muon identification consistency of 30.8%.

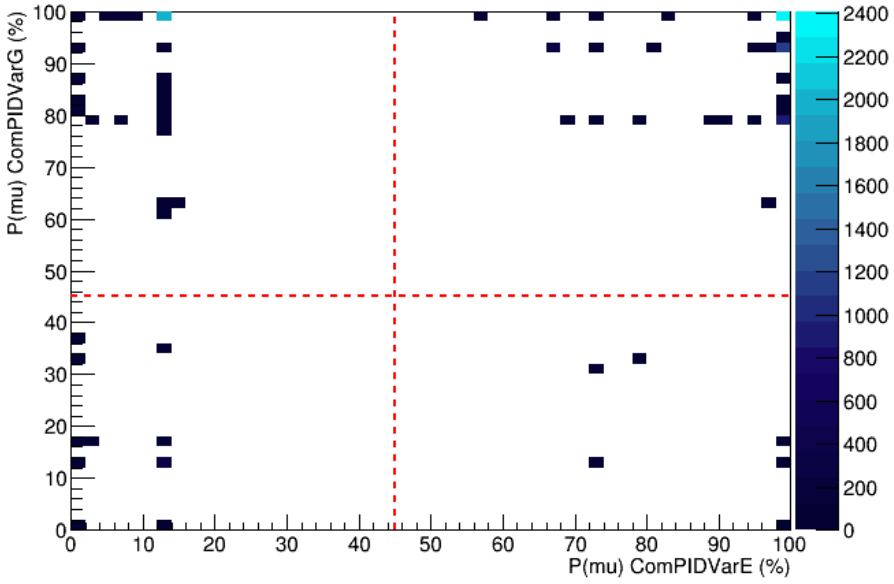

Figure A.62: Comparison of P(μ) returned by ComPIDVarE and ComPIDVarG for LiH dataset. For all particles identified by both variables, there was a muon identification consistency of 71.5%.

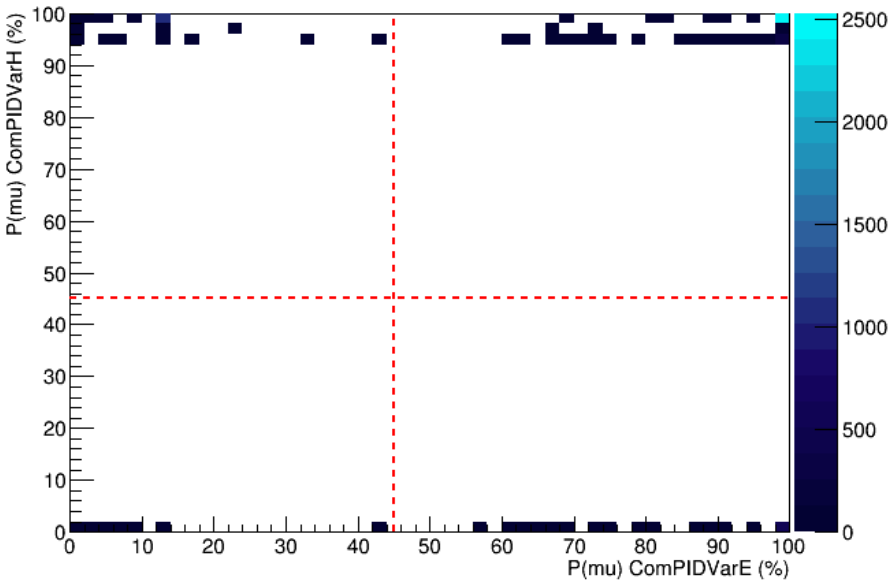

Figure A.63: Comparison of P(μ) returned by ComPIDVarE and ComPIDVarH for LiH dataset. For all particles identified by both variables, there was a muon identification consistency of 64.4%.

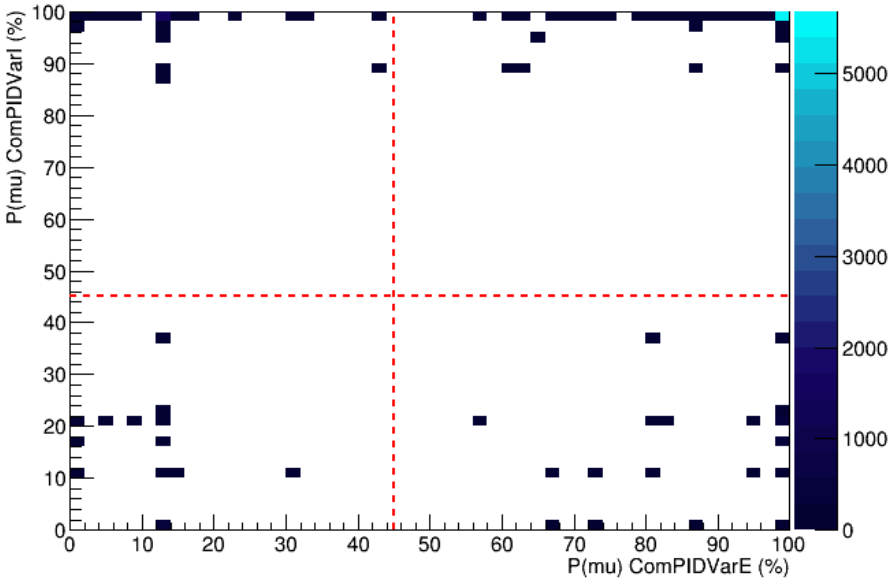

Figure A.64: Comparison of P(μ) returned by ComPIDVarE and ComPIDVarI for LiH dataset. For all particles identified by both variables, there was a muon identification consistency of 64.0%.

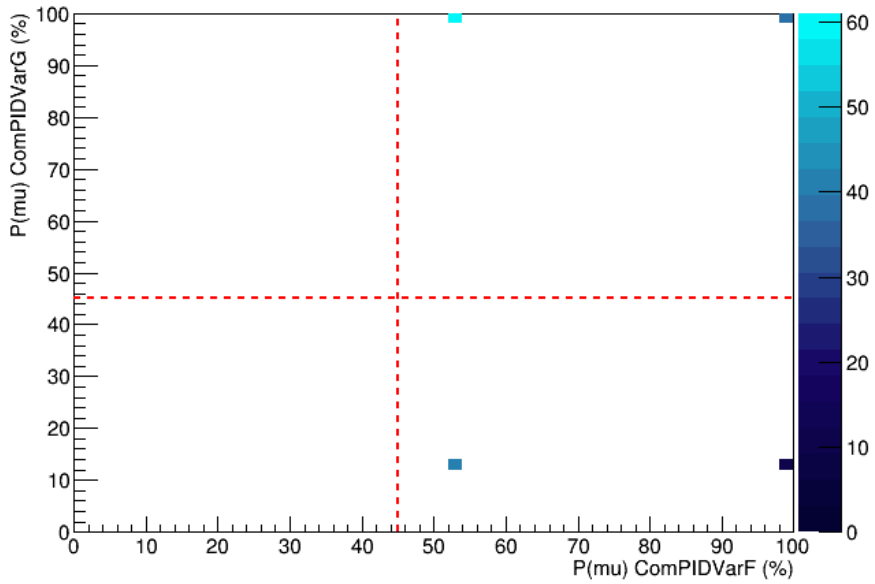

Figure A.65: Comparison of P(μ) returned by ComPIDVarF and ComPIDVarG for LiH dataset. For all particles identified by both variables, there was a muon identification consistency of 65.8%.

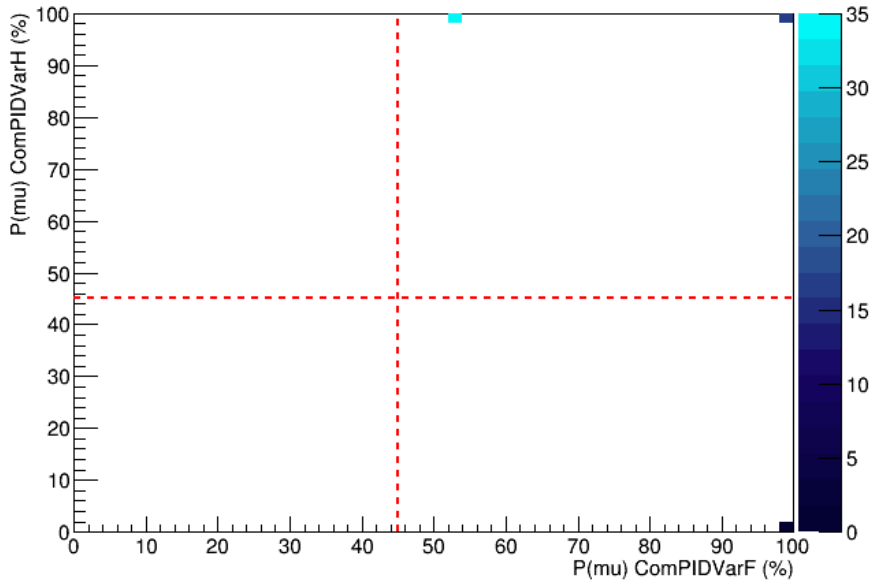

Figure A.66: Comparison of P(μ) returned by ComPIDVarF and ComPIDVarH for LiH dataset. For all particles identified by both variables, there was a muon identification consistency of 98.1%.

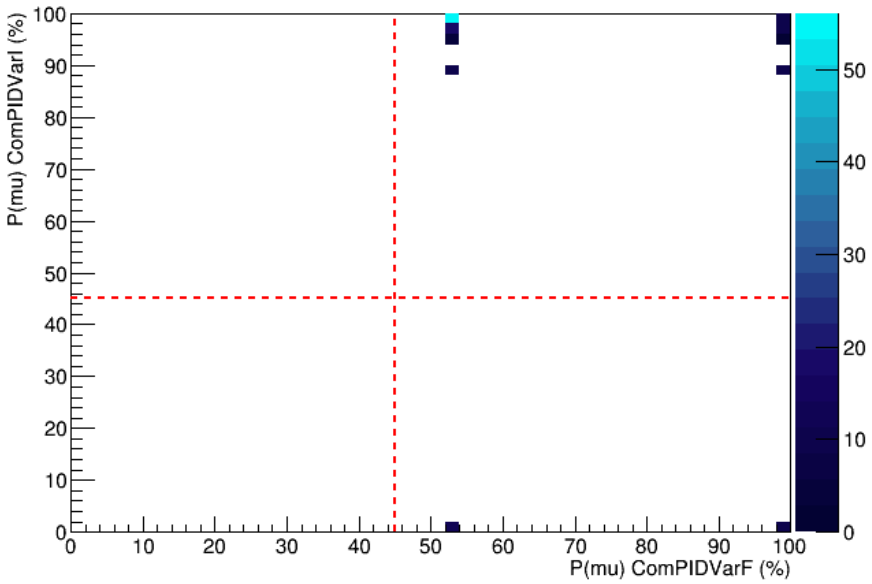

Figure A.67: Comparison of P(μ) returned by ComPIDVarF and ComPIDVarI for LiH dataset. For all particles identified by both variables, there was a muon identification consistency of 83.7%.

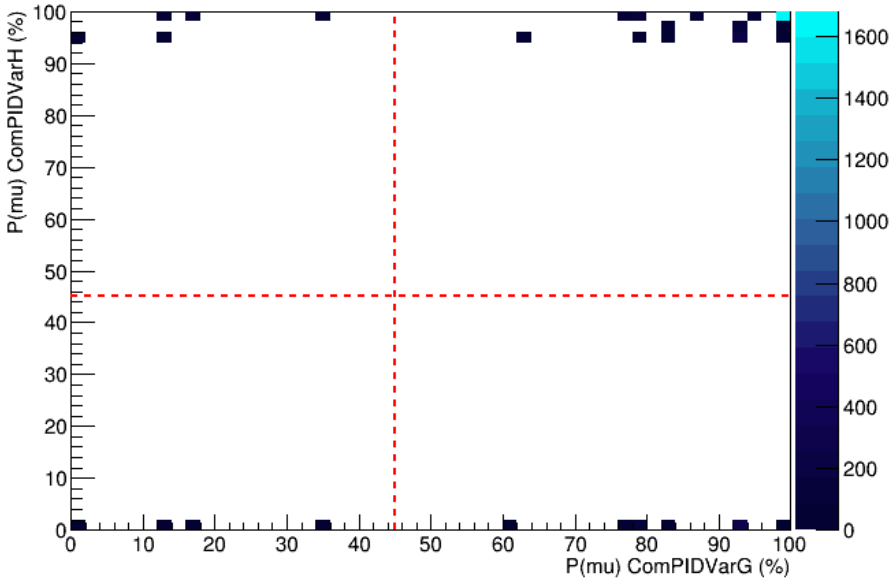

Figure A.68: Comparison of P(μ) returned by ComPIDVarG and ComPIDVarH for LiH dataset. For all particles identified by both variables, there was a muon identification consistency of 81.0%.

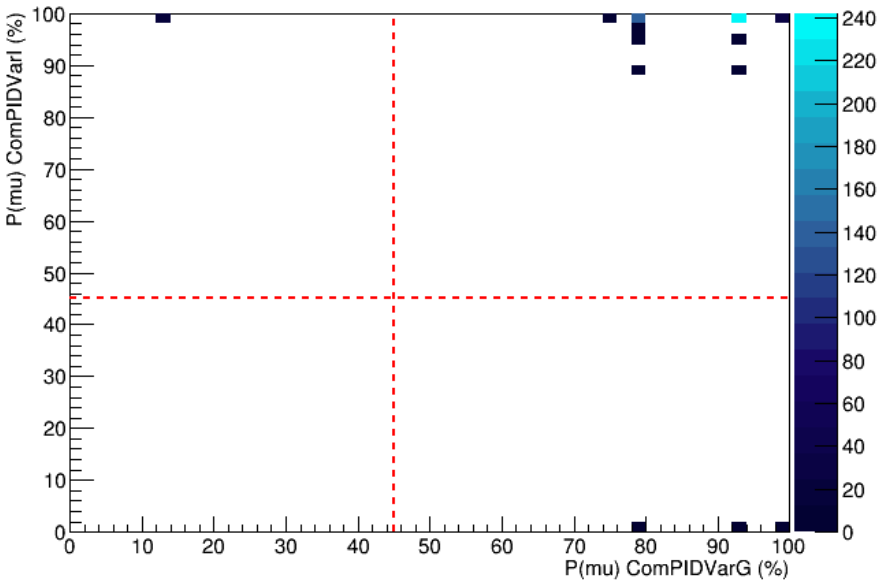

Figure A.69: Comparison of P(μ) returned by ComPIDVarG and ComPIDVarI for LiH dataset. For all particles identified by both variables, there was a muon identification consistency of 82.6%.

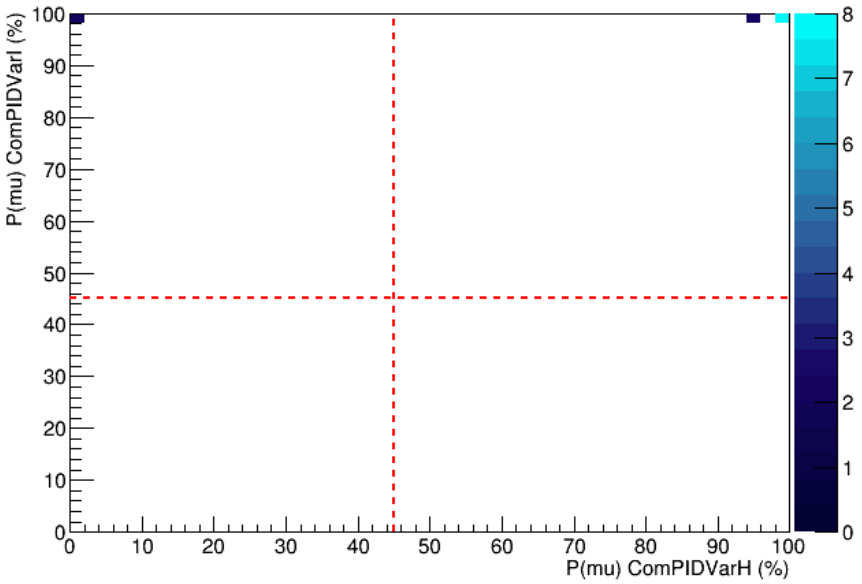

Figure A.70: Comparison of P(μ) returned by ComPIDVarH and ComPIDVarI for LiH dataset. For all particles identified by both variables, there was a muon identification consistency of 74.1%.

A.3 Step IV Downstream Variable Consistency Plots

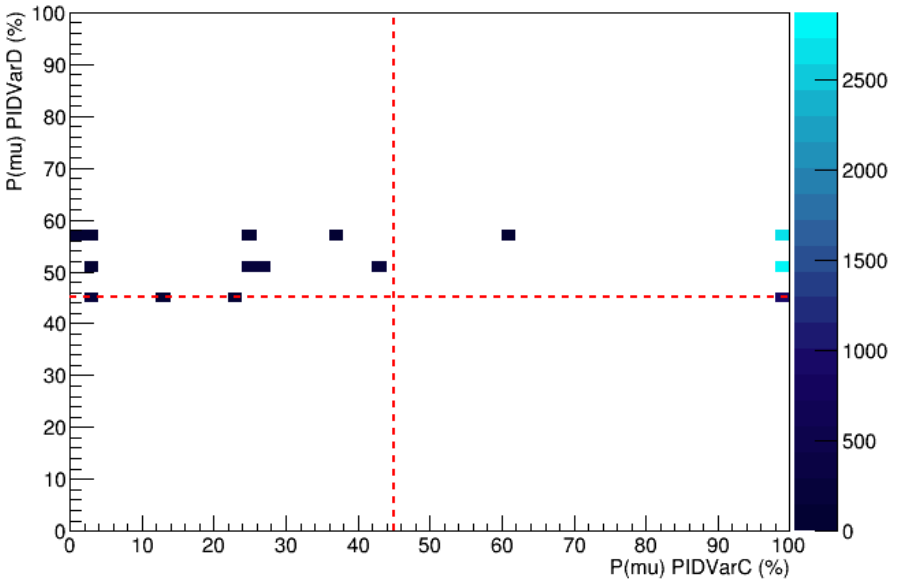

Figure A.71: Comparison of P(μ) returned by PIDVarC and PIDVarD on MC dataset. For all particles identified by both variables, there was a muon identification consistency of 85.9%.

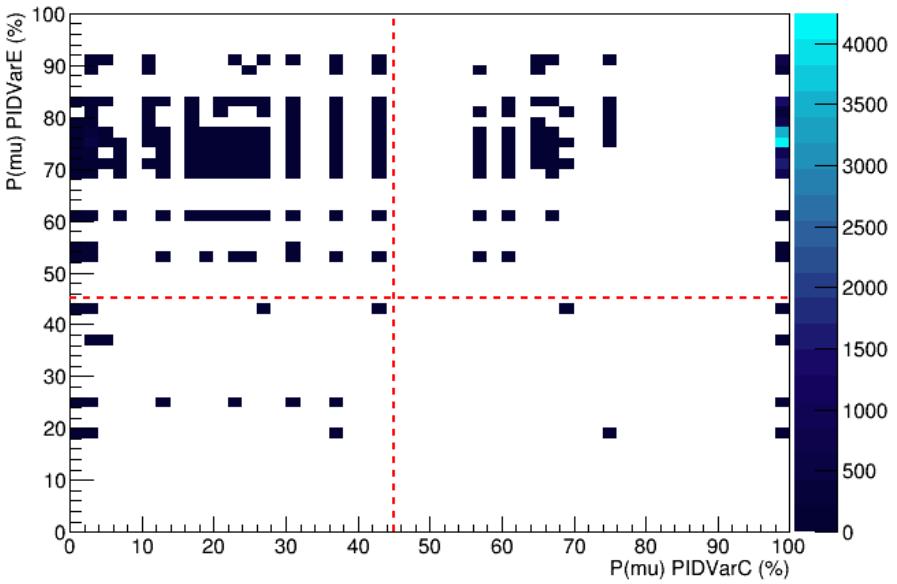

Figure A.72: Comparison of P(μ) returned by PIDVarC and PIDVarE on MC dataset. For all particles identified by both variables, there was a muon identification consistency of 80.9%.

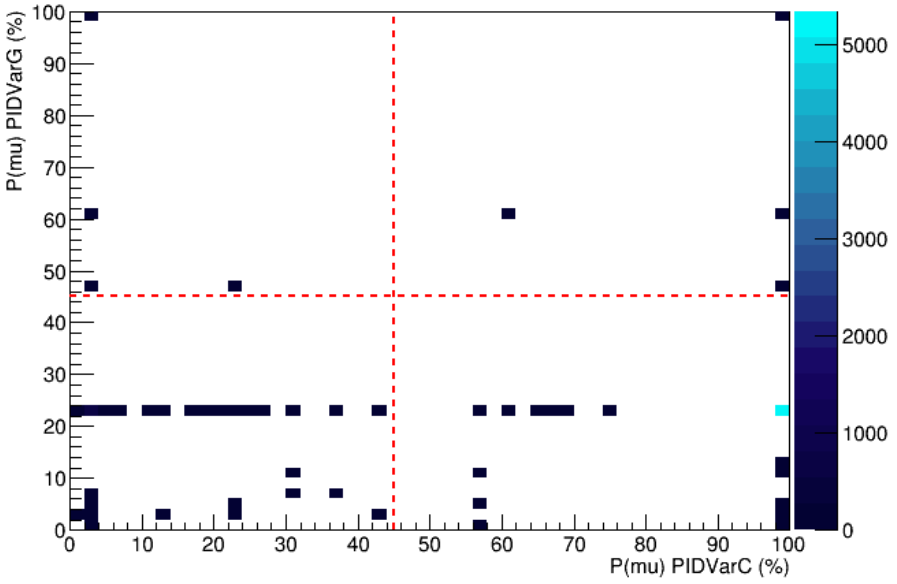

Figure A.73: Comparison of P(μ) returned by PIDVarC and PIDVarG on MC dataset. For all particles identified by both variables, there was a muon identification consistency of 22.3%.

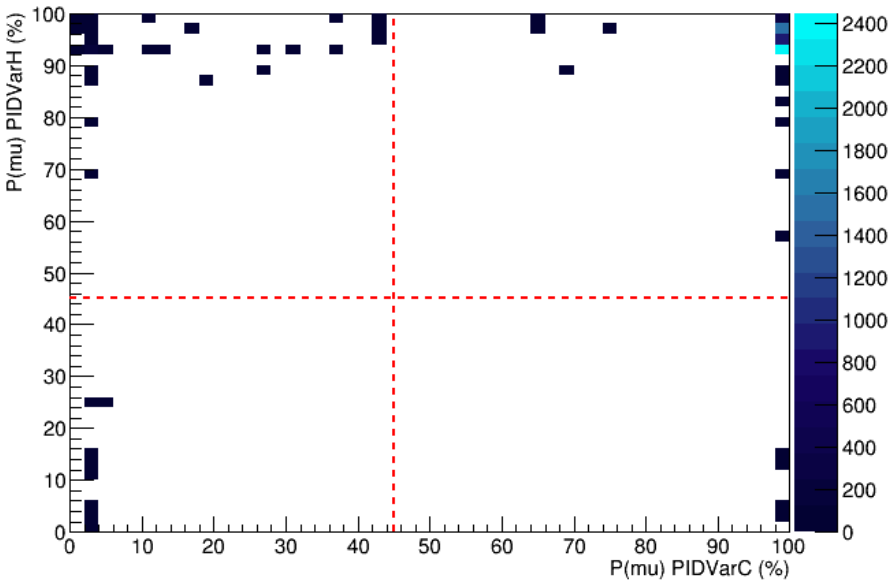

Figure A.74: Comparison of P(μ) returned by PIDVarC and PIDVarH on MC dataset. For all particles identified by both variables, there was a muon identification consistency of 90.3%.

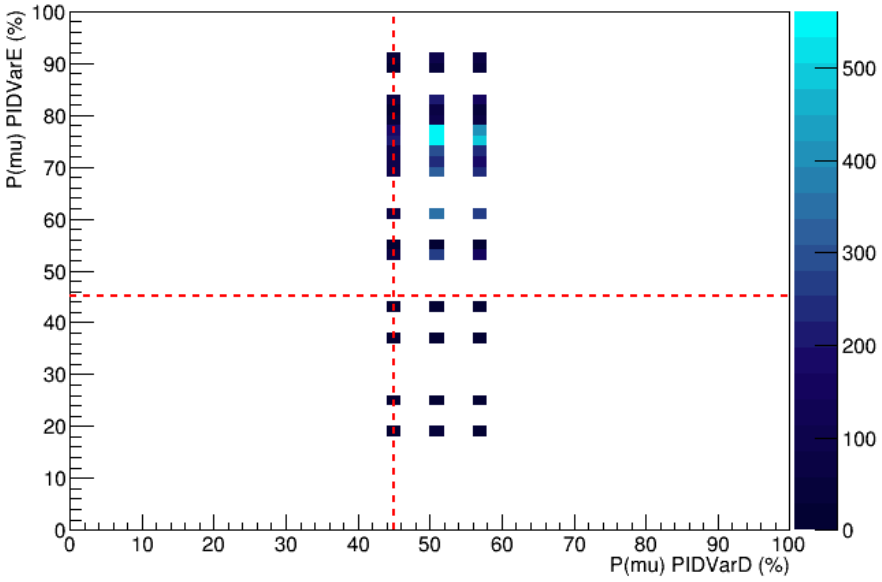

Figure A.75: Comparison of P(μ) returned by PIDVarD and PIDVarE on MC dataset. For all particles identified by both variables, there was a muon identification consistency of 98.0%.

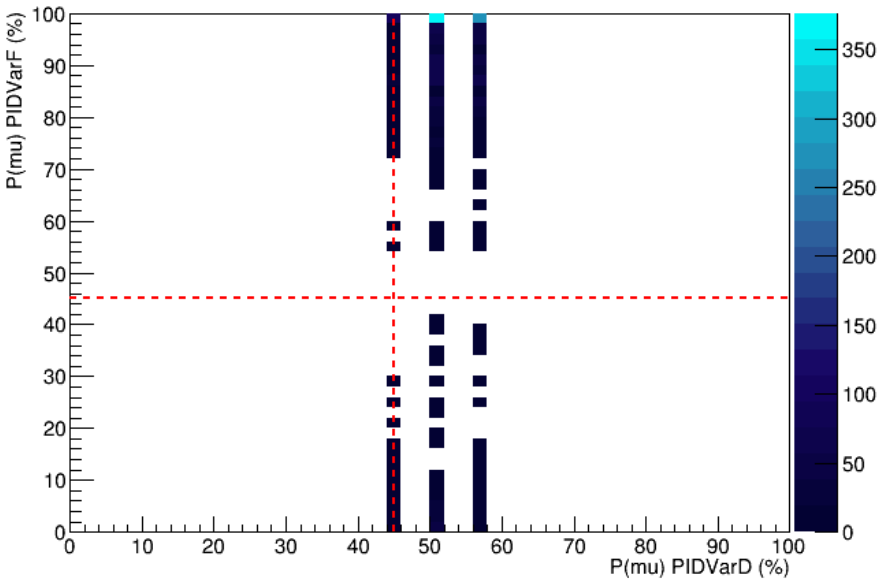

Figure A.76: Comparison of P(μ) returned by PIDVarD and PIDVarF on MC dataset. For all particles identified by both variables, there was a muon identification consistency of 87.3%.

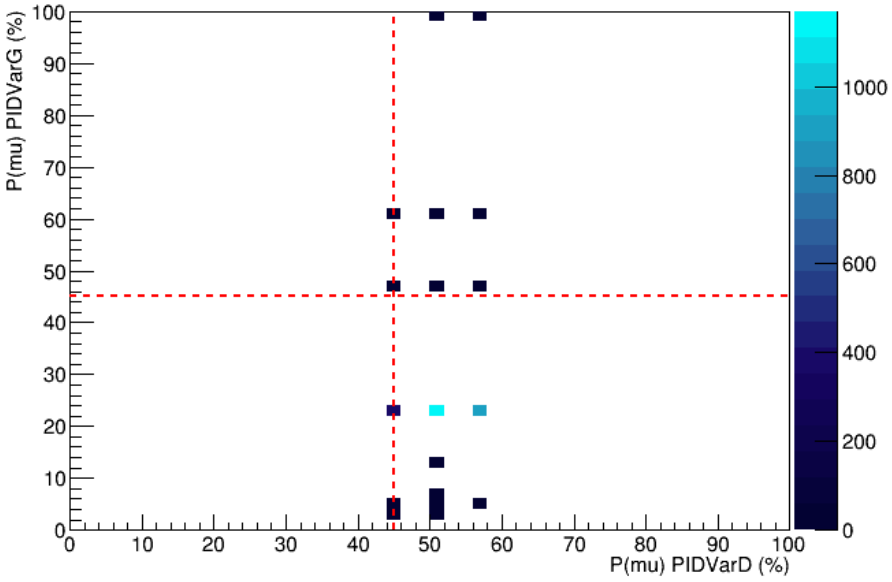

Figure A.77: Comparison of P(μ) returned by PIDVarD and PIDVarG on MC dataset. For all particles identified by both variables, there was a muon identification consistency of 1.56%.

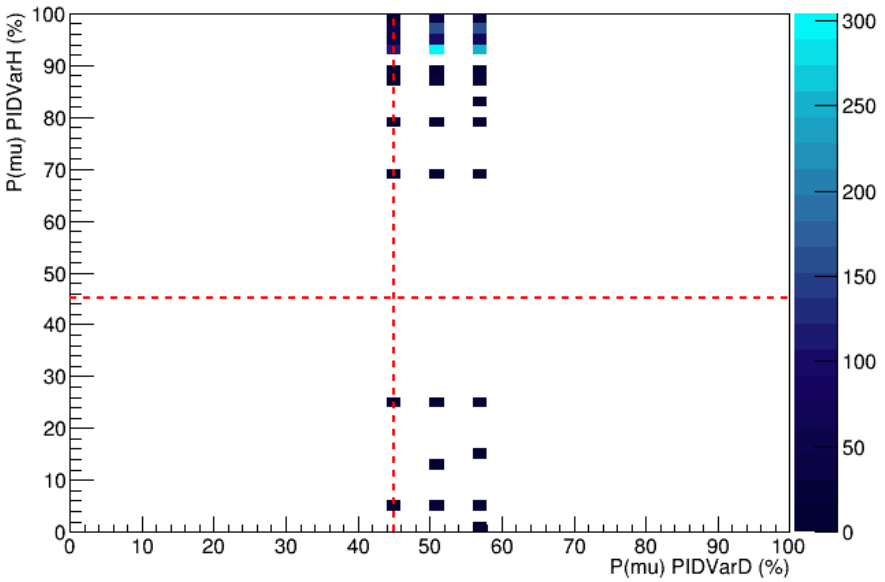

Figure A.78: Comparison of P(μ) returned by PIDVarD and PIDVarH on MC dataset. For all particles identified by both variables, there was a muon identification consistency of 98.8%.

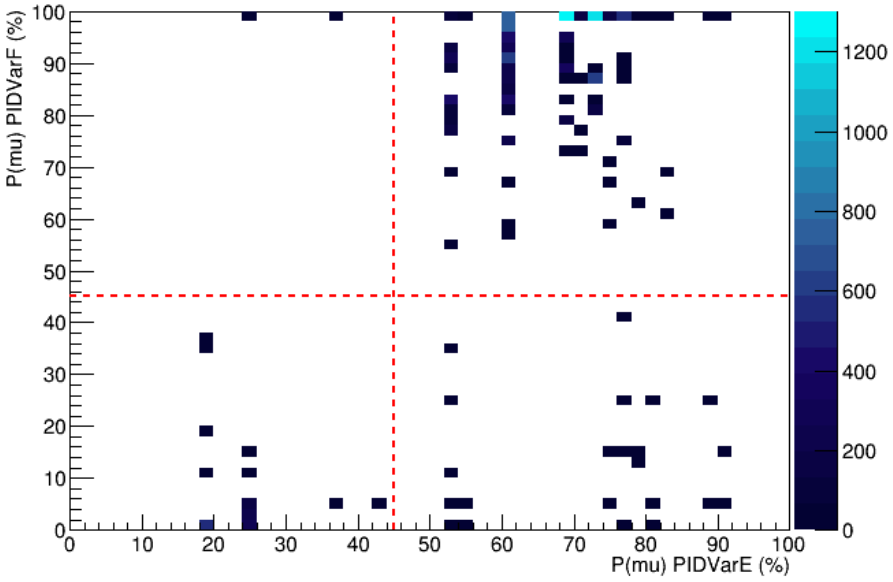

Figure A.79: Comparison of P(μ) returned by PIDVarE and PIDVarF on MC dataset. For all particles identified by both variables, there was a muon identification consistency of 98.7%.

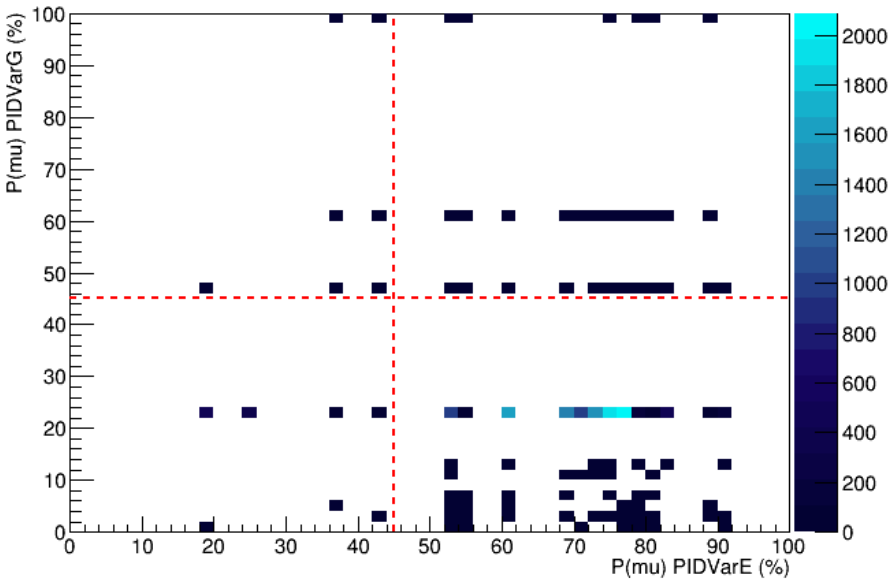

Figure A.80: Comparison of P(μ) returned by PIDVarE and PIDVarG on MC dataset. For all particles identified by both variables, there was a muon identification consistency of 7.55%.

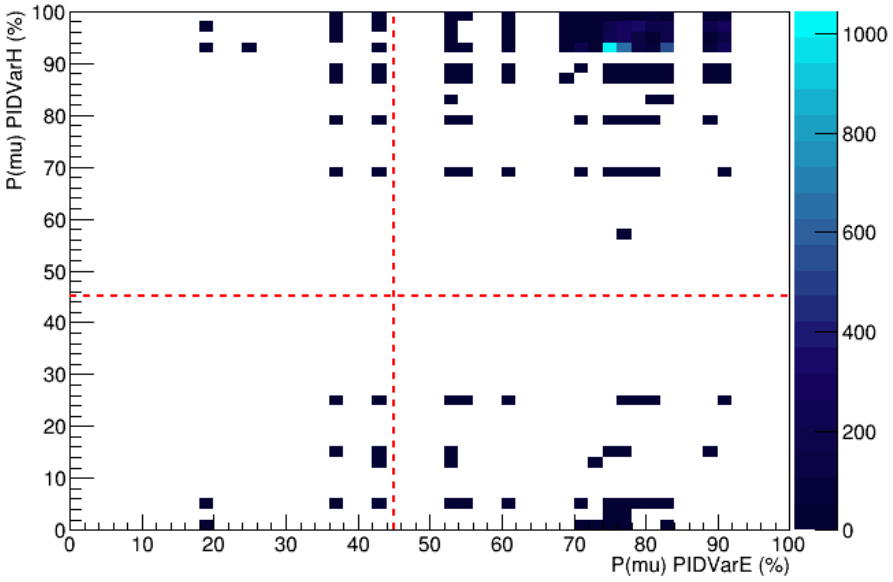

Figure A.81: Comparison of P(μ) returned by PIDVarE and PIDVarH on MC dataset. For all particles identified by both variables, there was a muon identification consistency of 97.6%.

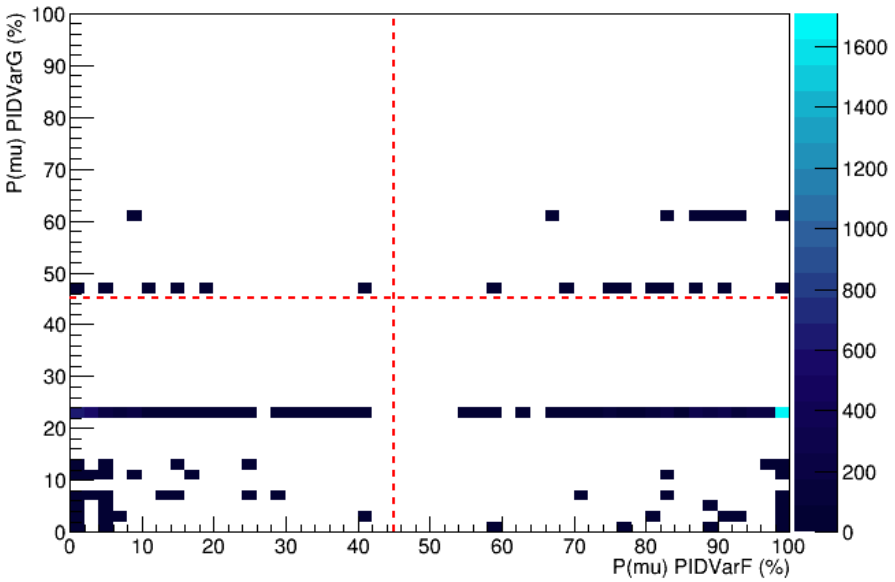

Figure A.82: Comparison of P(μ) returned by PIDVarF and PIDVarG on MC dataset. For all particles identified by both variables, there was a muon identification consistency of 36.7%.

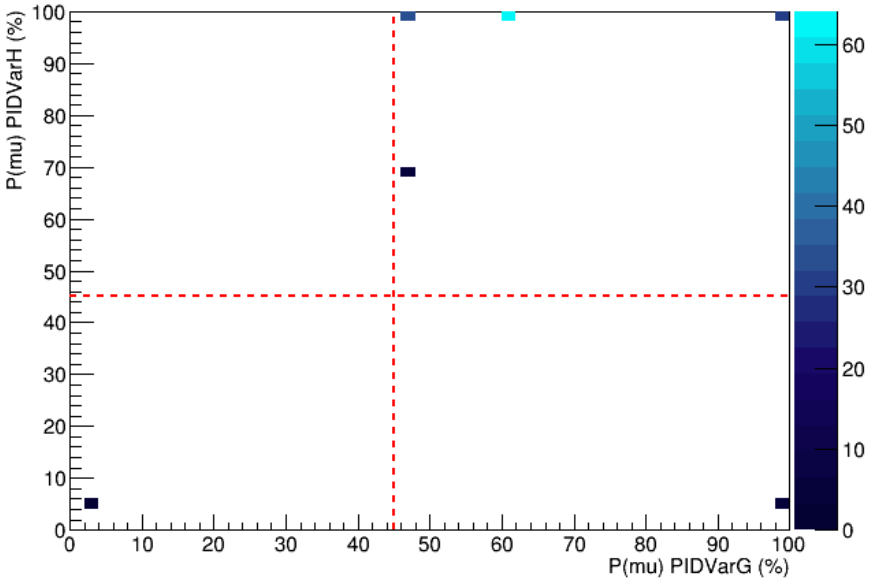

Figure A.83: Comparison of P(μ) returned by PIDVarG and PIDVarH on MC dataset. For all particles identified by both variables, there was a muon identification consistency of 95.7%.

Appendix B

Multiple Coulomb Scattering Error Tables

	Probability per radian											
	θ_X						θ_Y					
Low edge of bin (radians)	Data			Geant			Data			Geant		
-0.1151	0.814	±	0.069	0.693	±	0.056	0.854	±	0.070	0.665	±	0.055
-0.0938	0.807	±	0.055	0.666	±	0.044	0.731	±	0.048	0.554	±	0.038
-0.0754	0.625	±	0.039	0.470	±	0.030	0.671	±	0.041	0.499	±	0.032
-0.0597	0.652	±	0.042	0.462	±	0.032	0.651	±	0.041	0.485	±	0.032
-0.0463	0.561	±	0.036	0.407	±	0.028	1.01	±	0.06	0.725	±	0.047
-0.0347	1.21	±	0.07	0.957	±	0.056	1.33	±	0.06	0.883	±	0.048
-0.0248	3.23	±	0.15	3.00	±	0.13	5.13	±	0.18	3.350	±	0.14
-0.0162	9.04	±	0.32	9.84	±	0.27	14.0	±	0.4	10.3	±	0.3
-0.00895	17.9	±	0.5	21.0	±	0.4	21.4	±	0.5	20.8	±	0.4
-0.00269	20.9	±	0.6	23.3	±	0.5	20.1	±	0.5	23.3	±	0.5
0.00269	20.7	±	0.5	20.7	±	0.4	17.5	±	0.5	20.7	±	0.4
0.00895	12.8	±	0.4	11.0	±	0.3	8.57	±	0.32	10.5	±	0.3
0.0162	4.75	±	0.18	3.52	±	0.14	2.75	±	0.15	3.40	±	0.14
0.0248	1.42	±	0.07	0.989	±	0.054	0.954	±	0.062	1.02	±	0.05
0.0347	0.746	±	0.044	0.533	±	0.034	0.936	±	0.060	0.812	±	0.049
0.0463	0.708	±	0.045	0.541	±	0.035	0.783	±	0.046	0.579	±	0.036
0.0597	0.954	±	0.056	0.735	±	0.044	0.888	±	0.051	0.576	±	0.037
0.0754	1.03	±	0.06	0.703	±	0.045	0.883	±	0.057	0.515	±	0.040
0.0938	1.04	±	0.07	0.629	±	0.052	0.697	±	0.054	0.395	±	0.039

Table B.1: $\theta_{X,Y}$ bin contents for an empty absorber for straight MC and data. Statistical errors only.

	Change in number of entries per bin					
	PID		TOF		Total Systematic Error	
Low edge of bin (radians)	θ_X	θ_Y	θ_X	θ_Y	θ_X	θ_Y
-0.1151	0.0685	0.00169	0.00987	0.0241	0.0692	0.0242
-0.0938	0.0346	0.0817	0.0196	0.0147	0.0398	0.0830
-0.0754	0.0489	0.0704	0.0166	0.00786	0.0517	0.0708
-0.0597	0.0245	0.00683	0.0129	0.0128	0.0277	0.0145
-0.0463	0.0451	0.0945	0.00816	0.0248	0.0458	0.0977
-0.0347	0.0750	0.0626	0.0288	0.0348	0.0804	0.0716
-0.0248	0.0649	0.0742	0.0423	0.0653	0.0774	0.0989
-0.0162	0.0880	0.111	0.0470	0.0780	0.0998	0.135
-0.00895	0.218	0.00266	0.0992	0.0667	0.240	0.0667
-0.00269	0.129	0.0389	0.231	0.302	0.264	0.304
0.00269	0.199	0.0324	0.0382	0.131	0.203	0.135
0.00895	0.0906	0.224	0.0397	0.117	0.0989	0.253
0.0162	0.139	0.0464	0.0181	0.0546	0.140	0.0716
0.0248	0.0170	0.0413	0.0340	0.00671	0.0380	0.0419
0.0347	0.00779	0.0298	0.0034	0.0134	0.00850	0.0327
0.0463	0.0655	0.0123	0.00882	0.00183	0.0661	0.0125
0.0597	0.0315	0.0570	0.0259	0.0237	0.0408	0.0617
0.0754	0.0075	0.0329	0.0159	0.0182	0.0176	0.0376
0.0938	0.0598	0.00542	0.0208	0.0120	0.0634	0.0132

Table B.2: Systematic errors on $\theta_{X,Y}$ bin contents for an empty absorber for data.

	Change in number of entries per bin					
	PID		TOF		Total Systematic Error	
Low edge of bin (radians)	θ_X	θ_Y	θ_X	θ_Y	θ_X	θ_Y
-0.1151	0.166	0.0937	0.00622	0.0137	0.166	0.0947
-0.0938	0.104	0.127	0.0139	0.00662	0.105	0.127
-0.0754	0.123	0.0162	0.00842	0.00137	0.124	0.0163
-0.0597	0.0960	0.0603	0.00439	0.00471	0.0961	0.0605
-0.0463	0.0245	0.159	0.00275	0.0113	0.0247	0.159
-0.0347	0.132	0.0523	0.0138	0.0192	0.132	0.0557
-0.0248	0.165	0.122	0.00163	0.0410	0.165	0.129
-0.0162	0.0240	0.0126	0.0135	0.0628	0.0275	0.0641
-0.00895	0.293	0.256	0.0367	0.00236	0.295	0.256
-0.00269	0.478	0.440	0.148	0.133	0.500	0.460
0.00269	0.549	0.488	0.0325	0.127	0.550	0.505
0.00895	0.109	0.00644	0.0491	0.0250	0.120	0.0258
0.0162	0.112	0.0410	0.00656	0.0345	0.112	0.0536
0.0248	0.0786	0.0647	0.0145	0.000360	0.0799	0.0647
0.0347	0.0489	0.133	0.00538	0.00600	0.0492	0.133
0.0463	0.0992	0.0944	0.00157	0.00483	0.0993	0.0945
0.0597	0.0917	0.0634	0.0118	0.0145	0.0924	0.0650
0.0754	0.0773	0.0825	0.00279	0.0118	0.0774	0.0834
0.0938	0.102	0.0878	0.00496	0.00814	0.102	0.0882

Table B.3: Systematic errors on $\theta_{X,Y}$ bin contents for an empty absorber for straight MC tracks.

	Probability per radian											
	θ_X						θ_Y					
Low edge of bin (radians)	Data			Geant			Data			Geant		
-0.1151	0.814	±	0.098	0.693	±	0.175	0.854	±	0.074	0.665	±	0.109
-0.0938	0.807	±	0.068	0.666	±	0.114	0.731	±	0.096	0.554	±	0.132
-0.0754	0.625	±	0.064	0.470	±	0.127	0.671	±	0.082	0.499	±	0.036
-0.0597	0.652	±	0.050	0.462	±	0.101	0.651	±	0.043	0.485	±	0.069
-0.0463	0.561	±	0.058	0.407	±	0.037	1.01	±	0.11	0.725	±	0.166
-0.0347	1.21	±	0.11	0.957	±	0.143	1.33	±	0.09	0.883	±	0.074
-0.0248	3.23	±	0.17	3.00	±	0.21	5.13	±	0.20	3.350	±	0.19
-0.0162	9.04	±	0.33	9.84	±	0.28	14.0	±	0.4	10.3	±	0.3
-0.00895	17.9	±	0.6	21.0	±	0.5	21.4	±	0.5	20.8	±	0.5
-0.00269	20.9	±	0.6	23.3	±	0.7	20.1	±	0.6	23.3	±	0.7
0.00269	20.7	±	0.6	20.7	±	0.7	17.5	±	0.5	20.7	±	0.7
0.00895	12.8	±	0.4	11.0	±	0.3	8.57	±	0.41	10.5	±	0.3
0.0162	4.75	±	0.23	3.52	±	0.18	2.75	±	0.17	3.40	±	0.15
0.0248	1.42	±	0.08	0.989	±	0.097	0.954	±	0.075	1.02	±	0.08
0.0347	0.746	±	0.045	0.533	±	0.060	0.936	±	0.068	0.812	±	0.142
0.0463	0.708	±	0.080	0.541	±	0.105	0.783	±	0.048	0.579	±	0.101
0.0597	0.954	±	0.070	0.735	±	0.102	0.888	±	0.080	0.576	±	0.075
0.0754	1.03	±	0.06	0.703	±	0.090	0.883	±	0.068	0.515	±	0.093
0.0938	1.04	±	0.10	0.629	±	0.115	0.697	±	0.056	0.395	±	0.096

Table B.4: $\theta_{X,Y}$ bin contents for an empty absorber for straight MC and data. Statistical and systematic errors combined.

Upper edge of bin (radians)	Probability per radian					
	Data			Geant		
0.002	8.01	±	0.54	9.34	±	0.47
0.004	11.3	±	0.5	13.3	±	0.4
0.006	11.9	±	0.3	13.9	±	0.3
0.008	11.3	±	0.5	12.5	±	0.4
0.010	10.7	±	0.6	10.8	±	0.5
0.012	9.63	±	0.40	8.89	±	0.35
0.014	8.52	±	0.34	7.33	±	0.28
0.016	6.39	±	0.30	5.41	±	0.25
0.018	4.66	±	0.25	4.12	±	0.21
0.020	3.25	±	0.20	3.10	±	0.17
0.022	2.01	±	0.14	2.06	±	0.12
0.024	1.55	±	0.12	1.61	±	0.10
0.026	1.07	±	0.09	1.05	±	0.08
0.028	0.930	±	0.087	0.838	±	0.072
0.030	0.727	±	0.071	0.581	±	0.057
0.032	0.519	±	0.050	0.367	±	0.040
0.034	0.410	±	0.038	0.261	±	0.029
0.036	0.417	±	0.037	0.244	±	0.028
0.038	0.321	±	0.028	0.179	±	0.022
0.040	0.367	±	0.033	0.203	±	0.025
0.042	0.254	±	0.024	0.147	±	0.018
0.044	0.250	±	0.025	0.155	±	0.019
0.046	0.217	±	0.024	0.147	±	0.019
0.048	0.175	±	0.021	0.131	±	0.017
0.050	0.158	±	0.021	0.131	±	0.017
0.052	0.0974	±	0.0145	0.0898	±	0.0122
0.054	0.151	±	0.025	0.155	±	0.021
0.056	0.0647	±	0.0115	0.0732	±	0.0099
0.058	0.105	±	0.020	0.130	±	0.017
0.060	0.110	±	0.021	0.146	±	0.019
0.062	0.0771	±	0.0148	0.106	±	0.013
0.064	0.0812	±	0.0144	0.106	±	0.013
0.066	0.148	±	0.024	0.179	±	0.022
0.068	0.138	±	0.021	0.155	±	0.019
0.070	0.147	±	0.021	0.156	±	0.019
0.072	0.170	±	0.023	0.173	±	0.020
0.074	0.151	±	0.020	0.149	±	0.017
0.076	0.162	±	0.020	0.157	±	0.017
0.078	0.128	±	0.015	0.124	±	0.012
0.080	0.363	±	0.038	0.354	±	0.032
0.084	0.482	±	0.046	0.463	±	0.039
0.088	0.449	±	0.040	0.406	±	0.033
0.092	0.461	±	0.039	0.376	±	0.032
0.096	0.534	±	0.042	0.393	±	0.033
0.100	0.530	±	0.035	0.368	±	0.028
0.104	0.594	±	0.036	0.414	±	0.027
0.108	0.649	±	0.044	0.475	±	0.034
0.112	0.707	±	0.060	0.550	±	0.048
0.116	0.465	±	0.046	0.377	±	0.037

Table B.5: θ_{3D} bin contents for an empty absorber for straight MC and data. Statistical errors only.

Upper edge of bin (radians)	Change in number of entries per bin		Total systematic error
	PID	TOF	
0.002	0.394	0.131	0.415
0.004	0.232	0.125	0.263
0.006	0.347	0.062	0.352
0.008	0.243	0.0236	0.244
0.010	0.0576	0.00282	0.0577
0.012	0.0547	0.0349	0.0649
0.014	0.226	0.0379	0.229
0.016	0.00637	0.00741	0.00978
0.018	0.126	0.0241	0.128
0.020	0.0285	0.00453	0.0288
0.022	0.0547	0.0226	0.0592
0.024	0.0565	0.0169	0.059
0.026	0.0119	0.0159	0.0198
0.028	0.0194	0.00565	0.0202
0.030	0.00449	0.00453	0.00638
0.032	0.0222	0.00592	0.023
0.034	0.0223	0.00708	0.0234
0.036	0.0326	0.00231	0.0327
0.038	0.00579	0.000495	0.00581
0.040	0.00124	0.00129	0.00179
0.042	0.0235	0.00459	0.024
0.044	0.0141	0.00393	0.0147
0.046	0.0147	0.0001	0.0147
0.048	0.00183	0.000705	0.00196
0.050	0.0334	0.00354	0.0336
0.052	0.01	0.00178	0.0102
0.054	0.013	0.00002	0.013
0.056	0.0201	0.00195	0.0201
0.058	0.00608	0.00343	0.00698
0.060	0.0135	0.00016	0.0135
0.062	0.0261	0.00271	0.0262
0.064	0.0175	0.00565	0.0184
0.066	0.0293	0.00064	0.0293
0.068	0.0316	0.00403	0.0318
0.070	0.0318	0.00015	0.0318
0.072	0.0218	0.00395	0.0222
0.074	0.0328	0.0039	0.033
0.076	0.0321	0.00412	0.0324
0.078	0.00781	0.00327	0.00847
0.080	0.0864	0.00532	0.0865
0.084	0.0565	0.00806	0.0571
0.088	0.0405	0.0068	0.0411
0.092	0.0235	0.00579	0.0242
0.096	0.0996	0.0019	0.0996
0.100	0.0467	0.00106	0.0467
0.104	0.0519	0.0104	0.053
0.108	0.112	0.00677	0.112
0.112	0.0935	0.0134	0.0945
0.116	0.077	0.00337	0.0771

Table B.6: Systematic errors on θ_{3D} bin contents for an empty absorber for straight MC tracks.

Upper edge of bin (radians)	Probability per radian					
	Data			Geant		
0.002	8.01	±	0.57	9.34	±	0.63
0.004	11.3	±	0.5	13.3	±	0.5
0.006	11.9	±	0.4	13.9	±	0.5
0.008	11.3	±	0.6	12.5	±	0.5
0.010	10.7	±	0.6	10.8	±	0.5
0.012	9.63	±	0.47	8.89	±	0.35
0.014	8.52	±	0.38	7.33	±	0.37
0.016	6.39	±	0.33	5.41	±	0.25
0.018	4.66	±	0.31	4.12	±	0.25
0.020	3.25	±	0.22	3.10	±	0.17
0.022	2.01	±	0.15	2.06	±	0.13
0.024	1.55	±	0.13	1.61	±	0.12
0.026	1.07	±	0.12	1.05	±	0.08
0.028	0.930	±	0.098	0.838	±	0.075
0.030	0.727	±	0.084	0.581	±	0.058
0.032	0.519	±	0.053	0.367	±	0.046
0.034	0.410	±	0.049	0.261	±	0.038
0.036	0.417	±	0.062	0.244	±	0.043
0.038	0.321	±	0.033	0.179	±	0.022
0.040	0.367	±	0.034	0.203	±	0.025
0.042	0.254	±	0.045	0.147	±	0.030
0.044	0.250	±	0.033	0.155	±	0.024
0.046	0.217	±	0.032	0.147	±	0.024
0.048	0.175	±	0.022	0.131	±	0.017
0.050	0.158	±	0.043	0.131	±	0.038
0.052	0.0974	±	0.0161	0.0898	±	0.0158
0.054	0.151	±	0.025	0.155	±	0.025
0.056	0.0647	±	0.0154	0.0732	±	0.0224
0.058	0.105	±	0.027	0.130	±	0.019
0.060	0.110	±	0.030	0.146	±	0.023
0.062	0.0771	±	0.0149	0.106	±	0.029
0.064	0.0812	±	0.0175	0.106	±	0.022
0.066	0.148	±	0.026	0.179	±	0.036
0.068	0.138	±	0.022	0.155	±	0.037
0.070	0.147	±	0.025	0.156	±	0.037
0.072	0.170	±	0.025	0.173	±	0.030
0.074	0.151	±	0.032	0.149	±	0.037
0.076	0.162	±	0.031	0.157	±	0.036
0.078	0.128	±	0.015	0.124	±	0.015
0.080	0.363	±	0.059	0.354	±	0.092
0.084	0.482	±	0.058	0.463	±	0.069
0.088	0.449	±	0.069	0.406	±	0.053
0.092	0.461	±	0.084	0.376	±	0.040
0.096	0.534	±	0.069	0.393	±	0.105
0.100	0.530	±	0.039	0.368	±	0.054
0.104	0.594	±	0.045	0.414	±	0.060
0.108	0.649	±	0.110	0.475	±	0.117
0.112	0.707	±	0.096	0.550	±	0.106
0.116	0.465	±	0.087	0.377	±	0.085

Table B.7: θ_{3D} bin contents for empty absorber for straight MC and data. Systematic and statistical errors combined.

	Probability per radian											
	θ_X						θ_Y					
Low edge of bin (radians)	Data			Geant			Data			Geant		
-0.1151	0.600	±	0.030	0.420	±	0.051	0.708	±	0.030	0.446	±	0.053
-0.0938	0.680	±	0.026	0.507	±	0.051	0.714	±	0.026	0.441	±	0.045
-0.0754	0.635	±	0.025	0.546	±	0.042	0.829	±	0.025	0.528	±	0.042
-0.0597	1.13	±	0.04	1.17	±	0.07	1.62	±	0.04	1.14	±	0.07
-0.0463	2.72	±	0.08	3.11	±	0.15	3.85	±	0.08	3.17	±	0.16
-0.0347	5.40	±	0.12	6.37	±	0.24	6.26	±	0.12	5.92	±	0.23
-0.0248	7.82	±	0.16	8.98	±	0.30	9.56	±	0.16	9.65	±	0.32
-0.0162	10.2	±	0.2	10.9	±	0.3	11.8	±	0.2	11.7	±	0.4
-0.00895	10.5	±	0.2	10.9	±	0.3	11.3	±	0.2	10.9	±	0.3
-0.00269	9.60	±	0.17	9.90	±	0.32	10.3	±	0.2	10.3	±	0.3
0.00269	11.5	±	0.2	11.5	±	0.4	10.7	±	0.2	11.3	±	0.4
0.00895	11.2	±	0.2	11.2	±	0.3	10.6	±	0.2	11.9	±	0.4
0.0162	10.3	±	0.2	10.4	±	0.3	8.45	±	0.15	9.49	±	0.31
0.0248	7.78	±	0.12	7.08	±	0.26	5.80	±	0.12	6.43	±	0.24
0.0347	4.27	±	0.08	3.43	±	0.16	3.56	±	0.08	3.75	±	0.17
0.0463	2.06	±	0.04	1.49	±	0.09	1.54	±	0.04	1.39	±	0.08
0.0597	1.47	±	0.03	0.996	±	0.068	0.839	±	0.026	0.633	±	0.047
0.0754	1.14	±	0.04	0.745	±	0.066	0.931	±	0.035	0.627	±	0.061
0.0938	0.670	±	0.027	0.425	±	0.046	0.622	±	0.027	0.402	±	0.049

Table B.8: $\theta_{X,Y}$ bin contents for LiH for straight MC and data. Statistical errors only.

	Change in number of entries per bin							
	PID		LiH Density		TOF		Total Systematic Error	
Low edge of bin (radians)	θ_X	θ_Y	θ_X	θ_Y	θ_X	θ_Y	θ_X	θ_Y
-0.1151	0.118	0.117	0.00944	0.0723	0.00344	0.00808	0.119	0.138
-0.0938	0.0845	0.0331	0.0427	0.0283	0.00639	0.000230	0.0949	0.0435
-0.0754	0.0751	0.0481	0.146	0.118	0.000155	0.00246	0.165	0.127
-0.0597	0.0645	0.104	0.0754	0.129	0.00677	0.0150	0.0995	0.167
-0.0463	0.236	0.202	0.0796	0.180	0.00473	0.0427	0.249	0.273
-0.0347	0.0509	0.146	0.612	0.0627	0.0356	0.0210	0.615	0.161
-0.0248	0.308	0.0718	0.432	0.274	0.0321	0.0341	0.531	0.285
-0.0162	0.222	0.190	0.438	0.293	0.000650	0.0209	0.491	0.350
-0.00895	0.383	0.555	0.0183	0.0924	0.0198	0.0556	0.384	0.565
-0.00269	0.171	0.204	0.0249	0.338	0.0397	0.112	0.178	0.410
0.00269	0.0912	0.344	0.147	0.215	0.0520	0.0427	0.180	0.408
0.00895	0.135	0.179	0.0530	0.355	0.0762	0.0508	0.164	0.401
0.0162	0.216	0.271	0.155	0.224	0.0428	0.0689	0.270	0.358
0.0248	0.152	0.0380	0.626	0.395	0.00230	0.000215	0.644	0.397
0.0347	0.169	0.342	0.405	0.230	0.00459	0.02585	0.439	0.413
0.0463	0.103	0.236	0.0638	0.153	0.0140	0.0000400	0.122	0.281
0.0597	0.0596	0.0933	0.146	0.0471	0.0125	0.0125	0.158	0.105
0.0754	0.0685	0.0602	0.143	0.0692	0.00644	0.0133	0.159	0.0927
0.0938	0.0103	0.0430	0.0884	0.120	0.00984	0.00072	0.0895	0.127

Table B.9: Systematic errors on $\theta_{X,Y}$ bin contents for LiH for straight MC tracks.

	Probability per radian											
	θ_X						θ_Y					
Low edge of bin (radians)	Data			Geant			Data			Geant		
-0.1151	0.600	±	0.064	0.420	±	0.129	0.708	±	0.114	0.446	±	0.148
-0.0938	0.680	±	0.057	0.507	±	0.108	0.714	±	0.066	0.441	±	0.062
-0.0754	0.635	±	0.150	0.546	±	0.170	0.829	±	0.121	0.528	±	0.134
-0.0597	1.13	±	0.12	1.17	±	0.12	1.62	±	0.14	1.14	±	0.18
-0.0463	2.72	±	0.13	3.11	±	0.29	3.85	±	0.22	3.17	±	0.32
-0.0347	5.40	±	0.63	6.37	±	0.66	6.26	±	0.15	5.92	±	0.28
-0.0248	7.82	±	0.48	8.98	±	0.61	9.56	±	0.35	9.65	±	0.43
-0.0162	10.2	±	0.5	10.9	±	0.6	11.8	±	0.4	11.7	±	0.5
-0.00895	10.5	±	0.3	10.9	±	0.5	11.3	±	0.5	10.9	±	0.7
-0.00269	9.60	±	0.25	9.90	±	0.36	10.3	±	0.4	10.3	±	0.5
0.00269	11.5	±	0.2	11.5	±	0.4	10.7	±	0.3	11.3	±	0.5
0.00895	11.2	±	0.3	11.2	±	0.4	10.6	±	0.4	11.9	±	0.5
0.0162	10.3	±	0.3	10.4	±	0.4	8.45	±	0.27	9.49	±	0.48
0.0248	7.78	±	0.64	7.08	±	0.69	5.80	±	0.41	6.43	±	0.46
0.0347	4.27	±	0.42	3.43	±	0.47	3.56	±	0.26	3.75	±	0.45
0.0463	2.06	±	0.09	1.49	±	0.15	1.54	±	0.16	1.39	±	0.29
0.0597	1.47	±	0.15	0.996	±	0.172	0.839	±	0.061	0.633	±	0.115
0.0754	1.14	±	0.15	0.745	±	0.172	0.931	±	0.083	0.627	±	0.111
0.0938	0.670	±	0.109	0.425	±	0.101	0.622	±	0.125	0.402	±	0.136

Table B.10: $\theta_{X,Y}$ bin contents for LiH for straight MC and data. Systematic and statistical errors combined.

Upper edge of bin (radians)	Probability per radian					
	Data			Geant		
0.002	1.59	±	0.08	1.52	±	0.17
0.004	2.56	±	0.11	2.41	±	0.22
0.006	3.54	±	0.10	3.29	±	0.20
0.008	4.38	±	0.09	4.09	±	0.18
0.010	4.68	±	0.12	4.51	±	0.24
0.012	4.74	±	0.16	4.74	±	0.32
0.014	5.19	±	0.17	5.41	±	0.35
0.016	4.66	±	0.13	5.03	±	0.27
0.018	5.14	±	0.14	5.69	±	0.29
0.020	5.24	±	0.16	5.86	±	0.32
0.022	5.52	±	0.17	6.16	±	0.34
0.024	4.61	±	0.14	5.01	±	0.28
0.026	4.81	±	0.14	5.03	±	0.28
0.028	5.12	±	0.15	5.11	±	0.29
0.030	4.54	±	0.13	4.45	±	0.26
0.032	4.07	±	0.12	4.06	±	0.24
0.034	3.56	±	0.12	3.71	±	0.24
0.036	3.01	±	0.11	3.26	±	0.21
0.038	2.37	±	0.08	2.61	±	0.17
0.040	2.44	±	0.09	2.66	±	0.19
0.042	1.85	±	0.07	1.94	±	0.15
0.044	1.77	±	0.07	1.78	±	0.14
0.046	1.74	±	0.07	1.67	±	0.14
0.048	1.17	±	0.05	1.10	±	0.10
0.050	1.01	±	0.05	0.949	±	0.089
0.052	0.925	±	0.043	0.871	±	0.084
0.054	0.638	±	0.031	0.595	±	0.061
0.056	0.569	±	0.029	0.517	±	0.057
0.058	0.569	±	0.031	0.501	±	0.061
0.060	0.622	±	0.035	0.531	±	0.069
0.062	0.342	±	0.020	0.289	±	0.039
0.064	0.337	±	0.021	0.289	±	0.040
0.066	0.375	±	0.024	0.335	±	0.046
0.068	0.210	±	0.013	0.199	±	0.026
0.070	0.250	±	0.016	0.245	±	0.031
0.072	0.296	±	0.019	0.292	±	0.036
0.074	0.293	±	0.017	0.278	±	0.034
0.076	0.372	±	0.020	0.325	±	0.038
0.078	0.251	±	0.012	0.201	±	0.023
0.080	0.500	±	0.023	0.367	±	0.042
0.084	0.502	±	0.023	0.347	±	0.040
0.088	0.663	±	0.029	0.444	±	0.051
0.092	0.422	±	0.018	0.277	±	0.032
0.096	0.404	±	0.017	0.266	±	0.030
0.100	0.302	±	0.012	0.202	±	0.021
0.104	0.545	±	0.022	0.372	±	0.039
0.108	0.532	±	0.024	0.377	±	0.042
0.112	0.427	±	0.022	0.311	±	0.039
0.116	0.414	±	0.023	0.306	±	0.041

Table B.11: θ_{3D} bin contents for LiH for straight MC and data. Statistical errors only.

Upper edge of bin (radians)	Change in number of entries per bin			Total systematic error
	PID	LiH Density	TOF	
0.002	0.0105	0.0498	0.0281	0.0581
0.004	0.2620	0.1200	0.0247	0.2890
0.006	0.0691	0.0210	0.0489	0.0872
0.008	0.0692	0.0514	0.0553	0.1020
0.010	0.0608	0.0671	0.0137	0.0916
0.012	0.1820	0.0887	0.0028	0.2030
0.014	0.1290	0.1470	0.0248	0.1970
0.016	0.1330	0.0718	0.0161	0.1520
0.018	0.1730	0.3350	0.0287	0.3780
0.020	0.1800	0.1170	0.0224	0.2160
0.022	0.2440	0.0322	0.0569	0.2530
0.024	0.1150	0.2750	0.0191	0.2990
0.026	0.0594	0.0600	0.0111	0.0852
0.028	0.0229	0.1480	0.0114	0.1500
0.030	0.0923	0.0356	0.0312	0.1040
0.032	0.0327	0.0041	0.0460	0.0566
0.034	0.0365	0.1970	0.0044	0.2000
0.036	0.1200	0.1440	0.0350	0.1900
0.038	0.0278	0.1740	0.0036	0.1770
0.040	0.0407	0.0659	0.0321	0.0838
0.042	0.0267	0.0067	0.0070	0.0284
0.044	0.0348	0.0107	0.0122	0.0384
0.046	0.1030	0.0173	0.0264	0.1080
0.048	0.0819	0.0589	0.0231	0.1040
0.050	0.1750	0.0110	0.0001	0.1750
0.052	0.0074	0.1120	0.0114	0.1130
0.054	0.0013	0.1080	0.0044	0.1080
0.056	0.0977	0.0560	0.0096	0.1130
0.058	0.1350	0.1220	0.0006	0.1820
0.060	0.0431	0.0601	0.0021	0.0740
0.062	0.0269	0.0229	0.0031	0.0355
0.064	0.0444	0.0134	0.0055	0.0467
0.066	0.0202	0.0318	0.0070	0.0384
0.068	0.0120	0.0059	0.0047	0.0141
0.070	0.0514	0.0286	0.0047	0.0590
0.072	0.0085	0.0199	0.0067	0.0227
0.074	0.0824	0.0535	0.0047	0.0983
0.076	0.0137	0.0320	0.0077	0.0356
0.078	0.0128	0.0810	0.0042	0.0821
0.080	0.0146	0.0166	0.0084	0.0237
0.084	0.0514	0.0201	0.0073	0.0557
0.088	0.0342	0.0384	0.0102	0.0524
0.092	0.0246	0.0197	0.0063	0.0321
0.096	0.0614	0.0486	0.0047	0.0784
0.100	0.0768	0.0121	0.0024	0.0778
0.104	0.0625	0.0008	0.0047	0.0627
0.108	0.0964	0.0175	0.0030	0.0980
0.112	0.0723	0.0801	0.0016	0.1080
0.116	0.0277	0.0314	0.0012	0.0419

Table B.12: Systematic errors on θ_{3D} measurement for straight MC tracks through LiH.

Upper edge of bin (radians)	Change in number of entries per bin			Total systematic error
	PID	LiH Density	TOF	
0.002	0.0984	0.0498	0.0360	0.116
0.004	0.109	0.12	0.0323	0.165
0.006	0.100	0.021	0.0449	0.112
0.008	0.0858	0.0514	0.0305	0.105
0.010	0.057	0.0671	0.0153	0.0893
0.012	0.0773	0.0887	0.00875	0.118
0.014	0.0147	0.147	0.0467	0.155
0.016	0.0266	0.0718	0.0677	0.102
0.018	0.0289	0.335	0.108	0.353
0.020	0.0942	0.117	0.108	0.185
0.022	0.220	0.0322	0.0198	0.223
0.024	0.118	0.275	0.0332	0.301
0.026	0.0775	0.06	0.00883	0.0984
0.028	0.0978	0.148	0.0488	0.184
0.030	0.173	0.0356	0.0581	0.186
0.032	0.0383	0.00408	0.038	0.0541
0.034	0.0105	0.197	0.0112	0.197
0.036	0.0859	0.144	0.0306	0.170
0.038	0.0254	0.174	0.00277	0.176
0.040	0.0258	0.0659	0.0384	0.0805
0.042	0.0124	0.00666	0.0191	0.0237
0.044	0.00556	0.0107	0.0343	0.0363
0.046	0.048	0.0173	0.0574	0.0768
0.048	0.0177	0.0589	0.0473	0.0776
0.050	0.102	0.011	0.0148	0.103
0.052	0.145	0.112	0.0281	0.186
0.054	0.118	0.108	0.00107	0.160
0.056	0.0138	0.056	0.0158	0.0597
0.058	0.0666	0.122	0.000685	0.139
0.060	0.0612	0.0601	0.00499	0.0859
0.062	0.0208	0.0229	0.00348	0.0311
0.064	0.0123	0.0134	0.00757	0.0197
0.066	0.0142	0.0318	0.00815	0.0358
0.068	0.0294	0.00586	0.00451	0.0303
0.070	0.0421	0.0286	0.00596	0.0512
0.072	0.0191	0.0199	0.0054	0.0281
0.074	0.0831	0.0535	0.00584	0.0989
0.076	0.0143	0.0320	0.00853	0.0360
0.078	0.0138	0.0810	0.00523	0.0823
0.080	0.0141	0.0166	0.0116	0.0247
0.084	0.0484	0.0201	0.0103	0.0534
0.088	0.0293	0.0384	0.014	0.0502
0.092	0.0389	0.0197	0.0077	0.0443
0.096	0.0179	0.0486	0.00489	0.0520
0.100	0.0653	0.0121	0.00218	0.0665
0.104	0.0304	0.000765	0.00392	0.0307
0.108	0.0306	0.0175	0.00295	0.0354
0.112	0.0146	0.0801	0.00246	0.0814
0.116	0.0574	0.0314	0.00289	0.0655

Table B.13: Systematic errors on θ_{3D} bin contents for LiH for data. Errors for denstiy taken from MC.

Upper edge of bin (radians)	Probability per radian					
	Data			Geant		
0.002	1.59	±	0.14	1.52	±	0.18
0.004	2.56	±	0.20	2.41	±	0.36
0.006	3.54	±	0.15	3.29	±	0.22
0.008	4.38	±	0.14	4.09	±	0.21
0.010	4.68	±	0.15	4.51	±	0.26
0.012	4.74	±	0.20	4.74	±	0.38
0.014	5.19	±	0.23	5.41	±	0.40
0.016	4.66	±	0.17	5.03	±	0.31
0.018	5.14	±	0.38	5.69	±	0.47
0.020	5.24	±	0.24	5.86	±	0.38
0.022	5.52	±	0.28	6.16	±	0.43
0.024	4.61	±	0.33	5.01	±	0.41
0.026	4.81	±	0.17	5.03	±	0.29
0.028	5.12	±	0.23	5.11	±	0.33
0.030	4.54	±	0.23	4.45	±	0.28
0.032	4.07	±	0.13	4.06	±	0.25
0.034	3.56	±	0.23	3.71	±	0.31
0.036	3.01	±	0.20	3.26	±	0.29
0.038	2.37	±	0.20	2.61	±	0.25
0.040	2.44	±	0.12	2.66	±	0.20
0.042	1.85	±	0.08	1.94	±	0.15
0.044	1.77	±	0.08	1.78	±	0.15
0.046	1.74	±	0.11	1.67	±	0.18
0.048	1.17	±	0.09	1.10	±	0.14
0.050	1.01	±	0.11	0.949	±	0.197
0.052	0.925	±	0.190	0.871	±	0.141
0.054	0.638	±	0.163	0.595	±	0.124
0.056	0.569	±	0.066	0.517	±	0.127
0.058	0.569	±	0.142	0.501	±	0.192
0.060	0.622	±	0.093	0.531	±	0.101
0.062	0.342	±	0.037	0.289	±	0.053
0.064	0.337	±	0.029	0.289	±	0.062
0.066	0.375	±	0.043	0.335	±	0.060
0.068	0.210	±	0.033	0.199	±	0.029
0.070	0.250	±	0.054	0.245	±	0.067
0.072	0.296	±	0.034	0.292	±	0.043
0.074	0.293	±	0.100	0.278	±	0.104
0.076	0.372	±	0.041	0.325	±	0.052
0.078	0.251	±	0.083	0.201	±	0.085
0.080	0.500	±	0.034	0.367	±	0.048
0.084	0.502	±	0.058	0.347	±	0.068
0.088	0.663	±	0.058	0.444	±	0.073
0.092	0.422	±	0.048	0.277	±	0.045
0.096	0.404	±	0.055	0.266	±	0.084
0.100	0.302	±	0.068	0.202	±	0.081
0.104	0.545	±	0.038	0.372	±	0.074
0.108	0.532	±	0.043	0.377	±	0.107
0.112	0.427	±	0.084	0.311	±	0.115
0.116	0.414	±	0.069	0.306	±	0.059

Table B.14: θ_{3D} bin contents for LiH for straight MC and data. Systematic and statistical errors combined.

Low edge of bin (radians)	Probability per radian					
	θ_X			θ_Y		
-0.1151	0.0142	±	0.0290	0.0115	±	0.0217
-0.0938	0.00908	±	0.01719	0.0226	±	0.0379
-0.0754	0.0131	±	0.0203	0.0112	±	0.0140
-0.0597	0.0262	±	0.0281	0.0245	±	0.0200
-0.0463	0.0801	±	0.0511	0.0740	±	0.0386
-0.0347	0.218	±	0.080	0.208	±	0.076
-0.0248	0.722	±	0.183	0.610	±	0.164
-0.0162	2.99	±	0.58	3.12	±	0.58
-0.00895	22.0	±	1.7	22.2	±	1.9
-0.00269	46.0	±	2.6	45.2	±	3.0
0.00269	23.6	±	1.8	24.0	±	2.0
0.00895	3.42	±	0.65	3.36	±	0.60
0.0162	0.698	±	0.187	0.753	±	0.199
0.0248	0.205	±	0.079	0.232	±	0.089
0.0347	0.0887	±	0.0525	0.0907	±	0.0536
0.0463	0.0287	±	0.0278	0.0242	±	0.0235
0.0597	0.0198	±	0.0276	0.0156	±	0.0221
0.0754	0.00668	±	0.01138	0.00903	±	0.01610
0.0938	0.0045	±	0.0084	0.0159	±	0.0316

Table B.15: $\theta_{X,Y}$ bin contents for an empty absorber for helical MC tracks. Statistical errors only.

	Change in number of entries per bin PID	
Low edge of bin (radians)	θ_X	θ_Y
-0.1151	0.00272	0.00278
-0.0938	0.0135	0.0136
-0.0754	0.00192	0.00193
-0.0597	0.00161	0.00161
-0.0463	0.00617	0.00632
-0.0347	0.00957	0.0177
-0.0248	0.112	0.115
-0.0162	0.129	0.141
-0.00895	0.232	0.264
-0.00269	0.742	0.780
0.00269	0.445	0.472
0.00895	0.0556	0.0839
0.0162	0.0553	0.0607
0.0248	0.0272	0.0228
0.0347	0.00203	0.00653
0.0463	0.00443	0.00434
0.0597	0.00424	0.00415
0.0754	0.00235	0.00241
0.0938	0.0114	0.0115

Table B.16: Systematic errors on $\theta_{X,Y}$ bin contents for an empty absorber for helical MC tracks.

Low edge of bin (radians)	Probability per radian					
	θ_X			θ_Y		
-0.1151	0.0142	±	0.0144	0.0115	±	0.0118
-0.0938	0.00908	±	0.01629	0.0226	±	0.0264
-0.0754	0.0131	±	0.0132	0.0112	±	0.0114
-0.0597	0.0262	±	0.0262	0.0245	±	0.0246
-0.0463	0.0801	±	0.0804	0.0740	±	0.0742
-0.0347	0.218	±	0.218	0.208	±	0.209
-0.0248	0.722	±	0.730	0.610	±	0.621
-0.0162	2.99	±	2.99	3.12	±	3.12
-0.00895	22.0	±	22.0	22.2	±	22.2
-0.00269	46.0	±	46.0	45.2	±	45.2
0.00269	23.6	±	23.6	24.0	±	24.0
0.00895	3.42	±	3.42	3.36	±	3.36
0.0162	0.698	±	0.700	0.753	±	0.756
0.0248	0.205	±	0.207	0.232	±	0.234
0.0347	0.0887	±	0.0887	0.0907	±	0.0909
0.0463	0.0287	±	0.0290	0.0242	±	0.0246
0.0597	0.0198	±	0.0203	0.0156	±	0.0161
0.0754	0.00668	±	0.00708	0.00903	±	0.00935
0.0938	0.0045	±	0.0123	0.0159	±	0.0196

Table B.17: $\theta_{X,Y}$ bin contents for an empty absorber for helical MC tracks. Statistical and systematic errors combined.

Upper edge of bin (radians)	Probability per radian			Upper edge of bin (radians)	Probability per radian		
0.001	2.81	±	0.85	0.036	0.0468	±	0.0315
0.002	7.95	±	1.8	0.037	0.0597	±	0.0411
0.003	11.7	±	1.6	0.038	0.0461	±	0.0329
0.004	13.1	±	1.3	0.039	0.0393	±	0.0292
0.005	13.1	±	1.7	0.040	0.0305	±	0.0237
0.006	11.6	±	1.8	0.041	0.0196	±	0.0160
0.007	9.59	±	1.59	0.042	0.0175	±	0.0149
0.008	7.30	±	1.26	0.043	0.0198	±	0.0175
0.009	5.47	±	0.99	0.044	0.0244	±	0.0219
0.010	3.89	±	0.76	0.045	0.0269	±	0.0241
0.011	2.80	±	0.60	0.046	0.0182	±	0.0160
0.012	2.08	±	0.49	0.047	0.0116	±	0.0098
0.013	1.51	±	0.38	0.048	0.0165	±	0.0134
0.014	1.23	±	0.34	0.049	0.0216	±	0.0167
0.015	0.776	±	0.238	0.050	0.0170	±	0.0127
0.016	0.708	±	0.242	0.051	0.0123	±	0.0089
0.017	0.557	±	0.207	0.052	0.00489	±	0.00349
0.018	0.468	±	0.187	0.053	0.00485	±	0.00347
0.019	0.328	±	0.140	0.054	0.00239	±	0.00175
0.020	0.296	±	0.132	0.055	0.00708	±	0.00538
0.021	0.279	±	0.129	0.056	0.0117	±	0.0092
0.022	0.230	±	0.109	0.057	0.00231	±	0.00192
0.023	0.220	±	0.107	0.058	0.00690	±	0.00601
0.024	0.233	±	0.118	0.059	0.00460	±	0.00416
0.025	0.198	±	0.105	0.060	0.00463	±	0.00433
0.026	0.165	±	0.093	0.061	0.0141	±	0.0136
0.027	0.155	±	0.092	0.062	0.00475	±	0.00484
0.028	0.112	±	0.070	0.063	0.00242	±	0.00262
0.029	0.116	±	0.076	0.064	0.00247	±	0.00287
0.030	0.0832	±	0.0560	0.065	0.00756	±	0.00946
0.031	0.0919	±	0.0629	0.066	0.0103	±	0.0138
0.032	0.0776	±	0.0533	0.067	0	±	0
0.033	0.0659	±	0.0449	0.068	0.00795	±	0.01180
0.034	0.0474	±	0.0321	0.069	0	±	0
0.035	0.0561	±	0.0376	0.070	0.00269	±	0.00416

Table B.18: θ_{3D} bin contents for an empty absorber for helical MC. Statistical errors only.

Upper edge of bin (radians)	Change in number of entries per bin PID	Upper edge of bin (radians)	Change in number of entries per bin PID
0.001	0.04	0.036	0.0022
0.002	0.09	0.037	0.0009
0.003	0.1	0.038	0.0038
0.004	0.1	0.039	0.0020
0.005	0.1	0.040	0.0003
0.006	0.1	0.041	0.0016
0.007	0.04	0.042	0.0016
0.008	0.06	0.043	0.0019
0.009	0.08	0.044	0.0022
0.010	0.04	0.045	0.0020
0.011	0.03	0.046	0.0014
0.012	0.01	0.047	0.0003
0.013	0.03	0.048	0.0001
0.014	0.04	0.049	0.0006
0.015	0.040	0.050	0.0008
0.016	0.041	0.051	0.0008
0.017	0.035	0.052	0.00033
0.018	0.027	0.053	0.00031
0.019	0.018	0.054	0.00013
0.020	0.009	0.055	0.00260
0.021	0.001	0.056	0.0005
0.022	0.008	0.057	0.00010
0.023	0.011	0.058	0.00032
0.024	0.009	0.059	0.00025
0.025	0.010	0.060	0.00031
0.026	0.009	0.061	0.0033
0.027	0.008	0.062	0.00048
0.028	0.006	0.063	0.00029
0.029	0.008	0.064	0.00035
0.030	0.0038	0.065	0.00124
0.031	0.0039	0.066	0.0019
0.032	0.0030	0.067	0
0.033	0.0000	0.068	0.00169
0.034	0.0012	0.069	0
0.035	0.0008	0.070	0.00269

Table B.19: Systematic errors on θ_{3D} bin contents for an empty absorber for helical MC tracks.

Upper edge of bin (radians)	Probability per radian			Upper edge of bin (radians)	Probability per radian		
0.001	2.81	±	0.847	0.036	0.0468	±	0.0316
0.002	7.95	±	1.84	0.037	0.0597	±	0.0411
0.003	11.7	±	1.6	0.038	0.0461	±	0.0331
0.004	13.1	±	1.3	0.039	0.0393	±	0.0292
0.005	13.1	±	1.7	0.040	0.0305	±	0.0237
0.006	11.6	±	1.8	0.041	0.0196	±	0.0161
0.007	9.59	±	1.59	0.042	0.0175	±	0.0150
0.008	7.30	±	1.26	0.043	0.0198	±	0.0176
0.009	5.47	±	1.00	0.044	0.0244	±	0.0220
0.010	3.89	±	0.76	0.045	0.0269	±	0.0242
0.011	2.80	±	0.60	0.046	0.0182	±	0.0161
0.012	2.08	±	0.49	0.047	0.0116	±	0.0098
0.013	1.51	±	0.38	0.048	0.0165	±	0.0134
0.014	1.23	±	0.34	0.049	0.0216	±	0.0167
0.015	0.776	±	0.241	0.050	0.0170	±	0.0127
0.016	0.708	±	0.245	0.051	0.0123	±	0.0089
0.017	0.557	±	0.210	0.052	0.00489	±	0.00351
0.018	0.468	±	0.189	0.053	0.00485	±	0.00348
0.019	0.328	±	0.141	0.054	0.00239	±	0.00175
0.020	0.296	±	0.132	0.055	0.00708	±	0.00598
0.021	0.279	±	0.129	0.056	0.0117	±	0.0093
0.022	0.230	±	0.109	0.057	0.00231	±	0.00192
0.023	0.220	±	0.108	0.058	0.00690	±	0.00602
0.024	0.233	±	0.118	0.059	0.00460	±	0.00417
0.025	0.198	±	0.106	0.060	0.00463	±	0.00434
0.026	0.165	±	0.093	0.061	0.0141	±	0.0140
0.027	0.155	±	0.093	0.062	0.00475	±	0.00486
0.028	0.112	±	0.071	0.063	0.00242	±	0.00264
0.029	0.116	±	0.076	0.064	0.00247	±	0.00289
0.030	0.0832	±	0.0561	0.065	0.00756	±	0.00954
0.031	0.0919	±	0.0630	0.066	0.0103	±	0.0139
0.032	0.0776	±	0.0534	0.067	0	±	0
0.033	0.0659	±	0.0449	0.068	0.00795	±	0.01190
0.034	0.0474	±	0.0321	0.069	0	±	0
0.035	0.0561	±	0.0376	0.070	0.00269	±	0.00495

Table B.20: θ_{3D} bin contents for an empty absorber for helical MC. Systematic and statistical errors combined.

Low edge of bin (radians)	Probability per radian					
	θ_X			θ_Y		
-0.1151	0.0303	±	0.0097	0.0437	±	0.0139
-0.0938	0.0775	±	0.0213	0.0648	±	0.0178
-0.0754	0.162	±	0.032	0.153	±	0.030
-0.0597	0.520	±	0.060	0.548	±	0.064
-0.0463	1.74	±	0.11	1.77	±	0.11
-0.0347	4.85	±	0.21	4.88	±	0.21
-0.0248	9.32	±	0.32	9.12	±	0.31
-0.0162	12.7	±	0.4	13.0	±	0.4
-0.00895	13.9	±	0.5	14.2	±	0.5
-0.00269	13.4	±	0.4	13.2	±	0.4
0.00269	14.3	±	0.5	14.2	±	0.5
0.00895	12.6	±	0.4	12.7	±	0.4
0.0162	9.22	±	0.32	9.07	±	0.31
0.0248	4.82	±	0.20	4.79	±	0.20
0.0347	1.78	±	0.11	1.56	±	0.10
0.0463	0.481	±	0.056	0.511	±	0.057
0.0597	0.170	±	0.034	0.195	±	0.037
0.0754	0.0557	±	0.0154	0.0878	±	0.0231
0.0938	0.0344	±	0.0111	0.0441	±	0.0136

Table B.21: $\theta_{X,Y}$ bin contents for LiH for helical MC tracks. Statistical errors only.

	Change in number of entries per bin					
	PID		LiH Density		Total Systematic Error	
Low edge of bin (radians)	θ_X	θ_Y	θ_X	θ_Y	θ_X	θ_Y
-0.1151	0.0000600	0.000110	0.00446	0.00674	0.00446	0.00674
-0.0938	0.000170	0.000170	0.00673	0.0145	0.0067	0.0145
-0.0754	0.000360	0.00809	0.000905	0.00777	0.000974	0.0112
-0.0597	0.00118	0.00542	0.0308	0.0309	0.0308	0.0314
-0.0463	0.00855	0.0128	0.0565	0.0414	0.0571	0.0434
-0.0347	0.00150	0.00984	0.130	0.0387	0.130	0.0399
-0.0248	0.00421	0.00862	0.120	0.129	0.120	0.129
-0.0162	0.00782	0.0374	0.0621	0.0487	0.0626	0.0614
-0.00895	0.00638	0.00933	0.0855	0.00887	0.0858	0.0129
-0.00269	0.000680	0.0161	0.0479	0.175	0.0479	0.176
0.00269	0.00706	0.0272	0.0510	0.0664	0.0515	0.0718
0.00895	0.0132	0.000250	0.177	0.127	0.177	0.127
0.0162	0.0124	0.00378	0.201	0.160	0.201	0.160
0.0248	0.00165	0.0103	0.0787	0.0135	0.0787	0.0169
0.0347	0.00850	0.000650	0.0374	0.0572	0.0383	0.0572
0.0463	0.00111	0.00124	0.0100	0.0280	0.0101	0.0281
0.0597	0.000400	0.000520	0.00783	0.00264	0.00784	0.00270
0.0754	0.000140	0.000230	0.00848	0.00300	0.00848	0.00300
0.0938	0.0000800	0.000120	0.00412	0.000865	0.00412	0.000873

Table B.22: Systematic errors on $\theta_{X,Y}$ bin contents for LiH for helical MC tracks.

Low edge of bin (radians)	Probability per radian θ_X			θ_Y		
-0.1151	0.0303	±	0.0106	0.0437	±	0.0154
-0.0938	0.0775	±	0.0223	0.0648	±	0.0229
-0.0754	0.162	±	0.032	0.153	±	0.032
-0.0597	0.520	±	0.068	0.548	±	0.071
-0.0463	1.74	±	0.12	1.77	±	0.12
-0.0347	4.85	±	0.24	4.88	±	0.22
-0.0248	9.32	±	0.35	9.12	±	0.33
-0.0162	12.7	±	0.4	13.0	±	0.4
-0.00895	13.9	±	0.5	14.2	±	0.5
-0.00269	13.4	±	0.4	13.2	±	0.5
0.00269	14.3	±	0.5	14.2	±	0.5
0.00895	12.6	±	0.4	12.7	±	0.4
0.0162	9.22	±	0.38	9.07	±	0.35
0.0248	4.82	±	0.22	4.79	±	0.20
0.0347	1.78	±	0.12	1.56	±	0.11
0.0463	0.481	±	0.057	0.511	±	0.064
0.0597	0.170	±	0.035	0.195	±	0.037
0.0754	0.0557	±	0.0176	0.0878	±	0.0233
0.0938	0.0344	±	0.0118	0.0441	±	0.0136

Table B.23: $\theta_{X,Y}$ bin contents for LiH for helical MC tracks. Statistical and systematic errors combined.

Upper edge of bin (radians)	Probability per radian			Upper edge of bin (radians)	Probability per radian		
0.001	0.246	±	0.031	0.036	1.23	±	0.12
0.002	0.671	±	0.082	0.037	1.01	±	0.10
0.003	1.15	±	0.13	0.038	0.972	±	0.102
0.004	1.35	±	0.13	0.039	0.893	±	0.098
0.005	1.72	±	0.14	0.040	0.737	±	0.086
0.006	2.11	±	0.13	0.041	0.661	±	0.081
0.007	2.30	±	0.11	0.042	0.629	±	0.082
0.008	2.64	±	0.09	0.043	0.546	±	0.074
0.009	2.95	±	0.10	0.044	0.512	±	0.073
0.010	3.26	±	0.13	0.045	0.483	±	0.071
0.011	3.20	±	0.16	0.046	0.366	±	0.056
0.012	3.38	±	0.19	0.047	0.391	±	0.061
0.013	3.47	±	0.21	0.048	0.331	±	0.053
0.014	3.69	±	0.22	0.049	0.301	±	0.049
0.015	3.61	±	0.21	0.050	0.262	±	0.043
0.016	3.67	±	0.19	0.051	0.211	±	0.035
0.017	3.79	±	0.19	0.052	0.163	±	0.028
0.018	3.58	±	0.17	0.053	0.200	±	0.034
0.019	3.42	±	0.17	0.054	0.143	±	0.025
0.020	3.32	±	0.17	0.055	0.202	±	0.037
0.021	3.37	±	0.18	0.056	0.121	±	0.023
0.022	3.14	±	0.18	0.057	0.133	±	0.026
0.023	2.90	±	0.18	0.058	0.136	±	0.029
0.024	3.06	±	0.20	0.059	0.119	±	0.027
0.025	2.88	±	0.19	0.060	0.112	±	0.027
0.026	2.72	±	0.18	0.061	0.0847	±	0.0216
0.027	2.51	±	0.16	0.062	0.0762	±	0.0207
0.028	2.30	±	0.15	0.063	0.0828	±	0.0238
0.029	2.12	±	0.14	0.064	0.0948	±	0.0287
0.030	1.97	±	0.14	0.065	0.0588	±	0.0186
0.031	1.91	±	0.14	0.066	0.0812	±	0.0266
0.032	1.80	±	0.14	0.067	0.0328	±	0.0111
0.033	1.54	±	0.13	0.068	0.0881	±	0.0304
0.034	1.45	±	0.13	0.069	0.0830	±	0.0291
0.035	1.34	±	0.12	0.070	0.0555	±	0.0196

Table B.24: θ_{3D} bin contents for LiH for helical MC. Statistical errors only.

Upper edge of bin (radians)	Change in number of entries per bin		Total systematic error	Upper edge of bin (radians)	Change in number of entries per bin		Total systematic error
	PID	LiH Density			PID	LiH Density	
0.001	0.006	0.026	0.027	0.036	0.01	0.01	0.004
0.002	0.016	0.034	0.038	0.037	0.01	0.09	0.086
0.003	0.02	0.00	0.016	0.038	0.020	0.017	0.026
0.004	0.01	0.03	0.035	0.039	0.016	0.019	0.025
0.005	0.01	0.05	0.049	0.040	0.023	0.030	0.038
0.006	0.01	0.11	0.106	0.041	0.020	0.020	0.029
0.007	0.03	0.02	0.035	0.042	0.024	0.046	0.052
0.008	0.03	0.02	0.038	0.043	0.022	0.029	0.037
0.009	0.02	0.04	0.043	0.044	0.010	0.002	0.011
0.010	0.02	0.08	0.086	0.045	0.007	0.002	0.007
0.011	0.01	0.09	0.091	0.046	0.005	0.019	0.019
0.012	0.00	0.05	0.050	0.047	0.006	0.017	0.018
0.013	0.02	0.05	0.051	0.048	0.003	0.018	0.018
0.014	0.01	0.08	0.077	0.049	0.008	0.016	0.018
0.015	0.02	0.15	0.150	0.050	0.001	0.018	0.018
0.016	0.00	0.06	0.065	0.051	0.006	0.011	0.013
0.017	0.03	0.06	0.069	0.052	0.006	0.003	0.007
0.018	0.06	0.01	0.062	0.053	0.010	0.005	0.011
0.019	0.05	0.12	0.132	0.054	0.008	0.009	0.012
0.020	0.05	0.19	0.193	0.055	0.012	0.014	0.019
0.021	0.03	0.03	0.038	0.056	0.007	0.032	0.032
0.022	0.00	0.08	0.075	0.057	0.006	0.008	0.010
0.023	0.02	0.11	0.108	0.058	0.003	0.004	0.005
0.024	0.04	0.05	0.058	0.059	0.004	0.019	0.020
0.025	0.05	0.02	0.054	0.060	0.002	0.025	0.025
0.026	0.07	0.03	0.075	0.061	0.0016	0.0183	0.018
0.027	0.05	0.10	0.111	0.062	0.0043	0.0071	0.008
0.028	0.02	0.01	0.025	0.063	0.0057	0.0058	0.008
0.029	0.00	0.04	0.043	0.064	0.0077	0.0106	0.013
0.030	0.01	0.03	0.035	0.065	0.0054	0.0087	0.010
0.031	0.02	0.09	0.087	0.066	0.0079	0.0018	0.008
0.032	0.03	0.04	0.046	0.067	0.0033	0.0058	0.007
0.033	0.02	0.03	0.042	0.068	0.0089	0.0078	0.012
0.034	0.01	0.01	0.016	0.069	0.0086	0.0028	0.009
0.035	0.01	0.02	0.018	0.070	0.0058	0.0030	0.007

Table B.25: Systematic errors on θ_{3D} bin contents for LiH for helical MC tracks.

Upper edge of bin (radians)	Probability per radian			Upper edge of bin (radians)	Probability per radian		
0.001	0.246	±	0.041	0.036	1.23	±	0.12
0.002	0.671	±	0.090	0.037	1.01	±	0.13
0.003	1.15	±	0.13	0.038	0.972	±	0.105
0.004	1.35	±	0.14	0.039	0.893	±	0.101
0.005	1.72	±	0.15	0.040	0.737	±	0.094
0.006	2.11	±	0.17	0.041	0.661	±	0.086
0.007	2.30	±	0.11	0.042	0.629	±	0.097
0.008	2.64	±	0.10	0.043	0.546	±	0.083
0.009	2.95	±	0.11	0.044	0.512	±	0.074
0.010	3.26	±	0.16	0.045	0.483	±	0.072
0.011	3.20	±	0.18	0.046	0.366	±	0.059
0.012	3.38	±	0.20	0.047	0.391	±	0.064
0.013	3.47	±	0.21	0.048	0.331	±	0.056
0.014	3.69	±	0.23	0.049	0.301	±	0.052
0.015	3.61	±	0.25	0.050	0.262	±	0.047
0.016	3.67	±	0.20	0.051	0.211	±	0.037
0.017	3.79	±	0.20	0.052	0.163	±	0.029
0.018	3.58	±	0.18	0.053	0.200	±	0.036
0.019	3.42	±	0.21	0.054	0.143	±	0.028
0.020	3.32	±	0.26	0.055	0.202	±	0.041
0.021	3.37	±	0.19	0.056	0.121	±	0.040
0.022	3.14	±	0.20	0.057	0.133	±	0.028
0.023	2.90	±	0.21	0.058	0.136	±	0.029
0.024	3.06	±	0.21	0.059	0.119	±	0.033
0.025	2.88	±	0.20	0.060	0.112	±	0.037
0.026	2.72	±	0.19	0.061	0.0847	±	0.0284
0.027	2.51	±	0.20	0.062	0.0762	±	0.0223
0.028	2.30	±	0.15	0.063	0.0828	±	0.0251
0.029	2.12	±	0.15	0.064	0.0948	±	0.0315
0.030	1.97	±	0.14	0.065	0.0588	±	0.0212
0.031	1.91	±	0.16	0.066	0.0812	±	0.0278
0.032	1.80	±	0.15	0.067	0.0328	±	0.0129
0.033	1.54	±	0.13	0.068	0.0881	±	0.0326
0.034	1.45	±	0.13	0.069	0.0830	±	0.0304
0.035	1.34	±	0.12	0.070	0.0555	±	0.0206

Table B.26: θ_{3D} bin contents for LiH for helical MC. Systematic and statistical errors combined.

Bibliography

[1] C.L. Cowan Jr., F. Reines, F.B. Harrison, H.W. Kruse and A.D. McGuire, Detection of the Free Neutrino: A Confirmation, Science 124:103 (1956)

[2] K. Kodama et al., Observation of tau neutrino interactions, Physics Letters 504B:218-224 (2001)

[3] R. Davis, A review of the Homestake solar neutrino experiment, Prog. Part. Nucl. Phys. 32:1332 (1994)

[4] D.H. Perkins, The Atmospheric neutrino problem: A Critique, Nucl. Phys. B 399, 3-14 (1993)

[5] K. Zuber, The discovery of neutrino oscillations, Annalen Phys. 528, 452-457 (2016)

[6] K. Zuber, Neutrino Physics, Second Edition, CRC Press (2012)

[7] The Super-Kamiokande Collaboration, The Super-Kamiokande detector, Nucl. Instrum. Meth. A 501:418-462 (2003)

[8] Q. R. Ahmad et al., Direct Evidence for Neutrino Flavor Transformation from Neutral-Current Interactions in the Sudbury Neutrino Observatory, Phys. Rev. Lett. 89, 011301 (2002)

[9] M. Jezabek and Y. Sumino, Neutrino mixing and see-saw mechanism, Physics Letters 440B:327-331 (1998)

[10] S. Mertens, T. Lasserre, S. Groh, F. Glueck, A. Huber, A. W. P. Poon, M. Steidl, N. Steinbrink and C. Weinheimer, Sensitivity of Next-Generation Tritium Beta-Decay Experiments for keV-Scale Sterile Neutrinos, arXiv:1409.0920v2 [physics.ins-det] (2014)

[11] KATRIN website, https://www.katrin.kit.edu

[12] NEMO Collaboration, Limits on different majoron decay modes of 100Mo and 82Se for neutrinoless double beta decays in the NEMO-3 experiment, Nuclear Physics A765:483494 (2006)

[13] R. Arnold et al., Probing New Physics Models of Neutrinoless Double Beta Decay with SuperNEMO, Eur. Phys. J. C70:927-943 (2010)

[14] SNO+ Collaboration, Current Status and Future Prospects of the SNO+ Experiment, arXiv:1508.05759v3 [physics.ins-det] (2016)

[15] MINOS+ website, http://www-numi.fnal.gov/MinosPlus/minosPlus.html

[16] A. Sousa, First MINOS+ Data and New Results from MINOS, arXiv:1502.07715v2 [hep-ex] (2015)

[17] NOvA website, https://www-nova.fnal.gov

[18] NOvA Collaboration, First measurement of muon-neutrino disappearance in NOvA, Phys. Rev. D 93, 051104 (2016)

[19] T2K Collaboration, The T2K experiment, Nucl. Instrum. Meth. A659:1:106-135 (2011)

[20] T2K collaboration, Measurement of Muon Antineutrino Oscillations with an Accelerator-Produced Off-Axis Beam, Phys. Rev. Lett. 116, 181801 (2016)

[21] K.A. Olive et al. (Particle Data Group), Chin. Phys. C, 38, 090001 (2014)

[22] S. F. King, Neutrino mass, Contemporary Physics, 48(4):195-211 (2007)

[23] R. Edgecock, Future R&D experiments for Super-Beams, Neutrino Factories and Beta-Beams, Journal of Physics: Conference Series 408, 012011 (2013)

[24] The IDS-NF collaboration. International design study for the neutrino factory: Interim design report (2011), https://www.ids-nf.org/wiki/FrontPage/Documentation

[25] The MICE Collaboration, The MICE Muon Beam on ISIS and the beam-line instrumentation of the Muon Ionization Cooling Experiment, JINST 7 P05009 arXiv:1203.4089 [physics.acc-ph] (2012)

[26] M.A. Clarke-Gayther, D.C. Faircloth, D.J.S. Findlay, F. Gerigk, P.F. Harrison, A.P. Letchford and K.R. Long, The RAL Front End Test Stand, Nuclear Physics B (Proc. Suppl.) 149:323325 (2005)

[27] K. T. McDonald et al., The MERIT High-Power Target Experiment at the CERN PS, Conf. Proc. C795 090504 (2009)

[28] EMMA website, http://www.astec.stfc.ac.uk/ASTeC/Programmes/17426.aspx

[29] E. Wilson, An introduction to Particle Accelerators, Oxford University Press (2006)

[30] K. Wille, The Physics of Particle Accelerators, an introduction, Oxford University Press (2005)

[31] C. T. Rogers, Definition of Optical Parameters in MICE, MICE Note 265

[32] J. Marriner, Stochastic Cooling Overview arXiv:physics/0308044v1 [physics.acc-ph] (2003)

[33] H. Poth, Electron cooling: Theory, experiment, application, Physics Reports, Volume 196, Issues 34 135-297 (1990)

[34] T. Carlisle, J. Cobb, The Expected Performance of MICE Step IV, Conf. Proc. C110328:151 (2011)

[35] K. Ronald, Muon Transit RF Phase Determination, MICE Note 433

[36] A. Dobbs et al., The Reconstruction Software for the MICE Scintillating Fibre Trackers, MICE Note 451

[37] The MICE Collaboration, Characterisation of the muon beams for the Muon Ionisation Cooling Experiment. Eur. Phys. J. C73 2582 (2013)

[38] R. Bertoni et.al, Analysis of PID detectors (TOF and KL) performances in the MICE 2010 run, MICE Note 337

[39] L. Cremaldi, D. Sanders, M. Drews, D. Kaplan, M. Winter, Progress on Cherenkov Reconstruction in MICE, MICE Note 473

[40] The MICE Collaboration, Electron-muon ranger: performance in the MICE muon beam, JINST 10(12), 12012 (2015)

[41] J. Allison et al., Recent developments in Geant4, Nucl. Instrum. Meth. A 835:186-225 (2016)

[42] P. Hanlet, The MICE Run Control System, J. Phys.: Conf. Ser. 513 012012 (2014)

[43] Y. Karadzhov, MICE Trigger System, MICE Note 487

[44] B. Laforge and L. Schoeffel, Elements of statistical methods in High Energy Physics analyses, Nucl. Instrum. Meth. A 394:115-120 (1997)

[45] K.A. Olive et al. (Particle Data Group), Chin. Phys. C, 38, 090001 (2014)

[46] V. N. Ivanchenko et al., Geant4 models for simulation of multiple scattering, J. Phys. Conf. Ser. 219 032045 (2010)

[47] G. Moliere, Theorie der streuung schneller geladener teilchen ii. mehrfach-und vielfachstreuung. Z. Naturforsch., 3a:78 (1948)

[48] H. Bethe. Molieres Theory of Multiple Scattering, Phys. Rev. 89:12561266 (1953)

[49] S.I. Striganov, On the theory and simulation of multiple Coulomb scattering of heavy charged particles, Radiat. Prot. Dosim. 116, 293-296 (2005)

[50] W. W. M. Allison, J. H. Cobb, S. J. Holmes, R. C. Fernow, and R. B. Palmer, Ab initio liquid hydrogen muon cooling simulations with ELMS, J. Phys. G, 34(4), 679 (2007)

[51] D. Attwood et al., The Scattering of Muons in Low Z materials. Nucl. Instrum. Meth. B, 251(1), 4155 (2006)

[52] US Muon Collaboration technical note 123, 1998. http://www-mucool.fnal.gov/notes/notes.html

[53] T. Carlisle, Step IV of the Muon Ionization Cooling Experiment (MICE) and the multiple scattering of muons, PhD thesis, University of Oxford

[54] E. Rutherford, The scattering of α and β particles by matter and the structure of the atom, Philosophical Magazine Series 6 21, 669 (1911)

[55] T. Adye, Unfolding algorithms and tests using RooUnfold, Proceedings of PHYSTAT 2011 Workshop, CERN, Geneva, Switzerland, January 2011, CERN-2011-006, 313-318 (2011)

[56] G. DAgostini, A Multidimensional unfolding method based on Bayes theorem, Nucl. Instrum. Meth. A362 487498 (1995)

[57] A. Hoecker and V. Kartvelishvili, SVD Approach to Data Unfolding, NIM A 372, 469-481 (1996)

[58] V. Kartvelishvili, Unfolding with Singular Value Decomposition, Proceedings of PHYSTAT 2011 Workshop, CERN, Geneva, Switzerland, January 2011, CERN-2011-006, 264-270 (2011)

[59] S. Boyd, private communication.

[60] G. Kafka, C.M. Lei, A. Bross, Lithium Hydride Heat Conduction and Density Study, MICE Note 448

[61] M. Green, S. Yang, Does One Know the Properties of a MICE Solid or Liquid Absorber to Better than 0.3 Percent?, MICE Note 155